ATMIRE

Title	Development of a physical metallurgy surrogate for the plutonium -1 wt. pct. gallium alloy
Item Type	Text
Authors	Gibbs, Frank E.
Publisher	Colorado School of Mines. Arthur Lakes Library
Rights	Copyright of the original work is retained by the author.
Download date	2026-11-28 09:45:21
Link to Item	https://hdl.handle.net/11124/177428

DEVELOPMENT OF A PHYSICAL METALLURGY SURROGATE FOR THE PLUTONIUM - 1 WT. PCT. GALLIUM ALLOY

by

Frank E. Gibbs

ProQuest Number: 10796759

All rights reserved

INFORMATION TO ALL USERS
The quality of this reproduction is dependent upon the quality of the copy submitted.

In the unlikely event that the author did not send a complete manuscript and there are missing pages, these will be noted. Also, if material had to be removed, a note will indicate the deletion.



ProQuest 10796759

Published by ProQuest LLC (2019). Copyright of the Dissertation is held by the Author.

All rights reserved.
This work is protected against unauthorized copying under Title 17, United States Code
Microform Edition © ProQuest LLC.

ProQuest LLC.
789 East Eisenhower Parkway
P.O. Box 1346
Ann Arbor, MI 48106 – 1346

A Thesis submitted to the Faculty and the Board of Trustees of the Colorado School of Mines in partial fulfillment of the requirements for the degree of Doctor of Philosophy in Metallurgical and Materials Engineering:

Golden, Colorado

Date: 6 April 1998

Signed: Frank E. Gibbs
Frank E. Gibbs

Approved: David L. Olson
David L. Olson
Thesis Advisor

Golden, Colorado

Date: 4/6/98

Dr. J. J. Moore
Head, Department of
Metallurgical Engineering

ABSTRACT

Several binary alloys were investigated for the potential to act as a surrogate for the plutonium - 1 wt. pct. gallium alloy. Two alloys, cerium - 5 wt. pct. neodymium and cerium - 5 wt. pct. lanthanum were shown to exhibit microsegregation similar to that seen in the plutonium - 1 wt. pct. gallium alloy. A homogenization experiment was conducted using the cerium - 5 wt. pct. lanthanum alloy to measure the activation energy for interdiffusion which was then analytically linked to the activation for interdiffusion in the plutonium alloy. Using this initial grounding point, and a fundamental connection between the electronic behavior of f-electrons in plutonium and cerium, several correlations between the behavior of plutonium and cerium were identified. Similarities in crystal structure, phase transformation characteristics, and mechanical properties were identified justifying the use of the cerium - 5 wt. pct. alloy as a metallurgical surrogate for plutonium - 1 wt. pct. gallium.

TABLE OF CONTENTS

ABSTRACT iii

LIST OF FIGURES vi

LIST OF TABLES xviii

ACKNOWLEDGEMENTS xxii

Chapter 1. INTRODUCTION 1

1.1 Overview 1
1.2 Statement of the Problem 3

Chapter 2. BACKGROUND 5

2.1 Introduction to Plutonium Metallurgy 5
2.2 Electronic Structure of Plutonium 8
2.3 Phase Transformation Behavior in Plutonium 13
2.4 Theory of Alloying 24
2.5 Plutonium-Gallium System 28
2.6 Diffusion Theory 48
2.7 Effect of Iron on the Diffusion of Gallium 52
2.8 Processing Impacts of Phase Transformations and the Diffusion Of Gallium 57
2.9 Surrogate Candidates 59
2.10 Rare-Earth Elements - Electronic Structure 63
2.11 Generalized Phase Diagram for the Rare-Earths 64
2.12 Comparison of the Rare-Earths to the Actinides 70
2.13 Comparison of Cerium to Plutonium 72
2.14 Diffusion of ^{140}La in bcc- γ-Lanthanum and δ-Cerium 75

Chapter 3. EXPERIMENTAL PROGRAM 78

3.1 Initial Experimental Work - Identification of a Cored Surrogate 78
3.2 Alloy Preparation 78
3.3 Cerium - Neodymium 80
3.4 Cerium - Lanthanum 96
3.5 Experimental Work - Measurement of Ce-La Diffusion Parameters 113

Chapter 4. RESULTS AND DISCUSSION 118

4.1 Onset of Lanthanum Microsegregation 118
4.2 Characterization of Microsegregation 126
4.3 Cerium - Lanthanum Homogenization 130
4.4 Determination of Activation Energy for Diffusion 162
4.5 Surrogate Relationship 175
4.6 Phase Transformations in Cerium 179
4.7 Metallurgical Surrogate 189
4.8 Case Studies 192

Chapter 5 CONCLUSIONS 198

REFERENCES 200

APPENDIX A 205

APPENDIX B 209

APPENDIX C 226

APPENDIX D 228

APPENDIX E 231

APPENDIX F 233

LIST OF FIGURES

Figure	Title	Page
1	Idealized temperature expansion behavior for plutonium [2].	7
2	The connected schematic binary alloy phase diagrams for the light actinides. The diagrams for Ac through U and for Am/Cm are estimates based upon the pure elements. The crystal structures are indicated on the figure[3].	9
3	Decrease in atomic volume with a minimum at plutonium and neptunium with localization of 5f electrons and significant increase in atomic volume starting at americium [4].	10
4	Minimization of crystal energy with respect to atomic volume. Calculated minimum energy shown to be alpha-Pu structure for plutonium [4].	12
5	Effect of beta plastic deformation at 140 C on the plutonium beta to alpha transformation at 80 C [8].	16
6	The Time-Temperature-Transformation curve for the beta to alpha transformation of plutonium [8].	17
7	The Time-Temperature-Transformation curve of the alpha to beta transformation of plutonium [8].	19
8	Dilatometer trace for the transition between the delta to gamma and gamma to delta phase transformation [10].	21
9	The Time-Temperature-Transformation curve of the delta to alpha transformation in a plutonium - 0.7 at. pct. gallium alloy [13].	23
10	Darken-Gurry map for determining which elements are favored for solution in delta plutonium. Only key elements were reproduced [15].	26

Figure	Title	Page
11	The plutonium-gallium phase diagram [2].	29
12	Partial plutonium-gallium phase diagram with focus on the plutonium-1 wt. pct. gallium alloy region. Alloy of interest is at 1 wt. pct. gallium [2].	30
13	Typical microstructure of plutonium 1 wt. pct. gallium alloy. Approximate core size is 30 um [22].	33
14	Partial plutonium-gallium phase diagram showing procedure for determining the gallium profile using the lever rule [22].	34
15	Gallium concentration profiles (measured) superimposed over theoretical curve. Data points were taken from electron microscopy measurements [22].	36
16	Partitioning coefficient plotted as a function of temperature for the plutonium - 1 wt. pct. gallium alloy calculated from the plutonium-gallium phase diagram.	40
17	Variation of gallium across a plutonium grain as predicted by the Scheil equation. A 40 um spherical grain was assumed in the calculation. Plot shows variation across half of a grain (20 um).	41
18	"Shell" model proposed by Erfurdt to describe the coring in plutonium - 1 wt. pct. gallium. Formation of Pu_6Fe is also shown in the triple point [2].	42
19	Relation between cooling rate from 540 to 590 deg C and grain size in cored plutonium - 1 wt. pct. gallium stabilized alloy [18].	43
20	Schematic reproduction of concentration-penetration profile for typical diffusion couple from Edwards et al [24].	46
21	Arrhenius plot for interdiffusion in delta plutonium: unalloyed delta plutonium and gallium stabilized. Reproduced from Edwards et al [24].	48
22	The activation energy for self-diffusion as a function of the melting temperature of bcc and fcc metals [26].	53

Figure	Title	Page
23	Schematic phase diagram for a metatectic phase transformation with applicable schematics of the Gibbs free energy relationships for each phase. Re-melting as a result of the phase transformation is believed to enhance diffusion [30].	57
24	Plot of the calculated mean radii <r> of the trivalent ions of the lanthanides and actinides, and of the experimental ionic radii for these ions [33].	65
25	Plot of the 4f, 5s, and 5p wave functions of Nd(3+) (rare earth) and the 5f, 6s, and 6p wave functions of U(3+) (actinide) [33].	66
26	Generalized phase diagram for the lanthanides. Each rare earth phase diagram was assembled on to the temperature/pressure diagram such that the phase transformation fell on a straight line. Note that in the case of the hcp to Sm transition, the line of transformation also coincided with the respective melting curves. The points represent actual measured data [31].	68
27	a)The atomic volume of the rare earth elements excluding europium and ytterbium. b) Ratio F between the Wigner-Seitz and the ionic radius for the rare earth elements. Note as pressure increases, R_{ws} decreases, F decreases and behavior reflects that of a lighter (larger volume) material [26,31].	69
28	Photograph of magnesium oxide crucibles used to cast cerium alloys. The cylindrical crucibles were used to produce castings with dimensions near to the finished dimensions required for the Gleeble thermo-mechanical apparatus. This "near-net-shape" casting minimized the production of cerium machining chips which are pyrophoric.	79
29	Photograph of vacuum furnace used to cast cerium alloys.	81
30	Schematic representation of the cerium-neodymium phase diagram showing a two-phase region which may lead to solid state microsegregation and thus a potential candidate for a plutonium-1 wt. pct. gallium surrogate. The two-phase region is exaggerated in this figure to show its location. The actual region is reported to be narrower [43].	82

Figure	Title	Page
31	Casting setup for the initial cerium-neodymium alloy to investigate the potential for microsegregation of neodymium. Shown are the mass balance for the casting and the furnace temperature profile. The sample was furnace cooled.	83
32	Photomicrograph of a cerium -5 wt. pct. neodymium sample furnace cooled through the two-phase region. Grain structure was poorly defined, but due to lack of microsegregation , no further preparation was performed. Magnification was 200X.	85
33	Microprobe trace of cerium - ~ 6 wt. pct. neodymium alloy of furnace cooled specimen showing essentially homogeneous distribution of neodymium. Neodymium concentration variation approximately 0.2 wt. pct.	86
34	Schematic of Gleeble thermo-mechanical setup used to obtain an enhanced cooling rate for cerium-neodymium alloy. Result was the melting of the specimen at the center.	88
35	Casting setup for two cerium-neodymium alloys to be machined and then inserted into the Gleeble instrument for rapid cooling through the two-phase region. Shown are the mass balance for the castings and the furnace temperature profile. The furnace treatment included a homogenization treatment to ensure adequate distribution of the neodymium. These samples were then heated in the Gleeble to above the two-phase region and then air-cooled rapidly to promote microsegregation of the neodymium.	90
36	Temperature data from cerium-neodymium run with the Gleeble instrument. Data stopped recording when specimen melted in the center and the thermocouple fell off of specimen. Cooling at the center of the specimen was a rapid air-quench as shown.	91
37	Temperature data from the second cerium-neodymium run with Gleeble instrument. Data stopped recording when specimen melted in the center and the thermocouple fell of specimen. Cooling at the center of the specimen was a rapid air-quench as shown.	92

Figure	Title	Page
38	Schematic of metallographic mount from cerium-neodymium Gleeble specimen. Area of interest is adjacent to melted zone which reached a temperature greater than the two-phase region and was cooled quickly through this region.	93
39	Photomicrograph of cerium-neodymium specimens rapidly cooled using the Gleeble instrument. Specimen was polished and allowed to oxidize slightly to highlight grain boundaries. Magnification is 200 X and approximate grain size is 12-20 um. Microprobe scan traversed approximately 5 grains.	94
40	Photomicrograph of cerium-neodymium Gleeble specimen with corresponding microprobe trace showing the concentration variation of neodymium. Approximate grain size is 12-20 um and microprobe scan traversed approximately 5 grains. Note the variation in neodymium is approximately equivalent to the grain size. Neodymium variation suggests microsegregation due to the incomplete homogenization of neodymium during the delta to gamma cerium phase transformation. Detection limit for neodymium was ±0.057 wt. pct. using a wavelength dispersive spectrometer.	95
41	Schematic representation of lanthanum-cerium phase diagram showing two-phase region which may lead to solid state microsegregation and thus a potential candidate for a plutonium - 1 wt. pct. gallium surrogate. The two-phase region is exaggerated to show its location. The actual region is reported to be much narrower [36].	98
42	Casting setup for the initial cerium-lanthanum alloy to investigate the potential for microsegregation of lanthanum. Shown are the mass balance for the casting and the furnace temperature profile. The sample was furnace cooled.	99
43	Photomicrograph of initial cerium-lanthanum alloy subjected to a furnace cool. Approximate grain size is 200 um. No appreciable microsegregation of lanthanum was seen in this sample.	100

Figure	Title	Page
44	Microprobe data from initial furnace cooled cerium lanthanum sample. Lanthanum concentration is essentially homogeneous. A faster cooling rate will be investigated to determine if microsegregation can be induced. The lanthanum detection limit was ± 0.071 wt. pct.	101
45	Casting setup for a cerium-lanthanum alloy to investigate the potential for microsegregation of lanthanum in a casting subjected to enhanced cooling with argon gas. Shown are the mass balance for the casting and the overall furnace temperature profile. An expanded plot of the cooling profile is given in a later figure.	104
46	Casting setup for a cerium-lanthanum alloy to investigate the potential for microsegregation of lanthanum in a casting subjected to enhanced cooling with helium gas. Shown are the mass balance for the casting and the overall furnace temperature profile. An expanded plot of the cooling profile is given in a later figure.	105
47	Furnace temperature data taken during both argon and helium gas cooling of the cerium-lanthanum alloy. Gas was introduced into the vacuum furnace to increase cooling and thereby promoting the microsegregation of lanthanum. The cooling rate achieved with argon was 30°C/min while the rate with helium was 60°C/min.	106
48	Microprobe trace for cerium-lanthanum alloy. This alloy was cooled using an argon backfill resulting in a 30°C/min cooling rate through the two-phase region. Some microsegregation is evident but not conclusive. Lanthanum detection limit was +/- 0.07 wt. pct.	107
49	Microprobe trace for cerium-lanthanum alloy. This alloy was cooled using a helium backfill resulting in a 60°C/min cooling rate through the two-phase region. A 200 μm trace was run for this sample and the results indicate that microsegregation has occurred. Further experiments with this alloy are warranted. Lanthanum detection limit was +/- 0.05 wt. pct.	108

Figure	Title	Page
50	Photomicrograph showing cerium-lanthanum alloy subjected to helium gas cooling which resulted in a cooling rate of 60°C/min. Microprobe results indicate a microsegregation of lanthanum commensurate with the approximate grain size of 80 μm.	112
51	Experimental approach used by Johnson [21] to determine homogenization response of plutonium-1wt. pct. gallium alloys. Activation energy for diffusion and an interdiffusion coefficient was determined using the rate at which homogenization was achieved.	114
52	Microprobe data showing the lanthanum concentration variation for a distance of 400 μm. This alloy had a nominal lanthanum concentration of 1.8 wt. pct. and provides some indication of the onset of microsegregation of lanthanum and the extent of the two-phase region.	120
53	Partitioning coefficient plotted as a function of temperature for a nominal cerium-5.5 wt. pct lanthanum alloy calculated from the cerium-lanthanum phase diagram. An estimate of the width of the two-phase region was made from the limited phase diagram data and the lever rule was used to calculate the distribution of lanthanum. The calculated variation in lanthanum was then compared to the actual coring data.	124
54	Assuming the upper transformation line of the $\gamma + \delta$ two-phase region was established, the lanthanum coring data for a nominal 5.5 wt. pct. alloy was used to predict the degree of microsegregation. A 70 μm diameter spherical grain was assumed for this calculation and the prediction for one half of a grain is shown. The calculation was made using the lever law, an intermediate calculation of the partitioning coefficient and the Scheil equation as described earlier.	125

Figure	Title	Page
55	Lanthanum concentration profile measured through the center of a grain from a cerium-lanthanum alloy subjected to helium cooling. Concentration profiles taken across the grain show lanthanum microsegregation due to the rapid cooling through the $\gamma + \delta$ two-phase region. This profile through the center of the grain indicates a constant lanthanum concentration that supports the conclusion that the segregation is transverse to the grain and is due to this phase transformation.	127
56	Photomicrograph showing microprobe scan of cerium-lanthanum specimen subjected to helium gas cooling to promote lanthanum microsegregation. Scan was made in the center of the grain for comparison to transverse scans showing significant microsegregation. Plot in Figure 55 shows very little microsegregation of lanthanum in the center of the grain.	129
57	Lanthanum concentration variation for sample cooled through the $\gamma + \delta$ two-phase region at 60°C/min via helium cooling and then homogenized at 546°C for four hours. This sample showed significant microsegregation of lanthanum due to the phase transformation.	131
58	Lanthanum concentration variation for sample cooled through the $\gamma + \delta$ two-phase region at 60°C/min via helium cooling and then homogenized at 546°C for twenty hours. This sample showed limited microsegregation of lanthanum due to the homogenization.	132
59	Lanthanum concentration variation for sample cooled through the $\gamma + \delta$ two-phase region at 60°C/min via helium cooling and then homogenized at 546°C for thirty-six hours. This sample showed substantial homogenization resulting in a flat concentration profile.	133
60	Lanthanum concentration variation for sample cooled through the $\gamma + \delta$ two-phase region at 60°C/min via helium cooling and then homogenized at 585°C for four hours. This sample showed significant homogenization resulting in a relatively small variation in the concentration profile.	134

Figure	Title	Page
61	Lanthanum concentration variation for sample cooled through the $\gamma + \delta$ two-phase region at 60°C/min via helium cooling and then homogenized at 585°C for eight hours. This sample showed significant homogenization resulting in a relatively small variation in the concentration profile. The significant drop in lanthanum concentration at approximately 140 μm was attributed to a microstructural defect and not representative of an actual variation in lanthanum concentration.	135
62	Lanthanum concentration variation for sample cooled through the $\gamma + \delta$ two-phase region at 60°C/min via helium cooling and then homogenized at 585°C for twenty hours. This sample showed complete homogenization resulting in essentially no variation in the lanthanum concentration profile.	136
63	Lanthanum concentration variation for sample cooled through the $\gamma + \delta$ two-phase region at 60°C/min via helium cooling and then homogenized at 633°C for four hours. This sample showed significant lanthanum microsegregation due to the phase transformation.	137
64	Lanthanum concentration variation for sample cooled through the $\gamma + \delta$ two-phase region at 60°C/min via helium cooling and then homogenized at 633°C for eight hours. This sample showed minimal lanthanum microsegregation due to homogenization.	138
65	Lanthanum concentration variation for sample cooled through the $\gamma + \delta$ two-phase region at 60°C/min via helium cooling and then homogenized at 633°C for twelve hours. This sample showed significant lanthanum microsegregation due to the higher lanthanum concentration resulting in cooling through a wider section of the two-phase region.	139
66	Lanthanum concentration variation for sample cooled through the $\gamma + \delta$ two-phase region at 60°C/min via helium cooling and then homogenized at 633°C for twenty-four hours. This sample showed complete homogenization resulting in essentially no variation in the lanthanum concentration profile.	140

Figure	Title	Page
67	Photomicrograph of cerium-lanthanum alloy subjected to helium cooling through the two-phase $\gamma + \delta$ region at 60°C/min. Sample was homogenized at 546°C for four hours. Sample was over-etched to highlight the grain boundaries. Average grain size was 90 μm.	151
68	Photomicrograph of cerium-lanthanum alloy subjected to helium cooling through the two-phase $\gamma + \delta$ region at 60°C/min. Sample was homogenized at 546°C for twenty hours. Average grain size was 100 μm.	152
69	Photomicrograph of cerium-lanthanum alloy subjected to helium cooling through the two-phase $\gamma + \delta$ region at 60°C/min. Sample was homogenized at 546°C for thirty-six hours. Average grain size was 100 μm.	153
70	Photomicrograph of cerium-lanthanum alloy subjected to helium cooling through the two-phase $\gamma + \delta$ region at 60°C/min. Sample was homogenized at 585°C for four hours. Average grain size was 100 μm.	154
71	Photomicrograph of cerium-lanthanum alloy subjected to helium cooling through the two-phase $\gamma + \delta$ region at 60°C/min. Sample was homogenized at 585°C for eight hours. Average grain size was 100 μm.	155
72	Photomicrograph of cerium-lanthanum alloy subjected to helium cooling through the two-phase $\gamma + \delta$ region at 60°C/min. Sample was homogenized at 585°C for twenty hours. Average grain size was 100 μm.	156
73	Photomicrograph of cerium-lanthanum alloy subjected to helium cooling through the two-phase $\gamma + \delta$ region at 60°C/min. Sample was homogenized at 633°C for four hours. Average grain size was 110 μm.	157
74	Photomicrograph of cerium-lanthanum alloy subjected to helium cooling through the two-phase $\gamma + \delta$ region at 60°C/min. Sample was homogenized at 633°C for eight hours. Average grain size was 115 μm.	158
75	Photomicrograph of cerium-lanthanum alloy subjected to helium cooling through the two-phase $\gamma + \delta$ region at 60°C/min. Sample was homogenized at 633°C for twelve hours. Average grain size was 100 μm.	159

Figure	Title	Page
76	Photomicrograph of cerium-lanthanum alloy subjected to helium cooling through the two-phase $\gamma + \delta$ region at 60°C/min. Sample was homogenized at 633°C for twenty-four hours. Average grain size was 100 μm.	160
77	The effect of diffusion on a sinusoidal variation of the lanthanum composition [23]	164
78	The natural log of the lanthanum concentration variation is plotted as a function of homogenization time. Homogenization temperature was 546 C. The exponential regression parameters are listed in Table XXX. The degree of microsegregation was determined by averaging the profile peaks taken from the electron microprobe peaks.	167
79	The natural log of the lanthanum concentration variation is plotted as a function of homogenization time. Homogenization temperature was 585 C. The exponential regression parameters are listed in Table XXX. The degree of microsegregation was determined by averaging the profile peaks taken from the electron microprobe peaks.	168
80	The natural log of the lanthanum concentration variation is plotted as a function of homogenization time. Homogenization temperature was 633 C. The exponential regression parameters are listed in Table XXX. The degree of microsegregation was determined by averaging the profile peaks taken from the electron microprobe peaks.	169
81	Plot used to determine the activation energy for diffusion utilizing the rate of homogenization. The rate equation is shown above based on a regression analysis. The correlation factor (R^2) was 0.8.	171
82	Relationship between the plutonium - 1 wt. pct. gallium alloy and cerium - 5 wt. pct. lanthanum alloy for an equivalent homogenization rate as detailed in the text.	178

Figure	Title	Page
83	Pseudo - equilibrium pressure - temperature diagram for cerium. Cerium is the only material known to exhibit a solid-solid critical point (C.P.) [47].	183
84	The non-equilibrium phase diagram for cerium. Results were averaged based on several studies. The significant hysteresis effects are shown on the diagram.[47].	185
85	Schematic diagram showing the behavior of cerium upon cooling [47]	186
86	Proposed cerium temperature-pressure diagram [48].	195
87	Temperature-pressure diagram for plutonium [48].	196

LIST OF TABLES

Table	Title	Page
I	Crystal structure data for plutonium [2].	6
II	Phase transformation temperatures and associated volume changes for plutonium [5].	14
III	Temperature and concentration data taken from the plutonium-gallium phase diagram. This data was used to calculate the partitioning coefficient to describe the coring which occurs in the $\varepsilon + \delta$ two-phase region [2].	39
IV	Variable definitions in the diffusion equation.	51
V	Self diffusion data for rare earth metals with close packed crystal structures [26].	54
VI	Self diffusion data for rare earth metals with bcc crystal structures [26].	55
VII	The rare earth and actinide series[26].	62
VIII	Correlation between the actinides and the rare earth elements. Rare earths are shifted to align materials with similar properties [33].	71
IX	Comparison between crystal structures and density of cerium and plutonium [31,36,37,38,39].	74
X	Summary of diffusion data for cerium-lanthanum alloys showing the significant difference between the bcc phases and the fcc phases [41].	76
XI	Microprobe data from initial cerium - 5 wt. pct. alloy as plotted in Figure 33. The beam size 1 um with detection limits of the first reported point was ± 0.061 wt. pct. neodymium.	87

Table	Title	Page
XII	Raw data from microprobe scan of cerium-neodymium specimen subjected to air quench using the Gleeble instrument. Data is plotted in Figure 40 and indicates a variation in neodymium resulting from cooling through the two-phase region.	97
XIII	Raw data from microprobe scan of initial cerium-lanthanum specimen subjected to a furnace cool. Data is plotted in Figure 44 indicating a homogeneous distribution of lanthanum.	102
XIV	Raw data from microprobe scan of cerium-lanthanum specimen subjected to argon gas cooling. Cooling rate through the two-phase region was measured at 30°C/min. Data is plotted in Figure 48 which did not conclusively indicate microsegregation of lanthanum.	109
XV	Raw data from microprobe scan of cerium-lanthanum specimen subjected to helium gas cooling. Cooling rate through the two-phase region was measured at 60°C/min. Data is plotted in Figure 49 which indicated microsegregation of lanthanum.	110
XVI	Experimental matrix for a nominal cerium - 5 wt. pct. lanthanum alloy for the determination of the activation energy for diffusion. Utilizing a similar approach used by Johnson, initially cored specimens were annealed at the times and temperatures listed to determine a rate of homogenization. The log of the rate of homogenization is then plotted as a function of absolute temperature and by calculating the slope, the activation energy for interdiffusion is determined.	117
XVII	Raw data from microprobe scan of cerium-lanthanum specimen subjected to helium gas cooling to promote microsegregation of lanthanum. Nominal alloy was prepared with 1.8 wt. pct. lanthanum to identify the onset of lanthanum segregation.	121
XVIII	Lever rule model for a nominal cerium - 5 wt. pct. lanthanum alloy. The width of the two-phase region was estimated in order to calculate the partitioning coefficient. The Scheil equation was then used to predict the lanthanum variation across a grain with a 70 um diameter such that the variation matched microsegregation seen from this experimental work.	122

Table	Title	Page
XIX	Raw data from microprobe scan of cerium-lanthanum specimen subjected to helium gas cooling to promote lanthanum microsegregation. Scan was made in the center of the grain for comparison to transverse scans showing significant coring.	128
XX	Raw data from microprobe scan of cerium-lanthanum specimen subjected to helium gas cooling to promote lanthanum microsegregation. Following helium cooling this sample was homogenized for four hours at 546°C. Scan indicated significant microsegregation of lanthanum corresponding to the measure grain size.	141
XXI	Raw data from microprobe scan of cerium-lanthanum specimen subjected to helium gas cooling to promote lanthanum microsegregation. Following helium cooling this sample was homogenized for twenty hours at 546°C. Scan indicated slight microsegregation of lanthanum suggesting nearly complete homogenization.	142
XXII	Raw data from microprobe scan of cerium-lanthanum specimen subjected to helium gas cooling to promote lanthanum microsegregation. Following helium cooling this sample was homogenized for thirty-six hours at 546°C. Scan indicated no microsegregation of lanthanum suggesting complete homogenization.	143
XXIII	Raw data from microprobe scan of cerium-lanthanum specimen subjected to helium gas cooling to promote lanthanum microsegregation. Following helium cooling this sample was homogenized for four hours at 585°C. Scan indicated microsegregation of lanthanum suggesting incomplete homogenization.	144
XXIV	Raw data from microprobe scan of cerium-lanthanum specimen subjected to helium gas cooling to promote lanthanum microsegregation. Following helium cooling this sample was homogenized for eight hours at 585°C. Scan indicated some microsegregation of lanthanum suggesting significant homogenization.	145
XXV	Raw data from microprobe scan of cerium-lanthanum specimen subjected to helium gas cooling to promote lanthanum microsegregation. Following helium cooling this sample was homogenized for twenty hours at 585°C. Scan indicated complete homogenization of lanthanum.	146

Table	Title	Page
XXVI	Raw data from microprobe scan of cerium-lanthanum specimen subjected to helium gas cooling to promote lanthanum microsegregation. Following helium cooling this sample was homogenized for four hours at 633°C. Scan indicated complete homogenization of lanthanum.	147
XXVII	Raw data from microprobe scan of cerium-lanthanum specimen subjected to helium gas cooling to promote lanthanum microsegregation. Following helium cooling this sample was homogenized for eight hours at 633°C. Scan indicated essentially complete homogenization of lanthanum	148
XXVIII	Raw data from microprobe scan of cerium-lanthanum specimen subjected to helium gas cooling to promote lanthanum microsegregation. Following helium cooling this sample was homogenized for twelve hours at 633°C. Scan indicated essentially complete homogenization of lanthanum.	149
XXIX	Raw data from microprobe scan of cerium-lanthanum specimen subjected to helium gas cooling to promote lanthanum microsegregation. Following helium cooling this sample was homogenized for twenty-four hours at 633°C. Scan indicated complete homogenization of lanthanum.	150
XXX	Data showing the degree of microsegregation as a function of homogenization temperature and time. Initial variation in lanthanum prior to homogenization was shown to be 0.5 wt. pct. on average. Raw data is plotted in Figures 78, 79 and 80 with the exponential regression lines plotted according to the regression results shown.	166
XXXI	Homogenization rate data used to determine the activation energy for diffusion as plotted in Figure 81. Regression data is also shown.	170
XXXII	Predicted homogenization temperatures for a cerium - 5 wt. pct. lanthanum alloy to be used as a surrogate for a plutonium - 1 wt. pct. gallium alloy.	177
XXXIII	Determination of equivalent cerium - 5 wt. pct. lanthanum homogenization parameters for homogenization time and temperatures for the plutonium - 1 wt. pct. gallium alloy.	
XXXIV	Crystal structures and lattice data for cerium phases.	180
XXXV	Phase transformation temperatures for cerium	181

ACKNOWLEDGEMENTS

I would like to thank the members of my thesis committee for their guidance, expertise, support and patience throughout this work. Committee members include Dr. David Olson, Dr. Fred Fraikor, Dr. Graham Mustoe, Dr. Bajendra Mishra, and Dr. Jim Selle. I would like to specifically thank Dr. David Olson for his faith in me, and his unique dedication to teaching. I would also like to thank Dr. Jim Selle whose mentoring and friendship has helped to guide my academic, professional, and personal life. Thanks to Mr. Butch Brewer whose expertise in the metallographic preparation of cerium was key to the success of this work. Several individuals from the Los Alamos National Laboratory have my sincere thanks including Mr. Bill Hutchinson for his expertise in conducting the microprobe analyses. Additionally, I would like to thank Dr. Bill McKerley for allowing the use of the laboratory and Dr. Mike Stevens for both technical and monetary support that was key to the completion of this work. No academic pursuit is possible without the support of friends and family which was critical particularly during the long nights. Finally, my love to my wife, Celeste, whose encouragement and patience somehow continued through the long study hours and the graveyard shifts.

1.0 INTRODUCTION

1.1 Overview

Metallurgical research involving plutonium and plutonium alloys has been ongoing since the establishment of the Manhattan Project. Extensive characterization studies are difficult due to the radiological hazards in handling plutonium, however fundamental investigations have provided a basis understanding of plutonium metallurgy. Future research with plutonium is expected to be limited due to the downsizing of the nuclear weapons complex, reduced funding levels, and a focus on environmental remediation of nuclear weapons manufacturing sites where plutonium metallurgical research was formerly conducted. The need to develop a better understanding of the chemical behavior of plutonium has not been reduced however, in view of the difficult issues still associated with the weapons complex. These issues include establishing processes for recovery of plutonium in high level residues, identifying process parameters in the development of long term storage forms, and maintaining existing recovery manufacturing technologies including process development capability. These factors provide a strong argument for the development of material surrogates for plutonium.

Surrogate materials, substitutes which exhibit similar behavior but do not present the health or environmental hazards, can provide a way to meet the needs of the weapons complex with significantly reduced risks and costs. Surrogates have been used successfully in plutonium manufacturing applications such as in the case of aluminum.

Aluminum has a similar melting point (Al - T_{mp} = 627°C, Pu - T_{mp} = 640°C) and is typically used as a "casting surrogate". In addition, aluminum has a similar crystal structure and tensile properties as δ-phase plutonium and has been used as a surrogate in forming operations. Additionally, cerium was demonstrated as a successful surrogate for plutonium electro-refining [1]. The key to finding a surrogate for plutonium is to identify a surrogate or family of surrogates that are not focused on just one property, but are justified based on fundamental aspects such as electronic structure and atomic interaction. Once the fundamental relationship is established, a series of material properties can be related including phase transformation behavior, atomic transport, and alloying behavior.

An area of particular interest in plutonium metallurgy and one that has been reasonably well studied, is the plutonium - gallium system and more specifically, the plutonium - 1 wt. pct. gallium alloy. This alloy exhibits solid state microsegregation of gallium that causes a dramatic impact on the cast microstructure. Homogenization is required to achieve consistent properties. This alloy provided an excellent starting point for the identification of a viable surrogate for plutonium in both fundamental research and in several manufacturing applications.

The following investigation is broken into five major components. First, a literature survey was conducted to both provide an overall introduction to plutonium metallurgy and to summarize the studies which have been conducted on the plutonium - 1 wt. pct. gallium alloy. Second, an investigation of potential surrogate systems was undertaken using factors such as electronic structure, crystal structure, and phase

transformation behavior to identify promising candidates. Third, using the results from this preliminary research, an experimental program was initiated to identify candidates which demonstrated the solid state microsegregation of solute seen in the plutonium - 1 wt. pct. gallium alloy. Fourth, an experimental matrix was created to measure the interdiffusion coefficient for the surrogate system such that the homogenization of solute in the surrogate could be analytically related to the plutonium system. Finally, several fundamental correlations between the two systems were drawn to establish the surrogate alloy not only as an homogenization surrogate, but justify it as an overall metallurgical surrogate for the plutonium - 1 wt. pct. gallium alloy.

1.2 Statement of the Problem

A strong justification for the need to develop a metallurgical surrogate for plutonium has been established. The plutonium - 1 wt. pct. gallium alloy presents a pathway to identification of a surrogate(s) by developing a connection to the relatively well studied homogenization of the gallium solute. This "homogenization surrogate" can be used to further explore the interdiffusion phenomena, but more importantly provides a grounding point to study other transport-related areas in plutonium metallurgy using the surrogate. Examples include the impact of impurities on the homogenization process, phase transformation behavior, and creep processes. The following questions will be explored in the course of this investigation:

1. Can a surrogate or surrogates be identified which exhibit similar phase transformation behavior and solid state micro segregation as the plutonium - 1 wt. pct. gallium system?

2. Does the surrogate candidate show a similar homogenization response?

3. What other fundamental connections (e.g., crystal structure, phase transformations, electronic structure) can be made between the surrogate and plutonium?

4. What is the analytical relationship between the interdiffusion of the surrogate material and the plutonium - 1 wt. pct. gallium alloy?

5. Given the analytical relationship between the fundamental transport properties of the surrogate and plutonium, can a basis be developed for an overall physical metallurgy surrogate?

This work was initiated to answer these questions and to identify areas of future work in the development of a metallurgical surrogate or family of surrogates for plutonium.

2.0 BACKGROUND

2.1 Introduction to Plutonium Metallurgy

Plutonium presents significant radiological hazards and must therefore be handled and processed inside gloveboxes. Because of its reactivity, it must be cast under vacuum and because of its pyrophoricity, cutting or machining must be performed in inert conditions. Once the difficult handling and processing rigors are overcome, one finds that plutonium exhibits interesting and unusual metallurgical behavior. Unalloyed plutonium solidifies at 640°C and undergoes six allotropic phase transformations upon cooling to room temperature. Crystal structure data are given in Table I [2]. Figure 1 [2] gives an idealized thermal expansion curve from melting to room temperature showing the large volume change associated with many of the solid state transformations. The low symmetry crystal structures and the large volume changes present several challenges in manufacturing applications, particularly casting. This behavior was one of the key reasons for interest in the plutonium - gallium system due to the stabilization of the delta phase with its face-centered cubic crystal structure that offers a big advantage in wrought operations.

Table I: Crystal structure data for plutonium [2].

Phase	Stability Range (°C)	Space Lattice	Unit Cell Dimensions, Angstroms	Atoms/ Unit Cell	Density g/cm^3
α	Below ~ 115	Simple Monoclinic	T = 21°C a = 6.183 +/- 0.001 b = 4.822 +/- 0.001 c = 10.963 +/- 0.001 β = 101.79° +/- 0.01°	16	19.86
β	~ 115 - 200	Body-centered Monoclinic	T = 190°C a = 9.284 +/- 0.003 b = 10.463 +/- 0.004 c = 7.859 +/- 0.003 β = 92.13° +/- 0.03°	34	17.70
γ	200 - 310	Face-centered Orthorhombic	T = 235°C a = 3.159 +/- 0.001 b = 5.768 +/- 0.001 c = 10.162 +/- 0.002	8	17.14
δ	310 - 452	Face-centered Cubic	T = 320°C a = 4.6371 +/- 0.0004	4	15.92
δ'	452 - 480	Body-centered Tetragonal	T = 465°C a = 3.34 +/- 0.01 c = 4.44 +/- 0.04	2	16.00
ε	480 - 640	Body-centered Cubic	T = 490°C a = 3.6361 +/- 0.0004	2	16.51

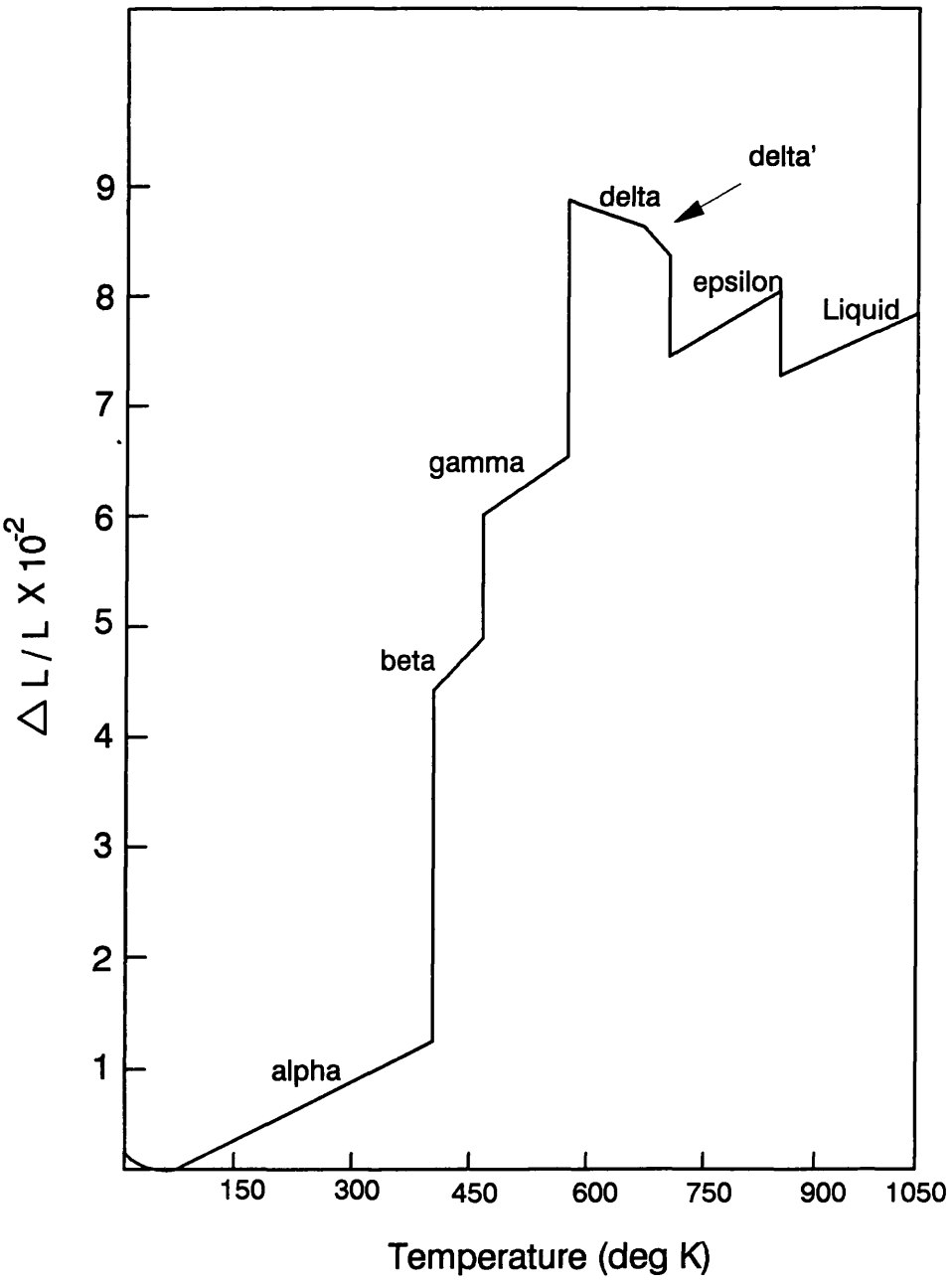

Figure 1: Idealized temperature expansion behavior of plutonium [2]

2.2 Electronic Structure of Plutonium

Carnal and Choppin [3] summarized the importance of the electronic structure of plutonium on the resulting properties and crystal structures. Figure 2 shows this impact on the crystal structures of the actinides highlighting the dramatic anisotropy seen with plutonium. Carnal and Choppin suggest that it is the behavior of the 5f electrons that reside in an itinerant state, both conducting and bonding that influence the crystal structure. As the f-band drops below the Fermi energy level, the crystallographic distortion is evident as with the alpha-phase of plutonium which has a monoclinic structure. The f-electrons in plutonium can be influenced relatively easily (and therefore the crystal structure) with the addition of small amounts of impurities or with the application of pressure.

The electronic structure of plutonium has been shown to have a direct relationship to the complex properties, crystal structure, and phase transformation behavior of plutonium. Plutonium is located at a position within the Periodic Table of the Elements where a transition of the 5f electron states change from a de-localized state to a localized state. Johansson and Eriksson [4] have analytically described the electronic behavior of plutonium to provide insight into its complex behavior. Experimental evidence for the de-localized, or itinerant behavior of the 5f electrons in the light actinide elements is seen in the change in atomic volume (or density) as a function of nuclear charge. Figure 3 shows a parabolic decrease in atomic volume for increasing nuclear charge with plutonium and neptunium at a minimum. The atomic volume of americium is

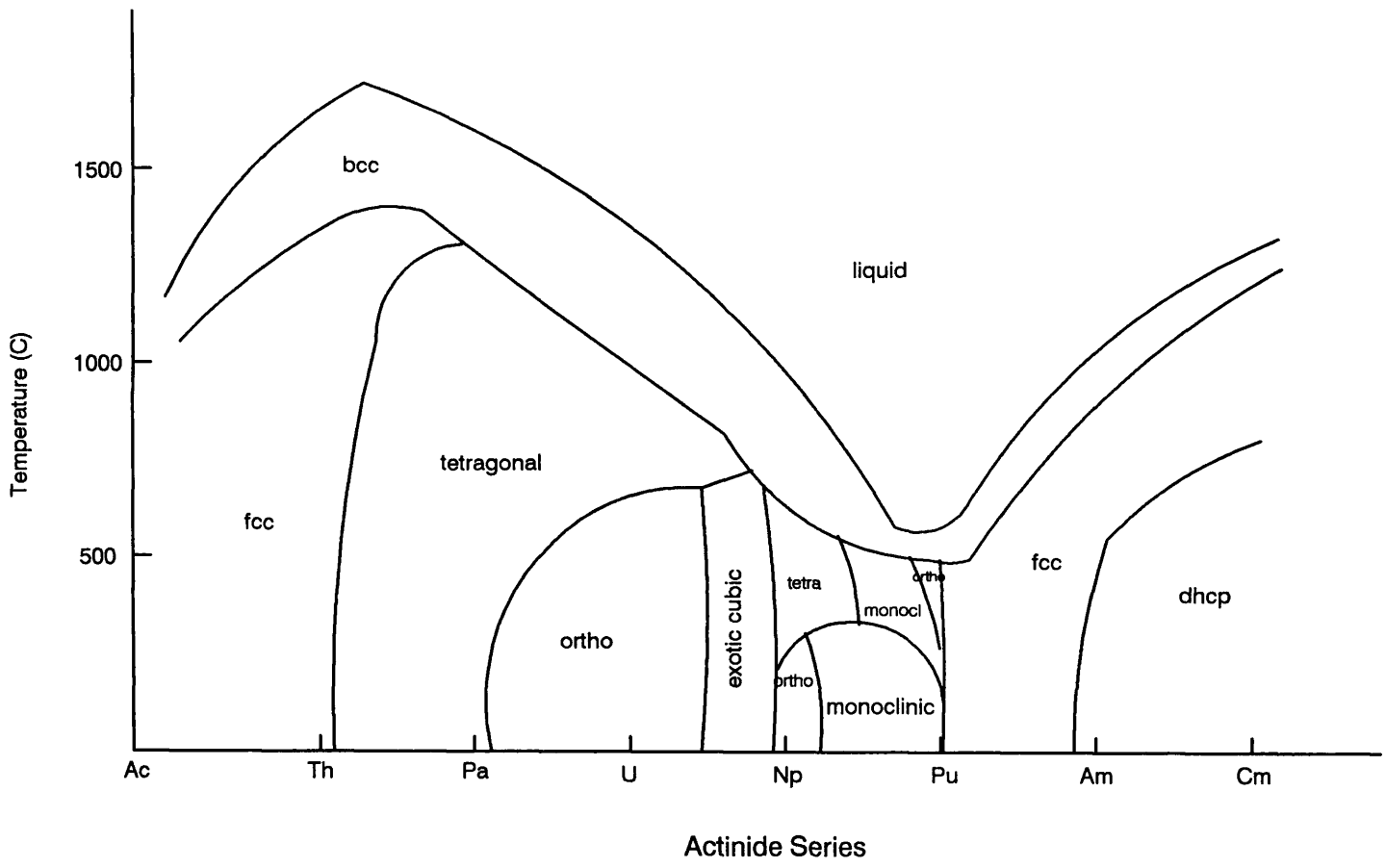

Figure 2: The connected schematic binary alloy phase diagrams for the light actinides. The diagrams for Ac through U and for AmCm are estimates based upon the pure elements. The crystal structures are indicated on the figure. [3]

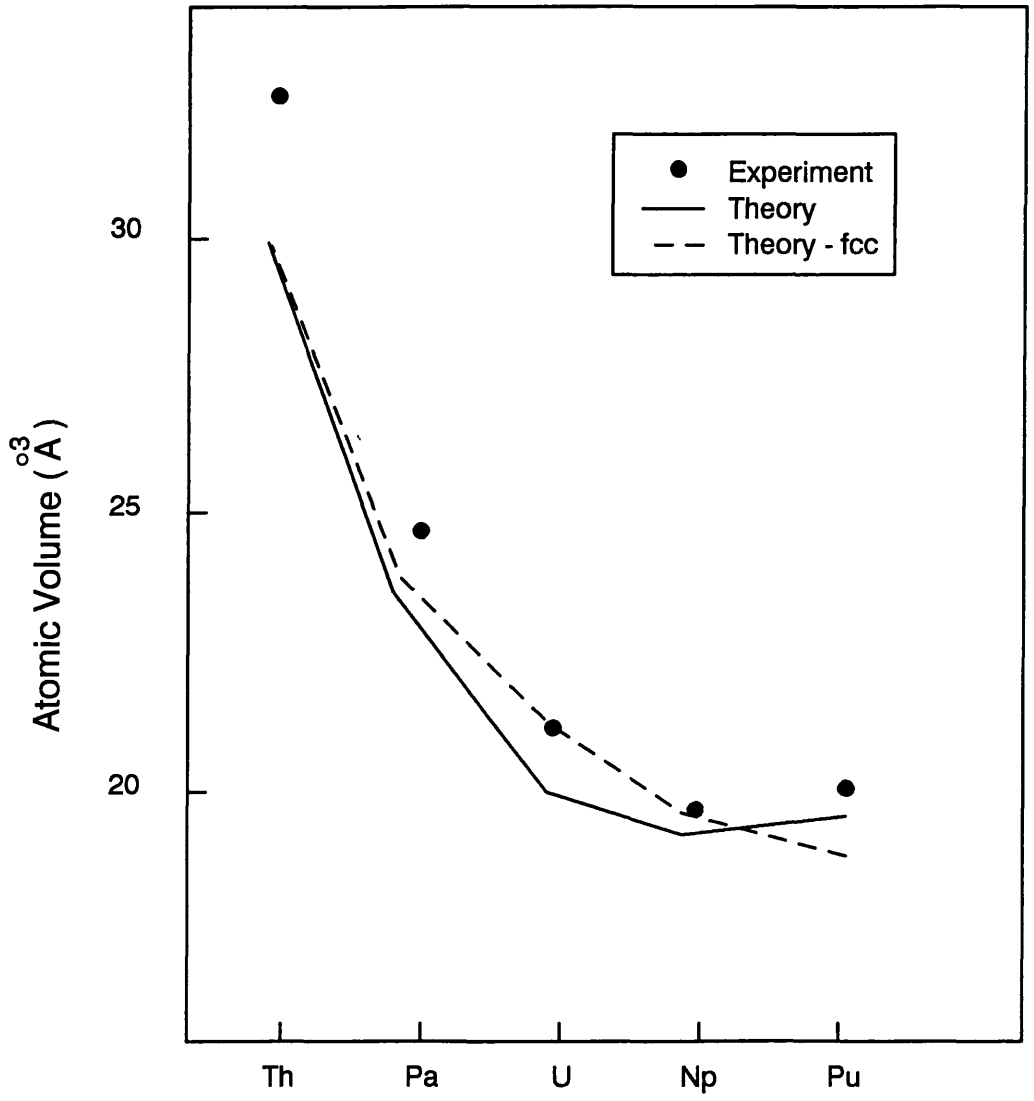

Figure 3: Decrease in atomic volume with a minimum at Pu and Np. with localization of 5f electrons and significant increase in atomic volume starting at americium. [4]

significantly larger (50% increase) which indicates a transition from de-localized to localized 5f electrons. The atomic volume behavior seen in the actinides is similar to that seen in the non-magnetic d-transition metals and can be understood in terms of filling bonding type orbitals first followed by anti-bonding orbitals. The smallest atomic volume (highest density) would be found when the most bonding orbitals are filled which coincides with plutonium.

In an effort to establish a fundamental understanding of the low symmetry crystal structure and the complex phase transformations of plutonium, Johansson and Eriksson [4] developed an expression for the total energy of a variety of crystal structures as a function of volume. Using a solution to the Dirac and a modified Schrodinger equation, the total energy of several selected crystal structures was minimized with respect to volume to identify the lowest energy structure. The result of this work is summarized in Figure 4 showing that in fact the alpha-plutonium structure represents the lowest energy for plutonium. The lowest energy, "high symmetry" structure was bcc, but a Peierls distortion mechanism was identified as promoting a low symmetry structure in this narrow energy band system. Under significant compression, however, plutonium has been shown to transform to a bcc structure due to the fact the compression broadens the 5f energy bands making the Peierls distortion mechanism less important. The behavior of the 5f electrons in plutonium have a direct correlation on its properties and later in this paper a direct relationship between the actinides and the rare-earth elements will be made by comparing a similar behavior of the 4f electrons. The localization/de-localization of

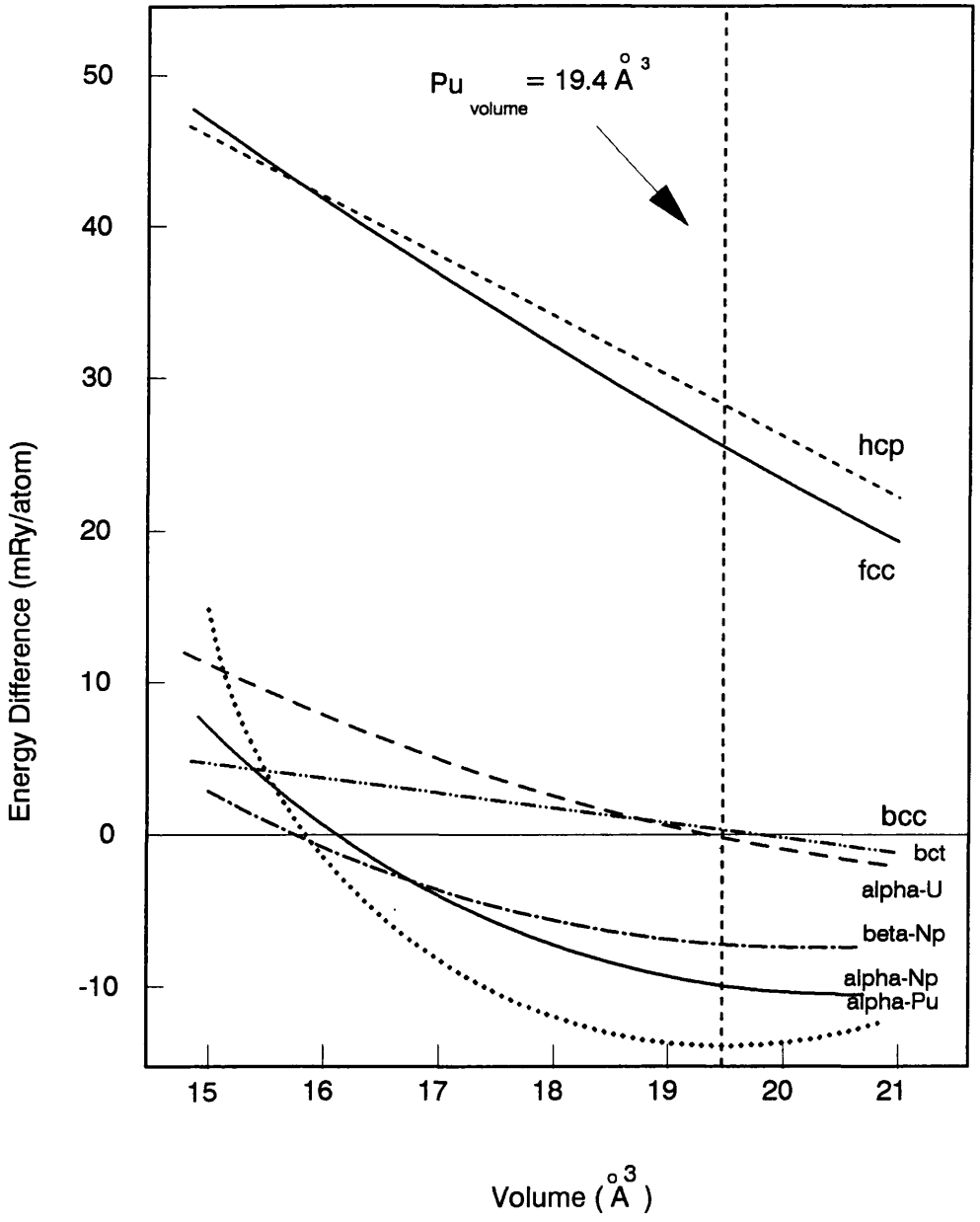

Figure 4: Minimization of crystal energy with respect to atomic volume. Calculated minimum energy shown to be alpha-Pu structure for plutonium. [4]

both the 5f and 4f electrons will be used to identify a metallurgical surrogate for plutonium in the rare-earth series of elements.

2.3 Phase Transformation Behavior in Plutonium

Table II [5] lists the equilibrium transformation temperatures and the volume changes associated with each of the phase transformations of plutonium including melting. The percent volume change for each transformation was calculated using unit cell dimensions and thermal expansion coefficients taken from x-ray measurements.

$\alpha \Leftrightarrow \beta$ Transformations

The $\beta \rightarrow \alpha$ and $\alpha \rightarrow \beta$ transformations have been extensively studied to identify the mechanism(s) of the transformations and the kinetics. The $\beta \rightarrow \alpha$ transformation is generally identified as a shear type transformation. Rosen et al [6] used ultrasonic pulse techniques to produce two separate "C" curves which they attributed to displacive type mechanisms. Selle [7] utilized internal friction measurements to indicate that the $\beta \rightarrow \alpha$ transformation proceeds via a shear mechanism. In a summary given in Plutonium 1970 [8] Nelson and Shyne strongly support the conclusion that the $\beta \rightarrow \alpha$ transition occurs by a shear mechanism. They studied both the effect of prior deformation on the beta phase and the effect of concurrent stressing during transformation on the kinetics of the transformation. Prior plastic deformation of the beta phase, either by compression or

Table II: Phase transformation temperatures and associated volume changes for plutonium [5].

Phase transformation	Transformation temperature °C	% Volume change ((V1 - V2) / V1) * 100
Alpha - Beta	110 ± 10	9.62
Beta - Gamma	190 ± 10	2.67
Gamma - Delta	310 ± 5	6.90
Delta - Delta prime	452 ± 2	-0.36
Delta - prime - Epsilon	480 ± 4	-2.16
Epsilon - Liquid	639.5 ± 2	-0.82

tension, delayed the start of the beta to alpha transformation and decreased its transformation rate. This stabilization effect of the parent phase by plastic deformation is analogous to the so-called mechanical stabilization (delay in the martensitic transformation) that is readily affected in some Fe-Ni base alloys that have been deformed above M_d." If the reaction were diffusion controlled, the prior deformation should have accelerated the transformation. " Figure 5 is a reproduction of the data from Nelson and Shyne in Plutonium 1970 [8] from which their conclusion was drawn.

The kinetics of the $\beta \rightarrow \alpha$ phase transformation have been studied by Nelson and Shyne [8], and Loasby and Lowe [9] and detailed transformation data has been produced. Time-Temperature-Transformation curves from Nelson and Shyne are shown in Figure 6. Nelson and Shyne also developed isothermal reaction curves that followed an Avrami equation expressed in general as:

$$f(t) = 1 - \exp(-At^k) \qquad (1)$$

where f(t) is the fraction transformed and t is the time for the transformation. The TTT curves given have been shown to be sensitive to small amounts of impurities that generally increase the incubation time for transformation.

The transition from beta to alpha during cooling is quite sluggish with the density of the resulting alpha phase between 19.3 g/cm^3 and 19.6 g/cm^3 compared to the theoretical value of 19.86 g/cm^3. The low density is attributed to formation of micro

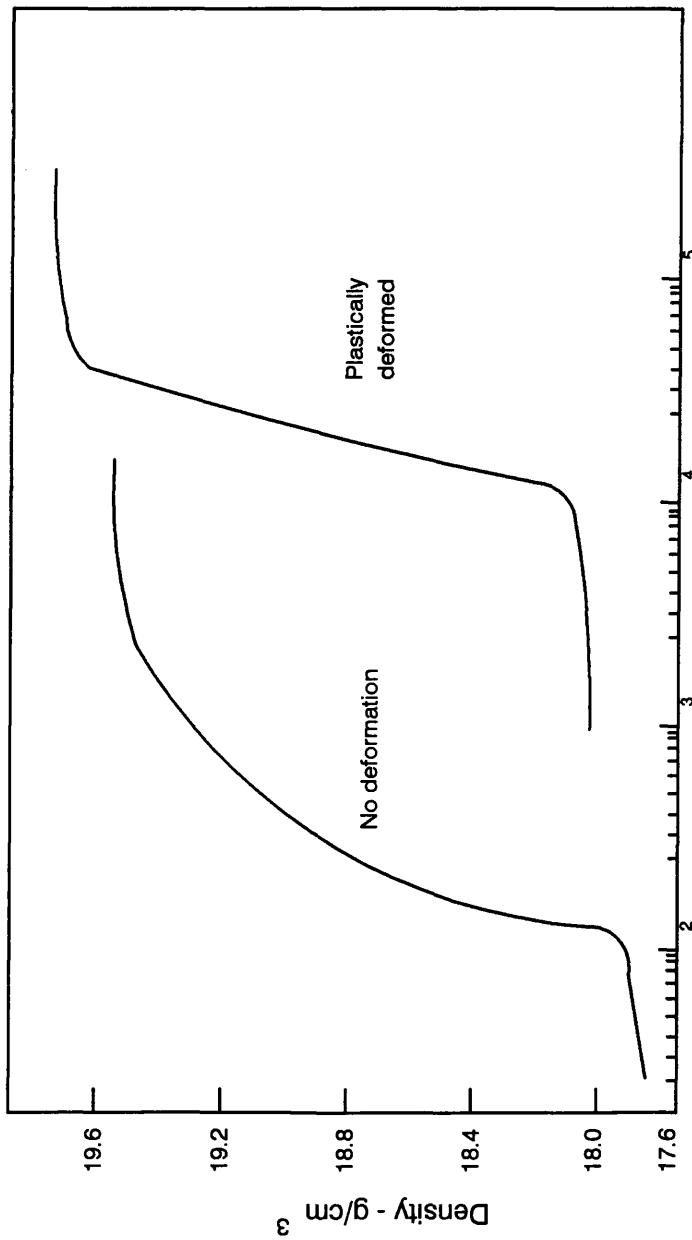

Figure 5: Effect of beta plastic deformation at 140 C on the plutonium beta to alpha transformation at 80 C [8].

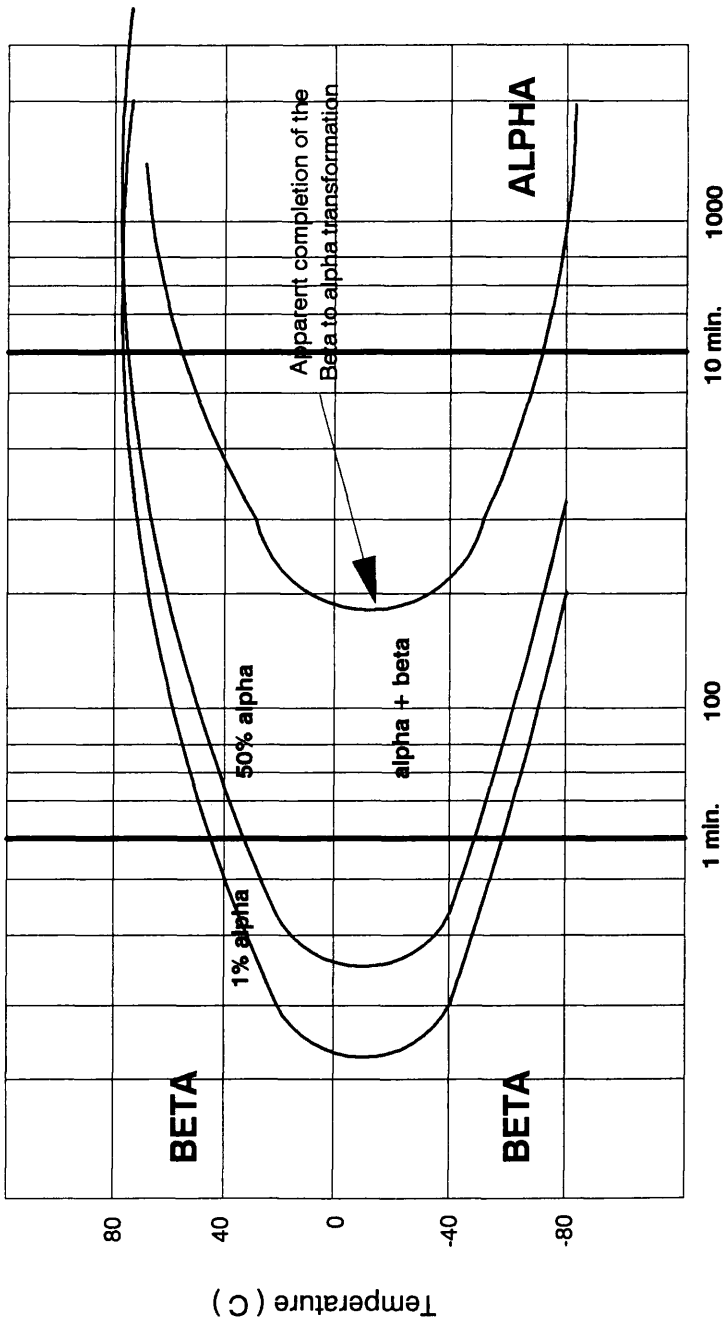

Figure 6: The time-temperature-transformation curve for the beta to alpha transformation of plutonium [8].

voids at the interface between beta and alpha phases due to the large volume change and the relatively brittle structures of each of these phases. During the transformation from beta to alpha, the alpha nucleus will achieve a critical size for growth, and as it grows, a strained area will form around the nucleus causing the transforming matrix to be deformed and to ultimately fracture. The sluggish nature of the beta to alpha transformation has also been attributed to the retention of beta phase or other higher temperature phases retained due to the presence of impurities.

Studies involving the $\alpha \rightarrow \beta$ transformation indicate that it also proceeds via a shear mechanism with similar kinetics to that of the $\beta \rightarrow \alpha$ transformation. Internal friction measurements made by Selle [7] indicated a shear type transformation. Nelson and Bowman [10] support this conclusion by demonstrating anisotropic expansion which is characteristic of a shear type mechanism. Using x-ray techniques they also proposed a crystallographic correlation between the two phases $(010)_\alpha \,||\, (-111)_\beta$ and $[10\text{-}2]_\alpha \,||\, [34\text{-}1]_\beta$ associated with a combination of shear and rotational translations typical of non-diffusional phase transformation. The kinetics of the transformation are similar to that of the $\beta \rightarrow \alpha$ with the Time-Temperature-Transformation diagram shown in Figure 7.

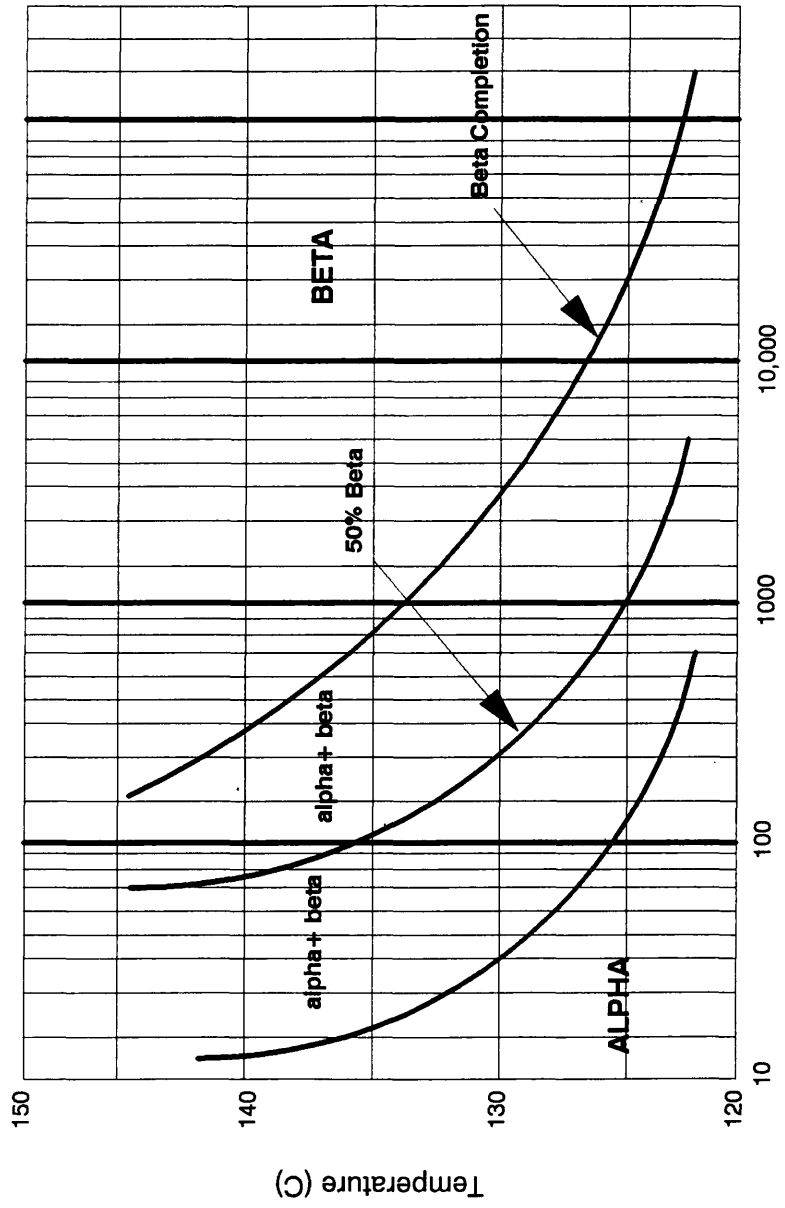

Figure 7: The time-temperature-transformation curve of the alpha to beta transformation of plutonium[8].

$\beta \Leftrightarrow \gamma$ Transformations

The $\beta \Leftrightarrow \gamma$ transformations are not well characterized although transformations in both directions are believed to be diffusional. The kinetics are extremely sluggish and similar to the $\alpha \Leftrightarrow \beta$ transformations are sensitive to small amounts of impurities.

$\gamma \Leftrightarrow \delta$ Transformations

The $\delta \rightarrow \gamma$ transformation can be characterized using the dilatometric data shown in Figure 8 [10]. Three regions are identified on the dilatometer trace indicating key steps in the overall transformation. Region I is an area of hysteresis in the transformation temperature and some investigators do not identify this behavioral area as a separate region. Region II is characterized by a smooth contraction with the initial formation of the γ phase. Region III exhibits "abrupt discontinuous contractions" which is also described as a "burst" type behavior. The transformation mechanism of the $\delta \rightarrow \gamma$ transition is believed to occur is a martensitic fashion by which Pascard [11] describes as an initial formation of γ platelets which after a buildup of microstructural constraints, then lead to a series of platelet avalanches crossing grain boundaries. Selle and Focke [12] support this conclusion via the measurement of elastic modulus and internal friction changes during the transition. A dilatometer trace for the $\gamma \rightarrow \delta$ transformation (heating) is also shown in Figure 8 and is does not show the same behavior as the reverse transformation. This transformation appears to occur by a diffusion mechanism.

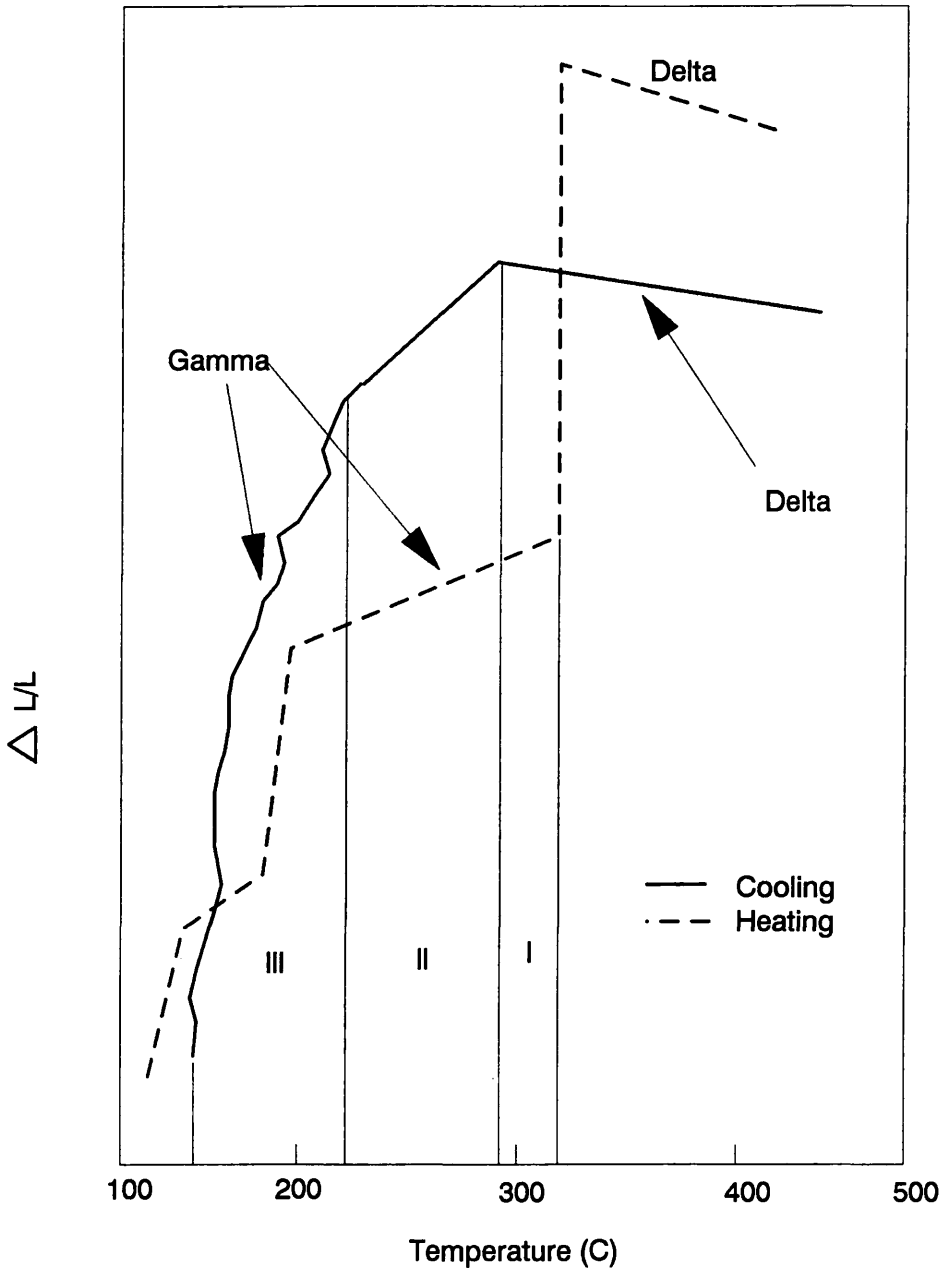

Figure 8: Dilatometer trace for the transition between the delta to gamma and gamma to delta phase transformation[10].

δ ⇔δ' and δ'⇔ε Transformations

The mechanisms for these transformations have not been characterized to the extent that the lower temperature transformations have been studied. The kinetics of the transformations are significantly faster given the higher transformation temperatures, but further study is required.

δ→α Skip Transformation

Resistivity and dilatometry were used to study the δ→α phase transformation taking advantage of the dramatic volume and resistivity changes that occur between these two phases [8,13]. Alloys containing less than 0.6 at. pct. gallium were annealed in the δ phase range, quenched, and then isothermally allowed to transform thereby describing the kinetics of the transformation via the Time-Temperature-Transformation curves shown in Figure 9[13]. Density and X-ray diffraction measurements were used to study the mechanism of the transformation. Results indicated that the δ→α transformation proceeds via an intermediate transformation to the γ phase before transforming to the α-phase. The addition of gallium in amounts greater than 0.6 at. pct. showed a dramatic effect on the transformation including:

- Depression of the TTT curve to lower temperatures
- Displacement of the TTT curves to longer times
- A "double-C-curve" in 1.4 and 1.9 at. pct. alloys.

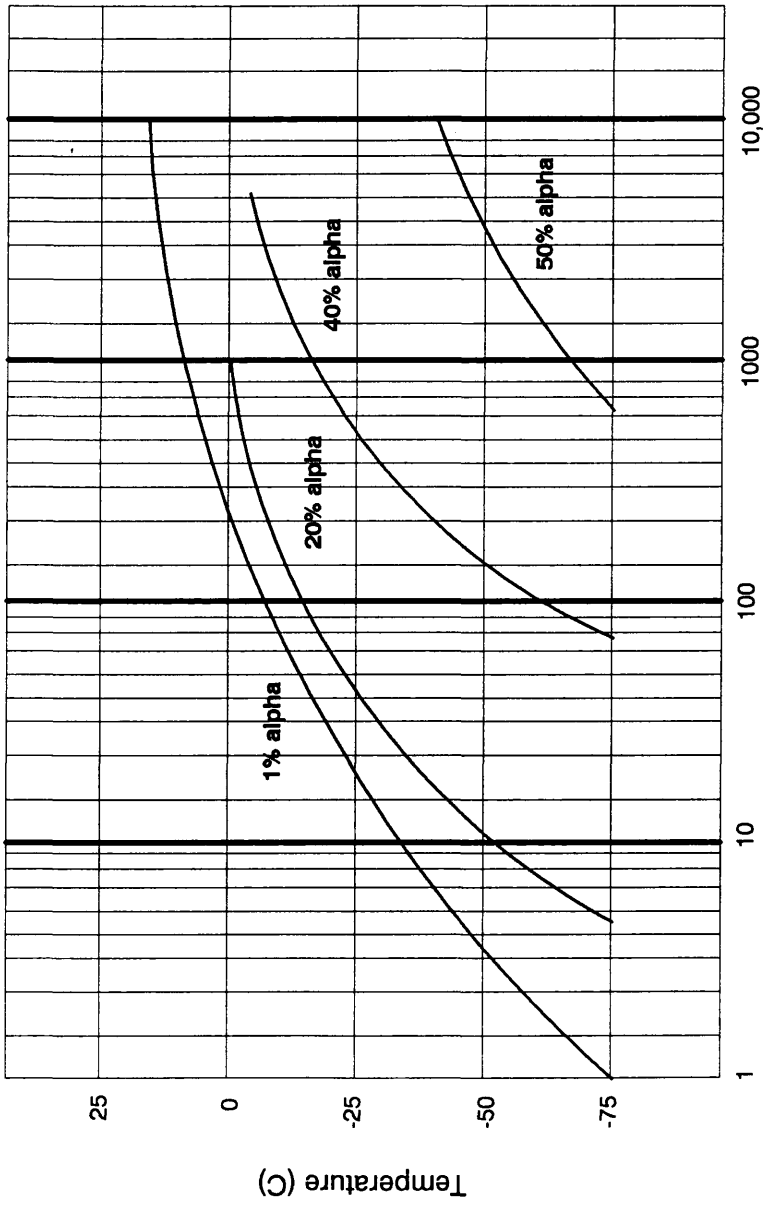

Figure 9: The time-temperature-transformation curve of the delta to alpha transformation in a plutonium - 0.7 at. pct. gallium alloy[13].

The low temperatures of the transformation would eliminate the possibility for long range diffusion suggesting a martensitic or massive type transformation where both the parent and product phases have the same composition. The C-curve type kinetics not normally seen with these types of transformations are attributed to a thermally activated nucleation and growth potentially caused by:

- Small, thermally activated atomic "shuffles" required to align the product and parent phases
- Growth of α phase restrained by opposing transformation stresses that are relaxed thermally.

A crystallographic calculation was performed by Adler et al [14] that showed potential lattice correspondences which would accommodate the significant volume change and the shear distortions necessary for a martensitic phase transformation.

2.4 Theory of Alloying

Waber [15] summarizes the alloying behavior of plutonium in terms of atomic radii and electronegativity, and discusses alloying predictions based on the Hildebrand and Mott models and Pauling's electron transfer theory. A Darken-Gurry map is used which represents an excellent graphical method combining electronegativity and atomic

radii to predict solubility of potential solutes in plutonium. Electronegativity is defined as follows:

$$\chi = 0.31(n/r + 1) + 0.50 \qquad (2)$$

where n is equal to the number of valence electrons (n=4 for δ-plutonium) and r is equal to the single bond covalent radius (r = 1.64 Angstroms for δ-plutonium). The calculated electronegativity for δ plutonium is then $\chi = 1.57$ and is plotted in the Darken-Gurry map given in Figure 10. The inner ellipse corresponds to ± 0.2 electronegativity units and ± 8 pct. difference in radii and elements within this ellipse can form substantial solid solutions with plutonium. The outer ellipse corresponds to ± 0.4 electronegativity units and ± 15 pct. difference in atomic radii. The outer ellipse represents the border at which solubility is not seen. The location of gallium with respect to plutonium indicates some solid solubility that is consistent with the plutonium-gallium phase diagram that indicates solubility up to approximately 12.4 at. pct.

Waber [15] also uses the Mott bonding number to predict the alloying behavior of gallium and plutonium. The Mott bonding number, k was modified from the Hildebrand rule used to predict miscibility in liquids such that it could be applied to metal systems. The Mott bonding number is defined as:

$$k = \frac{\text{Energy of Mixing - Thermal Energy}}{\text{Binding energy of A-B bond}} \qquad (3)$$

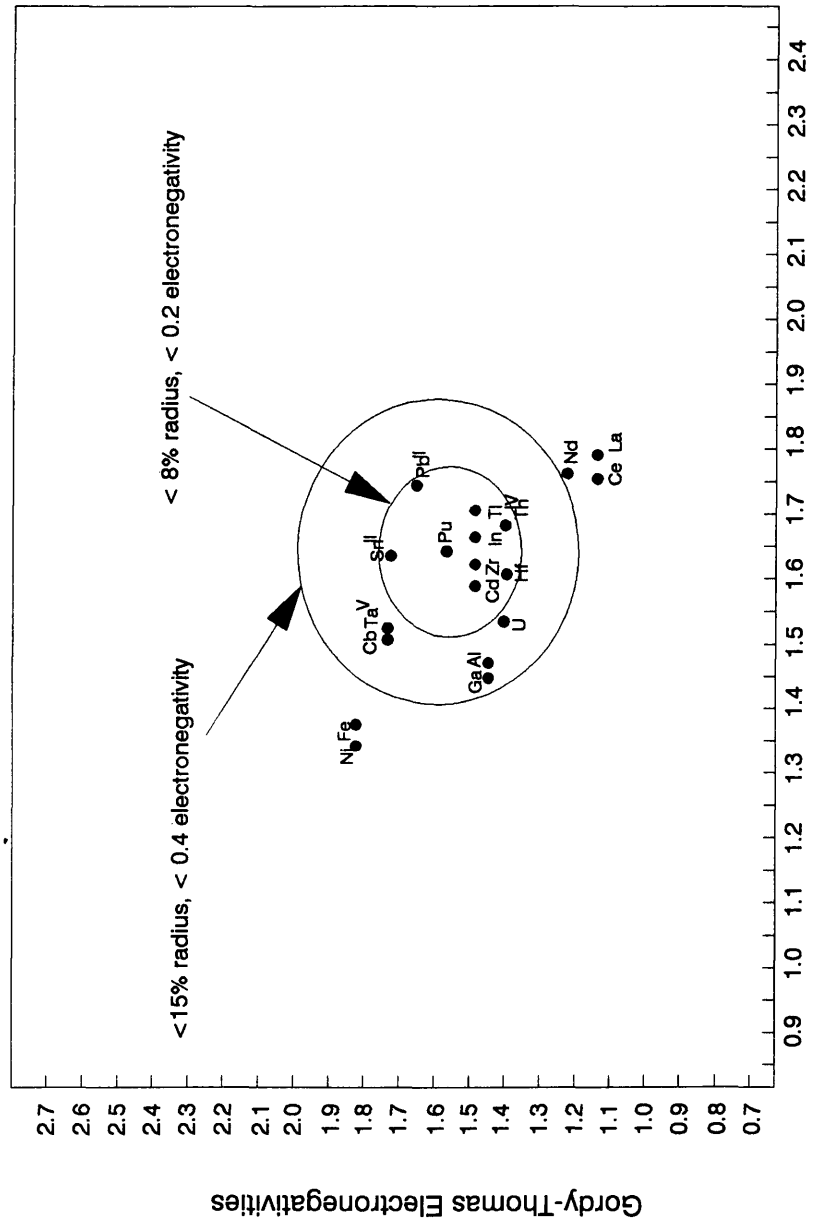

Figure 10: Darken-Gurry map for determining which elements are favored for solution in delta plutonium. Only key elements were reproduced [15].

The terms in Mott equation are defined in equations (4), (5), (6), and (7) as follows:

$$\text{Energy of Mixing} = \tfrac{1}{2}(V_A + V_B)(\delta_A - \delta_B)^2 \quad (4)$$

$$V = \text{atomic volume} \quad (5)$$

$$\delta = \left(\frac{\text{heat of vaporization}}{\text{atomic volume}}\right)^{\frac{1}{2}} \quad (6)$$

$$\text{Thermal energy} = 2RT_m \quad (7)$$

The binding energy of an A-B bond is equal to 23060 $(\Delta X)^2$, where ΔX is defined as the difference in electronegativity between solvent and solute. As summarized by Erfurdt[2], low values of k (negative values) would indicate highly ionic A-B bonds and high values of k suggest covalent bonds. The calculated value of k for gallium in plutonium is -1.0. This value corresponds to the phase diagram that indicates the formation of high melting intermetallic compounds.

Erfurdt [2] summarized the correlation between electron number and compound formation tendencies based on Pauling's electron transfer theory. Plutonium is hypoelectronic with unfilled d and f orbitals. Compound formation with gallium would be expected as gallium is hyperelectronic and can act as an electron donor.
Finally, Engel-Brewer [16] theories of metals correlate to the behavior seen in the plutonium gallium system. Engel-Brewer theory states that the number of s and p electrons determine crystal structure. Gallium donates s and p electrons and provides no

d-electrons thereby stabilizing the face-centered cubic delta phase. Again, this correlates with the plutonium-gallium phase diagram.

2.5 Plutonium-Gallium System

The plutonium - gallium system has been studied extensively, providing a well established foundation of metallurgical properties of the system. The complete plutonium -gallium phase diagram is shown in Figure 11[2,17]. The area of focus in this work is the plutonium - 1 wt. pct. gallium region of the phase diagram that is shown in Figure 12. The area of interest in this section of the phase diagram is the two phase epsilon + delta region. During cooling of an alloy through this region, significant gallium solute microsegregation is seen which results in an acicular morphology containing high gallium regions in the center of the grain, and low gallium regions near the grain boundaries [18].

The microsegregation occurs in the epsilon plus delta two-phase region with the positive partitioning coefficient evident on the phase diagram. The magnitude of the microsegregation remaining at room temperature is determined by the difference in diffusion characteristics between the epsilon phase and the delta phases. A comparison between the interdiffusion coefficient of plutonium and gallium in epsilon phase (10^{-7}cm^2/sec - Harvey[19]) versus delta phase (10^{-10} cm^2/sec-Rafalski[20]) shows that diffusion in delta is three orders of magnitude slower in delta phase. The implication of this difference in diffusion characteristics is that the coring occurs during the solid state

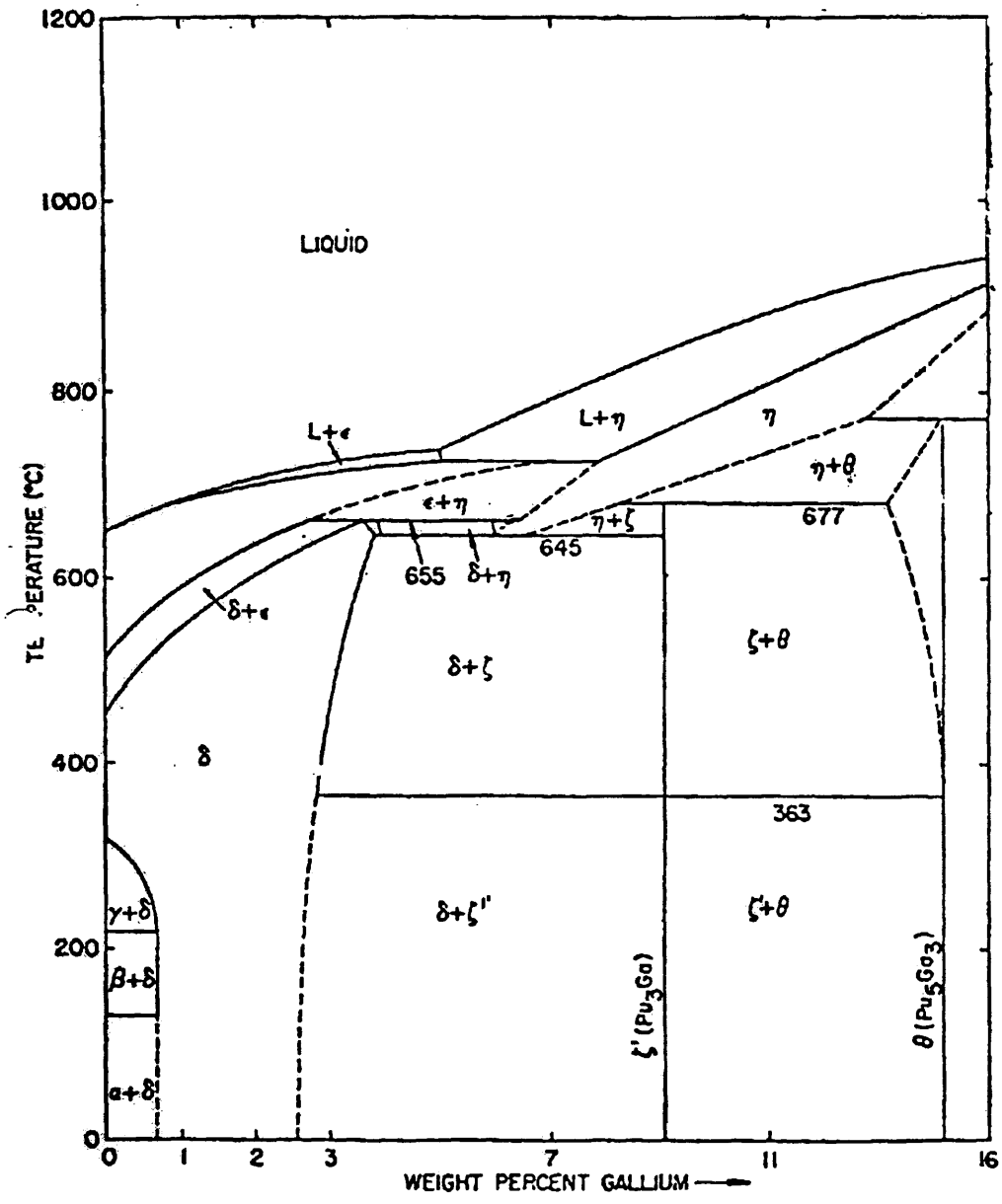

Figure 11: The plutonium - gallium phase diagram [2].

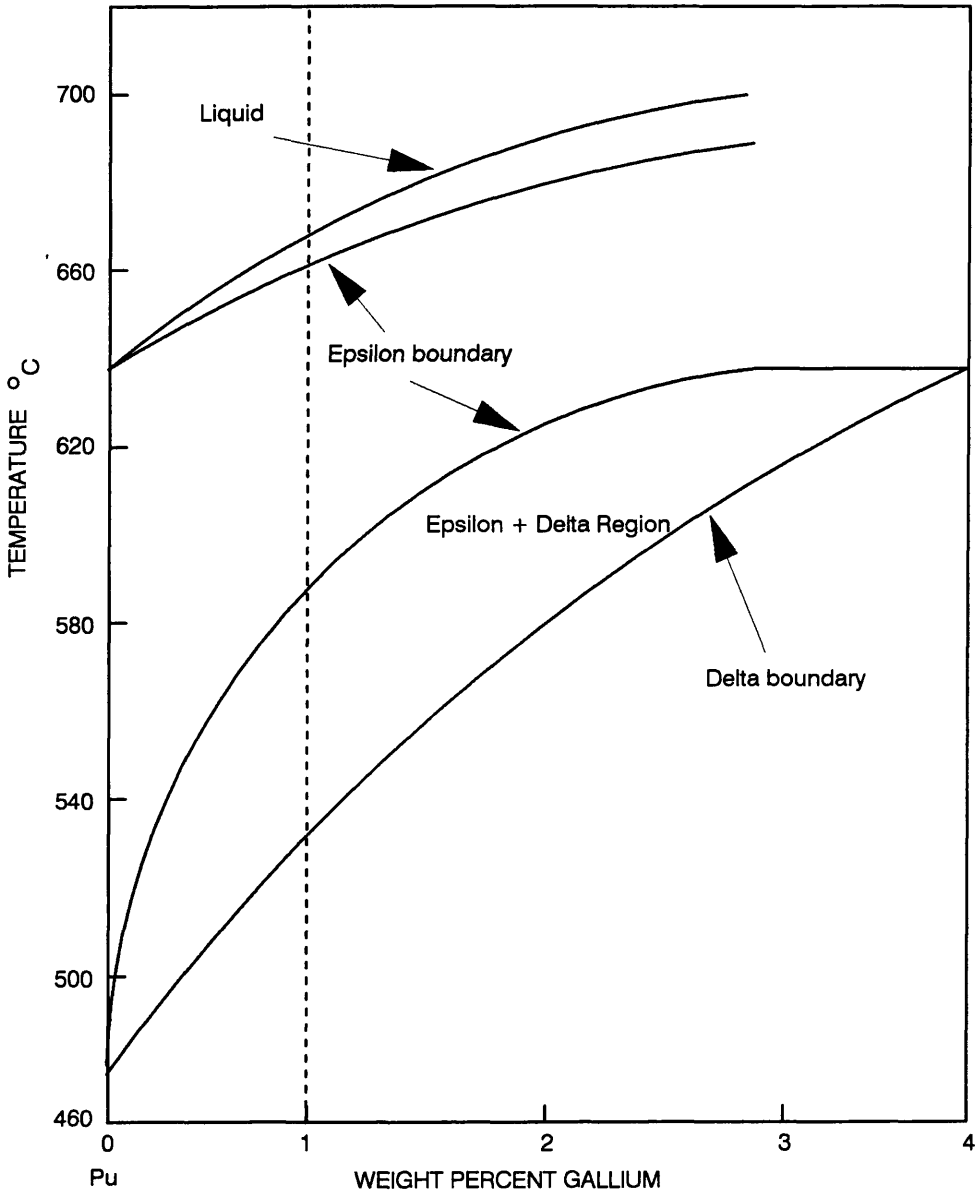

Figure 12: Partial plutonium-gallium phase diagram with focus on the plutonium - 1wt. pct. gallium alloy region. Alloy of interest is at 1 wt. pct. gallium [2].

transformation rather than during solidification. Furthermore, diffusion in the delta phase is sufficiently slow such that the distribution of gallium in the epsilon phase is homogeneous and the coring profile can be estimated from the equilibrium phase diagram as discussed later.

An analytical approximation of the diffusion distance using these diffusion coefficients illustrates the point. The diffusion distance for a solute can be calculated using the following equation from the random walk development described by Shewman [25]:

$$x = k\sqrt{Dt} \tag{8}$$

where x is equal to the diffusion distance, k is a constant related to system geometry, D is the diffusivity, and t is the time for diffusion. Due to the low concentration of gallium (~ 1 wt. pct.), the intrinsic diffusivity of gallium is assumed to be approximately equal to the interdiffusion coefficient. For a cooling rate of 10°C/min, the time in the two-phase epsilon plus delta region is approximately four minutes (240 seconds). Diffusion distances for gallium in epsilon and delta phase are calculated:

$$x_\varepsilon = [10^{-7}\ (cm^2/sec)\ (240\ sec)]^{\frac{1}{2}} * (10^4\ \mu m/cm) \cong 49\mu m \tag{9}$$

$$x_\delta = [10^{-10}\ (cm^2/sec)\ (240\ sec)]^{\frac{1}{2}} * (10^4\ \mu m/cm) \cong 1.6\ \mu m \tag{10}$$

Given that the core size of a plutonium-gallium alloy cooled at 10°C/min is approximately 40 μm[18], the transport of gallium is determined by the slower diffusion in the delta phase. This result is confirmed by, Johnson [21], Gardner [16], and Ferrera et al [22] who have asserted that the liquid plus epsilon micro segregation is insignificant and the coring profile is driven by the difference in diffusion characteristics in the two-phase epsilon plus delta region.

An example of a plutonium - 1 wt. pct. gallium microstructure is shown in Figure 13 [22]. The low gallium regions which result from the microsegregation contain a metastable delta phase which can undergo the multiple allotropic phase transformations ultimately reaching the room temperature alpha phase. As discussed above, the brittle, high density, monoclinic alpha phase is not desirable in a wrought manufacturing application as it results in inconsistent properties and severe cracking during processing. To eliminate these metastable regions, homogenization treatments are required which allow gallium diffusion within the grain to achieve the equilibrium concentration described on the phase diagram and to obtain the face centered cubic delta phase.

Microsegregation of Gallium

Ferrera et al [22] calculated a theoretical microsegregation profile for gallium in a plutonium-1 wt. pct. gallium alloy using the lever rule for equilibrium phase diagrams as shown in Figure 14. The lever rule was applied to analytically determine the gallium concentration during cooling of the 1 wt. pct. alloy through the two phase ($\varepsilon + \delta$) region.

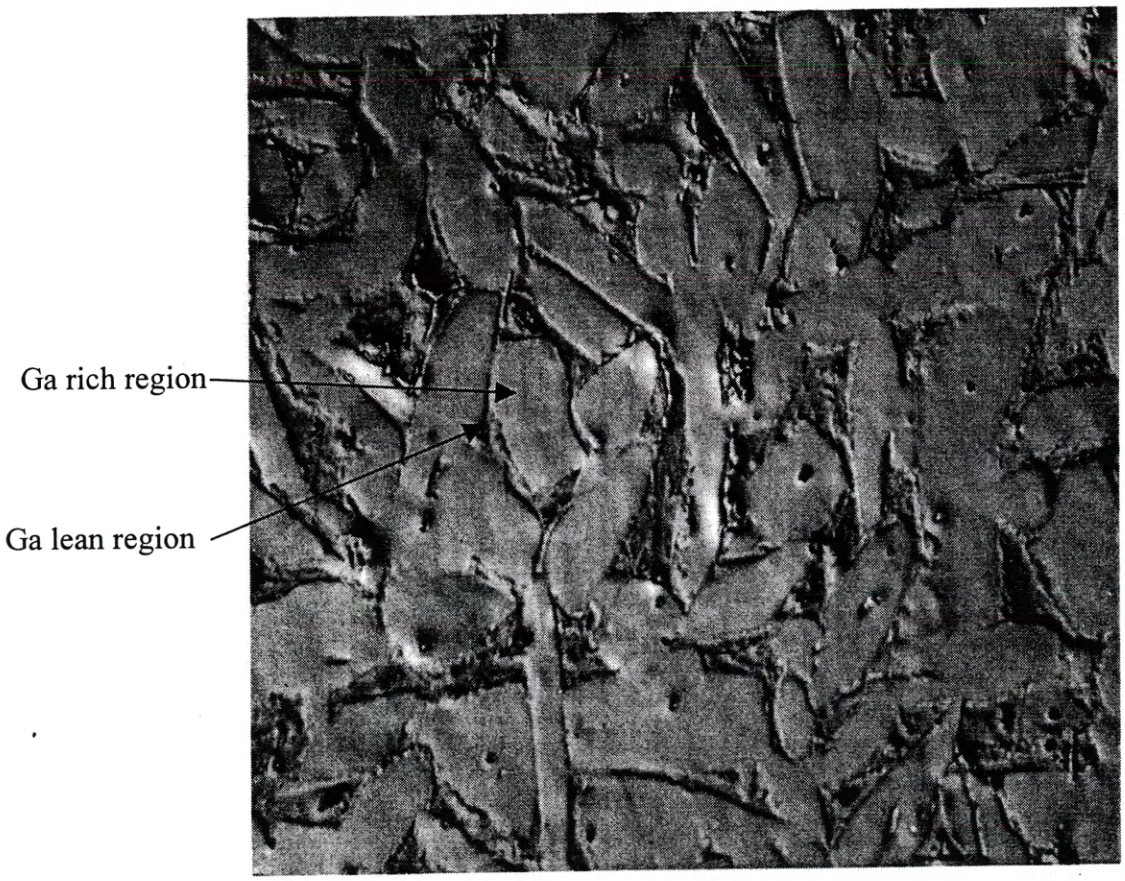

Figure 13: Typical microstructure of plutonium-1 wt. pct. gallium alloy. Approximate core size is 30 um. [22]

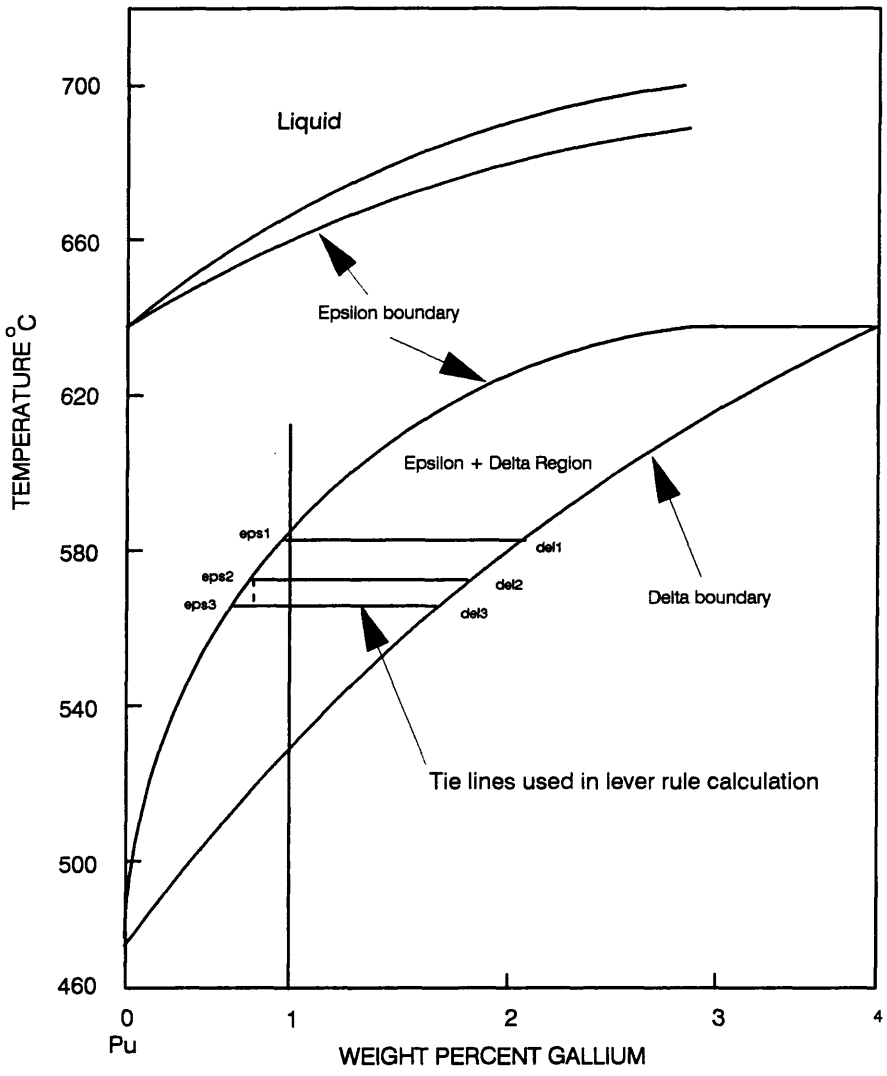

Figure 14: Partial plutonium-gallium phase diagram showing procedure for determining the gallium profile using the lever rule [22].

Fractions of each phase were determined with gallium concentrations determined based on the phase diagram. These results showed reasonable agreement with the concentration profile measured using a scanning electron microprobe particularly when slower cooling rates were studied. This comparison is shown in Figure 15. The deviation of the experimental data from the calculated data was attributed to the uncertainty in the equilibrium phase boundaries and the super cooling which would lower the epsilon to delta transformation start temperature.

To further develop the approach used by Ferrera [22] a partitioning coefficient, kp [23] is defined to describe the segregation of the gallium solute as a function of the phase diagram:

$$k_p = \frac{X_\delta}{X_\varepsilon} \qquad (11)$$

where X_δ is equal to the mole fraction of gallium in the δ - phase and X_ε is equal to the mole fraction of gallium in the ε phase. The partitioning coefficient is a measure of the degree of segregation of a solute (gallium) as described by the phase diagram. Traditionally, the partitioning coefficient is used in the analytical description of microsegregation of a solute during solidification. The solidification model is simplified by assuming that the liquidus and solidus lines are linear and the partitioning coefficient is constant. "Perfect mixing" is assumed in the liquid phase given the high rate of

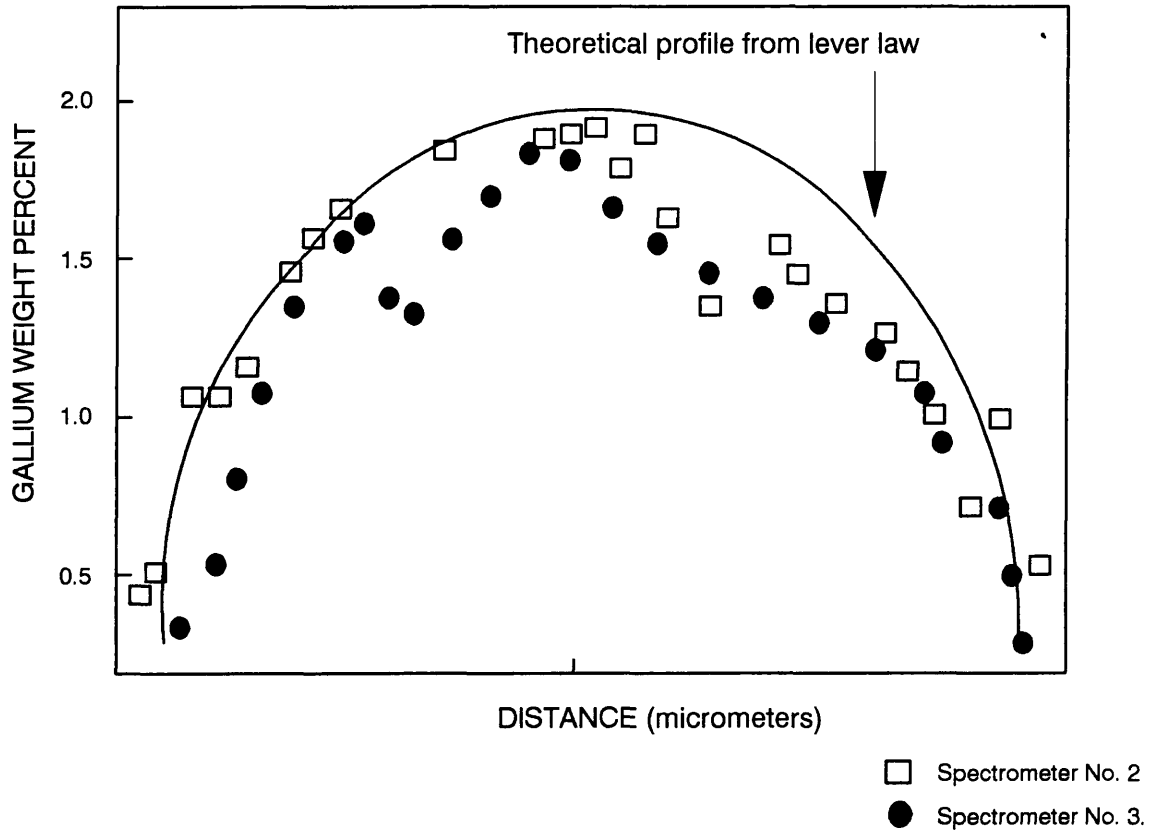

Figure 15: Gallium concentration profiles (measured) superimposed over theoretical curve. Data points were taken from electron microprobe measurements [22].

diffusion seen in a liquid versus a solid. A similar approach was used for the plutonium - 1 wt. pct. gallium alloy taking advantage of the relative values of the interdiffusion coefficients in ε and δ phases as described above. Despite the fact that the plutonium phase transformation is solid state, the small interdiffusion coefficient in ε allows "perfect mixing" to be assumed relative to the δ phase. Further, the curvature of the two-phase region was estimated using linear increments instead of assuming a constant partitioning coefficient.

The phase diagram in Figure 14 was used to determine the partitioning coefficient as a function of temperature, as a plutonium - 1 wt. pct. gallium alloy is cooled through the ε + δ two-phase region. Applying the solidification model to the solid state transformation as described above, the Scheil Equation [23]is developed where the amount of gallium which enters the δ phase is set equal to that remaining in the ε phase:

$$(X_\varepsilon - X_\delta)\, df_s = (1 - f_s)\, dX_\varepsilon \qquad (12)$$

where f_s is the volume fraction of δ phase formed during the transformation. Integrating this equation using the boundary condition:

$$X_\delta = k_p X_o \text{ when } fs = 0 \qquad (13)$$

results in the following:

$$X_\delta = k_p X_o (1 - f_\delta)^{kp-1} \qquad (14)$$

The data shown in Table III takes the input from the phase diagram to produce Figure 16 and Figure 17. Figure 16 shows the partitioning coefficient as a function of temperature. Figure 17 shows the predicted concentration profile based on the Scheil equation assuming a 40 um grain size. The concentration profile of Figure 17 is similar to that shown in Figure 15 which compares the calculated profiles with measurements taken using a scanning electron microprobe. As stated by Ferrera et al, [22] the calculated profile showed reasonable agreement particularly when slower cooling rates were studied. The deviation of the experimental data from the calculated data was attributed to the uncertainty in the equilibrium phase boundaries and the supercooling which would lower the ε to δ transformation start temperature.

Erfurdt [2] proposed a "shell" model to describe the cored plutonium-gallium grain. Figure 18 provides a schematic of the shell model indicating a gallium rich region (δ-phase) and a gallium lean shell (α-phase or metastable δ-phase) surrounding the δ-phase. Erfurdt [2] also identified the formation of Pu_6Fe which is the result of the eutectic reaction between plutonium and iron and was a focus of his study.

The average grain diameter as a function of cooling rate was studied by Gardner [18] as shown in Figure 19. For example, a cooling rate of 10°C/min results in an

Table III: Temperature and concentration data taken from the plutonium-gallium phase diagram. This data was used to calculate the partitioning coefficient to describe the coring which occurs in the $\varepsilon + \delta$ two-phase region [3].

Alloy (Ga)	Temperature (C)	Wt% Ga in Delta	Wt% Ga in Epsilon	Wt% Delta
1.00	590		1.00	0
1.00	585	1.84	0.96	4.55
1.00	580	1.65	0.86	17.72
1.00	577	1.62	0.83	21.52
1.00	570	1.5	0.72	35.90
1.00	567	1.46	0.7	39.47
1.00	560	1.4	0.59	50.62
1.00	555	1.25	0.52	65.75
1.00	550	1.16	0.48	76.47
1.00	545	1.1	0.42	85.29
1.00	540	1	0.36	100.00

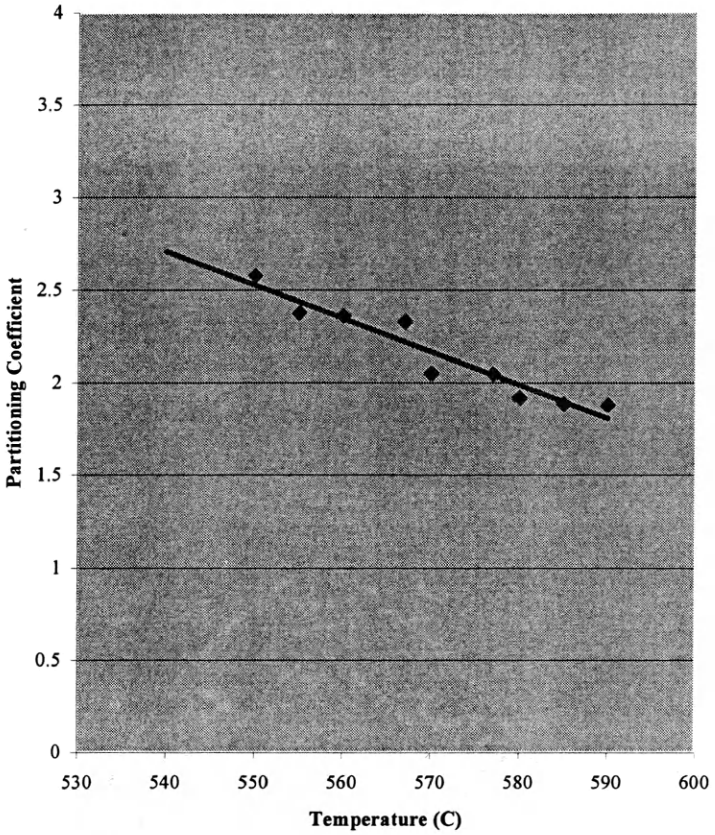

Figure 16: Partitioning coefficient plotted as a function of temperature for the plutonium - 1 wt. pct. gallium alloy calculated from the plutonium - gallium phase diagram.

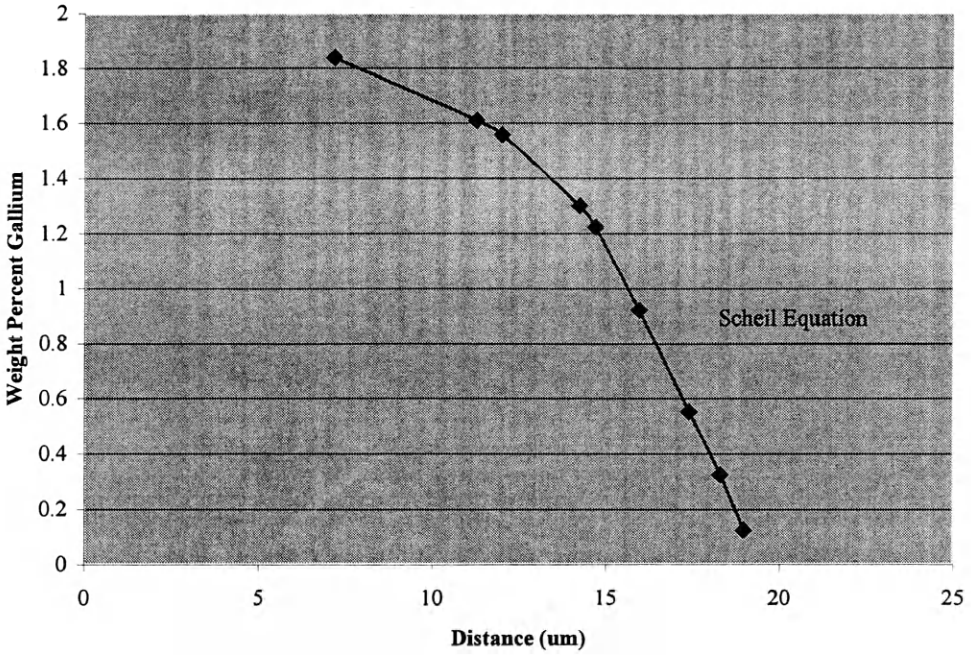

Figure 17: Variation of gallium across a plutoniun grain as predicted by the Scheil equation. A 40 μm spherical grain was assumed in the calculation. Plot shows variation across half of a grain (20 μm).

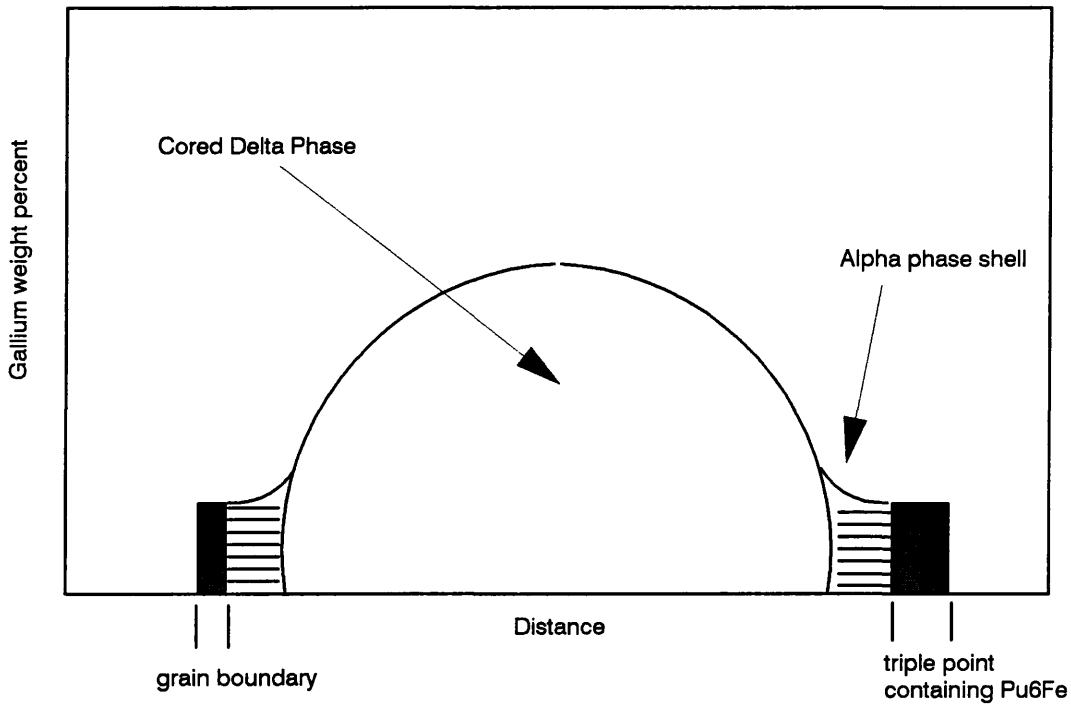

Figure 18: "Shell" model proposed by Erfurdt to describe the coring in plutonium-1 wt. pct. gallium. Formation of Pu6Fe is also shown in the triple point. [2]

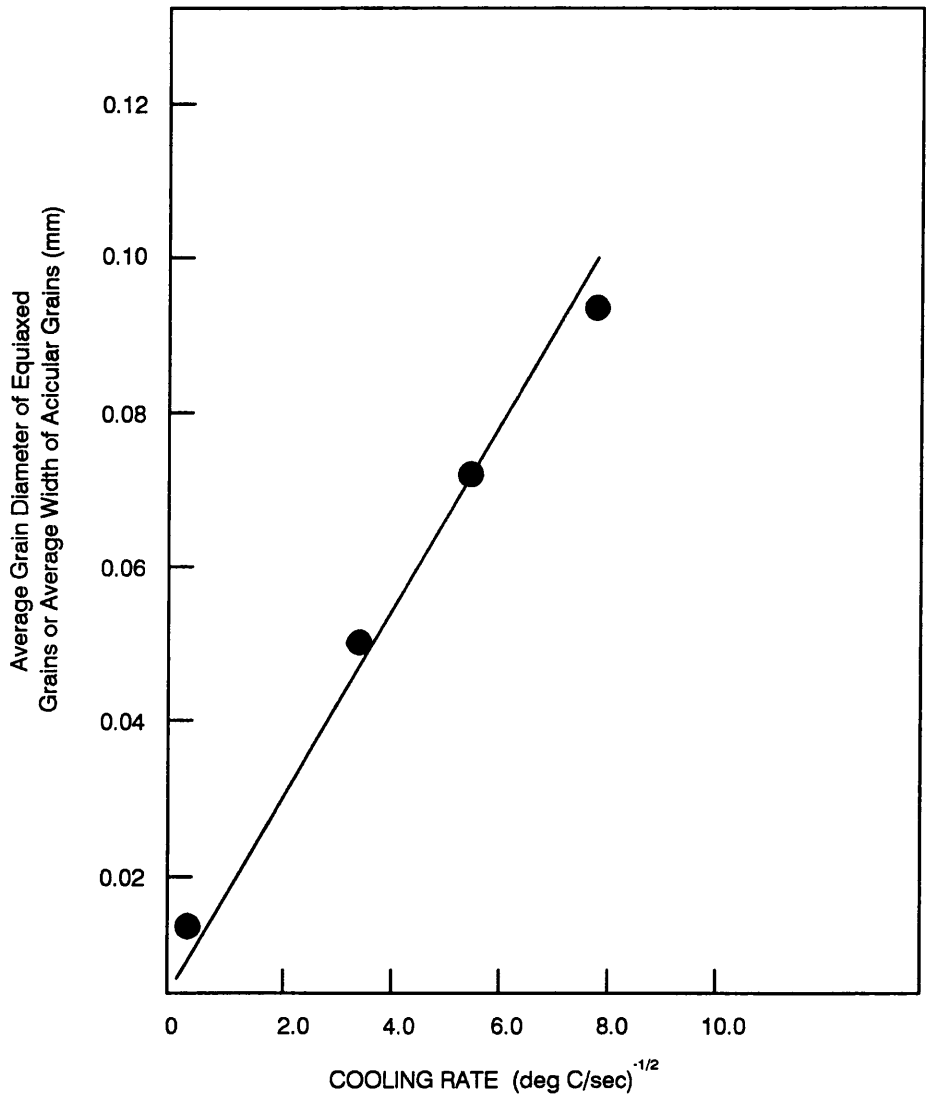

Figure 19: Relation between cooling rate from 540 to 590 deg C and grain size in cored plutonium-1 wt. pct. gallium stabilized alloy [18].

average diameter of the cored grain of approximately forty microns. A finer structure reduces the diffusion distance necessary to achieve complete homogenization of the segregated gallium.

Gallium Diffusion and Homogenization

Radioactive tracer techniques are probably the best and most accurate for measurement of diffusion parameters. A radioactive tracer is deposited on a surface of a sample, then heated to a certain temperature and concentrations of the diffusing solute measured using thin sectioning techniques. Accuracy is improved with single crystal specimens to avoid short circuit grain boundary diffusion and to identify anisotropy in non-cubic crystals. For materials such as plutonium or rare-earths, vacuum evaporation of metallic tracers are most effective due to the formation of an oxide barrier on the surface. Samples must be protected during diffusion anneals using inert or evacuated capsules protected by a tantalum foil.

Extensive work has been conducted to characterize the homogenization of the plutonium - 1 wt. pct. gallium alloy including the measurement of the interdiffusion coefficient. Three fundamental papers are summarized which detail the current understanding of the mass transport behavior of this material. Johnson [21] prepared plutonium - 1wt. pct. gallium specimens that in the as-cast condition exhibited the micro segregation of gallium described previously. Specimens were homogenized at different temperatures in the delta phase region and the homogenization process was monitored

utilizing a scanning electron microprobe. Given the core size as measured by the photomicrographs, the starting high and low gallium concentrations, and the gallium concentrations at some intermediate time, a relationship for the interdiffusion coefficient was determined:

$$D = (65 \pm 5)\ \exp(-40{,}100/RT)\ cm^2/sec \qquad (15)$$

where, R is the universal gas constant in calories/mole * deg K and T is the absolute temperature in deg K.

Edwards, Tate, and Hakkila [24] measured the interdiffusion coefficient in plutonium - gallium alloys including 3.0 and 7.9 at. pct. gallium alloys. After an initial homogenization at 500°C, specimens of each composition were roll-bonded to create diffusion couples. The diffusion couples were then annealed in the temperature range 350 to 517°C and the resulting concentration profiles for gallium were measured using an electron microprobe as shown in Figure 20. The following solution to Fick's equation for diffusion was used to calculate the interdiffusion coefficient:

$$\frac{(C-C_1)}{(C_o-C_1)} = \tfrac{1}{2}\left[1 + 2\pi^{-1/2} \int_o^k \exp(-\lambda^2)d\lambda\right] \qquad (16)$$

$$\text{where } k = \frac{(\tfrac{1}{2})x}{(Dt)} \qquad (17)$$

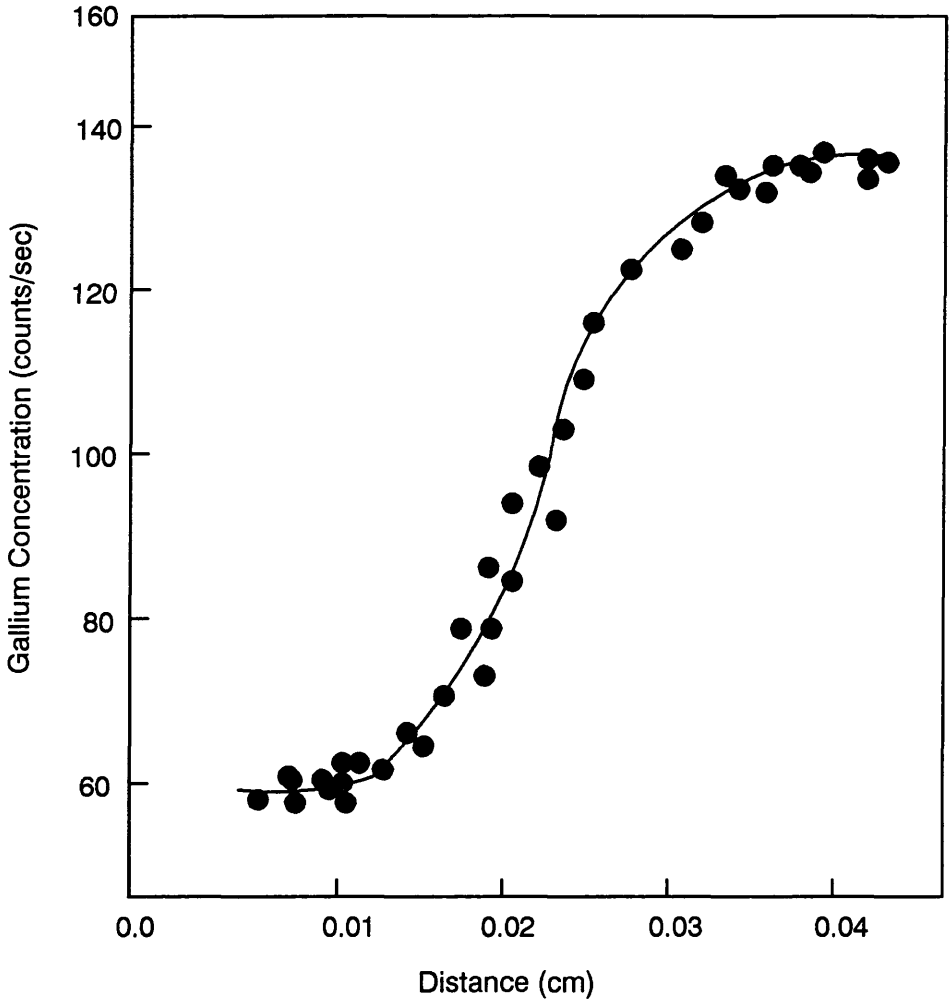

Figure 20: Schematic reproduction of concentration-penetration profile for typical diffusion couple from Edwards et al [24].

C is equal to the concentration of gallium at a distance x from the couple interface, C_1 is equal to the initial concentration of gallium on the side of low concentration, C_o is equal to the initial concentration of gallium on the side of high concentration, and D is equal to the interdiffusion coefficient. An Arrhenius plot was constructed using the concentration penetration data for each alloy couple and the calculated interdiffusion coefficient at each temperature. Figure 21 is a reproduction of this data including the resulting expression for the interdiffusion coefficient as a function of absolute temperature. The relationship for the interdiffusion coefficient determined to be:

$$D = 1.3\exp[-37350/RT] \text{ cm}^2/\text{sec} \qquad (18)$$

where, R is the universal gas constant in calories/mole * deg K and T is the absolute temperature in deg K. Also shown in Figure 21 is a plot of the self-diffusion coefficient for unalloyed delta plutonium. As discussed by Edwards et al [24], the difference between the self-diffusion coefficient and the interdiffusion coefficient is consistent with Shewman [25] stating that solutes that raise the melting point of a binary alloy decrease the interdiffusion coefficient.

Rafalski, Harvey, and Riefenberg [20] used a similar approach to Edwards et al [24] to measure the interdiffusion coefficient for the plutonium - 1 wt. pct. gallium system. Two alloys containing 0.73 and 1.97 wt. pct. gallium were bonded to form diffusion couples and concentration profiles were measured at various annealing

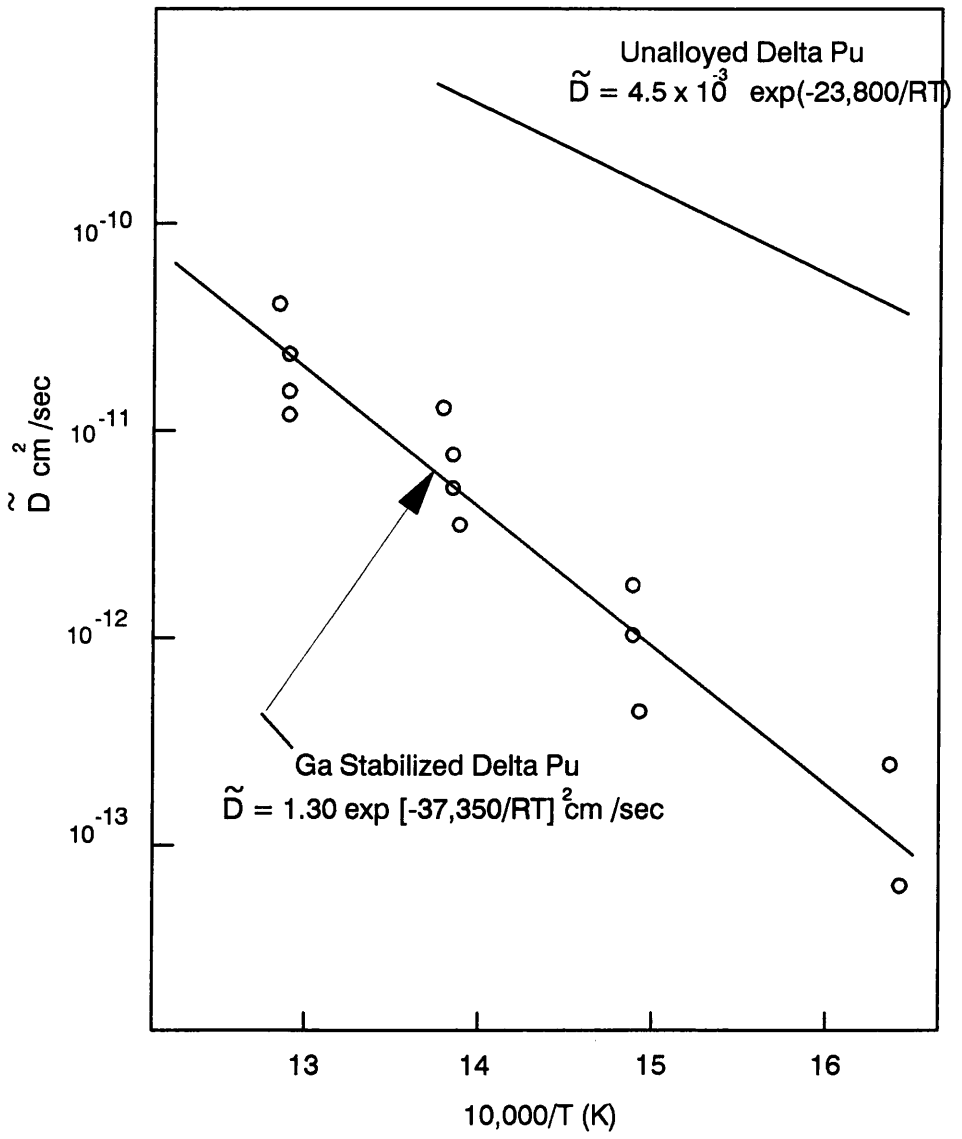

Figure 21: Arrhenius plot for interdiffusion in delta plutonium: unalloyed delta plutonium and gallium stabilized. Reproduced from Edwards et al[24].

temperatures and annealing times. An Arrhenius type plot was used resulting in the following relationship for the interdiffusion coefficient:

$$D = 0.098 \exp [-33{,}000 \pm 2100 /RT] \ cm^2/sec \qquad (19)$$

Note: Error reported for $D_o = 0.098 \ + 0.029$ and -0.023

Both Edwards [24] and Rafalski [20] confirmed that grain boundary diffusion did not play a part in the determination of the interdiffusion coefficients. This conclusion was primarily based on the fact that annealing treatments were performed at a temperature greater than 2/3 of the melting point (T_m). According to Shewman [25], grain boundary diffusion is not significant at temperature greater than $2/3T_m$.

2.6 Diffusion Theory

An expression for the diffusion coefficient can be developed starting with an atomistic approach. Appendix A details this atomistic development and shows how the mechanisms of diffusion can be tied to thermodynamic quantities. The key results are shown in the following equations for the diffusion coefficient, activation energy and the pre-exponential factor:

$$D = \gamma a_o^{\,2} f \upsilon \exp [-\Delta S_m/R] \exp [-\Delta S_v/R] \exp[- (\Delta H_v + \Delta H_m) /RT] \qquad (20)$$

$$Q = \Delta H_v + \Delta H_m \quad (21)$$

$$D_o = \gamma a_o{}^2 f \upsilon \exp[-\Delta S_m/R] \exp[-\Delta S_v/R] \quad (22)$$

with variables defined in Table IV. This development derives the relationship between "first principles" mechanisms and ties them to fundamental parameters that are measurable. Parameters such as activation energy will be used to initially link the plutonium 1 wt. pct. gallium alloy, the measurement of which is discussed above, to the potential surrogate alloy.

Diffusion as a Function of Crystal Structure

The diffusion data measured for delta phase plutonium is consistent with values measured for other materials with close packed crystal structures. Furthermore, the higher diffusion value in the bcc epsilon phase is consistent with other bcc materials which exhibit "anomalous diffusion" characterized as follows:

- Activation energy for the diffusion process is significantly lower than predicted on the basis of melting point or other empirical methods
- Pre-exponential terms (D_o) are generally lower than the range seen for close packed structures.

Table IV: Variable definitions in the diffusion equation.

t = time	a_o = lattice parameter
Γ = jump frequency	ΔS_v = entropy for the creation of vacancies
υ = Debye frequency	ΔS_m = entropy associated with atom motion
N_v = equilibrium concentration of vacancies	ΔH_v = enthalpy associated with the creation of vacancies
ΔG_v = Gibbs free energy for vacancy formation	ΔH_m = enthalpy associate with atom motion
ΔG_m = Gibbs free energy for atom motion	Q = activation energy
n = # atoms / area	J = flux of atoms
β = jump distance	f = jump correlation factor
Do = pre-exponential factor	γ = geometric factor

An excellent illustration of the difference in diffusion in bcc structures versus close packed structures is seen in comparing the data within the rare-earth materials. In rare-earth metals, self-diffusion data appears to conform to empirical equations for close-packed structures with a vacancy controlled mechanism. For example, the activation energy can be estimated as $Q = 34\ T_m$ as shown in Figure 22, and the pre-exponential factor is estimated between $10^{-1} < D_o < 10\ cm^2/sec$. Table V gives diffusion data for several rare-earths (close packed structures). The diffusion data suggests a vacancy type mechanism, although interstitial type mechanisms have been suggested for cerium.

Self-diffusion in bcc rare-earth metals exhibit comparable diffusion rates to other bcc metals that are approximately two orders of magnitude higher than rates observed in close packed structures. Table VI gives diffusion parameters for bcc rare-earth metals. Plutonium diffusion data for the bcc and fcc phases are included for comparison and it can be seen that the plutonium data is consistent with materials with corresponding crystal structures.

2.7 Effect of Iron on the Diffusion of Gallium

Iron has been shown to have a substantial impact on the homogenization response of the plutonium - 1 wt. pct. gallium alloy. Erfurdt [2] studied this impact with additions of iron up to 3000 ppm and concluded, in general, that high iron content enhances the

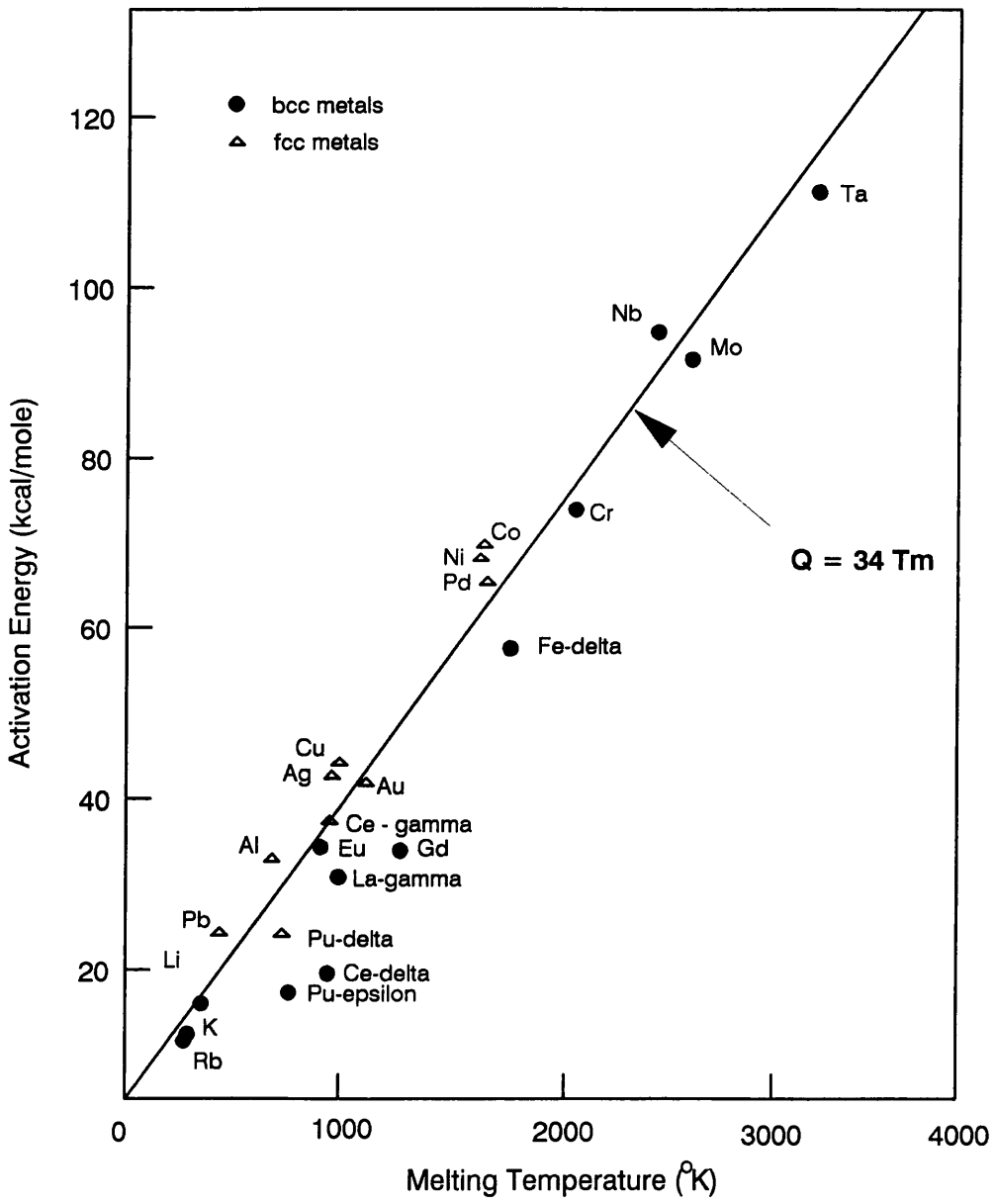

Figure 22: The activation energy for self-diffusion as a function of the melting temperature of bcc and fcc metals [26].

Table V: Self-diffusion data for rare-earth metals with close packed crystal structures[26].

Element	Structure	D_o Cm^2/sec	Q (kcal/mole)	Q/T_m	Temperature Interval (K)
$Y_{//}$	Hcp	0.82	60.3	33.8	1173-1173
$Y_{\perp}$	Hcp	5.2	67.1	37.6	1173-1573
La	Fcc	1.5	45.1	37.9	437-1110
Ce	Fcc	0.6	36.6	34.3	800-970
$Er_{//}$	Hcp	3.7	72.05	40.4	1475-1685
$Er_{\perp}$	Hcp	4.5	72.27	40.5	1475-1685
Yb	Hcp	3.4E-02	35.06	32.1	800-990
δ-Pu	Fcc	1.3	37.4	40.9	600-770

Table VI: Self-diffusion data for rare-earth metals with bcc crystal structures [26]

Element	D_o cm^2/sec	Q (kcal/mole)	Q/T_m	Temperature Interval (K)	ΔV	$\Delta V/V_o$
La	1.3E-02 0.11	24.5	20.5	1140-1173 1143-1183	- 2.20	- 0.1
Ce	1.2E-02 7.0E-03	21.5 20.5	20.0 19.0	1000-1073 1000-1073	- -2.1	- -0.1
Pr	8.7E-02	29.4	24.3	1050-1200		
Gd	8.5E-03	32.2	20.3	1538-1585		
Eu	1	34.5	31.4	773-1073		
Yb	0.12	28.9	26.3	1003-1073	15.7	0.59
ε-Pu	3 E-03	15.7	17.2	773-885	-4.9	-0.34

homogenization rate in a cored material. The increase in iron produced two counteracting effects: (1) increased as-cast stability and (2) decreased rate (homogenization) coefficients. The effect of iron content for homogenization was attributed to:

- A downward shift of the ε / $\varepsilon + \delta$ phase equilibria such that significantly less segregated as-cast alloy is produced.
- The diffusion mechanism changes from substitutional to interstitial evidenced by a dramatic decrease in the activation energy with an increase in iron content.

A second study suggested an alternative mechanism for the enhanced diffusion caused by additions of iron. Lograsso and Hellawell [30] suggested a metatectic type reaction where the plutonium-gallium-iron alloy solidified initially and then a new liquid phase forms again upon subsequent transformation. This type of transformation would explain the rapid diffusion rates (low activation energy) reported by Erfurdt[2]. Figure 23 is a proposed set of free energy diagrams showing the metatectic phase transformation. The diagrams show the free energy relationships between two solid phases and the liquid during cooling. Schematically, all three phases are in equilibrium at T = Tm but upon further cooling, the solid phase, S2 and the liquid represent the lowest

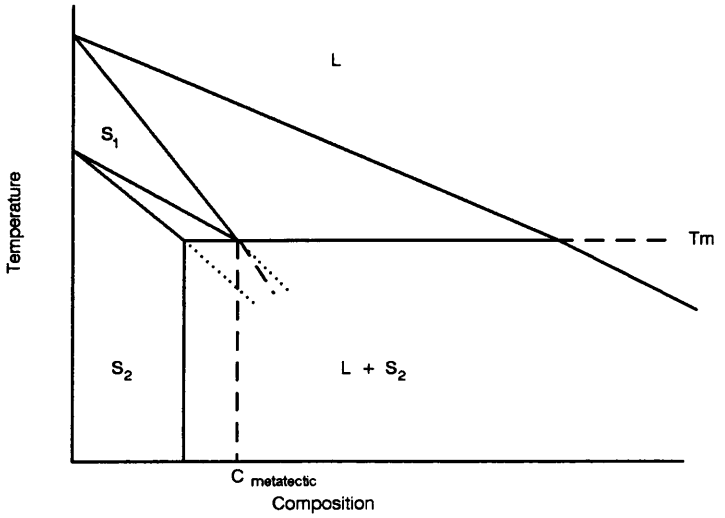

Metatectic construction arising from polymorphic phase change in one component

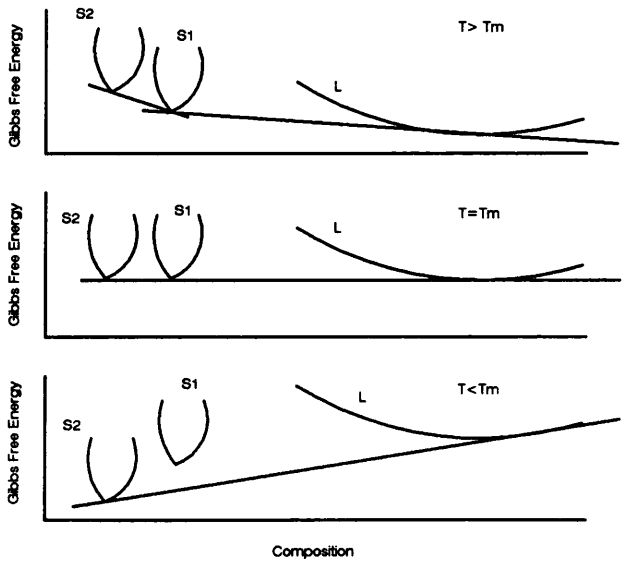

Schematic free energy composition curves for a metatectic system.

Figure 23: Schematic phase diagram for a metatectic phase transformation with applicable schematics of the Gibbs free energy relationships for each phase. Remelting as a result of the phase transformation is believed to enhance diffusion [30].

free energy and the material "re-melts". An additional study by Beitscher [28] identified "hot shortness" in plutonium- 1 wt. pct. gallium alloys with elevated iron content which would support the theory proposed by Lograsso and Hellawell [30]. A similar effect of iron on diffusion is seen in rare-earth materials which may be an additional area of study to be pursued using the surrogate system.

2.8 Processing Impacts of Phase Transformations and the Diffusion of Gallium

The microsegregation of gallium has a dramatic affect on the behavior of plutonium 1 wt. pct. gallium alloys during mechanical processing and ultimately on the mechanical properties. Gardner [18] and Erfurdt [29] studied the effects of rolling on both homogenized and non-homogenized samples. Non-homogenized samples exhibited the greatest increase in strength due to strain hardening and the formation of α-phase plutonium. Hardness and density also increased as expected. Deformation of homogenized samples resulted in a smaller increase in strength primarily due to strain hardening. The resulting microstructure was a mixture of δ-phase and α-phase plutonium formed as the regions containing lower amounts of gallium transformed to α-phase. Erfurdt [2] reported a significant increase in homogenization rate for samples annealed after rolling.

The plutonium - 1 wt. pct. gallium system has been well characterized and a reasonable understanding of the diffusion behavior and the homogenization response of

the alloy has been established. The next step is to identify a similar binary system that can act as a surrogate, but not present the radiological hazards posed by plutonium

2.9 Surrogate Candidates

The investigation to identify a metallurgical surrogate for the plutonium - 1 wt. pct. gallium alloy followed the same approach outlined earlier. The first effort involved finding a material that exhibited similar solid state microsegregation as in the plutonium alloy and establish a strong connection to the established plutonium interdiffusion data. By utilizing the existing homogenization data for plutonium - 1 wt. pct. gallium and measuring similar interdiffusion data for the surrogate, a "homogenization surrogate" could be established. This connection could be expanded to other transport-related phenomena. The second and concurrent effort was to establish a more fundamental correlation between plutonium and the surrogate to establish the candidate as an overall metallurgical surrogate.

The first review consisted of evaluating binary phase diagrams to determine if a two-phase region similar to that in the plutonium - gallium system could be found which leads to the solid state microsegregation discussed earlier [27]. The shape of the two-phase region was also evaluated such that the lower temperature phase exhibited increased solute solubility. For the systems that exhibited the potential for a two-phase region, additional selection criteria were applied including electronic structure, crystal structure, transport data, availability, cost and ease of experimentation. For example,

several zirconium binary systems were evaluated because of promising two-phase regions and the solidification to a body-centered-cubic phase (β-Zr) and a subsequent transformation upon cooling to a close-packed structure (α-Zr, hexagonal-close-packed). This is similar to plutonium that solidifies to a body-centered-cubic phase (ε-Pu) and then transforms to a close-packed structure (δ-Pu, face-centered-cubic). Sixteen candidate systems were identified and the phase diagrams are listed in Appendix B. These systems include:

cobalt - osmium	aluminum - titanium	cerium - samarium
lanthanum - thorium	gallium - titanium	antimony - zirconium
calcium - strontium	hafnium - zirconium	lead - zirconium
europium - ytterbium	cerium - zirconium	tin - zirconium
cerium - neodymium	aluminum - zirconium	
cerium - lanthanum	bismuth - zirconium	

As mentioned above, several zirconium-based phase diagrams indicated potential two-phase regions, but the melting point of zirconium (1855°C) is nearly three times that of plutonium which is a disadvantage for a surrogate. The room-temperature phase of zirconium, while close-packed, is hexagonal rather than face-centered-cubic as seen in plutonium. These are also disadvantages for the titanium-based binary systems. The lanthanum-thorium system exhibits an excellent two-phase region, but thorium is radioactive which provides no advantage over plutonium. The cobalt-osmium system shows a two-phase region, but osmium is expensive and forms a toxic oxide (OsO_4) with a low boiling point. The europium-ytterbium system is promising and warrants further

investigation, but was not chosen due to the high cost of europium. The cerium-based systems including cerium-neodymium, cerium-lanthanum, and cerium- samarium each showed potential two-phase regions. Each of these systems exhibited a body-centered-cubic to face-centered-cubic phase transformation, reasonable cost, and the melting point of cerium is near to that of plutonium (798°C).

Electronic structure was used to establish a more fundamental correlation between plutonium and the list of potential surrogate candidates. This important part of the investigation identified some startling similarities between plutonium and rare-earth candidates, and established the foundation for the development of an overall metallurgical surrogate that will be discussed later.

Extensive work has been conducted showing that the rare-earth elements, also known as the lanthanides, exhibit similar characteristics to the actinide series that contains plutonium. The series of elements are shown in Table VII. A review has been conducted evaluating correlations that have been drawn between the rare-earths and the actinides. The review focused on electronic structure and how this structure leads to specific bulk properties. A specific comparison between plutonium and cerium was explored to establish an initial justification for the use of cerium as a surrogate for plutonium.

Table VII: The rare-earth and actinide series [26]

RARE-EARTHS

57	58	59	60	61	62	63	64	65	66	67	68	69	70	71
La	Ce	Pr	Nd	Pm	Sm	Eu	Gd	Tb	Dy	Ho	Er	Tm	Yb	Lu

ACTINIDES

89	90	91	92	93	94	95	96	97	98	99	100	101	102	103
Ac	Th	Pa	U	Np	Pu	Am	Cm	Bk	Cf	Es	Fm	Md	No	Lr

2.10 Rare-Earth Elements - Electronic Structure

The fourteen elements in the rare-earth series are unique in that the 4f shell fills as one traverses the series. In general, these elements have very similar properties. The 4f shell is an inner shell and the successive addition of electrons does not significantly impact their behavior. A notable exception is cerium which exhibits unusual, "non rare-earth like" behavior.

In the atomic state, most of the rare-earth elements have a divalent configuration except for lanthanum, cerium, gadolinium, and lutetium [31,32]. When the atoms are brought together to form a solid, however, nearly all take on a trivalent character by undergoing a valence transition from the divalent state. This valence transition is of the type:

$$6s^2 4f^{n+1} \text{ ---------- } 6s^2 5d^1 4f^n \qquad (23)$$

The transition involves the promotion of a 4f electron from a localized state to the extended 5d band. Two rare-earths, europium and ytterbium, remain divalent in the solid phase due to the large energy transition required in these materials to achieve the trivalent state. As stated above, cerium is trivalent in the atomic and solid state with the configuration as follows:

$$[Xe]\ 6s^2 5d^1 4f^1 \qquad (24)$$

Figures 24 and 25 provide further insight into the electronic layout of the rare-earths. Figure 24 shows a plot of the mean radius as a function of atomic number. The mean radius was defined using the radial wave function from the solution of the Schrödinger equation [28]:

$$\langle r^k \rangle = \int P^*_{nl}(r)\, r^*\, P_{nl}(r)\, dr \qquad (25)$$

where $P_{nl}(r)$ is the radial wave function with principal quantum numbers n, angular quantum number l and k=1. The mean radii for the actinides are also shown in Figure 24 and are shown for comparison between the two series. Additionally, experimentally measured ionic radii for lanthanides and actinides are shown. The ionic radii are significantly larger than the atomic radii defined by the f wave function because the overall ionic radii are determined by the culmination of the $5s^2\ 5p^6$, or the $6s^2\ 6p^6$ shells. Figure 25 shows the relative intensities of the wave functions for the lanthanides and for the actinides indicating their similarities [33].

2.11 Generalized Phase Diagram for the Rare - Earths

Johansson [31] has established a generalized phase diagram for the rare-earth elements which not only describes phase transformation characteristics of these materials, but provides key information to the anomalous behavior of cerium [31,34]. Johansson [31] summarized the available experimental data for rare-earth phase diagrams and

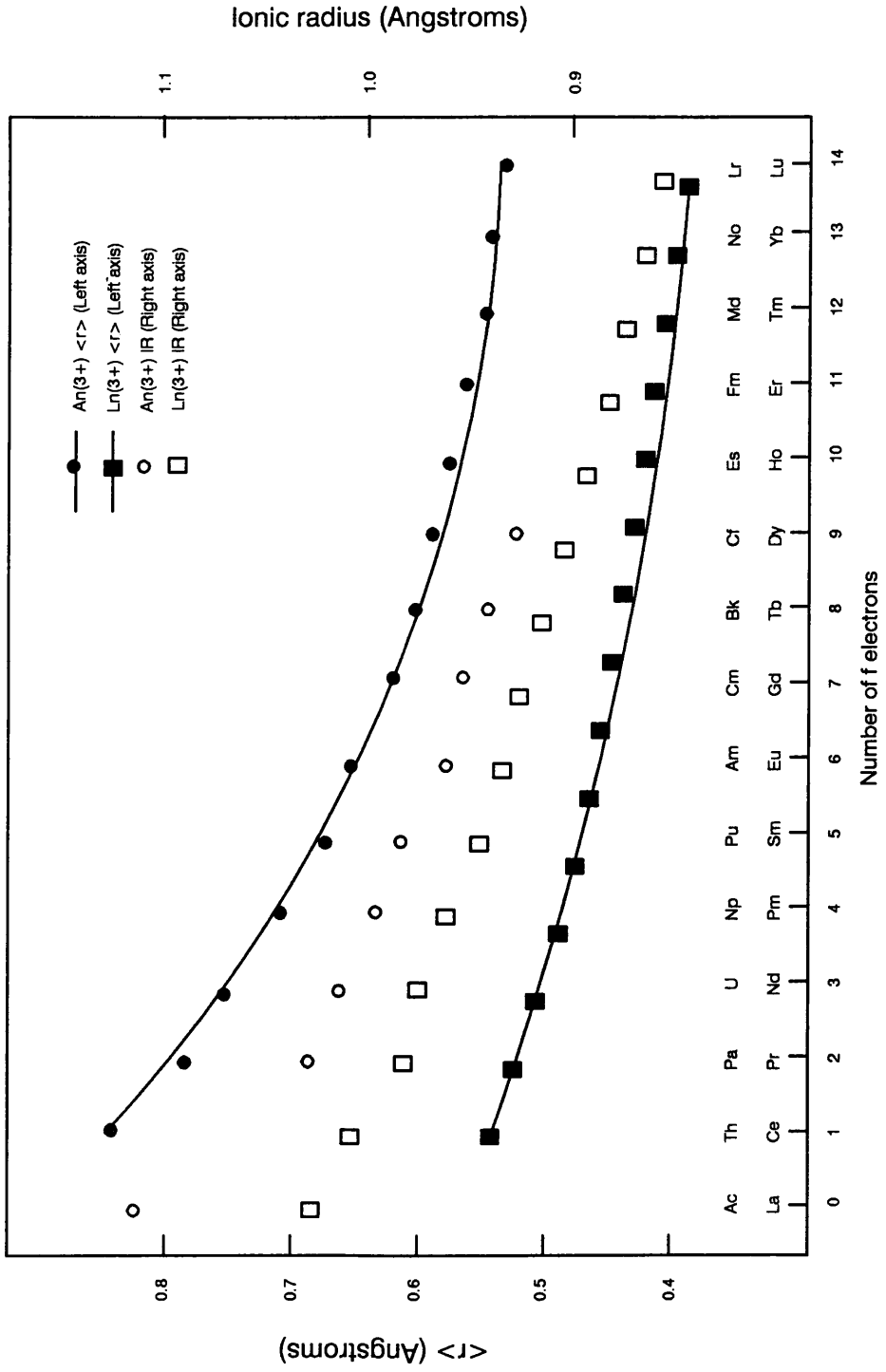

Figure 24: Plot of the calculated mean radii <r> of the trivalent ions of the lanthanides and actinides, and of the experimental ionic radii for these ions [33].

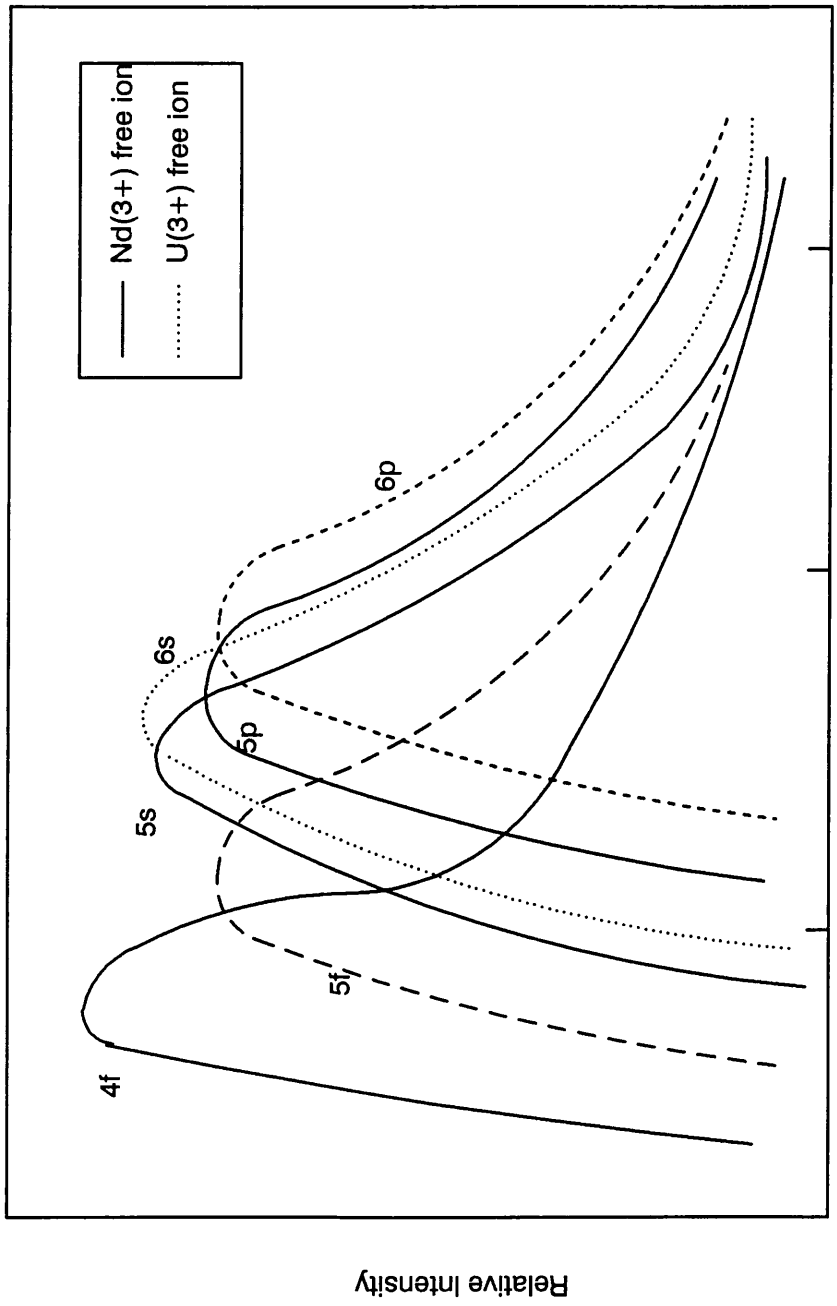

Figure 25: Plot of the 4f, 5s, and 5p wave functions of Nd(3+)(rare-earth), and the 5f, 6s, and 6p wave functions of U(3+) (actinide) [33].

constructed the diagram in Figure 26. Figure 26 shows a structure sequence (heavier rare-earths to lighter rare-earths) as follows:

hcp ----- samarian type ----- dhcp ----- fcc (26)

Most of the rare-earths undergo a phase transformation to a bcc phase prior to melting.

An interesting aspect of the rare-earths is the effect of pressure on the crystal structure sequence shown in the phase diagram. As one proceeds across the series, the atomic volume decreases (22.602 cm^3/mol - lanthanum to 17.779 cm^3/mol - lutetium) [26] with exceptions for europium and ytterbium. When the atomic volume of a given element is decreased by pressure, the structural sequence is changed to reflect that of a larger volume (lower density) element which is the opposite of what one would expect. Johansson [31] explains this apparent problem using a parameter F defined as the ratio of the Wigner-Seitz radius (R_{ws}) to the ionic radius (R_I). The calculation of the Wigner-Seitz radius is dependent upon atomic volume and is pressure sensitive, whereas the ionic radius is pressure insensitive. When pressure is increased, the R_{ws} decreases giving the electrons "less space". However, for the same pressure increase, the ionic radius stays approximately the same and in a relative sense electrons "see" R_I larger than R_{ws}. Therefore, as seen in Figure 27 the parameter F plotted as a function of atomic number shows how a heavier (smaller volume) element can behave like a lighter (larger volume)

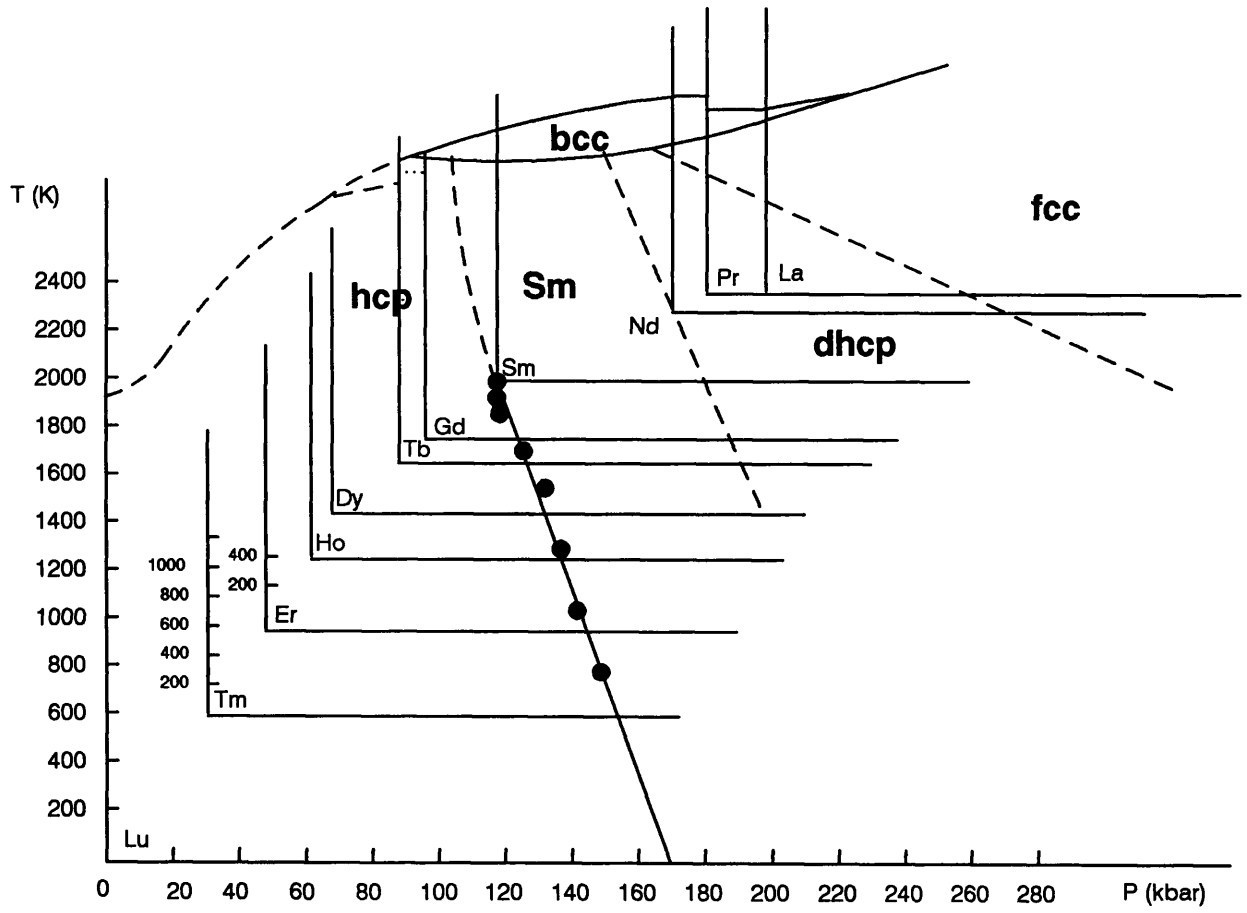

Figure 26: Generalized phase diagram for the lanthanides. Each rare-earth phase diagram was assembled onto the temperature/pressure diagram such that the phase transformation fell on a straight line. Note that in the case of the hcp to Sm transition, the line of transformation also coincided with the respective melting curves. The points represent actual measured data[31].

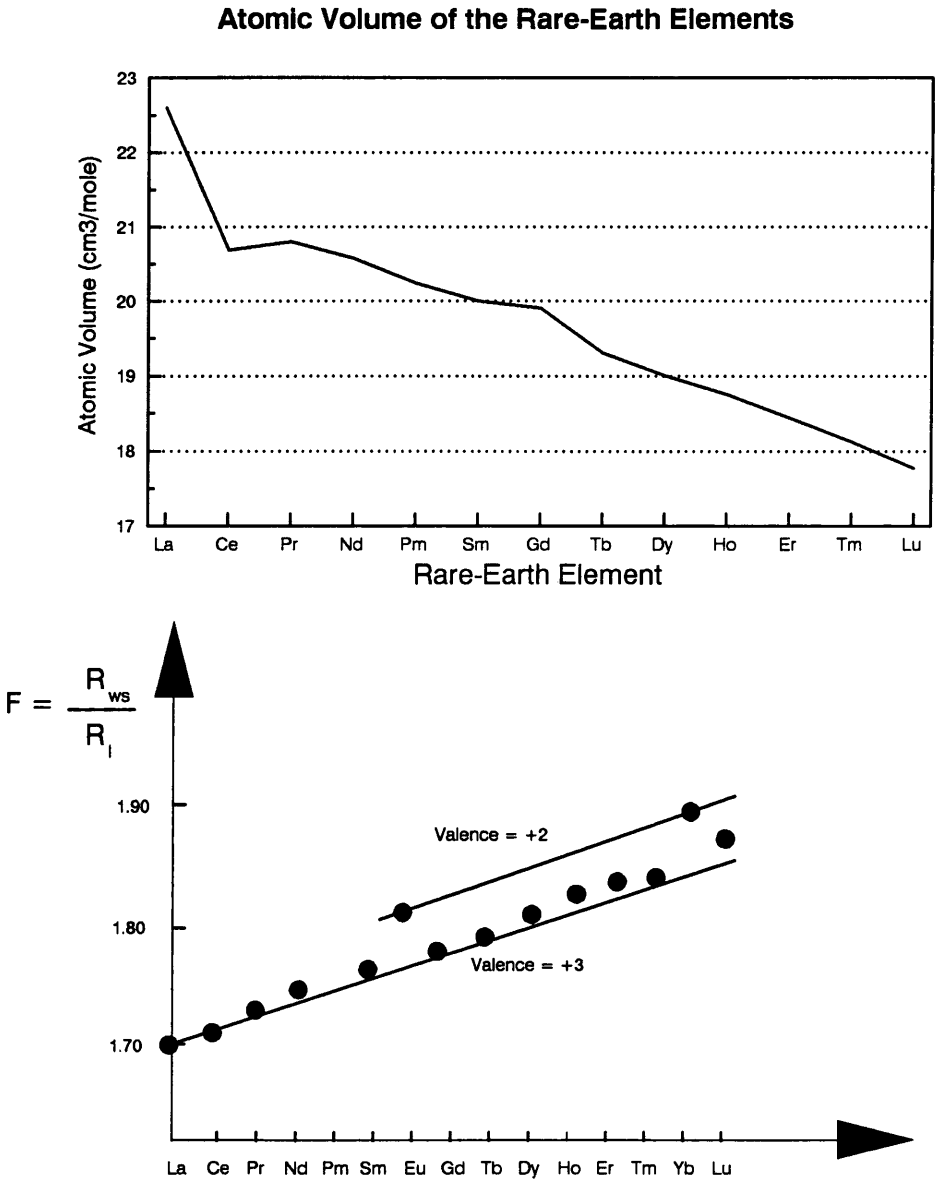

Figure 27: a) The atomic volume of the rare-earth elements excluding europium and ytterbium. b) Ratio F between the Wigner-Seitz and the ionic radius for the rare-earth elements [26,31].

element with an increase in pressure. An increase in pressure decreases R_{ws} and the parameter F is decreased to that of a lighter element.

The two divalent rare-earths, europium and ytterbium, are not shown on the generalized phase diagram but under high pressure one of the 4f electrons can be promoted, resulting in a trivalent state and these elements are "pressured" into the general diagram. Application of pressure to cerium (even atmospheric pressure) on the other hand, will de-localize its 4f electron and it does not fit on the general diagram. At low pressures and above 120 deg K, cerium has been shown to behave like the other rare-earths and will fit into the diagram.

The melting points of the trivalent lanthanide metals as a whole are anomalous when compared to those elements of the remainder of the periodic table. The melting points of the light lanthanides are 500 to 700°C too low from that expected from the trends in the melting points in the first and second transition groups of metals. The elements of the heavy lanthanides are near what one expects, especially near the end of the lanthanide series. Gschneidner [26] has suggested that the low melting points are due to the hybridization of the 4f electrons with the 5d valence electrons.

2.12 Comparison of the Rare - Earths to the Actinides

The actinide series of metals has been labeled as a second rare-earth series based on many similarities between the two series. Table VIII represents a correlation between the two series and aligns the elements in each series that exhibit similar behavior. The

Table VIII: Correlation between the actinides and the rare-earth elements. Rare-earths are shifted to align materials with similar properties [31].

ACTINIDES

89 Ac	90 Th	91 Pa	92 U	93 Np	94 Pu	95 Am	96 Cm	97 Bk	98 Cf	99 Es

"SHIFTED" RARE-EARTHS

				57 La	58 Ce	59 Pr	60 Nd	61 Pm	62 Eu	63 Sm

similarities between the series of elements can be justified in terms of electronic structure. The fact that the actinides beyond uranium have been labeled as a delayed rare-earth series has been attributed to the degree of localization of the 4f (rare-earths) electrons and the 5f electrons (actinides) [31,35].

Data from spectroscopy and trends in atomic volume support the idea that in the early actinides the 5f electrons are itinerant, or de-localized, and participate to a significant extent in atomic bonding. Furthermore, data shows that the 5f electrons become localized around plutonium and the remaining actinides behave more like rare-earths. For example, the "localized 5f electron actinides" including americium, curium, and berkelium exhibit a dhcp phase as in their "light rare-earth 4f electron localized counterparts" and show a similar axial ratio (c/a) of approximately 1.62. These localized 5f actinides thus behave like the localized 4f rare-earths [31].

The discussion of the localization (or itinerancy) of 4f electrons in the rare-earths and 5f electrons in the actinides sets the stage for a correlation of properties between plutonium and cerium. These two materials are seated in a f-electron itinerancy transition zone and, as a result, exhibit similar bulk properties and phase transformation characteristics.

2.13 Comparison of Cerium to Plutonium

The first significant similarity between cerium and plutonium is seen in their unusually low melting temperatures (cerium - 798°C, plutonium - 640°C) and the

pressure dependence of these melting temperatures. Both materials show a decrease in melting temperature, with an increase in pressure toward a minimum temperature, and then a gradual increase. The initial decrease has been attributed to f-orbital repulsion. In addition, both materials show multiple allotropic forms and large volume changes associated with phase transformations between these forms. For example, in the cerium case, the γ - α phase transformation results in a ~ 14 pct. volume change. Plutonium exhibits a volume change of ~ 15 to 20 pct. between the highest and lowest temperature solid phases. The formation of non-symmetrical crystal structures in both plutonium and cerium further demonstrates their link. The room temperature phase of plutonium (α) is monoclinic and the low temperature phase of cerium (α) under pressure (> 62 kbar) has been shown to be monoclinic body centered structure. Table IX summarizes these data and the correlation drawn between cerium and plutonium [24,36,37,38]. A fundamental discussion focused on electronic structure showed a definitive link between the rare-earth series of elements and the actinides. Similarities in the electronic configuration and the itinerancy of the f electrons resulted in similar properties and behavior. A detailed correlation between plutonium and cerium was demonstrated in melting temperature, crystal structures, and phase transformation characteristics. The connection between the rare-earths and the actinides and, more specifically, between cerium and plutonium defines a foundation for the use of cerium as a surrogate for plutonium.

Table IX: Comparison between crystal structures and density of cerium and plutonium [31,36,37,38,39,40]

Plutonium phases	Crystal Structure	Density (g/cm^3)		Cerium Phases	Crystal Structure	Density (g/cm^3)
α	Monoclinic	19.86		α'	c-centered orthorhombic	9.76
β	Body centered monoclinic	17.70		α	face centered cubic	8.29
γ	Orthorhombic	17.14		β	d- hexagonal close packed	6.69
δ	face centered cubic	15.92		γ	face centered cubic	6.77
δ'	body centered tetragonal	16.00		δ	body centered cubic	6.71
ε	body centered cubic	16.51				

2.14 Diffusion of ^{140}La in bcc γ-Lanthanum and δ-Cerium

A dramatic link between cerium and plutonium is discussed by Dariel [41] with his initial measurement of transport data in rare-earth materials. Dariel [41] draws a fundamental comparison between the self-diffusion coefficients of bcc plutonium and bcc cerium. Both materials exhibit unusually low activation energies - half that expected from a normal vacancy mechanism. Cornet [42] proposed an activated interstitial model where the migrating ion at the saddle point is in an electronically excited state having given up part of its 5f electrons to the conduction band - thus reducing its ionic radius. It is recognized that ε-plutonium and δ-cerium are similar to many other bcc metals exhibiting anomalously high diffusion. "While cerium is well known for its variable valence (and therefore ionic radius), praseodymium is considered as being trivalent in its metallic state. The activated interstitial model does not seem at first sight to be applicable to either praseodymium or to the other anomalous bcc metals." [41]

Dariel [41] took the approach of measuring the self-diffusion of γ-La (with no 4f electrons) to decide if the anomalous diffusion is associated with the solvent matrix or with the migrating atom. The diffusion data from this work is summarized in Table X. Dariel [41] concludes from this data: "With respect to the solute diffusion of lanthanum in cerium, it seems reasonable to assume that lanthanum diffuses in cerium by a mechanism identical to that of self-diffusion in cerium. This conclusion is based on the similar activation energies and pre-exponential terms and discontinuity in the diffusivities at the phase transformation. (Preliminary results indicate that there is a hundred-fold

Table X: Summary of diffusion data for cerium-lanthanum alloys showing the significant difference between the bcc phases and the fcc phases [41].

Matrix	Diffusing Tracer	Q (kcal/mole)	D_o (cm^2/sec)
β - La (fcc)	^{140}La	45.1	1.5
γ - Ce (fcc)	^{141}Ce	36.6	5.5
δ - Ce (bcc)	^{141}Ce	21.5	1.2×10^{-2}
δ - Ce (bcc)	^{140}La	24.5	3.8×10^{-2}
γ - La (bcc)	^{140}La	24.5	1.3×10^{-2}

increase of the diffusivities of lanthanum at the phase transformation from fcc to bcc cerium.)" The reference to preliminary results indicating a 100-fold change in transport characteristics at the phase transformation between δ-Ce (bcc) and γ-Ce (fcc) is essentially identical to that discussed earlier with ε-Pu (bcc) and δ-Pu (fcc). The evidence presented strongly supports development of a cerium based surrogate material. The electronic correlation between the behavior of 4f versus 5f electrons provides an opportunity to evaluate fundamental mechanisms in the surrogate and directly correlating them to plutonium. Furthermore, while the phase diagrams for the cerium-based candidates are not well established, the preliminary evidence reported by Dariel [41] provides an overwhelming argument to pursue cerium-based binaries. Finally, based on material availability and cost considerations the cerium-neodymium and cerium lanthanum systems were chosen for further investigation.

3.0 EXPERIMENTAL PROGRAM

3.1 Initial Experimental Work - Identification of a Cored Surrogate

The goal of the initial experimental work was to determine whether a cerium-neodymium or cerium-lanthanum alloy would exhibit solid state microsegregation. The general approach was to cast cerium- ~5 wt. pct. alloy samples and cool them through the two-phase regions indicated on the applicable phase diagram. A scanning electron microprobe was used to evaluate the degree of microsegregation that was then correlated to the microstructure metallographically. Once solid state microsegregation was achieved, a subsequent experiment was designed to measure transport data for the surrogate. The surrogate was then analytically correlated to the plutonium-gallium system as an initial link that would establish a foundation for development of a metallurgical surrogate.

3.2 Alloy Preparation

The raw materials for the cerium alloys were reported at 99.9 wt. pct. purity for cerium, neodymium and lanthanum. Feed ingots were sectioned with a hacksaw utilizing mineral oil to minimize the fire hazard presented by these pyrophoric materials. The ingot sections were cleaned in ethanol to remove the mineral oil and the surfaces cleaned with an abrasive cloth prior to charging into a magnesium oxide crucible. Figure 28 shows the magnesium oxide crucible used for the casting. A cylindrical crucible

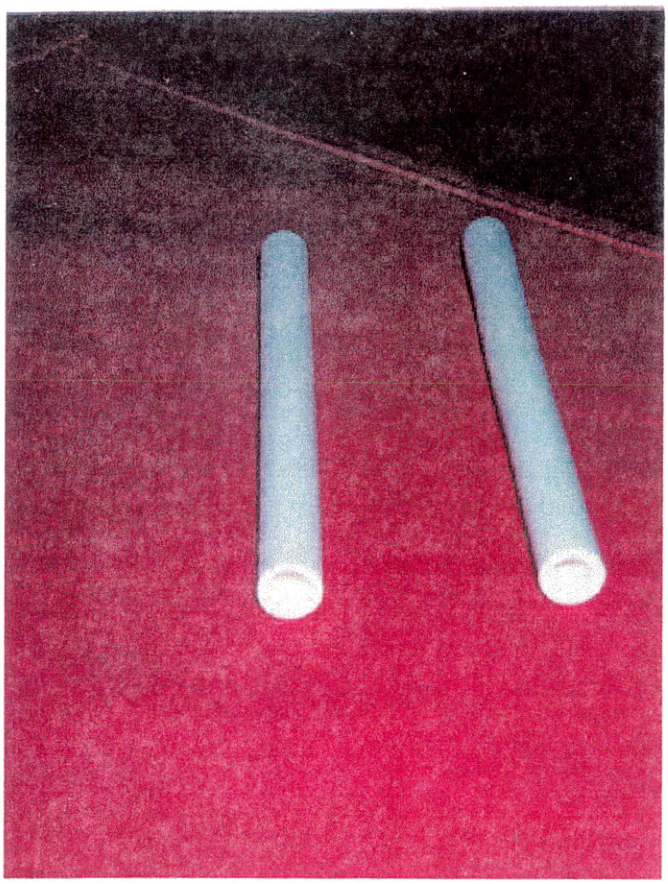

Figure 28: Photograph of magnesium oxide crucibles used to cast cerium alloys. The cylindrical crucibles were used to produce castings with dimensions near to the finished dimensions required for the Gleeble thermo-mechanical apparatus. This "near-net-shape" casting minimized the production of cerium machining chips which are pyrophoric.

approximately 180 mm long and 8.4 mm diameter was used for the cerium-neodymium castings which produced a casting near to the shape of the machined specimen needed for the Gleeble thermo-mechanical simulator instrument discussed later. The "near-net" shape minimized the amount of machining required for these specimens and again reduced the amount of pyrophoric turnings. A high temperature vacuum furnace was utilized to cast the cerium alloys identified. A photograph of the furnace is shown in Figure 29. The vacuum system consisted of a roughing pump combined with a diffusion pump capable of achieving vacuum levels to 1×10^{-7} torr. The castings were loaded into the vacuum furnace and the system was allowed to "pump-down" overnight at a slightly elevated temperature (150°C) to obtain the best vacuum possible. Prior to heating the vacuum chamber was filled with high purity argon gas until the chamber was slightly positive to prevent the vaporization of neodymium and lanthanum. For example the vapor pressure of neodymium at 950°C is approximately 1×10^{-5} torr. During heating, the pressure was relieved manually via a separate chamber vent valve to avoid over-pressurization of the chamber.

3.3 Cerium - Neodymium

Figure 30 shows a schematic reproduction of the cerium-neodymium system and identifies the two-phase region of interest. To investigate this material, a sample was prepared as described above with the mass balance and furnace profile shown in Figure 31. The alloy was held at 950°C for two hours and the neodymium was initially

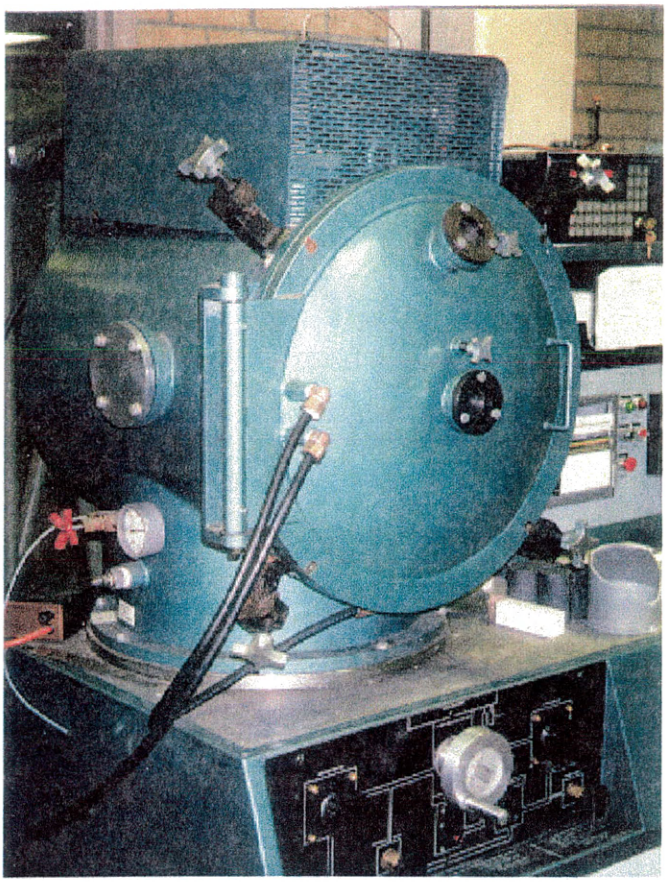

Figure 29: Photograph of vacuum furnace used to cast cerium alloys.

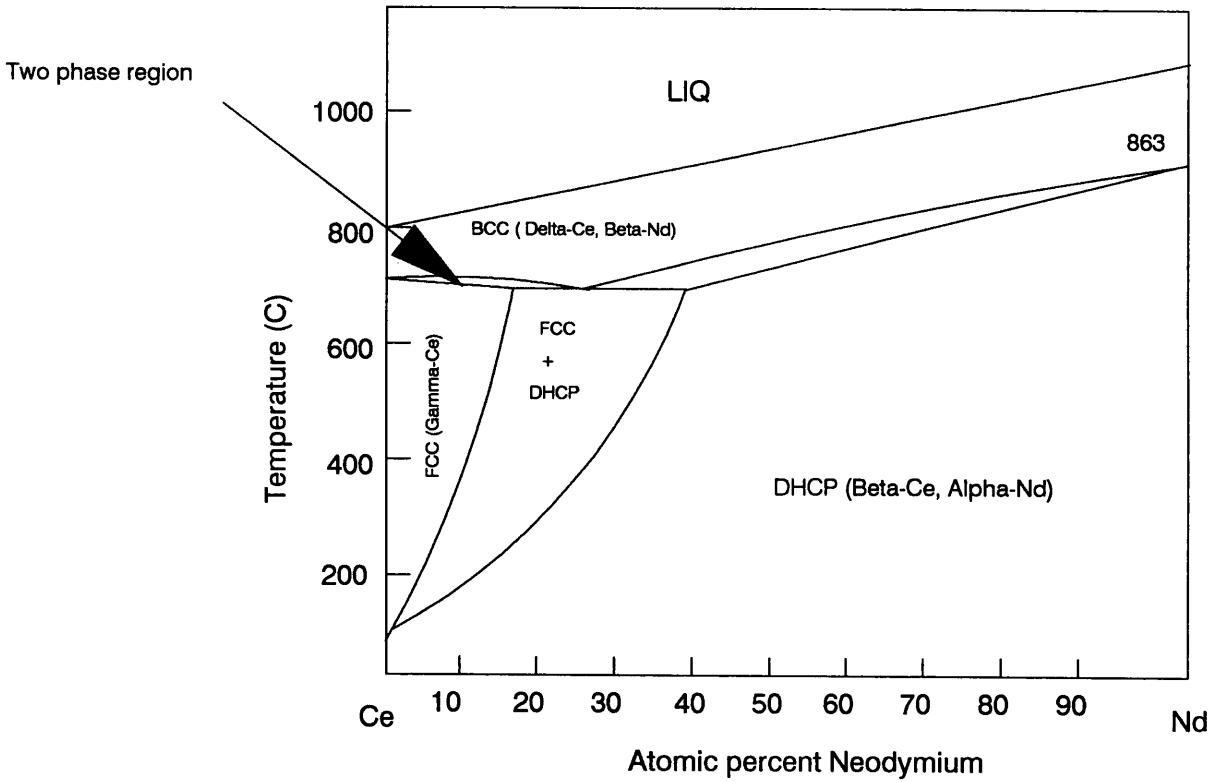

Figure 30: Schematic representation of the cerium-neodymium phase diagram showing a two-phase region which may lead to solid state microsegregation and thus a potential candidate for a plutonium - 1 wt. pct. gallium surrogate. The two-phase region is exaggerated in this figure to show its location. The actual region is reported to be narrower [43].

Casting Conditions

Casting Temperature: 950°C
Vacuum Level: 5 x 10^{-4} torr
Grade 5 Argon Backfill

Mass Balance

MgO Crucible		70.6 g
Charge + Crucible		139.4 g
Cerium		68.8 g
Neodymium		4.5 g
Casting Charge		73.3 g
Alloy Comp:	6.1 % Nd	

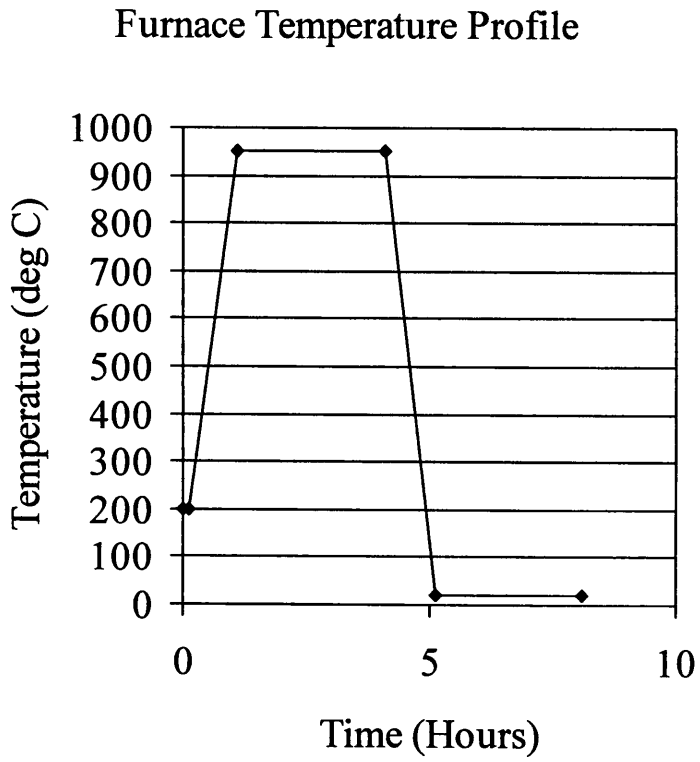

Figure 31: Casting setup for the initial cerium-neodymium alloy to investigate the potential for microsegregation of neodymium. Shown are the mass balance for the casting and the furnace temperature profile. The sample was furnace cooled.

distributed evenly throughout the crucible to ensure a homogenous starting alloy. A sample from this casting was mounted and a photomicrograph is shown in Figure 32. To evaluate distribution of the neodymium solute, microprobe trace was made of the sample using a wavelength dispersive spectrometer. A 200 um trace was scanned across the specimen in 2 um steps. The results from this trace are shown in Figure 33. Table XI shows the raw data from this microprobe scan. These figures show that the distribution of neodymium in this sample is essentially homogenous with a variation of approximately +\- 0.2 wt. pct. neodymium. With the slow cooling rate used for this initial run, and resulting large grain size (200 - 300 um), a significantly higher cooling rate was required to induce microsegregation within the grains. A microprobe scan across a representative number of grains can then be run to determine if coring occurs.

To achieve a higher cooling rate, a Gleeble thermo-mechanical simulator was employed as shown in the schematic of Figure 34. The Gleeble is an instrument designed for mechanical testing of metal specimens including the capability to heat the specimens while undergoing a mechanical test. The specimens are heated as a result of their electrical resistance via the connections to the two copper grips shown in the schematic. This arrangement provides the capability for rapid heating or cooling with excellent temperature control. While the Gleeble offers significant capabilities for mechanical testing, the rapid cooling was the primary capability needed for this experiment.



Figure 32: Photomicrograph of a cerium- 5 wt. pct. neodymium sample furnace cooled through the two-phase region. Grain structure was poorly defined, but due to lack of microsegregation, no further preparation was performed. Magnification shown was 200 X.

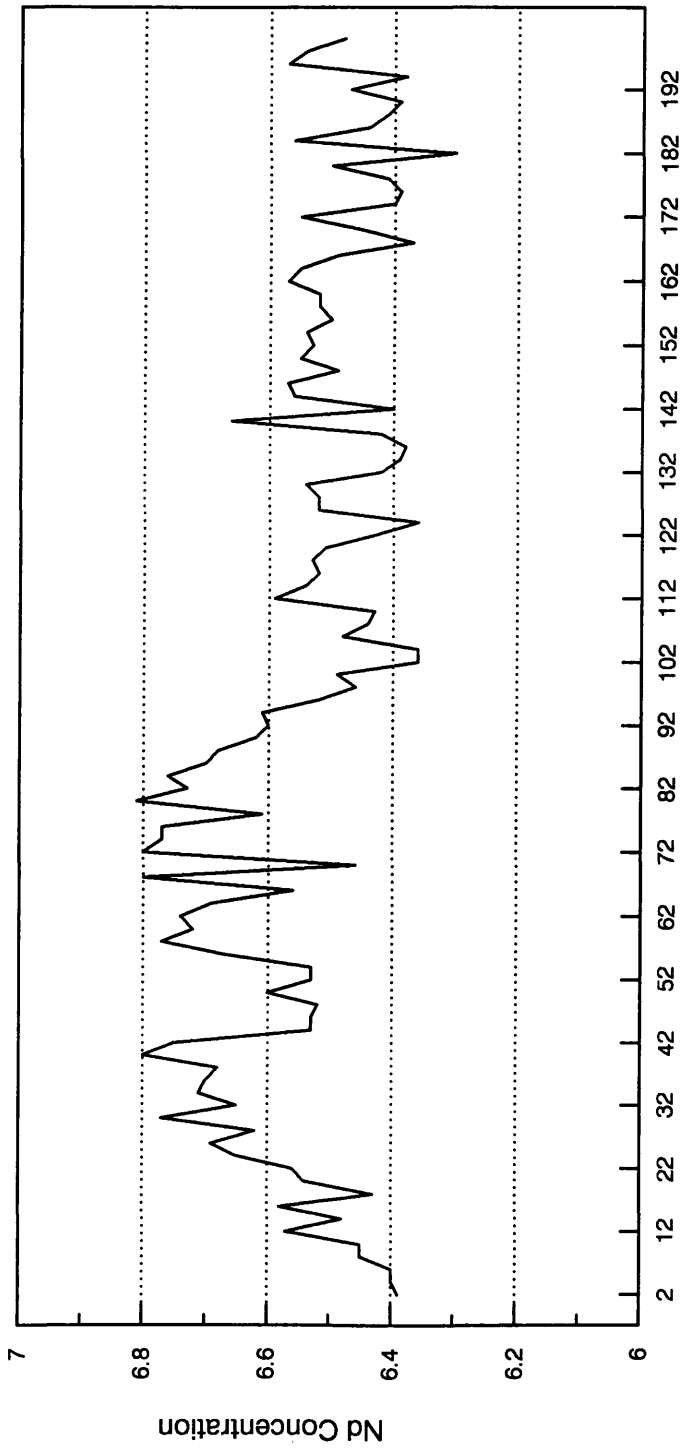

Figure 33: Microprobe trace of cerium ~ 6 wt. pct. neodymium alloy of furnace cooled specimen showing essentially homogeneous distribution of neodymium. Neodymium concentration variation approximately 0.2 wt. pct.

Table XI: Microprobe data from initial cerium - 5 wt. pct. alloy as plotted in Figure 33. The beam size was 1 μm with detection limits of the first reported point at ±0.061 wt. pct. neodymium.

Distance (um)	Nd (wt. pct.)	Distance (um)	Nd (wt. pct.)
2	6.39	102	6.36
4	6.26	104	6.36
6	6.4	106	6.48
8	6.45	108	6.44
10	6.45	110	6.43
12	6.57	112	6.59
14	6.48	114	6.54
16	6.58	116	6.52
18	6.43	118	6.24
20	6.54	120	6.51
22	6.56	122	6.43
24	6.65	124	6.36
26	6.69	126	6.52
28	6.62	128	6.52
30	6.77	130	6.54
32	6.65	132	6.42
34	6.71	134	6.39
36	6.7	136	6.38
38	6.68	138	6.42
40	6.8	140	6.66
42	6.75	142	6.4
44	6.53	144	6.56
46	6.43	146	6.57
48	6.52	148	6.49
50	6.6	150	6.55
52	6.22	152	6.53
54	6.16	154	6.54
56	6.67	156	6.5
58	6.77	158	6.71
60	6.72	160	6.52
62	6.74	162	6.57
64	6.69	164	6.55
66	6.56	166	6.49
68	6.8	168	6.37
70	6.46	170	6.45
72	6.8	172	6.55
74	6.77	174	6.4
76	6.77	176	6.39
78	6.61	178	6.41
80	6.81	180	6.5
82	6.73	182	6.3
84	6.76	184	6.56
86	6.7	186	6.44
88	6.68	188	6.41
90	6.62	190	6.39
92	6.6	192	6.47
94	6.61	194	6.38
96	6.52	196	6.57
98	6.46	198	6.54
100	6.49	200	6.48

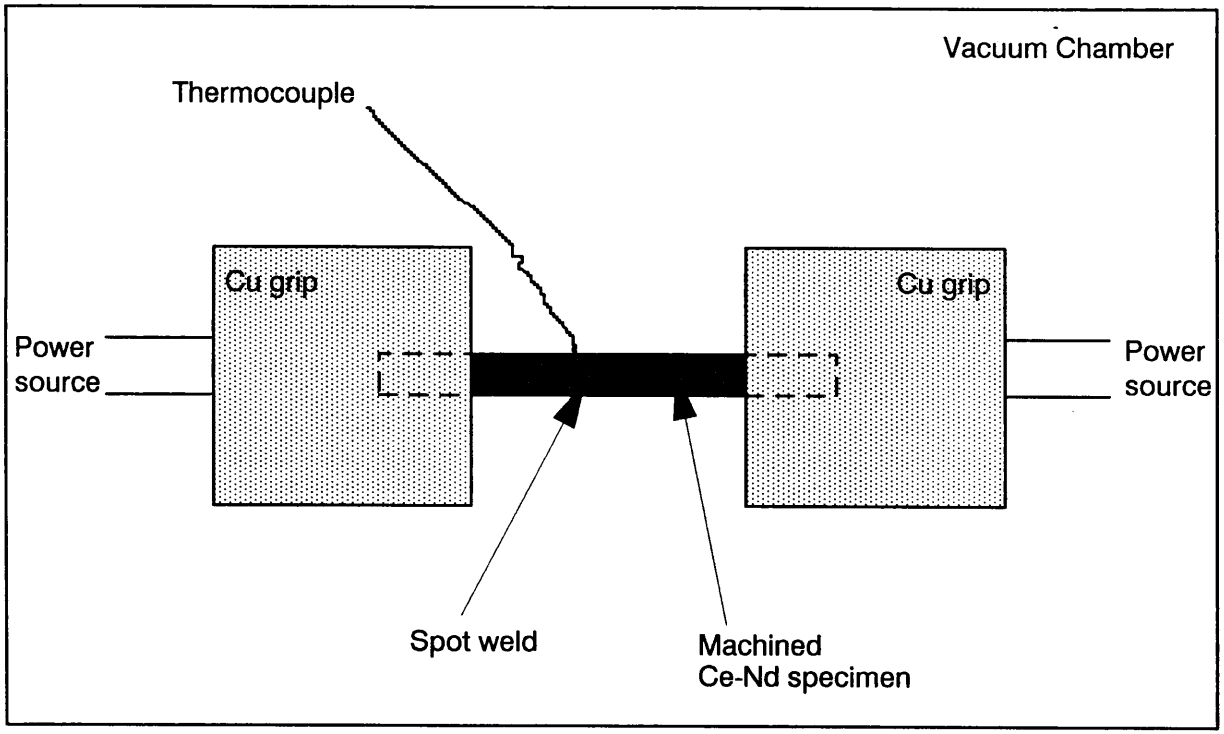

Figure 34: Schematic of Gleeble thermo-mechanical setup used to obtain an enhanced cooling rate for cerium-neodymium alloy. Result was the melting of the specimen at the center.

Two cerium-neodymium alloys were cast as detailed in Figure 35. After melting, the specimens were heated to 550°C to ensure a homogenous distribution of neodymium prior to the Gleeble run. The homogenization temperature profile is also shown in Figure 35. As mentioned above, a cylindrical crucible was used to produce a casting that was near to the shape of the size of the machined specimen needed to fit the Gleeble fixture. Due to the pyrophoric nature of cerium, a slow machining rate was used while manually applying mineral oil liberally to the specimen. Three passes were used to machine the cerium-neodymium specimen to a 6.35 mm diameter and the machining chips were collected and converted to an oxide in a muffle furnace for safe disposal. A Chromel-Alumel thermocouple was spot welded to the specimen to allow temperature measurement and control during the Gleeble run.

A temperature of 745°C was used as the setpoint for two Gleeble runs to heat the specimens above the two- phase region shown on the cerium-neodymium phase diagram. The Gleeble was then programmed to quench the specimens through the two-phase region as quickly as possible to promote microsegregation. Figures 36 and 37 show plots of temperature data from both Gleeble runs. Temperature control of the Gleeble was unpredictable (cerium has not been tested with the Gleeble previously) and, both specimens melted at the center. While not optimum, the center of the specimens did achieve a temperature above that of the two-phase region and were mounted as shown in Figure 38 to determine if coring had occurred. The metallographic preparation technique used for the cerium samples is summarized in Appendix C. Figures 39 and 40 show a

Casting Conditions

Casting Temperature: 950°C
Furnace Conditions = 5×10^{-6} torr (sample #`1)
= 2×10^{-5} torr (sample #1)
Grade 5 Argon Backfill

Mass Balance

MgO Crucible (sample #1)	35.4 g
MgO Crucible (sample #2)	39.2 g
Ce + MgO Crucible (sample #1)	58.5 g
Ce + MgO Crucible (sample #2)	59.9 g
Ce (sample #1)	23.1 g
Ce (sample #2)	20.7 g
Nd addition (sample #1)	1.0 g
Nd Addition (sample #2)	1.0 g
Casting Charge (sample #1)	24.1 g
Casting Charge (sample #2)	21.7 g
Alloy composition (sample #1)	4.2 % Nd
Alloy composition (sample #2)	4.6 % Nd

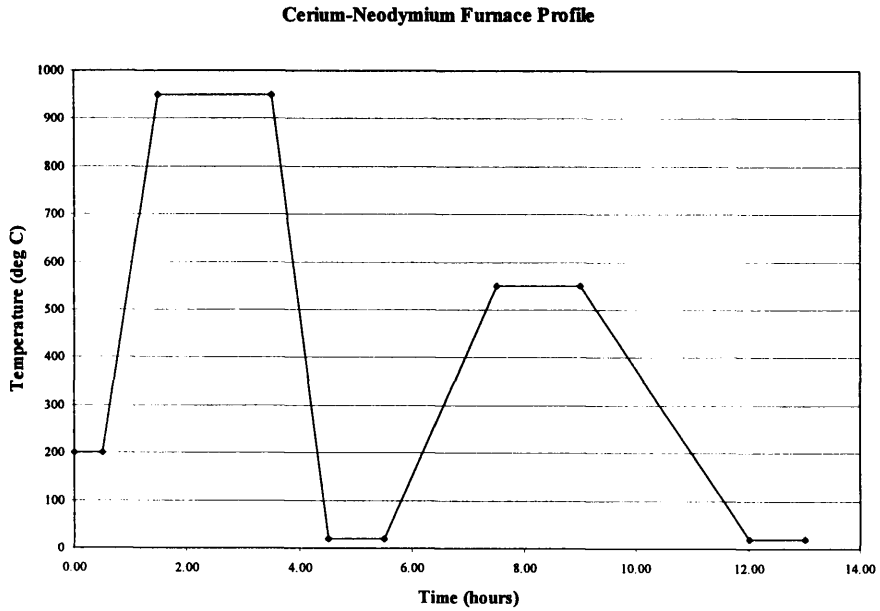

Figure 35: Casting setup for two cerium-neodymium alloys to be machined and then inserted into the Gleeble instrument for rapid cooling through the two-phase region. Shown are the mass balance for the castings and the furnace temperature profile. The furnace treatment included a homogenization treatment to ensure adequate distribution of the neodymium. These samples were then heated in the Gleeble to above the two-phase region and then air-cooled rapidly to promote microsegregation of the neodymium.

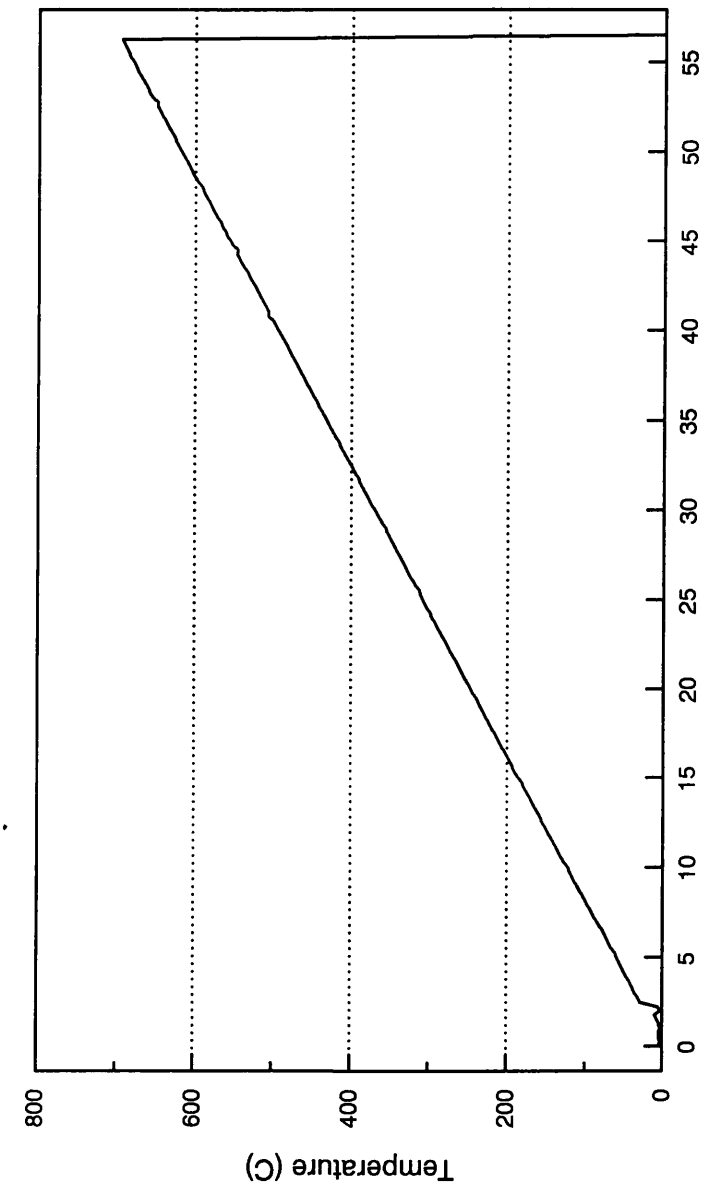

Figure 36: Temperature data from cerium-neodymium run with the Gleeble instrument. Data stopped recording when specimen melted in the center and the thermocouple fell off of specimen. Cooling at the center of the specimen was a rapid air quench as shown.

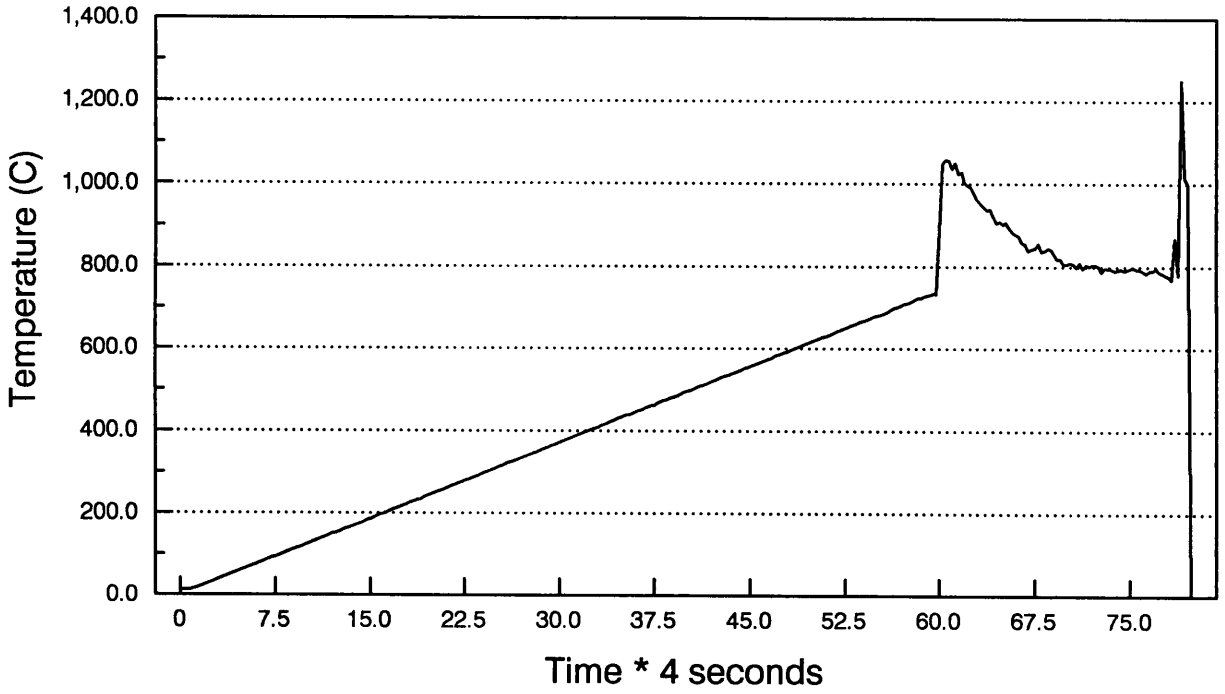

Figure 37: Temperature data from the second cerium-neodymium run with Gleeble instrument. Data stopped recording when specimen melted in the center and the thermocouple fell off of specimen. Cooling at the center of the specimen was a rapid air quench as shown.

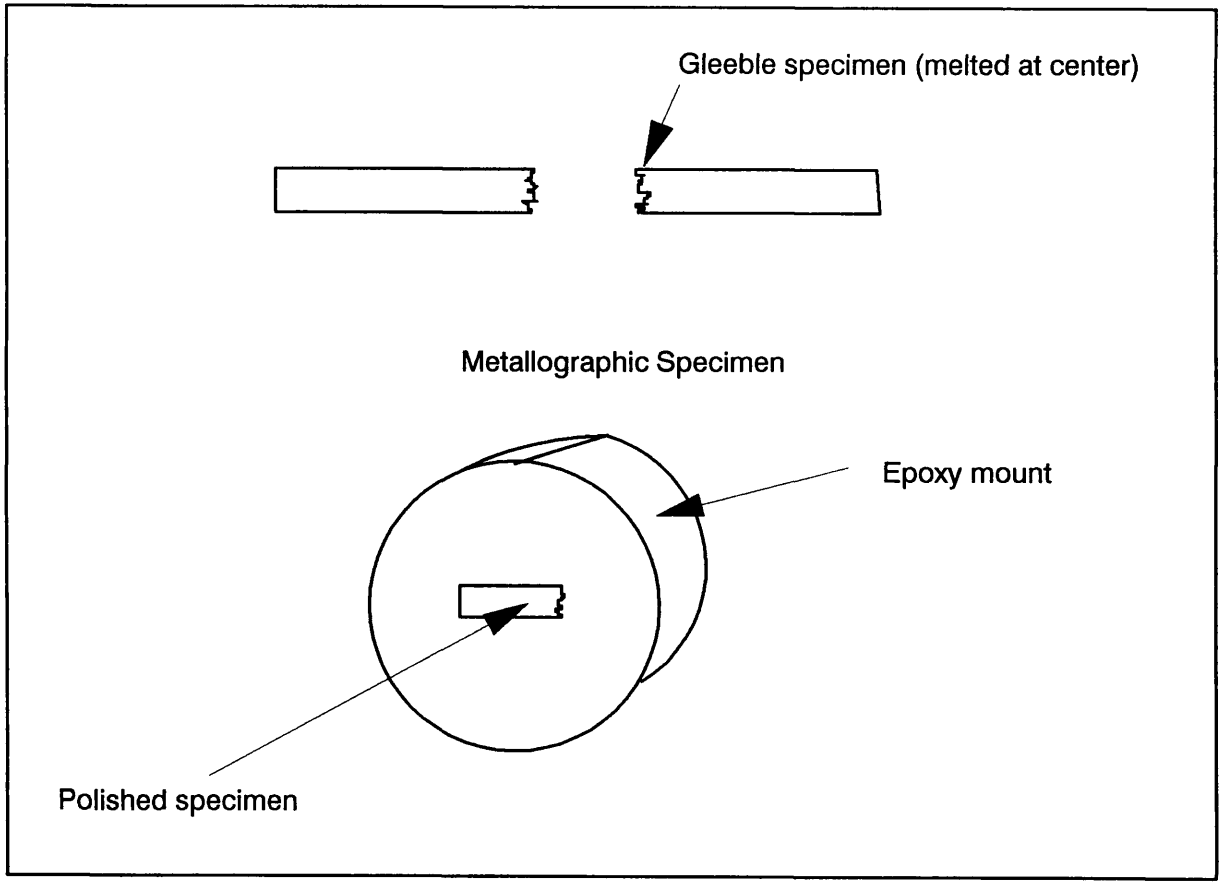

Figure 38: Schematic of metallographic mount from cerium-neodymium Gleeble specimen. Area of interest is adjacent to melted zone which reached a temperature greater than the two-phase region and was cooled quickly through this region.

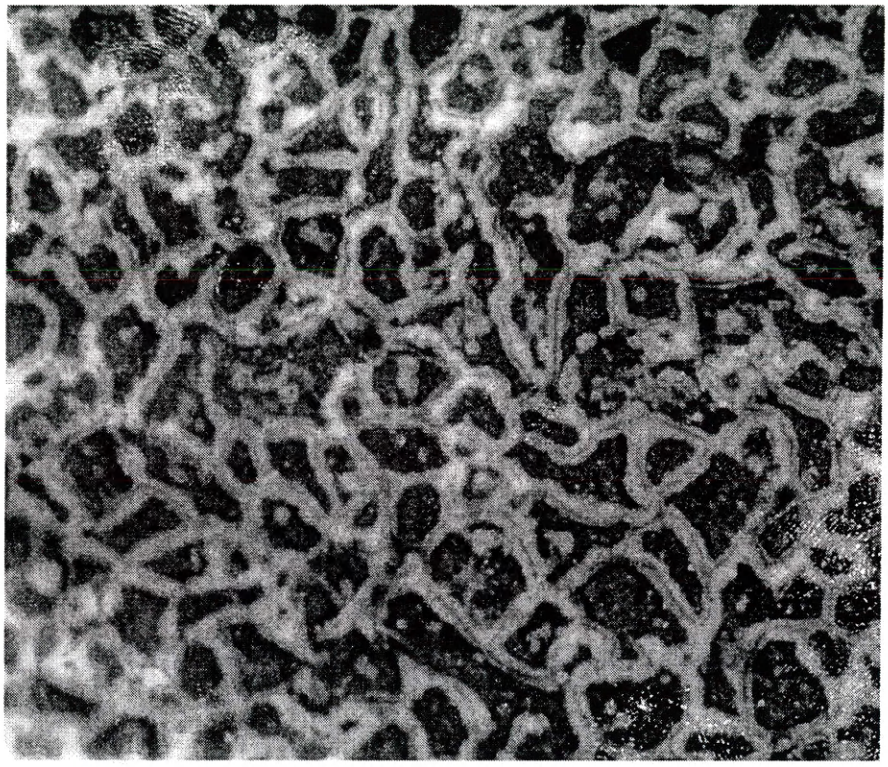

Figure 39: Photomicrograph of cerium-neodymium specimens rapidly cooled using the Gleeble instrument. Specimen was polished and allowed to oxidize slightly to highlight grain boundaries. Magnification is 200 X and approximate grain size is 12 - 20 um. Microprobe scan traversed approximately 5 grains.

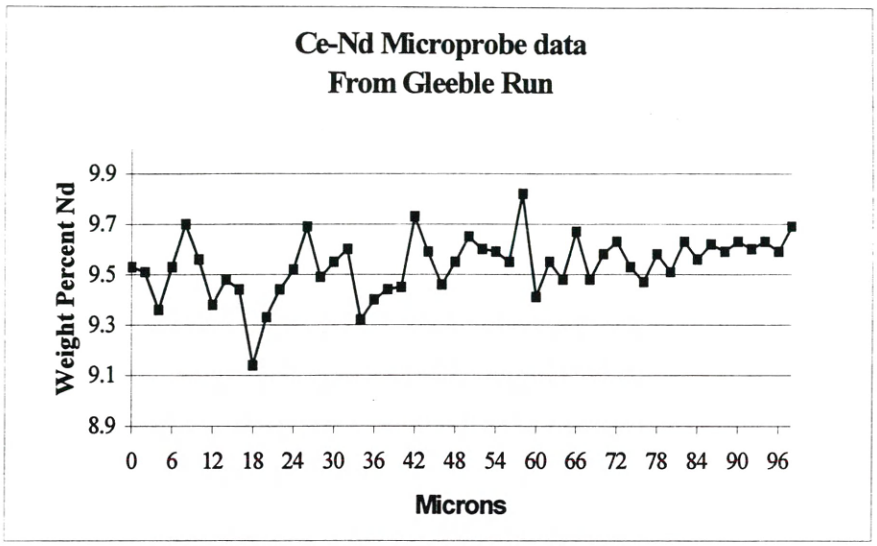

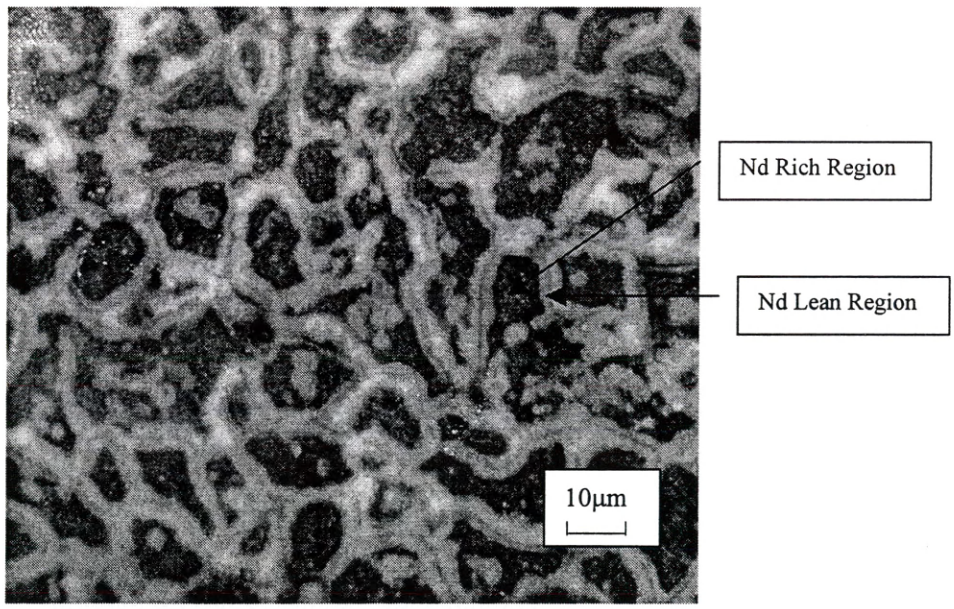

Figure 40: Photomicrograph of cerium-neodymium Gleeble specimen with corresponding microprobe trace showing the concentration variation of neodymium. Approximate grain size is 12-20 μm and microprobe scan traversed approximately 5 grains. Note the variation in neodymium is approximately equivalent to the grain size. Neodymium variation suggests microsegregation due to the incomplete homogenization of neodymium during the delta to gamma cerium phase transformation. Detection limit for neodymium was +/- 0.057 wt. pct. using a wavelength dispersive spectrometer.

photomicrograph and the results of a microprobe scan respectively. The raw microprobe data is shown in Table XII. A variation in the neodymium concentration can be seen in the microprobe data at approximately 20 μm increments. This variation corresponds to the "core" size seen in the photomicrograph that suggests that solid state microsegregation has occurred. It is recognized that the phase diagram is not well established and the width of the two-phase region is only an approximation, but the initial results warranted further investigation of this system as a potential homogenization surrogate.

3.4 Cerium - Lanthanum

Figure 41 shows a schematic reproduction of the cerium-lanthanum system and identifies the two-phase region of interest. To investigate this material, a casting was prepared for melting in a magnesium oxide crucible as shown in Figure 42. The alloy was held at 950 °C for two hours and the lanthanum was distributed evenly throughout the crucible to ensure a homogenous starting alloy. A sample from this casting was mounted and a representative photomicrograph is shown in Figure 43. Again the metallographic techniques described in Appendix C were used to prepare the photomicrographs. To evaluate distribution of the lanthanum solute, a microprobe trace was made of the sample using a wavelength dispersive spectrometer. The results from the microprobe scan are shown in Figure 44 and indicate a homogeneous distribution of the lanthanum. The raw data from this microprobe scan is shown in Table XIII. As with

Table XII: Raw data from microprobe scan of cerium-neodymium specimen subjected to air quench using the Gleeble instrument. Data is plotted in Figure 40 and indicates a variation in neodymium resulting from cooling through the two-phase region.

Distance	**Nd**	**Distance**	**Nd**
um	**wt. pct.**	**um**	**wt. pct.**
0	9.53	50	9.65
2	9.51	52	9.6
4	9.36	54	9.59
6	9.53	56	9.55
8	9.7	58	9.82
10	9.56	60	9.41
12	9.38	62	9.55
14	9.48	64	9.48
16	9.44	66	9.67
18	9.14	68	9.48
20	9.33	70	9.58
22	9.44	72	9.63
24	9.52	74	9.53
26	9.69	76	9.47
28	9.49	78	9.58
30	9.55	80	9.51
32	9.6	82	9.63
34	9.32	84	9.56
36	9.4	86	9.62
38	9.44	88	9.59
40	9.45	90	9.63
42	9.73	92	9.6
44	9.59	94	9.63
46	9.46	96	9.59
48	9.55	98	9.69

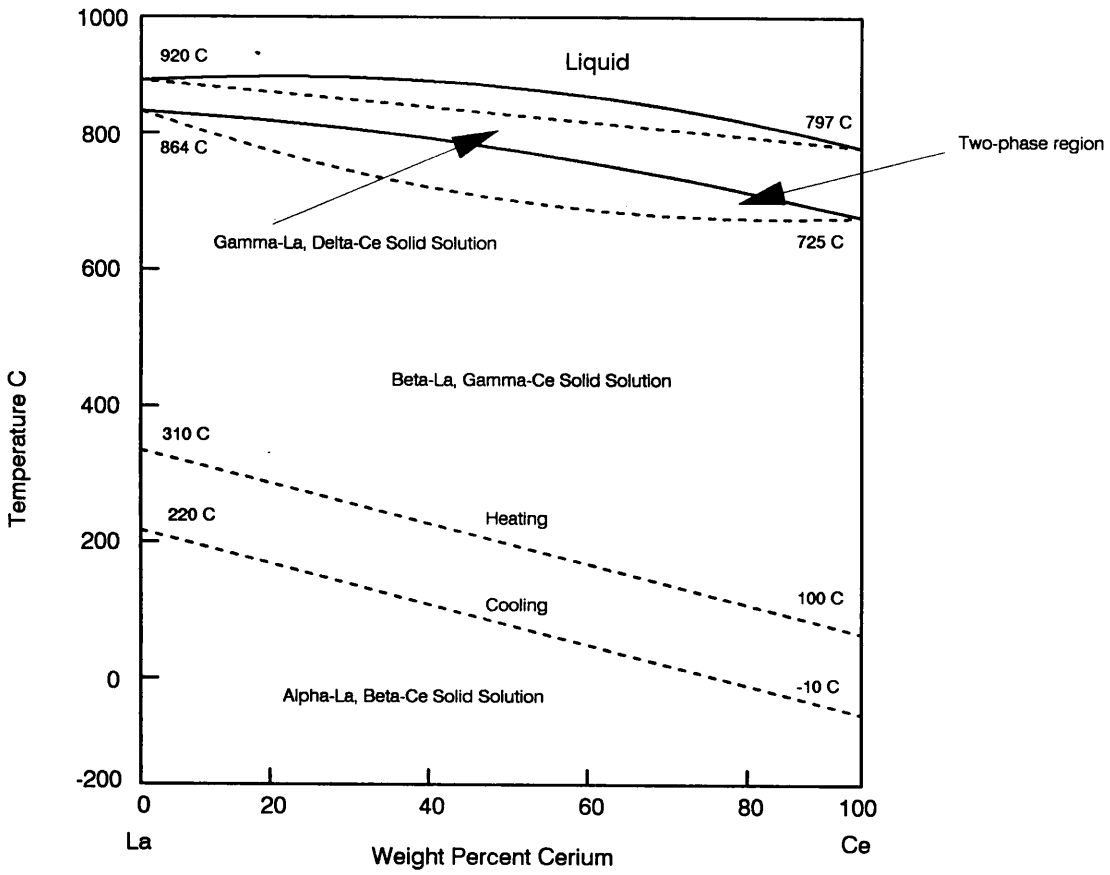

Figure 41: Schematic representation of lanthanum-cerium phase diagram showing two-phase region which may lead to solid state microsegregation and thus a potential candidate for a plutonium - 1 wt. pct. gallium surrogate. The two-phase region is exaggerated to show its location. The actual region is reported to be much narrower [36].

Casting Conditions

Casting Temperature: 950°C
Furnace Conditions = 5×10^{-6} torr (sample #`1)
Grade 5 Argon Backfill

Mass Balance

MgO Crucible	29.4 g
Ce + MgO Crucible	55.2 g
Ce	25.8 g
La addition	0.9 g
Casting Charge	26.7 g
Alloy composition	3.4 % La

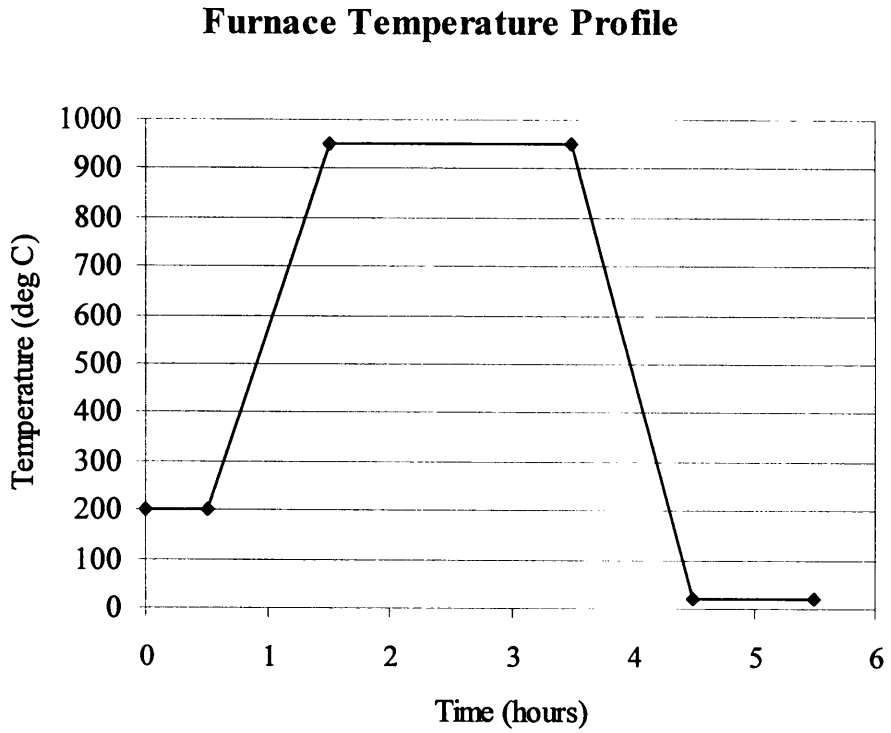

Figure 42: Casting setup for the initial cerium-lanthanum alloy to investigate the potential for microsegregation of lanthanum. Shown are the mass balance for the casting and the furnace temperature profile. The sample was furnace cooled.

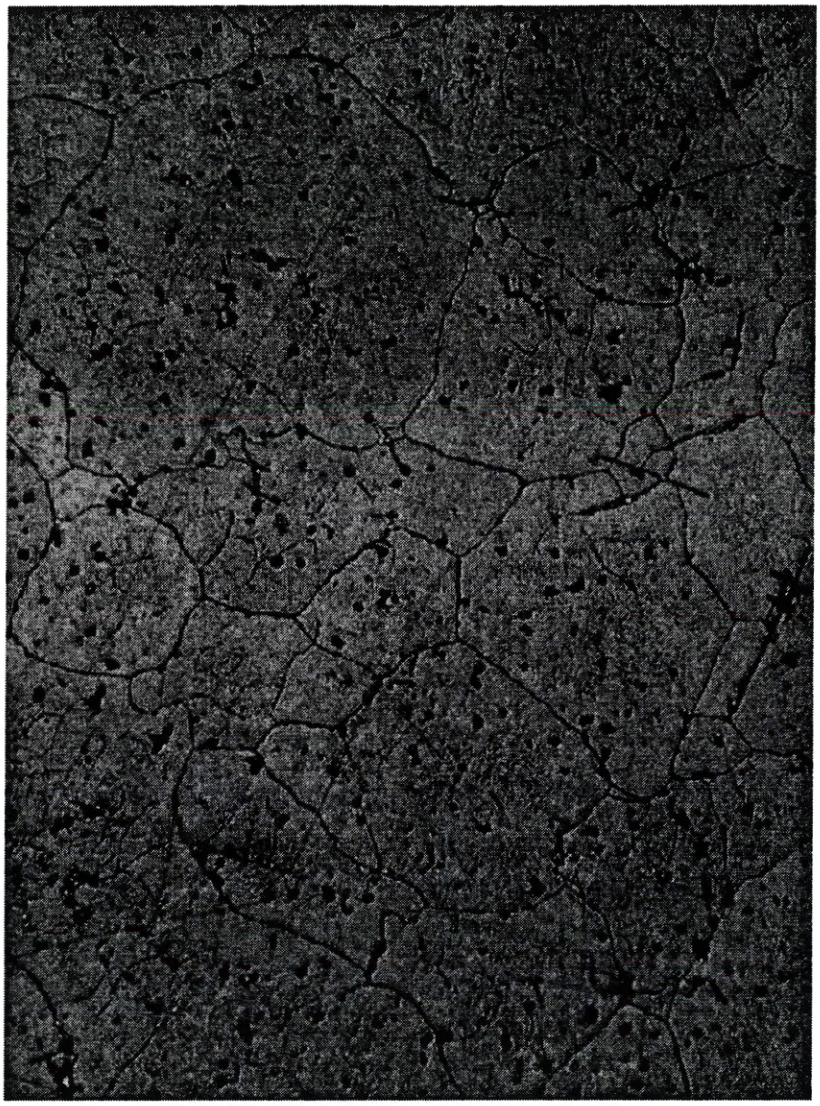

Figure 43: Photomicrograph of initial cerium-lanthanum alloy subjected to a furnace cool. Approximate grain size is 200 μm. No appreciable microsegregation of lanthanum was seen in this sample.

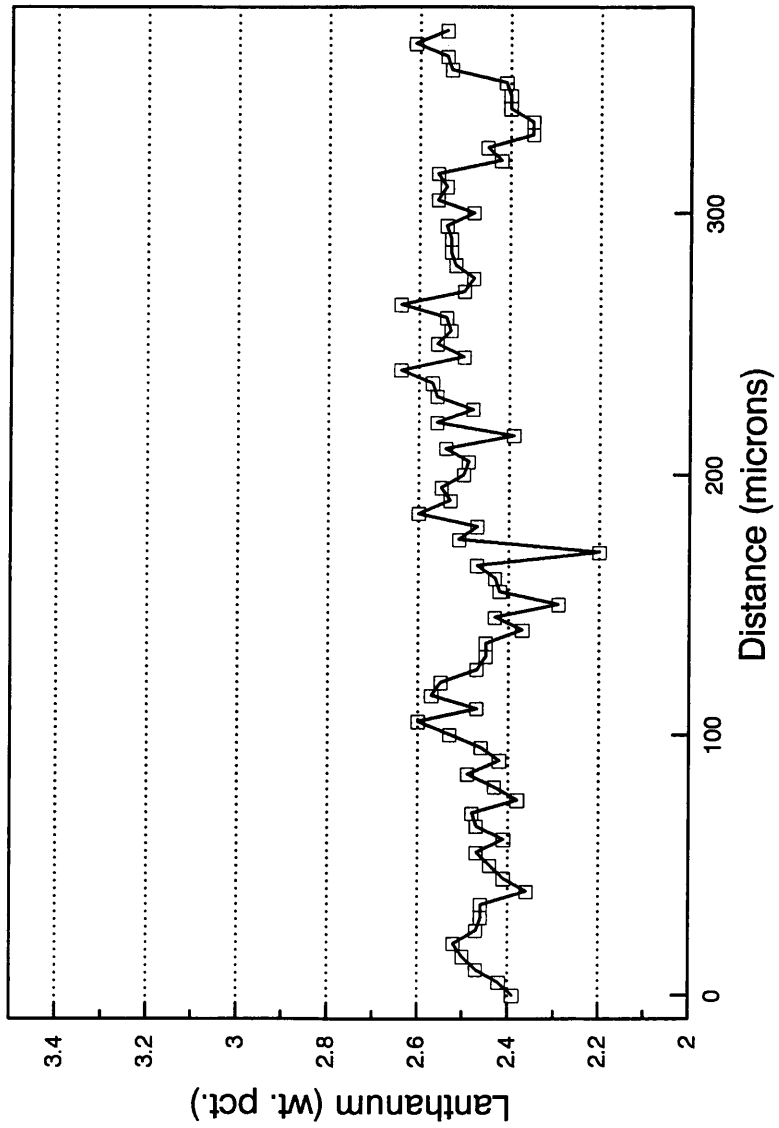

Figure 44: Microprobe data from initial furnace cooled cerium-lanthanum sample. Lanthanum concentration is essentially homogeneous. A faster cooling rate will be investigated to determine if microsegregation can be induced. The lanthanum detection limit was 0.071 wt. pct.

Table XIII: Raw data from microprobe scan of initial cerium-lanthanum specimen subjected to a furnace cool. Data is plotted in Figure 44 indicating a homogeneous distribution of lanthanum.

Distance um	La wt. pct.	Distance um	La wt. pct.
0	2.39	190	2.53
5	2.42	195	2.55
10	2.47	200	2.5
15	2.5	205	2.49
20	2.52	210	2.54
25	2.47	215	2.39
30	2.46	220	2.56
35	2.46	225	2.48
40	2.36	230	2.56
45	2.41	235	2.57
50	2.44	240	2.64
55	2.47	245	2.5
60	2.41	250	2.56
65	2.47	255	2.53
70	2.48	260	2.54
75	2.38	265	2.64
80	2.43	270	2.5
85	2.49	275	2.48
90	2.42	280	2.52
95	2.46	285	2.53
100	2.53	290	2.53
105	2.6	295	2.54
110	2.47	300	2.48
115	2.57	305	2.56
120	2.55	310	2.54
125	2.47	315	2.56
130	2.45	320	2.42
135	2.45	325	2.45
140	2.37	330	2.35
145	2.43	335	2.35
150	2.29	340	2.4
155	2.42	345	2.4
160	2.43	350	2.41
165	2.47	355	2.53
170	2.2	360	2.54
175	2.51	365	2.61
180	2.47	370	2.54
185	2.6		

the cerium-neodymium alloy, a more rapid cooling rate was necessary to induce microsegregation of the lanthanum during cooling through the two- phase region. Two additional cerium-lanthanum castings were prepared using a continuous flow of argon and helium to enhance the cooling rate through the two-phase region. The casting setups for these castings are shown in Figures 45 and 46. The cooling rate through the two-phase $\gamma + \delta$ region that was achieved with the argon gas was approximately 30°C/min. Using helium, the cooling rate was approximately 60°C/min through the two-phase region. These data are plotted in Figure 47.

Samples from these castings were mounted, ground, and polished, and results from microprobe scans are shown in Figures 48 and 49 using a wavelength dispersive spectrometer. The raw microprobe data is listed in Tables XIV and XV respectively. A variation in the lanthanum concentration can be seen in the microprobe data in Figure 49 at approximately 60-80 μm increments. This measurement corresponds to the "core" size seen in the photomicrograph of Figure 50 that suggests that solid state microsegregation has occurred. Again, the metallographic techniques described in Appendix C were used to prepare the photomicrographs. Apparently the two-phase region seen on the cerium-lanthanum phase diagram is sufficiently broad such that microsegregation of lanthanum occurs. As with cerium-neodymium system, the phase diagram for cerium-lanthanum is not well established and this diagram is only an approximation, but the initial results warrant further investigation of this system as a potential homogenization surrogate.

Casting Conditions

Casting Temperature: 950°C
Furnace Conditions = 2×10^{-7} torr
Grade 5 Argon Backfill
Cooling: Continuous Argon Flow

Mass Balance

MgO Crucible	74.9 g
Ce + MgO Crucible	136.9 g
Ce	62.0g
La addition	3.5 g
Casting Charge	65.5 g
Alloy composition	5.3 % La

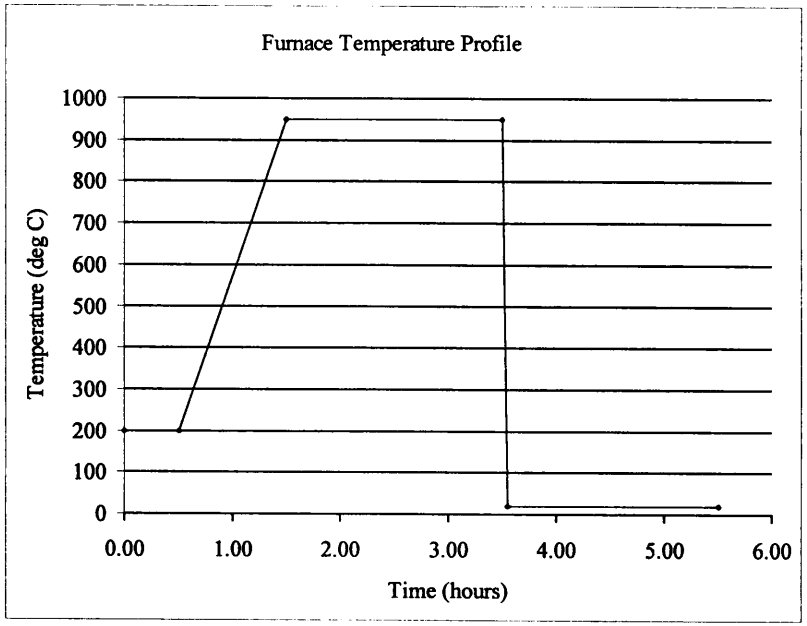

Figure 45: Casting setup for a cerium-lanthanum alloy to investigate the potential for microsegregation of lanthanum in a casting subjected to enhanced cooling with Argon gas. Shown are the mass balance for the casting and the overall furnace temperature profile. An expanded plot of the cooling profile is given in a later figure.

Casting Conditions

Casting Temperature: 950°C
Furnace Conditions = 2×10^{-7} torr
Grade 5 Argon Backfill
Cooling: Continuous Helium Flow

Mass Balance

MgO Crucible	50.7 g
Ce + MgO Crucible	111.9 g
Ce	61.2 g
La addition	3.1 g
Casting Charge	64.3 g
Alloy composition	4.82 % La

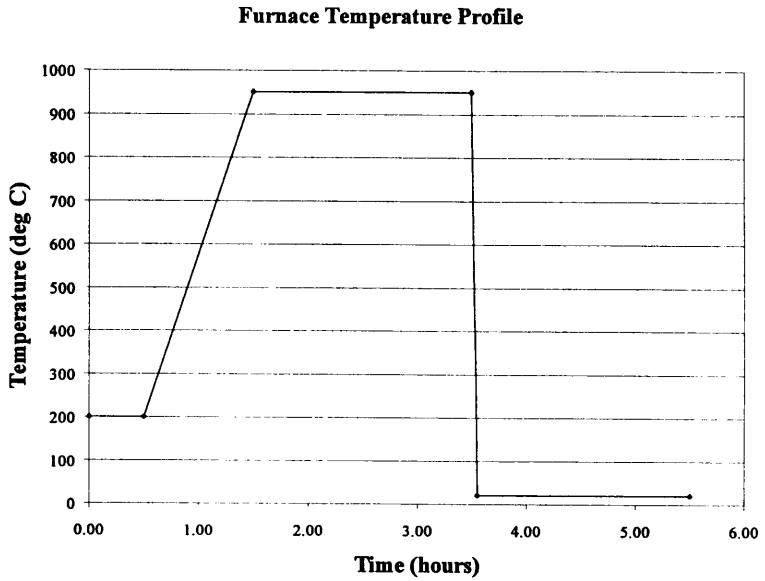

Figure 46: Casting setup for a cerium-lanthanum alloy to investigate the potential for microsegregation of lanthanum in a casting subjected to enhanced cooling with helium gas. Shown are the mass balance for the casting and the overall furnace temperature profile. An expanded plot of the cooling profile is given in a later figure.

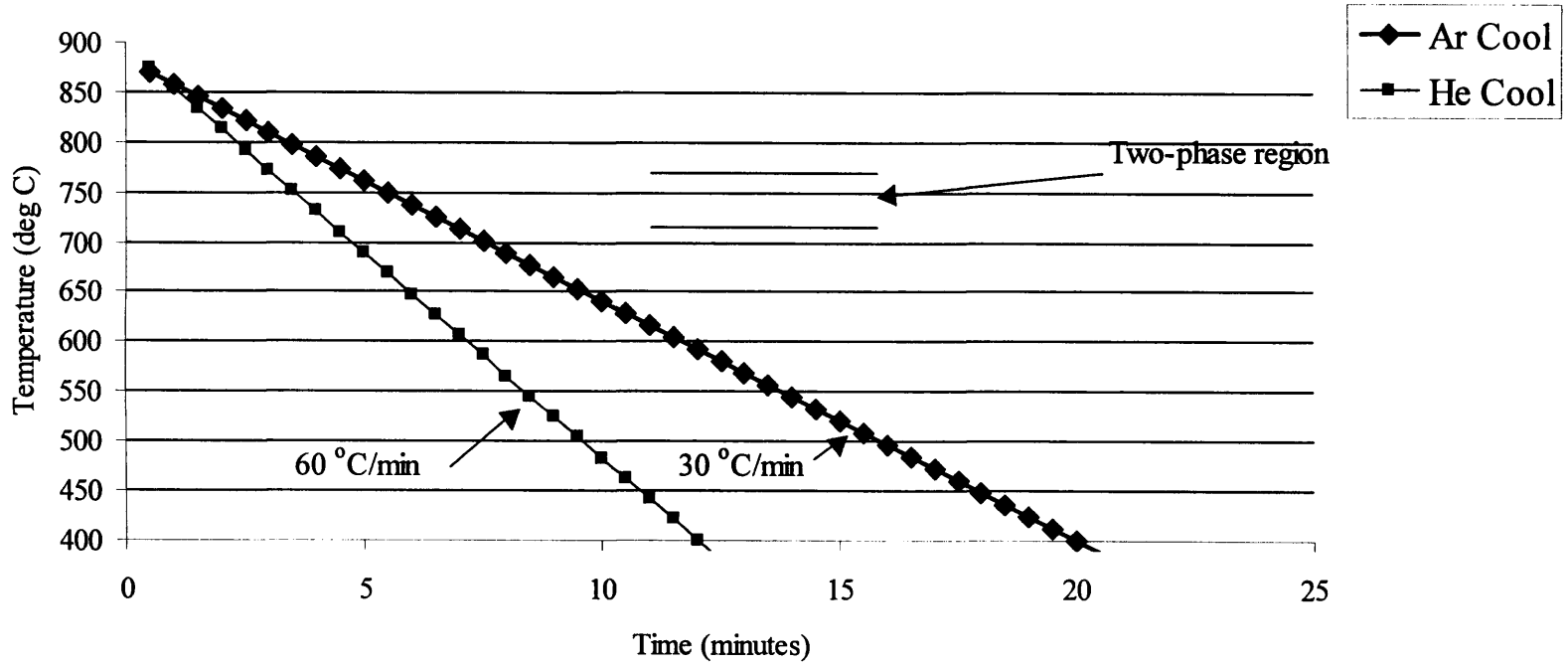

Figure 47: Furnace temperature data taken during both argon and helium gas cooling of the cerium-lanthanum alloy. Gas was introduced into the vacuum furnace to increase cooling and thereby promoting the microsegregation of lanthanum. The cooling rate achieved with argon was 30°C/min while the rate with helium was 60°C/min.

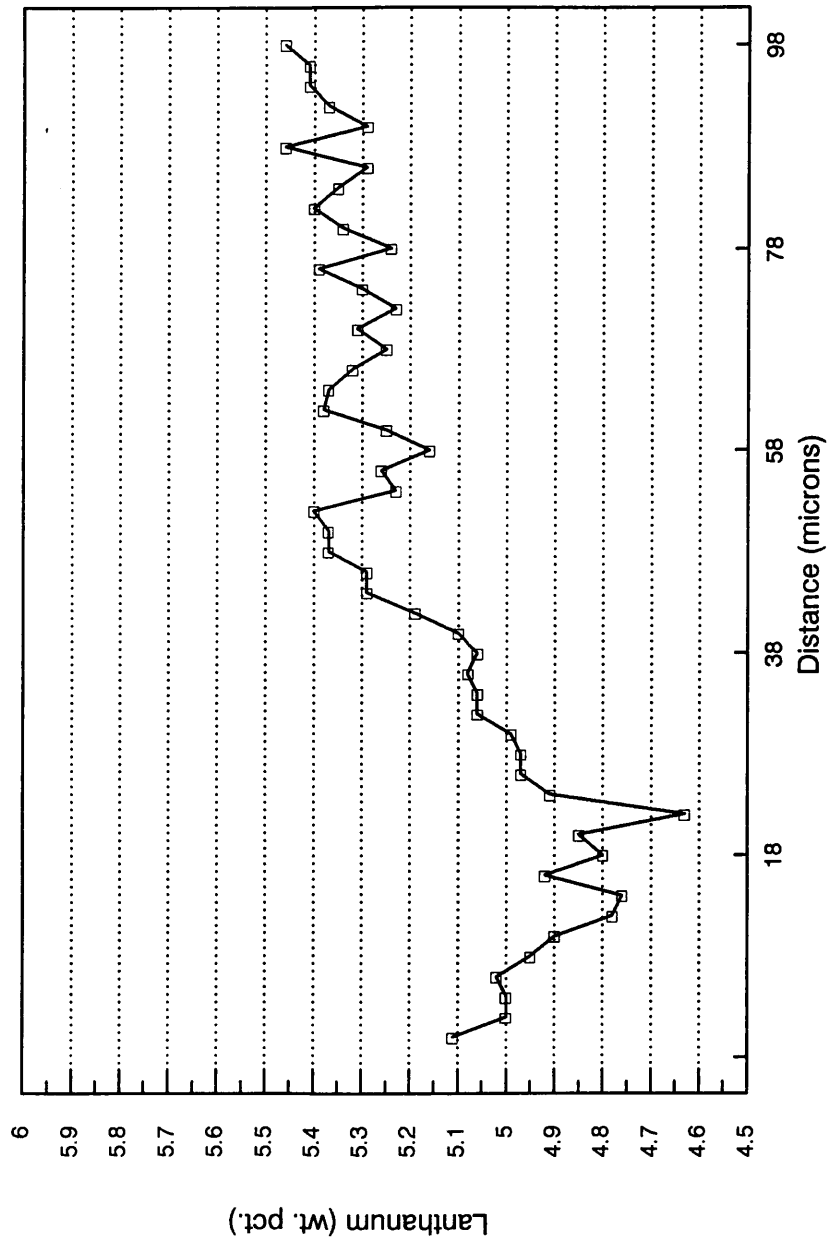

Figure 48: Microprobe trace for cerium-lanthanum alloy. This alloy was cooled using an Argon backfill resulting in a 30 C/min cooling rate through the two-phase region. Some microsegregation is evident but not conclusive. Lanthanum detection limit was +/- 0.07 wt. pct.

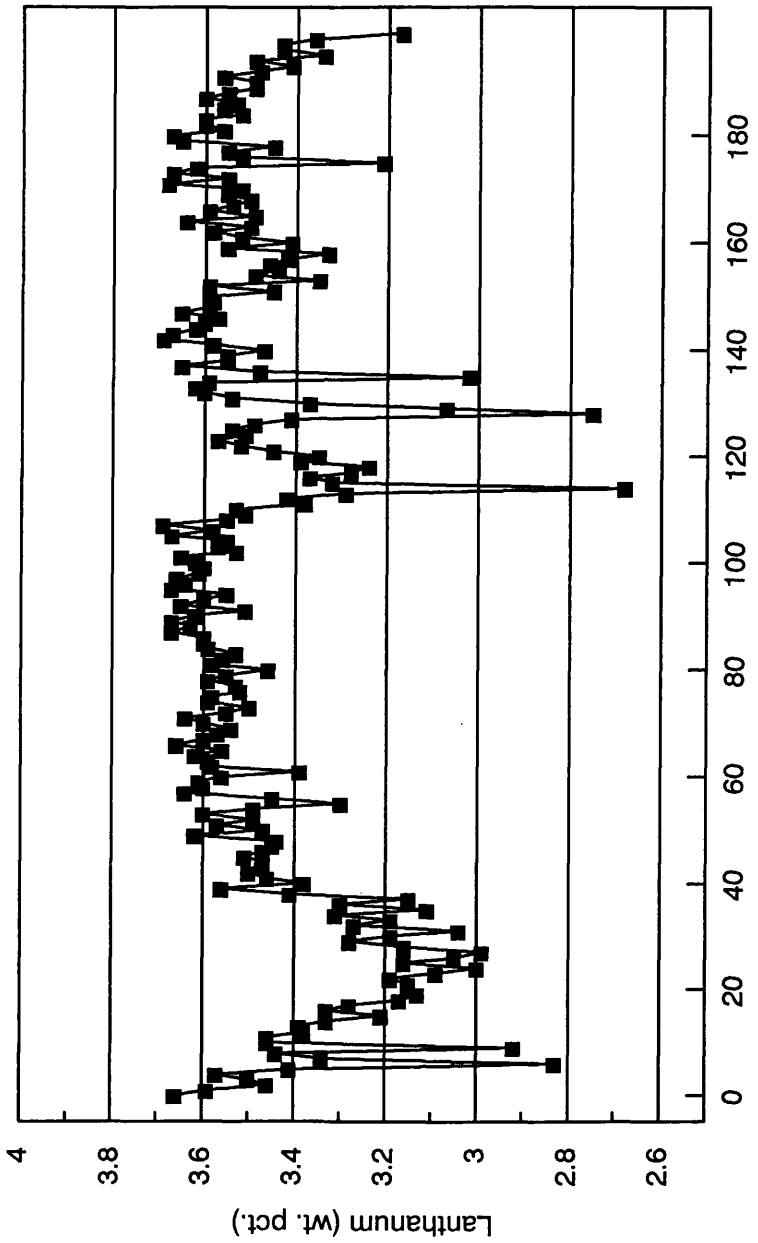

Figure 49: Microprobe trace for cerium-lanthanum alloy. This alloy was cooled using a helium backfill resulting in a 60 C/min cooling rate through the two-phase region. A 200 um trace was run for this sample and the results indicate that microsegregation has occurred. Further experiments with this alloy are warranted. Lanthanum detection limit was +/- 0.05 wt.pct.

Table XIV: Raw data from microprobe scan of cerium-lanthanum specimen subjected to argon gas cooling. Cooling rate through the two-phase region was measured at 30 °C/min. Data is plotted in Figure 48 which did not conclusively indicate microsegregation of lanthanum.

Distance μm	La (wt. pct.)	Distance μm	La (wt. pct.)
0	5.11	50	5.37
2	5	52	5.4
4	5	54	5.23
6	5.02	56	5.26
8	4.95	58	5.16
10	4.9	60	5.25
12	4.78	62	5.38
14	4.76	64	5.37
16	4.92	66	5.32
18	4.8	68	5.25
20	4.85	70	5.31
22	4.63	72	5.23
24	4.91	74	5.3
26	4.97	76	5.39
28	4.97	78	5.24
30	4.99	80	5.34
32	5.06	82	5.4
34	5.06	84	5.35
36	5.08	86	5.29
38	5.06	88	5.46
40	5.1	90	5.29
42	5.19	92	5.37
44	5.29	94	5.41
46	5.29	96	5.41
48	5.37	98	5.46

Table XV: Raw data from microprobe scan of cerium-lanthanum specimen subjected to helium gas cooling. Cooling rate through the two-phase region was measured at 60°C/min. Data is plotted in Figure 49 which indicated microsegregation of lanthanum.

Distance μm	La (wt. pct.)	Distance μm	La (wt. pct.)	Distance μm	La (wt. pct.)
0	3.66	44	3.47	88	3.63
1	3.59	45	3.51	89	3.67
2	3.46	46	3.47	90	3.62
3	3.5	47	3.45	91	3.51
4	3.57	48	3.44	92	3.65
5	3.41	49	3.62	93	3.6
6	2.83	50	3.47	94	3.55
7	3.34	51	3.57	95	3.67
8	3.44	52	3.49	96	3.64
9	2.92	53	3.6	97	3.66
10	3.46	54	3.49	98	3.61
11	3.46	55	3.3	99	3.6
12	3.38	56	3.45	100	3.62
13	3.39	57	3.64	101	3.65
14	3.33	58	3.6	102	3.53
15	3.21	59	3.61	103	3.57
16	3.33	60	3.56	104	3.55
17	3.28	61	3.39	105	3.67
18	3.17	62	3.58	106	3.58
19	3.13	63	3.59	107	3.69
20	3.15	64	3.62	108	3.55
21	3.15	65	3.56	109	3.51
22	3.19	66	3.66	110	3.53
23	3.09	67	3.6	111	3.38
24	3	68	3.57	112	3.42
25	3.16	69	3.54	113	3.29
26	3.05	70	3.6	114	2.68
27	2.99	71	3.64	115	3.32
28	3.16	72	3.55	116	3.37
29	3.28	73	3.5	117	3.28
30	3.19	74	3.59	118	3.24
31	3.04	75	3.58	119	3.39
32	3.27	76	3.52	120	3.35
33	3.19	77	3.53	121	3.45
34	3.31	78	3.59	122	3.52
35	3.11	79	3.55	123	3.57
36	3.3	80	3.46	124	3.51
37	3.15	81	3.58	125	3.54
38	3.41	82	3.56	126	3.49
39	3.56	83	3.53	127	3.41
40	3.38	84	3.59	128	2.75
41	3.46	85	3.6	129	3.07
42	3.5	86	3.6	130	3.37
43	3.47	87	3.67	131	3.54

Distance μm	La (wt. pct.)	Distance μm	La (wt. pct.)
132	3.6	173	3.67
133	3.62	174	3.62
134	3.59	175	3.21
135	3.02	176	3.52
136	3.48	177	3.55
137	3.65	178	3.45
138	3.55	179	3.65
139	3.55	180	3.67
140	3.47	181	3.56
141	3.58	182	3.6
142	3.69	183	3.6
143	3.67	184	3.52
144	3.62	185	3.56
145	3.6	186	3.53
146	3.57	187	3.6
147	3.65	188	3.55
148	3.59	189	3.49
149	3.58	190	3.49
150	3.59	191	3.56
151	3.45	192	3.48
152	3.59	193	3.41
153	3.35	194	3.49
154	3.49	195	3.34
155	3.44	196	3.43
156	3.46	197	3.43
157	3.42	198	3.36
158	3.33	199	3.17
159	3.55		
160	3.41		
161	3.52		
162	3.58		
163	3.5		
164	3.64		
165	3.49		
166	3.59		
167	3.54		
168	3.5		
169	3.55		
170	3.52		
171	3.68		
172	3.55		

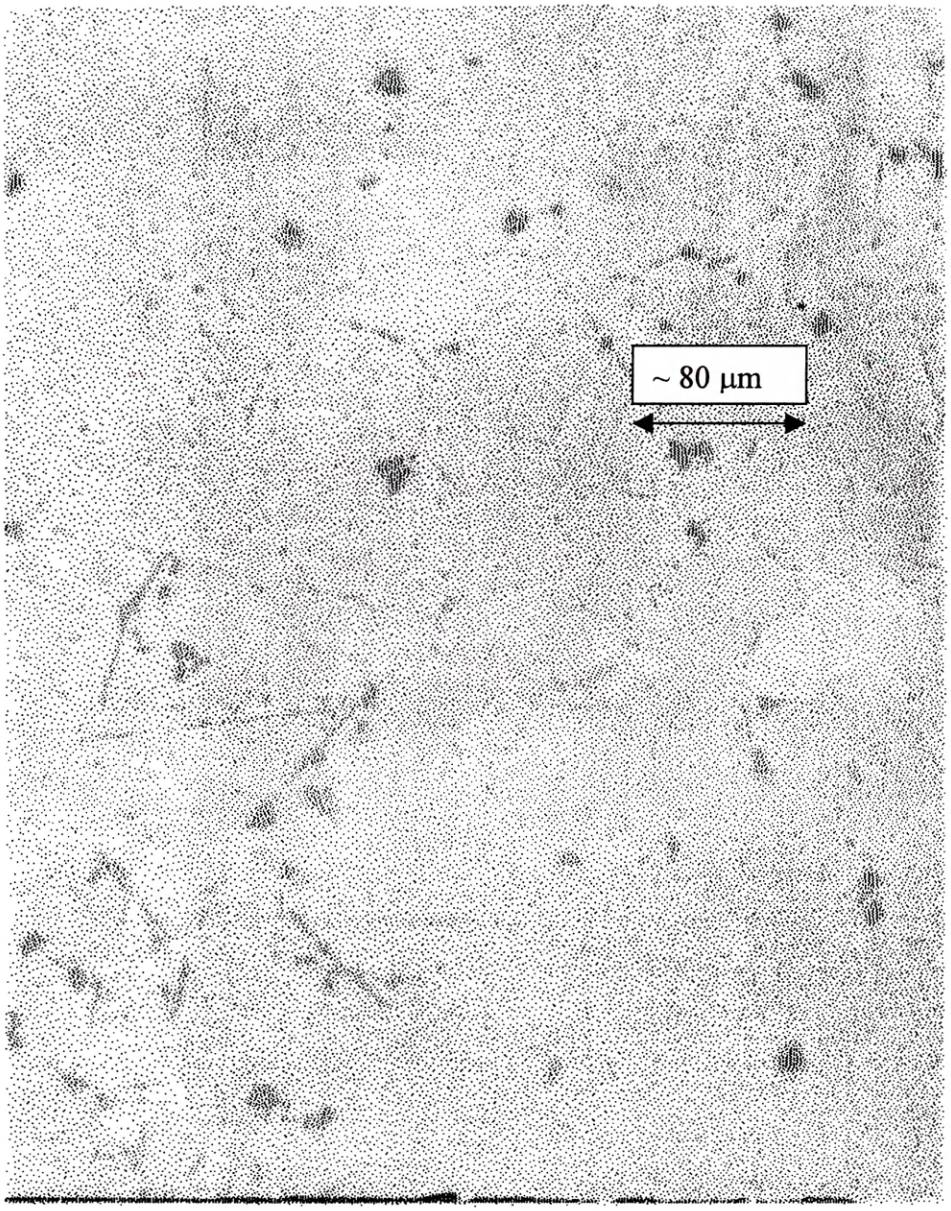

Figure 50: Photomicrograph showing cerium-lanthanum alloy subjected to helium gas cooling which resulted in a cooling rate of 60°C/min. Microprobe results indicate a microsegregation of lanthanum commensurate with the approximate grain size of 80 μm.

The initial results from the cerium-neodymium and cerium-lanthanum systems indicate that microsegregation similar to that seen in the plutonium-gallium system is apparent.

While both systems show promise, the cerium-lanthanum system offers an advantage experimentally as the "cored" specimen can be achieved using just the casting furnace. This practice avoids the machining of pyrophoric cerium specimens which is required to utilize the Gleeble instrument. Furthermore, experimental data from Dariel [41], that was summarized earlier, indicated a two order of magnitude decrease in the interdiffusion coefficient during the phase transformation from the body-centered-cubic phase of cerium to the face-centered-cubic phase. Given the initial data reported by Dariel [41] and the promising results reported here, further investigation of the cerium-lanthanum system was warranted.

3.5 Experimental Work - Measurement of Ce-La Diffusion Parameters

The viability of the cerium-lanthanum alloy as a homogenization surrogate for the plutonium - 1 wt. pct. gallium alloy can be demonstrated using a similar approach as that used by Johnson [21]. This fundamental study provided some of the first transport data for plutonium - 1 wt. pct. gallium and more importantly provides the "grounding link" to the cerium homogenization surrogate and as discussed earlier the opportunity to expand the relationship to an overall metallurgical surrogate.

Figure 51 details the experimental approach used by Johnson [21]. The experiment consisted of preparing several plutonium - 1 wt. pct. gallium alloys and

Homogenization Parameters for Cored Specimens	
Annealing Temperatures	Homogenization times (hours)
425 C	1, 8, 24, 50, 120, 504
500 C	1, 2, 8, 16, 50, 248
525 C	1, 2, 4, 8, 24

Homogenization Response Plots

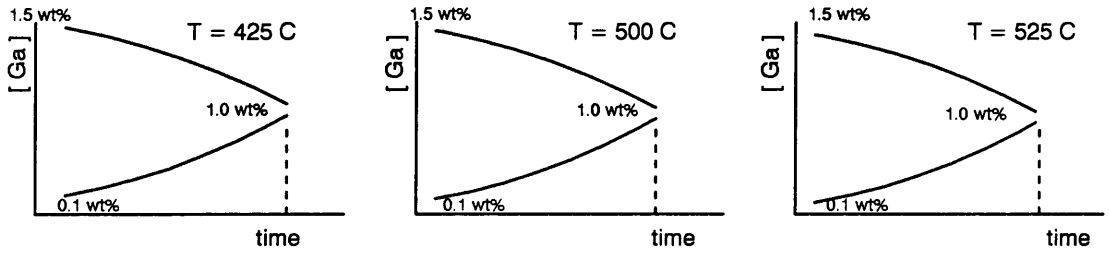

Minimum times for Homogenization

500 hours at 425 C
60 hours at 500 C
16 hours at 525 C

Activation Energy Determination

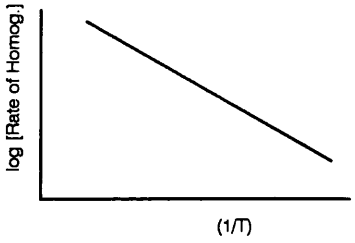

Diffusion Coefficient Determination

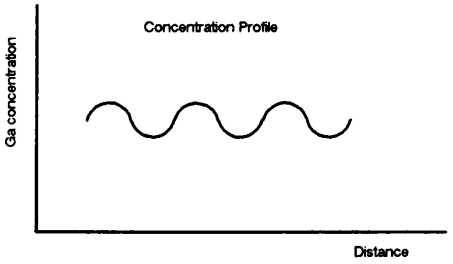

Figure 51: Experimental approach used by K. Johnson to determine homogenization response of plutonium - 1 wt. pct. gallium alloys. Activation energy for diffusion and an interdiffusion coefficient was determined using the rate at which homogenization was achieved [21].

casting specimens such that microsegregation of gallium occurred via cooling through the $\varepsilon + \delta$ two-phase region. Samples were annealed at three different temperatures for several different times to obtain a rate of homogenization of the gallium. The fundamental mechanism by which homogenization takes place is via the diffusion of gallium, driven by the difference in chemical potential between the center of the grain and the grain boundary. Accordingly, by plotting the log of the rate of homogenization as a function of the reciprocal of absolute temperature, the activation energy for diffusion was determined as shown in the following equation:

$$\text{Rate} = \upsilon_o \exp [-Q/RT] \qquad (27)$$

where υ_o is a constant, Q is the activation energy for diffusion, R is the universal gas constant in calories/mole * deg K and T is absolute temperature. This equation is then put into a linear form:

$$\text{Log (Rate)} = \log \upsilon_o - Q/RT \qquad (28)$$

The activation energy reported by Johnson [21] was 40,100 cal/mole. Furthermore, the interdiffusion coefficient was determined:

$$D = (65 \pm 5) \exp [-40{,}100/RT] \quad cm^2/sec \qquad (29)$$

An experimental matrix for the cerium-lanthanum system using a nominal 5 wt. pct. lanthanum alloy was developed to determine the activation energy for the surrogate system. As described previously, cerium-lanthanum specimens were prepared in a vacuum furnace and subjected to continuous helium cooling through the two-phase $\delta + \gamma$ region to provide initially cored specimens. The cored specimens were then homogenized at the temperatures and times shown in Table XVI. The specimens were then mounted, ground, and polished for metallographic evaluation. Concentration profiles were measured using a scanning electron microprobe with a wavelength dispersive spectrometer as described earlier. The resulting concentration profiles were utilized to determine the rate of homogenization of lanthanum. The log of the rate of homogenization was plotted as a function of reciprocal absolute temperature to determine the activation energy for diffusion. Photomicrographs of the specimens were taken to correlate to the microprobe data. The results and discussion of these data are detailed in the next section.

The results from the homogenization data for cerium-lanthanum and the determination for the activation energy for diffuison will be related to the plutonium -1 wt. pct. gallium alloy using a calculated surrogate factor. This factor will allow the homogenization of the surrogate alloy to be analytically linked to the plutonium alloy. Again, this fundamental link is the first step in defining this cerium-based alloy as an overall metallurgical surrogate for the plutonium - 1 wt. pct. gallium alloy.

Table XVI: Experimental matrix for a nominal cerium - 5 wt. pct. lanthanum alloy for the determination of the activation energy for diffusion. Utilizing a similar approach used by Johnson, initially cored specimens were annealed at the times and temperatures listed to determine a rate of homogenization. The log of the rate of homogenization is then plotted versus the reciprocal of absolute temperature and by calculating the slope, the activation energy for interdiffusion is determined.

Homogenization Temperature	Homogenization Times (Hours)			
546 °C	4	12	20	36
585 °C	2	4	8	20
633 °C	4	8	12	24

4.0 RESULTS AND DISCUSSION

The results from microprobe analysis of the cerium-lanthanum alloys prepared in accordance with the experimental matrix are presented here. Initially, a characterization of the nature of the lanthanum concentration variation and preliminary data indicating the "width" of the two-phase region is provided. Concentration profiles and the corresponding photomicrographs are presented followed by subsequent calculation of the activation energy for diffusion. A fundamental transport relationship between the cerium-lanthanum system and the plutonium - gallium system is developed such that homogenization of gallium in plutonium can be represented by homogenization of lanthanum in cerium. Finally, an overall correlation is made between the plutonium alloy and cerium alloys to establish a case for a cerium based metallurgical surrogate.

4.1 Onset of Lanthanum Microsegregation

While the cerium-lanthanum system indicated great promise in the search for a material that would exhibit microsegregation, the phase diagram is not well established particularly in the area of interest. Appendix B contains a phase diagram produced by Gschneidner and Calderwood [43] that indicates essentially no two-phase region between δ - cerium and γ - cerium. Alternatively, the two-phase region in other references is indicated as "estimated" and a personal communication with Gschneidner [44] suggested

a potential for a two-phase region. This estimated two-phase region was discussed earlier and was shown in Figure 41. The initial work presented here indicated microsegregation in alloys containing approximately 3.5 wt. pct. lanthanum as shown in Figure 49. In an effort to identify the onset of microsegregation, an additional alloy was prepared using the vacuum casting parameters described earlier. The alloy contained nominally 1.8 wt. pct. lanthanum and was helium cooled as described earlier. The profile shown in Figure 52 indicates slight microsegregation, but at this concentration the two-phase region is apparently not wide enough to result in a significant variation in lanthanum. Note a 400 μm trace was run to provide a representative sample. Table XVII contains the raw data from the microprobe trace. The significant decrease in lanthanum concentration at approximately 280 μm was attributed to a surface defect and was not considered as result of the phase transformation. These results would indicate that the two-phase region begins to broaden such that initial microsegregation occurs at approximately 2 wt. pct. lanthanum.

The initial coring data allows a better understanding of the cerium rich part of the cerium-lanthanum phase diagram to be drawn. Using the microsegregation data and the phase diagram from Figure 41, a lever rule calculation was made to establish the boundaries of the $\delta + \gamma$ two-phase region for a nominal 5.5 wt. pct. alloy. An estimate from the phase diagram was made assuming the width of the two-phase region at 5.5 wt. pct. lanthanum was 10°C. Table XVIII shows the application of the lever rule with the calculated distribution of lanthanum between the $\gamma + \delta$ phases. The ratio of the mole

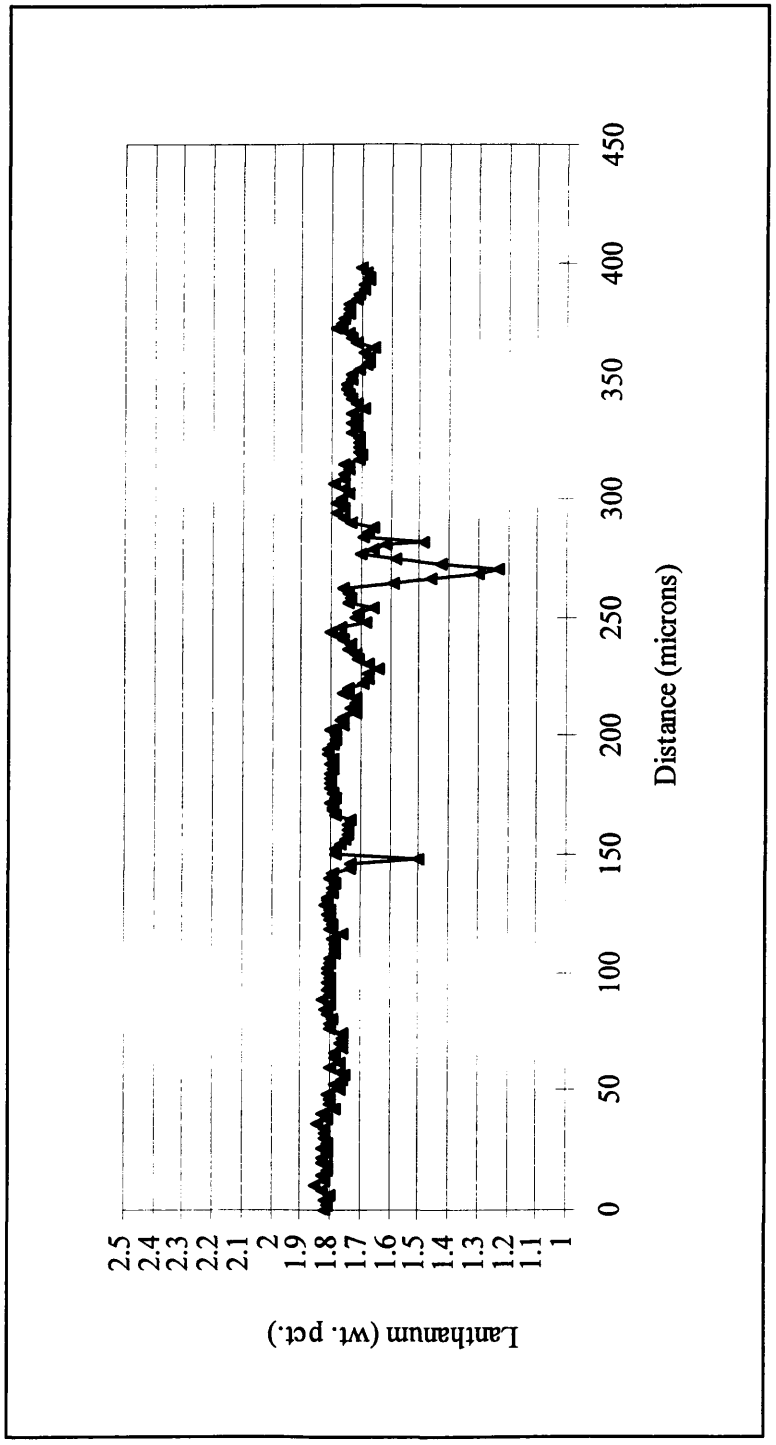

Figure 52: Microprobe data showing the lanthanum concentration variation for a distance of 400 μm. This alloy had a nominal lanthanum concentration of 1.8 wt. pct. and provides some indication of the onset of microsegregation of lanthanum and the extent of the two-phase region.

Table XVII: Raw data from microprobe scan of cerium-lanthanum specimen subjected to helium gas cooling to promote microsegregation of lanthanum. Nominal alloy was prepared with 1.8 wt. pct. lanthanum to identify the onset of lanthanum segregation.

Distance μm	La (wt. pct.)	Distance μm	La (wt. pct.)	Distance μm	La (wt.pct.)	Distance μm	La (wt. pct.)
0	1.82	102	1.81	204	1.76	306	1.79
2	1.81	104	1.8	206	1.77	308	1.76
4	1.82	106	1.8	208	1.76	310	1.76
6	1.8	108	1.78	210	1.72	312	1.74
8	1.83	110	1.78	212	1.73	314	1.76
10	1.85	112	1.78	214	1.72	316	1.71
12	1.82	114	1.79	216	1.72	318	1.7
14	1.83	116	1.76	218	1.76	320	1.71
16	1.81	118	1.8	220	1.74	322	1.71
18	1.81	120	1.79	222	1.69	324	1.71
20	1.83	122	1.8	224	1.67	326	1.71
22	1.83	124	1.81	226	1.67	328	1.73
24	1.81	126	1.8	228	1.64	330	1.72
26	1.83	128	1.82	230	1.67	332	1.73
28	1.81	130	1.81	232	1.71	334	1.72
30	1.82	132	1.81	234	1.72	336	1.73
32	1.82	134	1.79	236	1.74	338	1.69
34	1.82	136	1.79	238	1.73	340	1.72
36	1.84	138	1.78	240	1.76	342	1.73
38	1.81	140	1.8	242	1.77	344	1.74
40	1.83	142	1.79	244	1.8	346	1.75
42	1.78	144	1.73	246	1.77	348	1.75
44	1.8	146	1.73	248	1.68	350	1.73
46	1.8	148	1.5	250	1.72	352	1.73
48	1.81	150	1.78	252	1.71	354	1.71
50	1.77	152	1.78	254	1.66	356	1.68
52	1.78	154	1.77	256	1.74	358	1.67
54	1.76	156	1.75	258	1.73	360	1.67
56	1.75	158	1.74	260	1.74	362	1.69
58	1.77	160	1.74	262	1.76	364	1.66
60	1.8	162	1.74	264	1.59	366	1.72
62	1.77	164	1.73	266	1.46	368	1.73
64	1.78	166	1.78	268	1.3	370	1.74
66	1.78	168	1.79	270	1.23	372	1.78
68	1.76	170	1.79	272	1.43	374	1.77
70	1.77	172	1.8	274	1.58	376	1.76
72	1.76	174	1.78	276	1.7	378	1.74
74	1.76	176	1.79	278	1.66	380	1.74
76	1.8	178	1.8	280	1.61	382	1.74
78	1.8	180	1.8	282	1.49	384	1.72
80	1.79	182	1.8	284	1.69	386	1.71
82	1.81	184	1.8	286	1.67	388	1.69
84	1.82	186	1.79	288	1.66	390	1.69
86	1.8	188	1.8	290	1.73	392	1.67
88	1.83	190	1.79	292	1.76	394	1.67
90	1.8	192	1.81	294	1.78	396	1.68
92	1.81	194	1.81	296	1.76	398	1.7
94	1.8	196	1.79	298	1.78		
96	1.81	198	1.78	300	1.77		
98	1.8	200	1.78	302	1.74		
100	1.81	202	1.8	304	1.76		

Table XVIII: Lever rule model for a nominal cerium - 5.5 wt. pct. lanthanum alloy. The width of the two-phase region was estimated in order to calculate the partitioning coefficient. The Scheil equation was then used to predict the lanthanum variation across a grain with a 70 μm diameter such that the variation matched microsegregation seen from this experimental work.

La Alloy	Temp (C)	Wt% La γ-Ce	Wt % La δ- Ce	Moles La γ-Ce	Moles La δ-Ce	Total Moles	La in γ-Ce (mole fract.)	La in δ-Ce (mole fract.)	Partitioning Coefficient	Vol. fraction γ-Ce	La Variation From Scheil (mole fract.)	La Variation Across grain (wt. pct.)
5.5	745	6.5	5.50	0.0000	0.0072	0.7143	0.0000	0.9899	0.0000	0.0000		
5.5	744	6.45	5.41	0.0040	0.0356	0.7146	0.0650	0.9455	1.1921	0.0865	0.0649	6.4443
5.5	743	6.4	5.32	0.0077	0.0319	0.7146	0.0645	0.9464	1.2029	0.1667	0.0642	6.3762
5.5	742	6.35	5.23	0.0110	0.0286	0.7146	0.0640	0.9473	1.2140	0.2411	0.0634	6.2949
5.5	741	6.3	5.14	0.0141	0.0255	0.7146	0.0635	0.9482	1.2256	0.3103	0.0625	6.1992
5.5	740	6.25	5.05	0.0169	0.0227	0.7146	0.0630	0.9491	1.2375	0.3750	0.0613	6.0878
5.5	739	6.15	4.96	0.0201	0.0195	0.7146	0.0620	0.9500	1.2398	0.4538	0.0594	5.8988
5.5	738	6.05	4.87	0.0233	0.0163	0.7146	0.0609	0.9509	1.2422	0.5339	0.0572	5.6791
5.5	737	5.95	4.78	0.0264	0.0132	0.7146	0.0599	0.9518	1.2447	0.6154	0.0546	5.4188
5.5	736	5.85	4.69	0.0294	0.0102	0.7146	0.0589	0.9527	1.2472	0.6983	0.0514	5.1012
5.5	735	5.5	4.6	0.0396	0.0000	0.7146	0.0554	-	-	1.0000	-	-

fraction of lanthanum in γ - cerium over the mole fraction of lanthanum in δ - cerium is the partitioning coefficient. The partitioning coefficient as a function of temperature is plotted in Figure 53. Assuming a spherical grain with a diameter of seventy microns, the Scheil equation was used to predict the lanthanum profile. The predicted lanthanum profile is shown in Figure 54. The same assumption made by Ferrera et al [22] for the plutonium - gallium alloy was applied where the diffusion in the lower temperature phase (γ -cerium) was assumed to be significantly slower relative to the high temperature phase (δ - cerium). This is also consistent with the assumptions in the Scheil equation development discussed earlier. The predicted profile in Figure 54 showed a lanthanum variation of approximately 1.35 wt. pct. The maximum lanthanum variation seen in this work was approximately 0.7 wt. pct. which suggests that some diffusion in γ - cerium takes place or the estimates on the boundaries of the two-phase γ + δ region are not accurate. The existing model provides a reasonable approximation of the equilibrium boundaries on the phase diagram and additional measurements are required to further clarify these boundaries.

An analysis of the partitioning coefficients for the plutonium - 1 wt. pct. gallium and the cerium - 5.5 wt. pct. lanthanum alloys shows that the degree of distribution of solute in the plutonium - gallium alloy is approximately twice that of the cerium - lanthanum alloy. A higher concentration of lanthanum is recommended to shift the cerium alloy to a broader region of the two-phase diagram. The broader region of the two-phase region would result in a larger amount of microsegregation and provide a

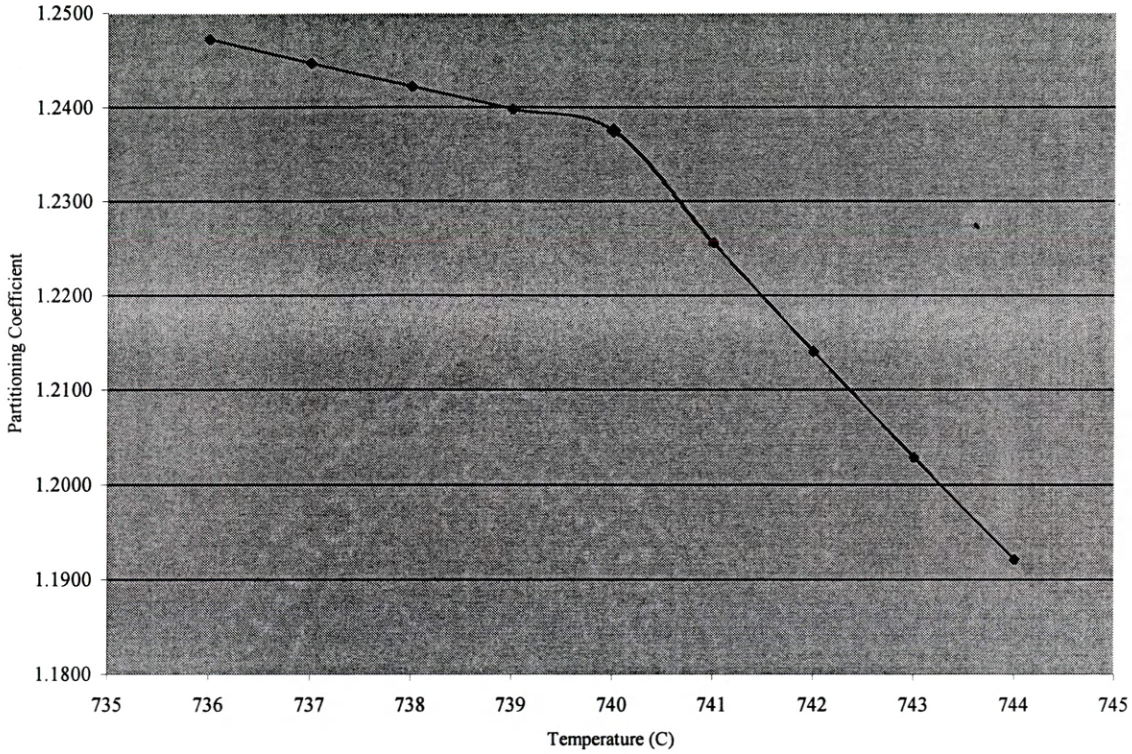

Figure 53: Partitioning coefficient plotted as a function of temperature for a nominal cerium -5.5 wt. pct. lanthanum alloy calculated from the cerium-lanthanum phase diagram. An estimate of he width of the two-phase region was made from the limited phase diagram data and the lever rule was used to calculate the distribution of lanthanum. The calculated variation in lanthanum was then compared to the actual coring data.

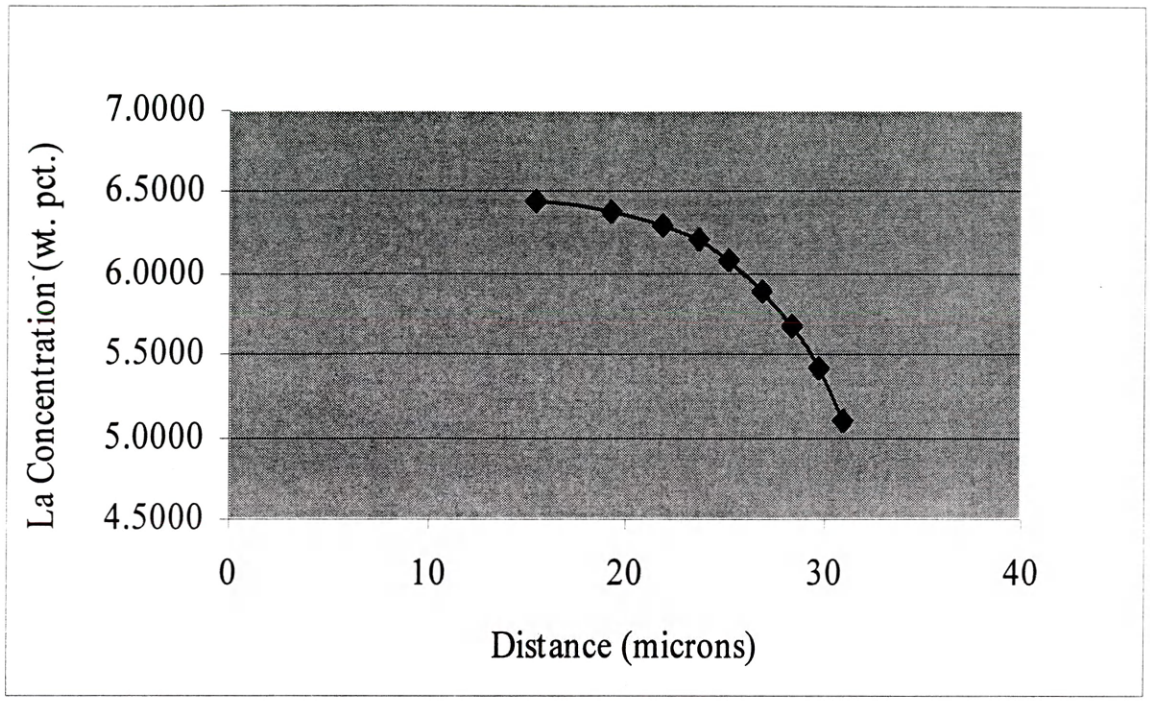

Figure 54: Assuming the upper transformation line of the $\gamma + \delta$ two-phase region was established, the lanthanum coring data for a nominal 5.5 wt. pct. alloy was used to predict the degree of microsegregation. A 70 μm diameter spherical grain was assumed for this calculation and the prediction for one half of a grain is shown. The calculation was made using the lever rule an intermediate calculation of the partitioning coefficient and the Scheil equation as described earlier.

greater sensitivity of measurement of the lanthanum concentration. As shown later, a higher than expected lanthanum concentration was measured in one of the cast specimens, resulting in greater microsegregation of lanthanum. This increase in alloy content may only be limited by "ideality" assumptions made in the analytical diffusion relationships between the two systems.

4.2 Characterization of Microsegregation

The initial experimental work with cerium-lanthanum indicated a correlation between the lanthanum segregation and the as-cast grain size. A direct microstructural correlation between the lanthanum variation and the microprobe results was established. Figure 55 is a plot of the concentration profile through the center of a grain in a cerium-lanthanum specimen with the raw microprobe data given in Table XIX. This specimen was cast as described previously and subjected to helium cooling such that microsegregation of lanthanum was achieved. The sample was ground and polished and microstructural markers were used to orient the microprobe scan in the center of the grain. Upon completion of the scan, the sample was removed from the microprobe and allowed to oxidize slightly in air which revealed the grain structure while leaving the scan mark. This technique proved to be more successful than a standard etching technique that tended to destroy the scan mark. Figure 56 shows the scan mark located in the center of the grain. The microprobe data from the center of the grain shows a flat profile

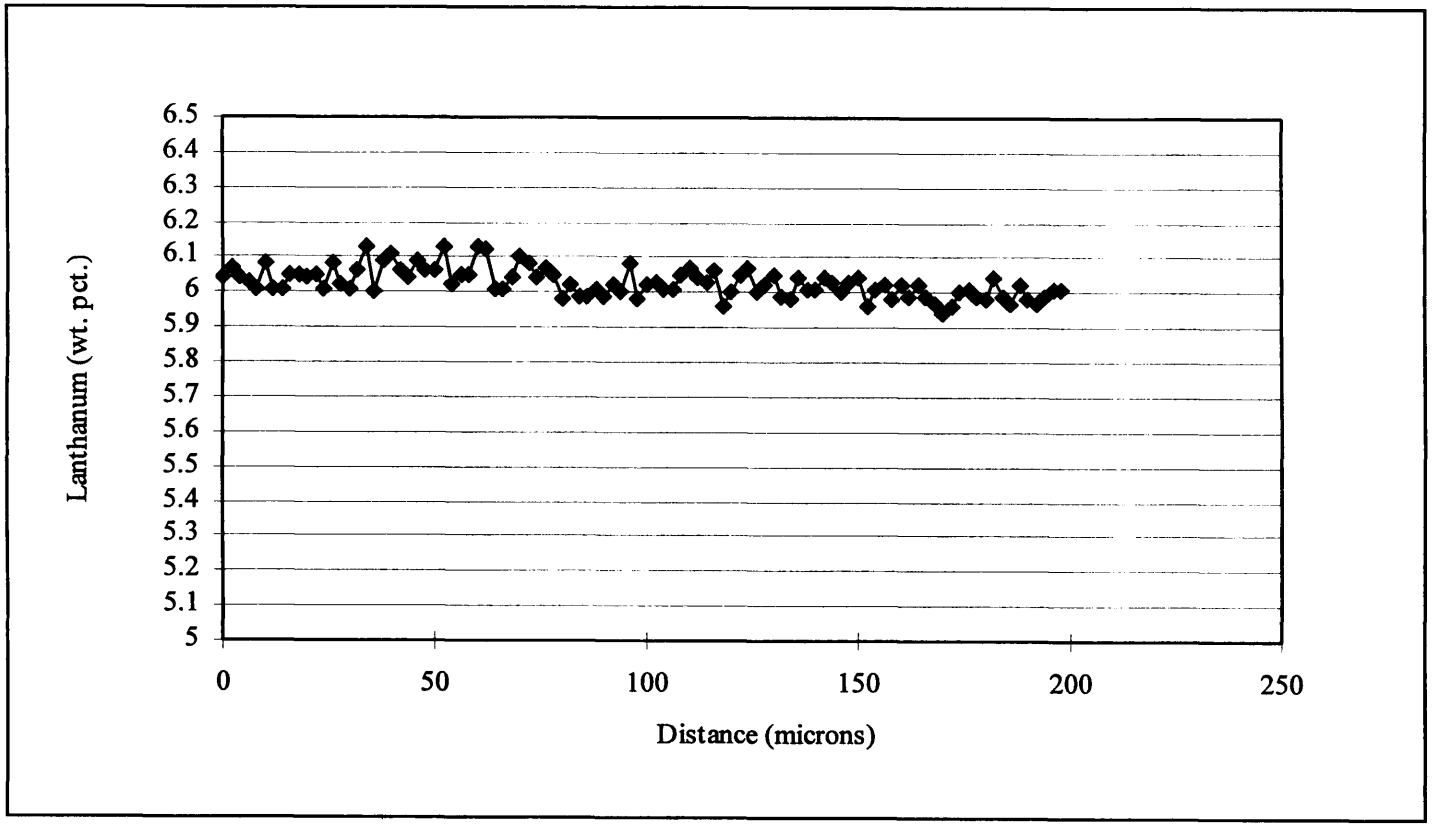

Figure 55: Lanthanum concentration profile measured through the center of a grain from a cerium-lanthanum alloy subjected to helium cooling. Concentration profiles taken across the grain show lanthanum microsegregation due to the rapid cooling through the $\gamma + \delta$ two-phase region. This profile through the center of the grain indicates a constant lanthanum concentration that supports the conclusion that the segregation is transverse to the grain and is due to this phase transformation.

Table XIX: Raw data from microprobe scan of cerium-lanthanum specimen subjected to helium gas cooling to promote lanthanum microsegregation. Scan was made in the center of the grain for comparison to transverse scans showing significant coring.

Distance μm	La (wt. pct.)	Distance μm	La (wt. pct.)
0	6.04	100	6.02
2	6.07	102	6.03
4	6.04	104	6.01
6	6.03	106	6.01
8	6.01	108	6.05
10	6.08	110	6.07
12	6.01	112	6.04
14	6.01	114	6.03
16	6.05	116	6.06
18	6.05	118	5.96
20	6.04	120	6
22	6.05	122	6.05
24	6.01	124	6.07
26	6.08	126	6
28	6.02	128	6.02
30	6.01	130	6.05
32	6.06	132	5.99
34	6.13	134	5.98
36	6	136	6.04
38	6.09	138	6.01
40	6.11	140	6.01
42	6.06	142	6.04
44	6.04	144	6.03
46	6.09	146	6
48	6.06	148	6.03
50	6.06	150	6.04
52	6.13	152	5.96
54	6.02	154	6.01
56	6.05	156	6.02
58	6.05	158	5.98
60	6.13	160	6.02
62	6.12	162	5.99
64	6.01	164	6.02
66	6.01	166	5.99
68	6.04	168	5.97
70	6.1	170	5.94
72	6.08	172	5.96
74	6.04	174	6
76	6.07	176	6.01
78	6.05	178	5.99
80	5.98	180	5.98
82	6.02	182	6.04
84	5.99	184	5.99
86	5.99	186	5.97
88	6.01	188	6.02
90	5.99	190	5.98
92	6.02	192	5.97
94	6	194	5.99
96	6.08	196	6.01

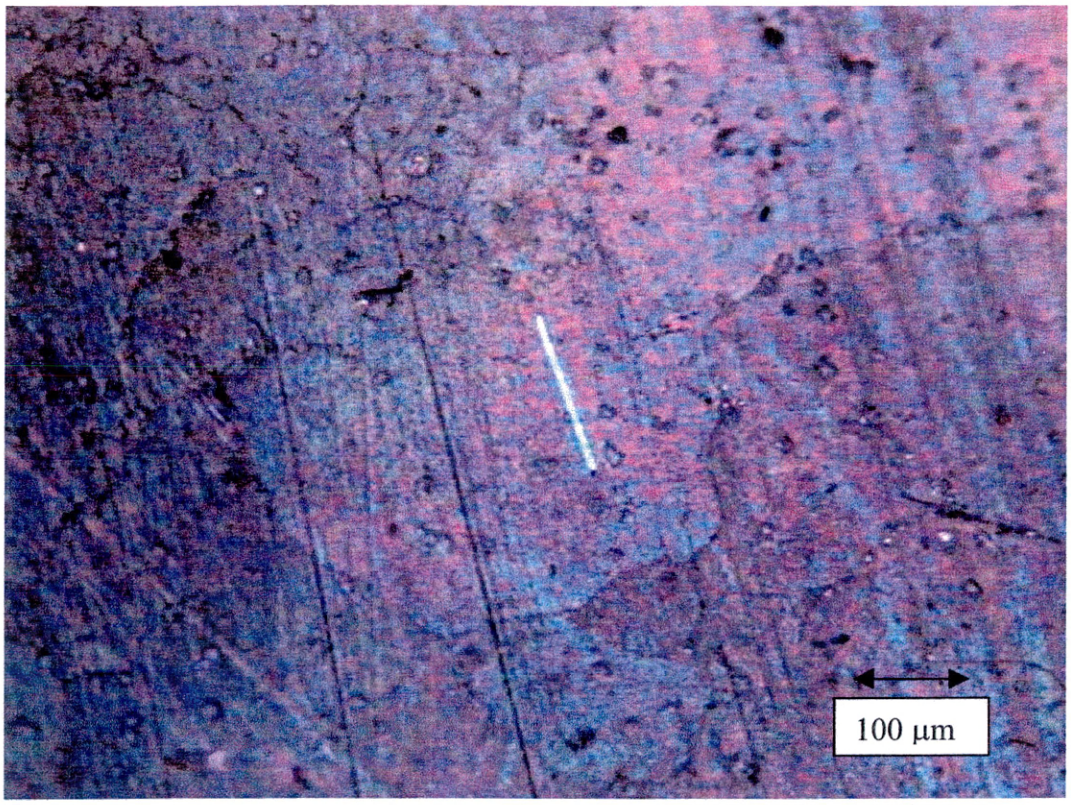

Figure 56: Photomicrograph showing microprobe scan of cerium-lanthanum specimen subjected to helium gas cooling to promote lanthanum microsegregation. Scan was made in the center of the grain for comparison to transverse scans showing significant microsegregation. Plot in Figure 55 shows very little microsegregation of lanthanum in the center of the grain.

indicating that the segregation seen in the other samples corresponds to a traverse across the grain(s).

4.3 Cerium - Lanthanum Homogenization

Twelve cerium-lanthanum specimens were cast containing nominally 5.5 wt. pct. lanthanum and were subjected to helium cooling such that a rate of 60°C/min was achieved through the $\gamma + \delta$ two-phase region. Results were produced from ten specimens however, two contained insufficient lanthanum for analysis due to macrosegregation during casting. Samples were then homogenized at the temperatures and times in the experimental matrix described previously. Each sample was mounted, ground, and polished by the method given in Appendix C and photomicrographs were produced. Polished specimens were then analyzed using an electron microprobe equipped with a wavelength dispersive spectrometer. The spectrometer(s) was calibrated prior to each scan using lanthanum oxide and cerium oxide standards. Beam voltage was 15 KEV and the beam current was approximately 58 nA. Counting times were sufficiently long to obtain a detection limit for lanthanum of on average 0.04 wt. pct. The results from each sample are given in Figures 57 through 66 and the raw microprobe data is given in Tables XX through XXIX. Each figure contains a plot of the electron microprobe data at the homogenization temperature and time indicated. Photomicrographs from each of the specimens are given in Figures 67 through 76.

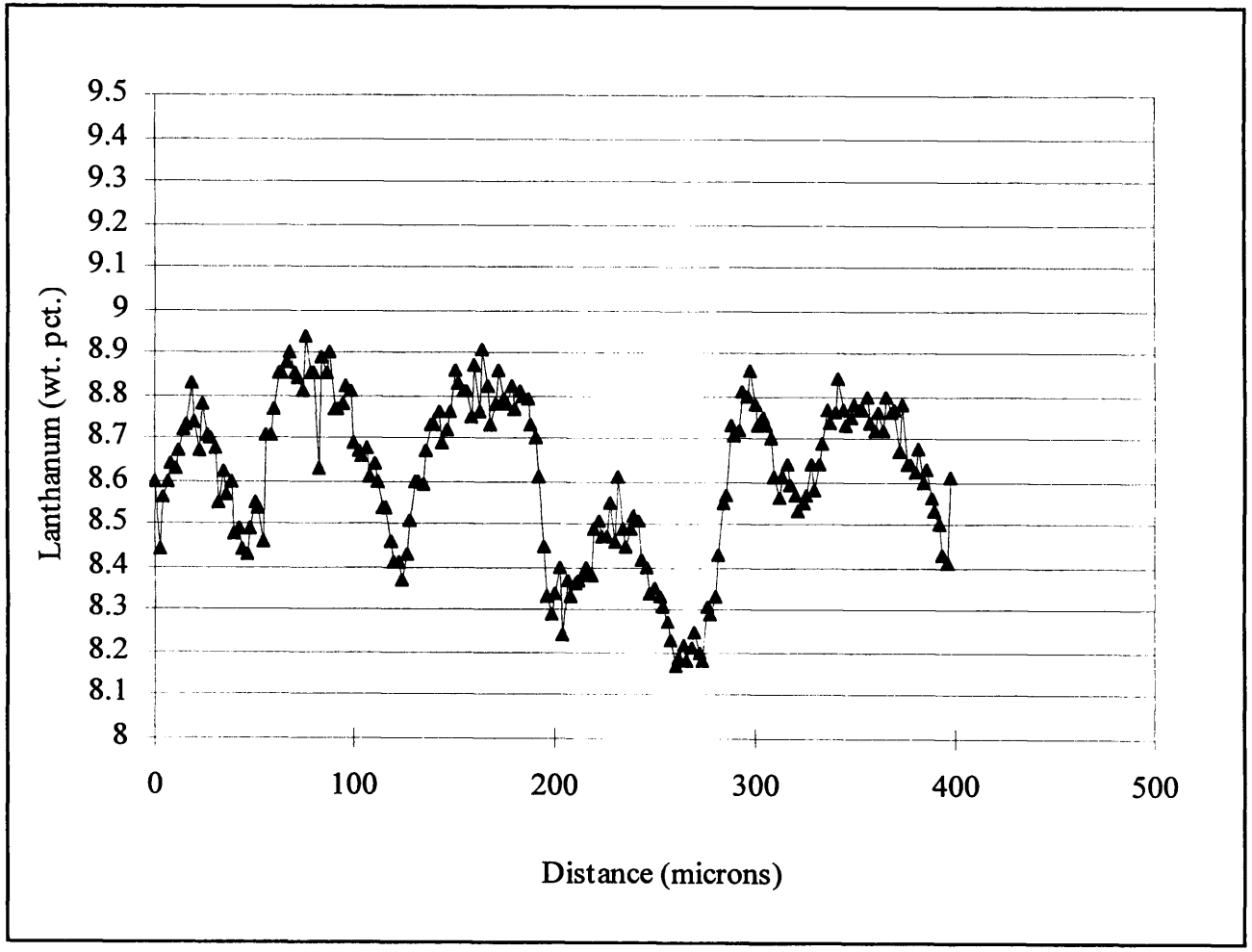

Figure 57: Lanthanum concentration variation for sample cooled through the $\gamma + \delta$ two-phase region at 60°C/min via helium cooling and then homogenized at 546°C for four hours. This sample showed significant microsegregation of lanthanum due to the phase transformation.

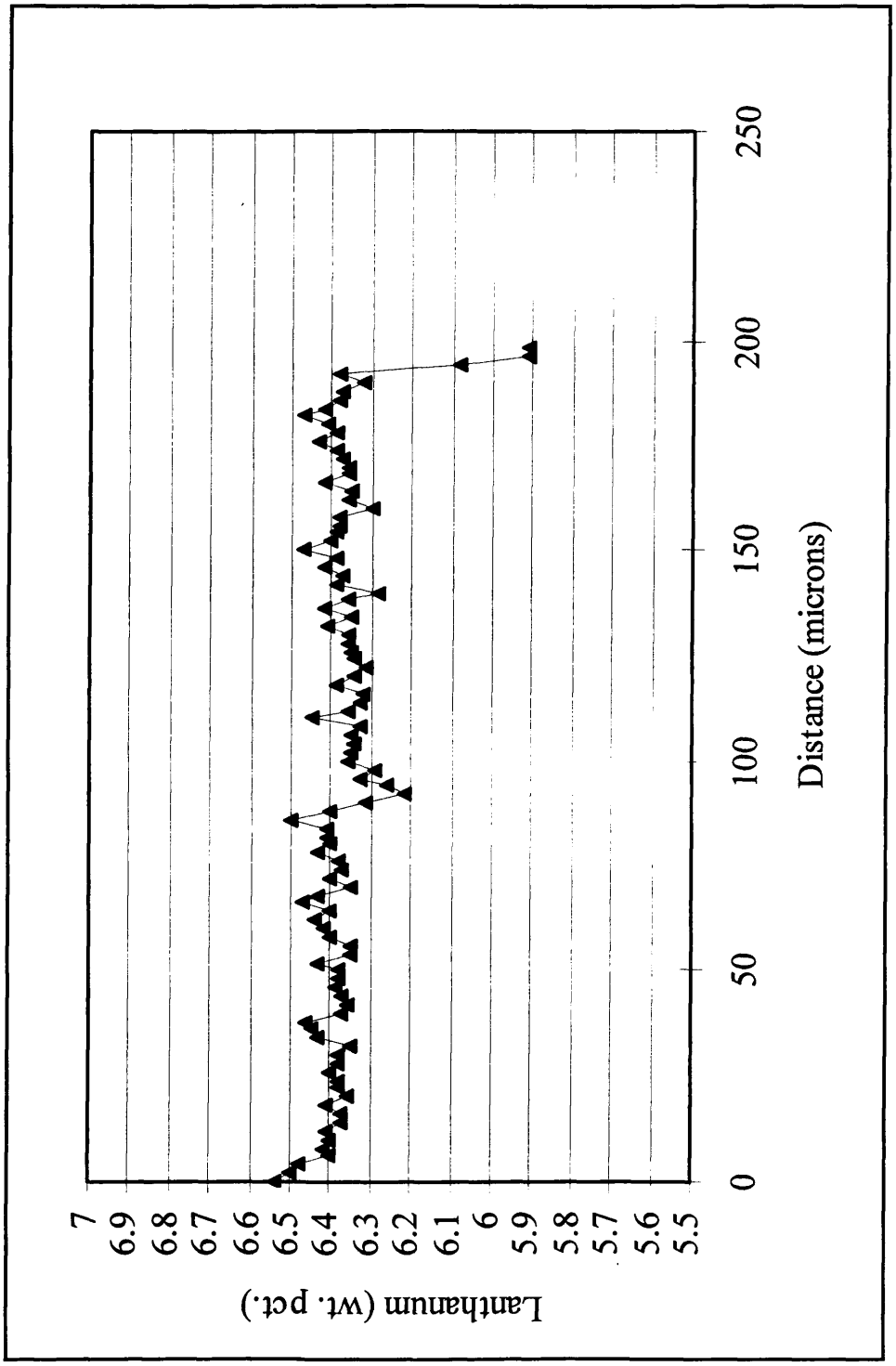

Figure 58: Lanthanum concentration variation for sample cooled through the $\gamma + \delta$ two-phase region at 60°C/min via helium cooling and then homogenized at 546°C for twenty hours. This sample showed limited microsegregation of lanthanum due to the homogenization.

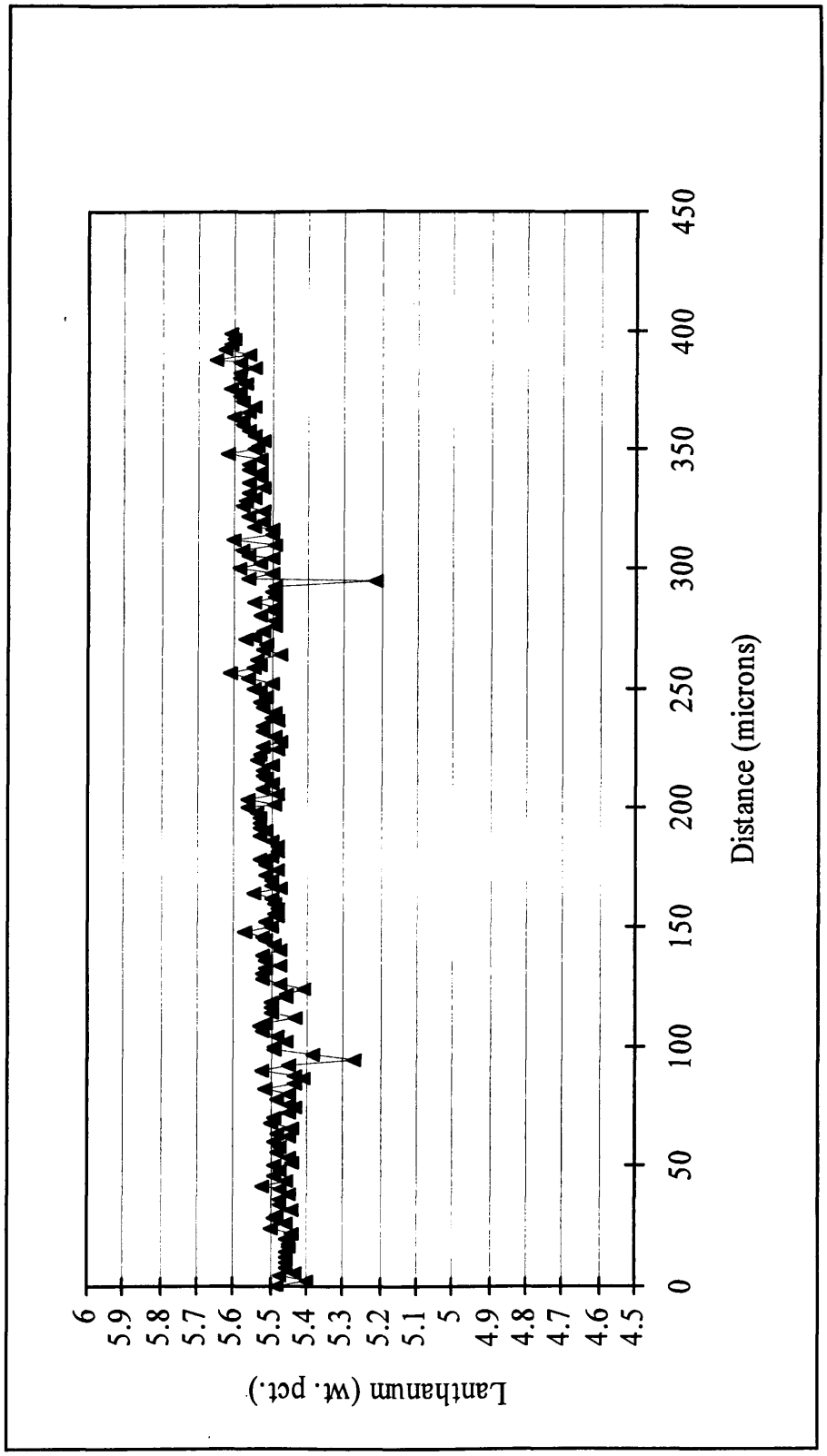

Figure 59: Lanthanum concentration variation for sample cooled through the $\gamma + \delta$ two-phase region at 60°C/min via helium cooling and then homogenized at 546°C for thirty-six hours. This sample showed substantial homogenization resulting in a flat concentration profile.

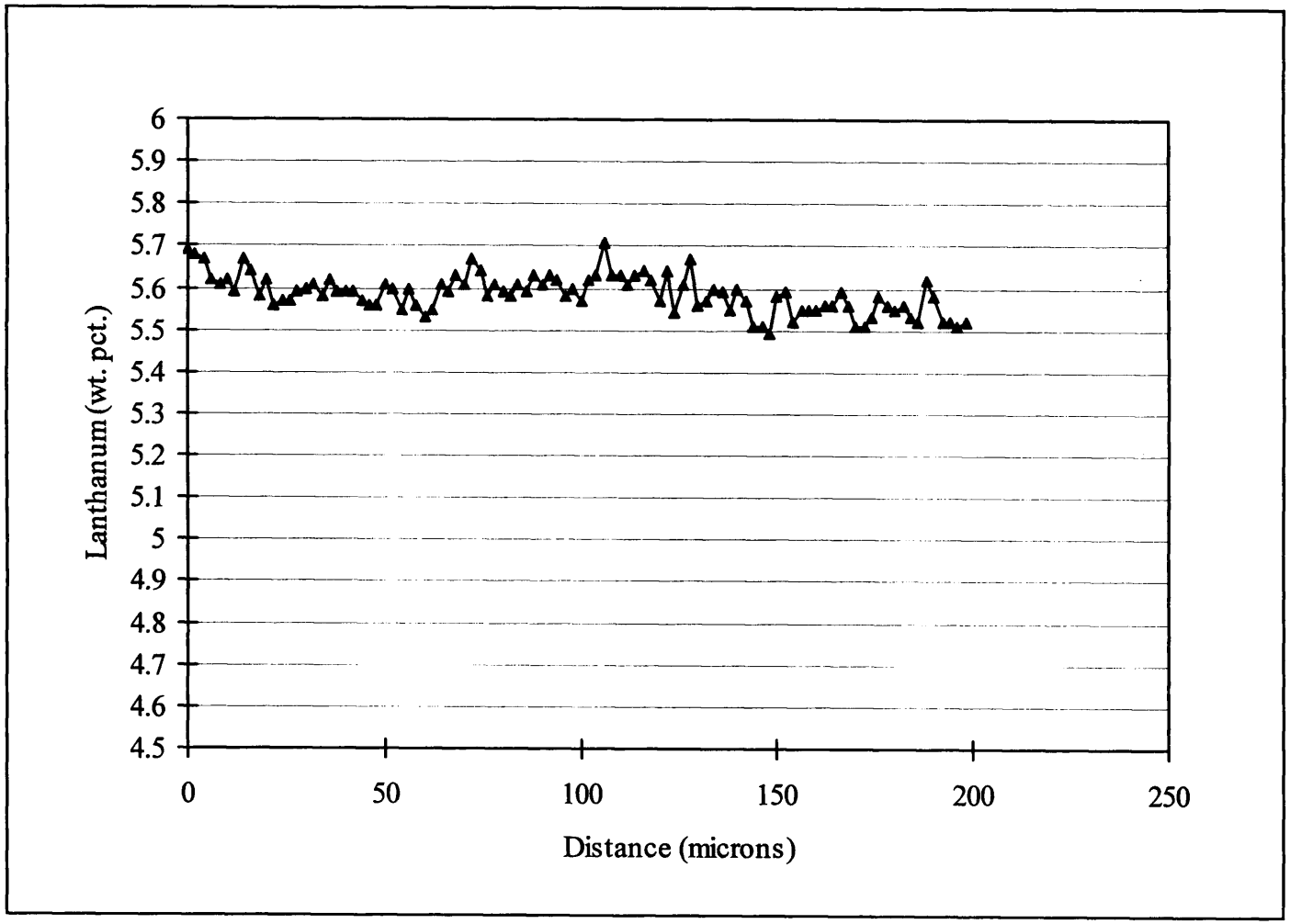

Figure 60: Lanthanum concentration variation for sample cooled through the $\gamma + \delta$ two-phase region at 60°C/min via helium cooling and then homogenized at 585°C for four hours. This sample showed significant homogenization resulting in a relatively small variation in the concentration profile.

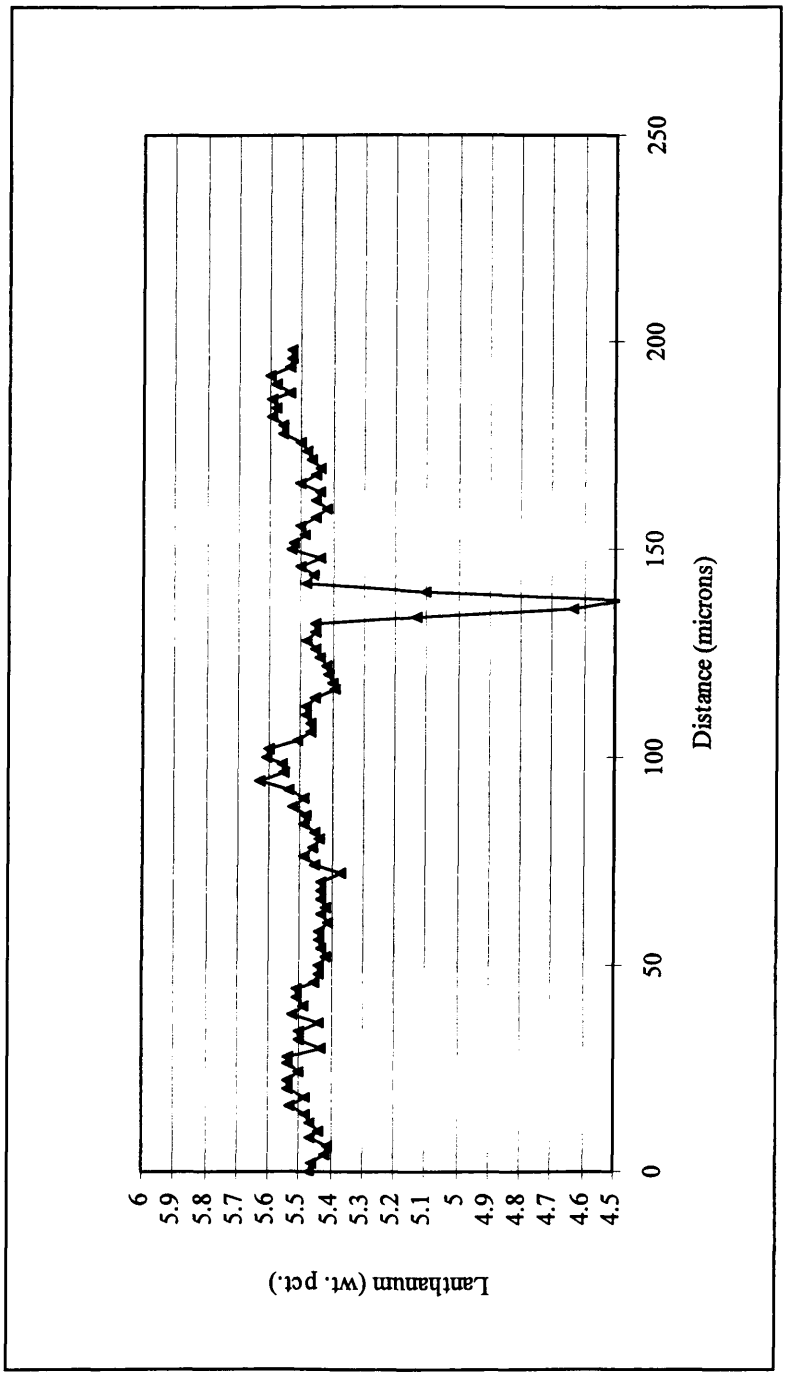

Figure 61: Lanthanum concentration variation for sample cooled through the $\gamma + \delta$ two-phase region at 60°C/min via helium cooling and then homogenized at 585°C for eight hours. This sample showed significant homogenization resulting in a relatively small variation in the concentration profile. The significant drop in lanthanum concentration at approximately 140 μm was attributed to a microstructural defect and not representative of an actual variation in lanthanum concentration

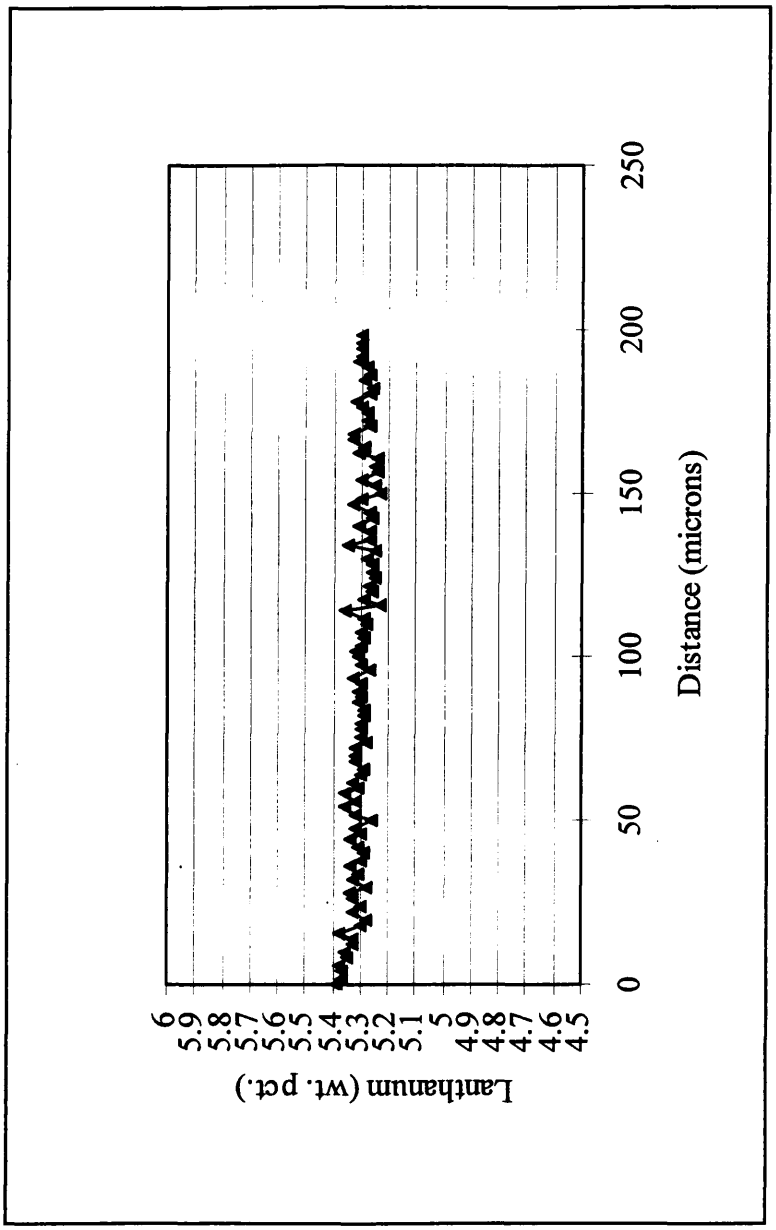

Figure 62: Lanthanum concentration variation for sample cooled through the $\gamma + \delta$ two-phase region at 60°C/min via helium cooling and then homogenized at 585°C for twenty hours. This sample showed complete homogenization resulting in essentially no variation in the lanthanum concentration profile.

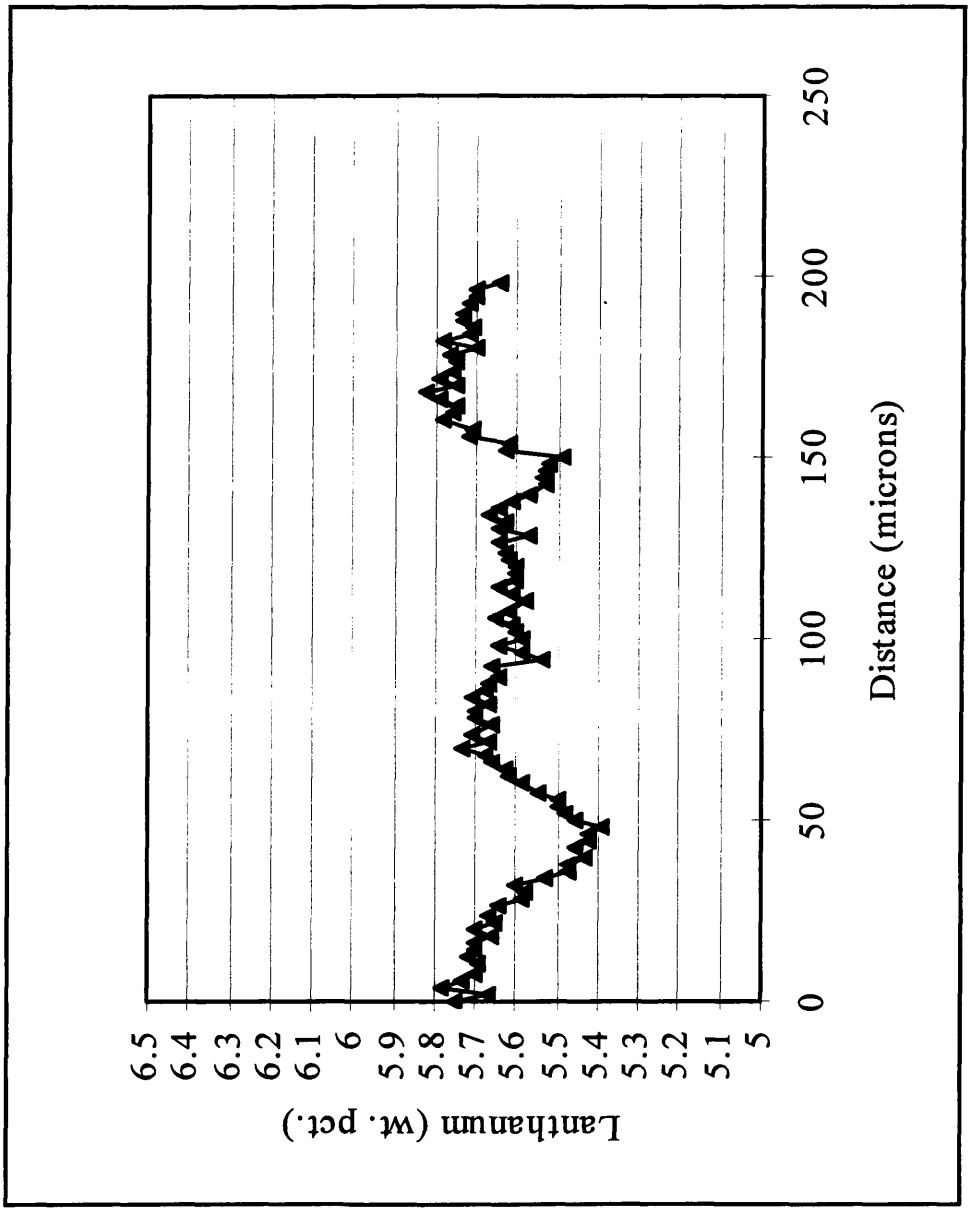

Figure 63: Lanthanum concentration variation for sample cooled through the $\gamma + \delta$ two-phase region at 60°C/min via helium cooling and then homogenized at 633°C for four hours. This sample showed significant lanthanum microsegregation due to the phase transformation.

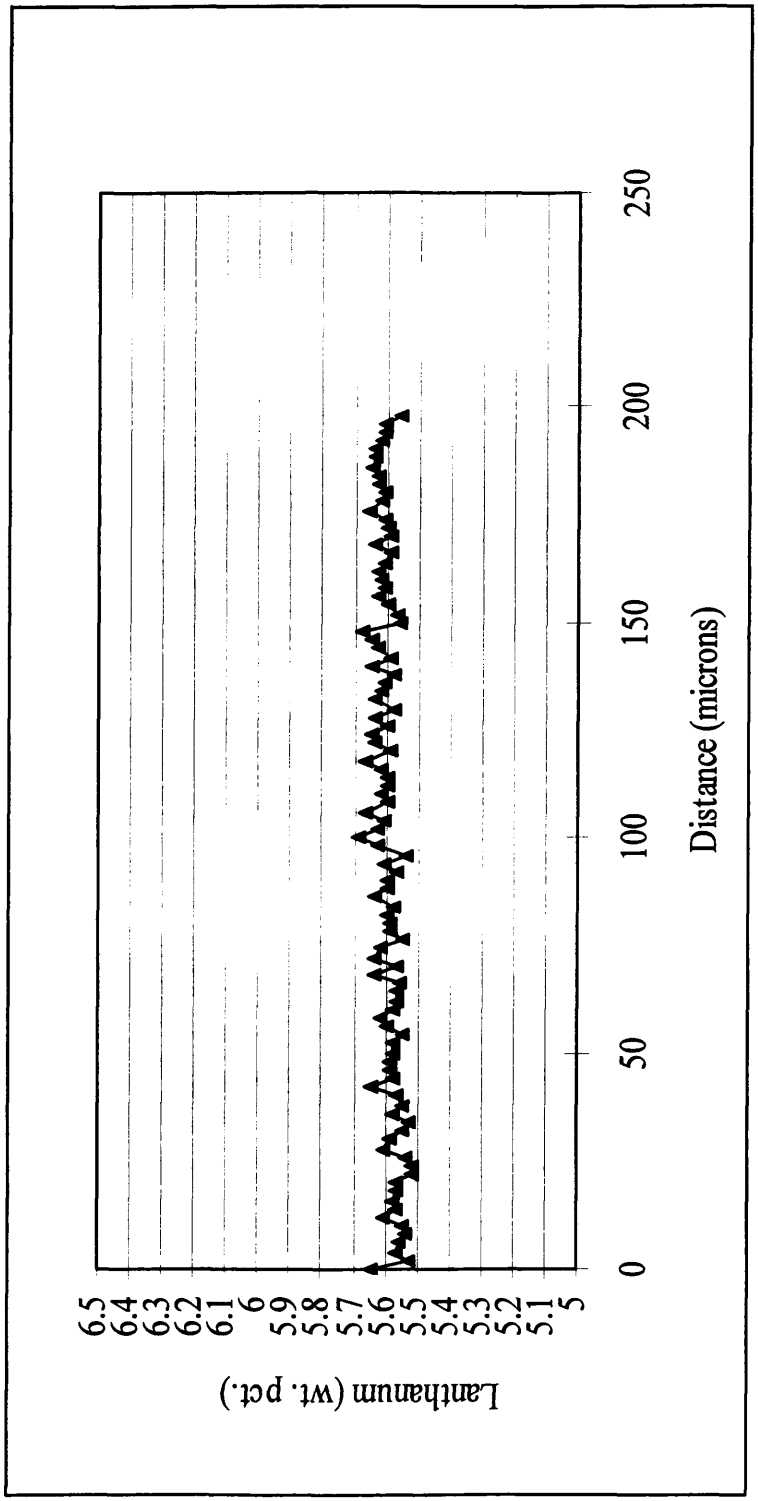

Figure 64: Lanthanum concentration variation for sample cooled through the $\gamma + \delta$ two-phase region at 60°C/min via helium cooling and then homogenized at 633°C for eight hours. This sample showed minimal lanthanum microsegregation due to homogenization.

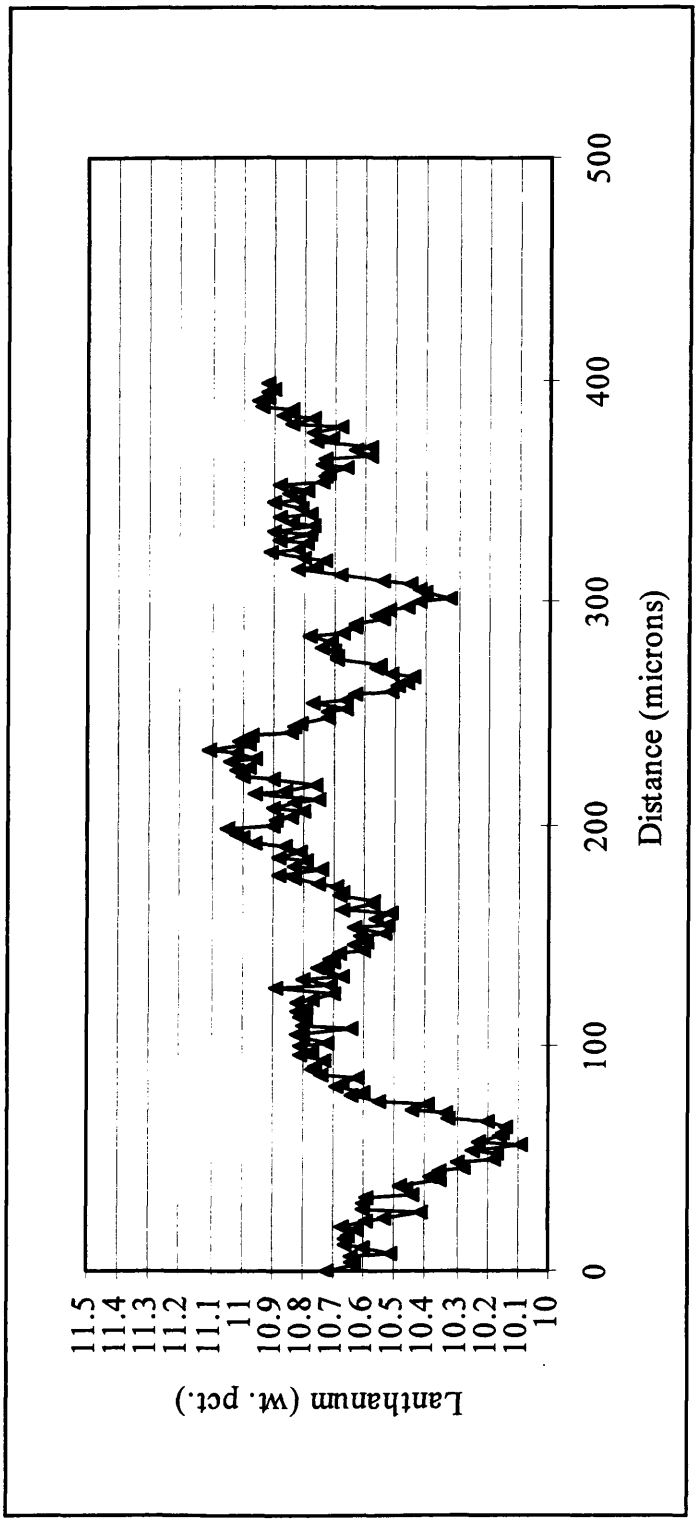

Figure 65: Lanthanum concentration variation for sample cooled through the $\gamma + \delta$ two-phase region at 60°C/min via helium cooling and then homogenized at 633°C for twelve hours. This sample showed significant lanthanum microsegregation due to the higher lanthanum concentration resulting in cooling through a wider section of the two-phase region.

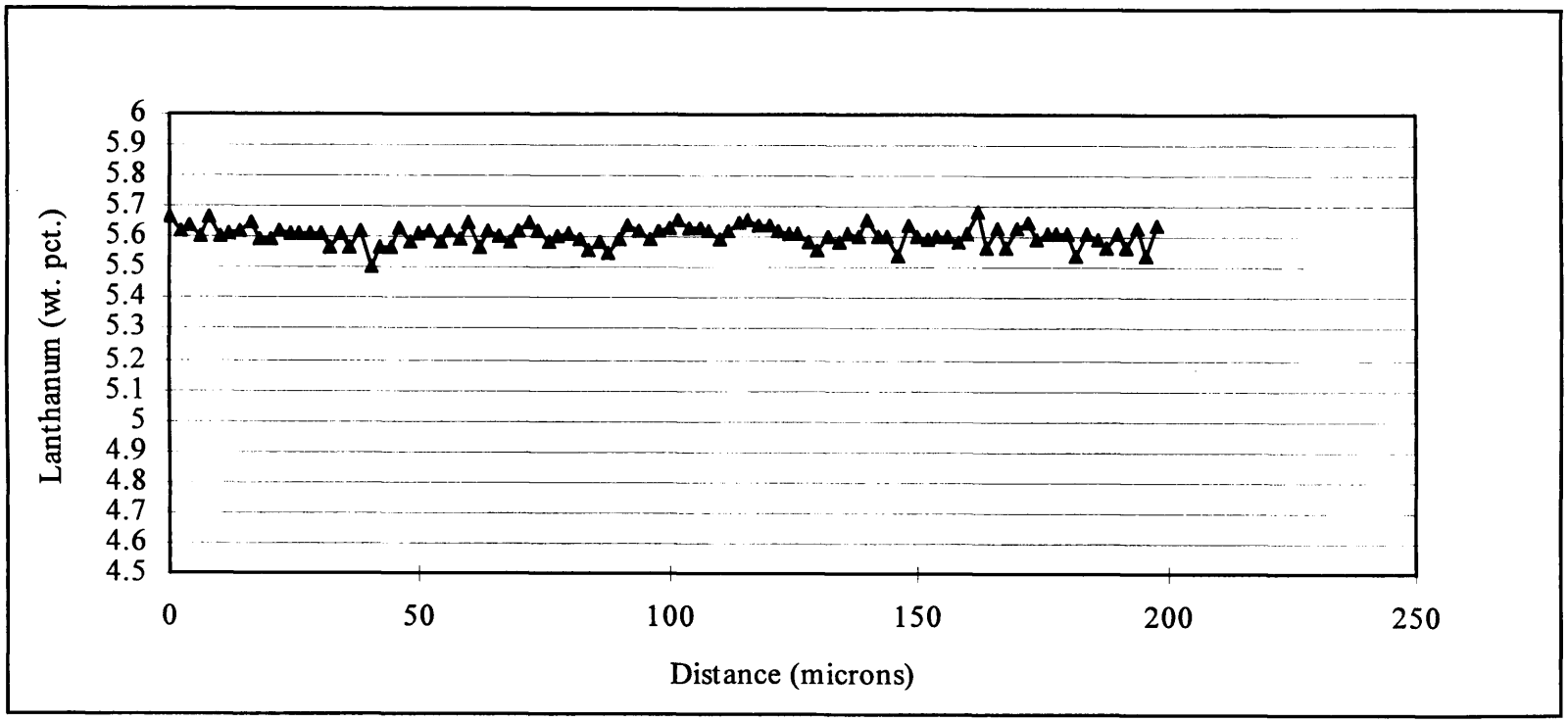

Figure 66: Lanthanum concentration variation for sample cooled through the $\gamma + \delta$ two-phase region at 60°C/min via helium cooling and then homogenized at 633°C for twenty-four hours. This sample showed significant lanthanum microsegregation due to the higher lanthanum concentration resulting in cooling through a wider section of the two-phase region.

Table XX: Raw data from microprobe scan of cerium-lanthanum specimen subjected to helium gas cooling to promote lanthanum microsegregation. Following helium cooling this sample was homogenized for four hours at 546°C. Scan indicated significant microsegregation of lanthanum corresponding to the measure grain size.

Distance μm	La (wt. pct.)	Distance μm	La (wt. pct.)	Distance μm	La (wt. pct.)	Distance μm	La (wt. pc
0	8.6	102	8.67	204	8.24	306	8.73
2	8.44	104	8.66	206	8.37	308	8.7
4	8.56	106	8.68	208	8.33	310	8.61
6	8.6	108	8.61	210	8.36	312	8.56
8	8.64	110	8.64	212	8.37	314	8.61
10	8.63	112	8.6	214	8.38	316	8.64
12	8.67	114	8.54	216	8.4	318	8.59
14	8.72	116	8.54	218	8.38	320	8.57
16	8.73	118	8.46	220	8.49	322	8.53
18	8.83	120	8.41	222	8.51	324	8.55
20	8.74	122	8.41	224	8.47	326	8.57
22	8.67	124	8.37	226	8.47	328	8.64
24	8.78	126	8.43	228	8.55	330	8.58
26	8.71	128	8.51	230	8.46	332	8.64
28	8.7	130	8.6	232	8.61	334	8.69
30	8.68	132	8.6	234	8.49	336	8.77
32	8.55	134	8.59	236	8.45	338	8.74
34	8.62	136	8.67	238	8.49	340	8.76
36	8.57	138	8.73	240	8.52	342	8.84
38	8.6	140	8.73	242	8.51	344	8.77
40	8.48	142	8.76	244	8.42	346	8.73
42	8.49	144	8.69	246	8.4	348	8.75
44	8.44	146	8.72	248	8.34	350	8.78
46	8.43	148	8.76	250	8.35	352	8.77
48	8.49	150	8.86	252	8.33	354	8.77
50	8.55	152	8.83	254	8.31	356	8.8
52	8.54	154	8.81	256	8.27	358	8.74
54	8.46	156	8.81	258	8.23	360	8.72
56	8.71	158	8.75	260	8.17	362	8.76
58	8.71	160	8.87	262	8.19	364	8.72
60	8.77	162	8.76	264	8.22	366	8.8
62	8.85	164	8.91	266	8.18	368	8.76
64	8.85	166	8.82	268	8.21	370	8.77
66	8.88	168	8.73	270	8.25	372	8.67
68	8.9	170	8.78	272	8.2	374	8.78
70	8.85	172	8.86	274	8.18	376	8.64
72	8.84	174	8.79	276	8.31	378	8.64
74	8.81	176	8.78	278	8.29	380	8.62
76	8.94	178	8.82	280	8.33	382	8.68
78	8.85	180	8.77	282	8.43	384	8.6
80	8.85	182	8.81	284	8.55	386	8.63
82	8.63	184	8.8	286	8.57	388	8.56
84	8.89	186	8.79	288	8.73	390	8.53
86	8.85	188	8.73	290	8.71	392	8.5
88	8.9	190	8.7	292	8.72	394	8.43
90	8.77	192	8.61	294	8.81	396	8.41
92	8.77	194	8.45	296	8.8	398	8.61
94	8.78	196	8.33	298	8.86		
96	8.82	198	8.29	300	8.78		
98	8.81	200	8.34	302	8.73		
100	8.69	202	8.4	304	8.75		

Table XXI: Raw data from microprobe scan of cerium-lanthanum specimen subjected to helium gas cooling to promote lanthanum microsegregation. Following helium cooling this sample was homogenized for twenty hours at 546°C. Scan indicated slight microsegregation of lanthanum suggesting nearly complete homogenization.

Distance μm	La (wt. pct.)	Distance μm	La (wt. pct.)
0	6.54	100	6.36
2	6.5	102	6.35
4	6.48	104	6.34
6	6.4	106	6.35
8	6.42	108	6.33
10	6.4	110	6.45
12	6.41	112	6.36
14	6.37	114	6.33
16	6.37	116	6.32
18	6.41	118	6.39
20	6.36	120	6.34
22	6.38	122	6.31
24	6.38	124	6.34
26	6.4	126	6.35
28	6.38	128	6.36
30	6.38	130	6.36
32	6.35	132	6.41
34	6.43	134	6.35
36	6.45	136	6.42
38	6.46	138	6.36
40	6.37	140	6.28
42	6.36	142	6.39
44	6.37	144	6.37
46	6.39	146	6.42
48	6.38	148	6.39
50	6.38	150	6.47
52	6.43	152	6.4
54	6.35	154	6.39
56	6.35	156	6.38
58	6.4	158	6.38
60	6.42	160	6.3
62	6.44	162	6.36
64	6.4	164	6.35
66	6.47	166	6.42
68	6.43	168	6.36
70	6.35	170	6.36
72	6.4	172	6.37
74	6.37	174	6.39
76	6.38	176	6.43
78	6.43	178	6.39
80	6.4	180	6.41
82	6.41	182	6.47
84	6.41	184	6.42
86	6.5	186	6.38
88	6.4	188	6.37
90	6.31	190	6.32
92	6.22	192	6.38
94	6.26	194	6.08
96	6.33	196	5.91
98	6.29	198	5.91

Table XXII: Raw data from microprobe scan of cerium-lanthanum specimen subjected to helium gas cooling to promote lanthanum microsegregation. Following helium cooling this sample was homogenized for thirty-six hours at 546°C. Scan indicated no microsegregation of lanthanum suggesting complete homogenization.

Distance μm	La (wt. pct.)	Distance μm	La (wt. pct.)	Distance μm	La (wt. pct.)	Distance μm	La (wt. pct.)
0	5.48	100	5.49	200	5.56	300	5.59
2	5.4	102	5.46	202	5.49	302	5.53
4	5.47	104	5.48	204	5.56	304	5.5
6	5.43	106	5.52	206	5.48	306	5.56
8	5.46	108	5.53	208	5.52	308	5.58
10	5.46	110	5.51	210	5.5	310	5.49
12	5.46	112	5.43	212	5.51	312	5.6
14	5.46	114	5.5	214	5.52	314	5.5
16	5.45	116	5.5	216	5.52	316	5.5
18	5.45	118	5.5	218	5.5	318	5.55
20	5.46	120	5.46	220	5.54	320	5.52
22	5.44	122	5.46	222	5.53	322	5.56
24	5.5	124	5.41	224	5.48	324	5.52
26	5.46	126	5.47	226	5.52	326	5.58
28	5.49	128	5.52	228	5.47	328	5.57
30	5.48	130	5.52	230	5.49	330	5.55
32	5.44	132	5.51	232	5.52	332	5.56
34	5.47	134	5.47	234	5.52	334	5.52
36	5.47	136	5.51	236	5.48	336	5.56
38	5.45	138	5.52	238	5.5	338	5.53
40	5.47	140	5.47	240	5.49	340	5.53
42	5.52	142	5.49	242	5.52	342	5.56
44	5.46	144	5.51	244	5.53	344	5.56
46	5.49	146	5.52	246	5.51	346	5.53
48	5.47	148	5.57	248	5.53	348	5.62
50	5.49	150	5.5	250	5.55	350	5.55
52	5.44	152	5.51	252	5.5	352	5.54
54	5.45	154	5.48	254	5.56	354	5.52
56	5.48	156	5.49	256	5.61	356	5.55
58	5.47	158	5.48	258	5.55	358	5.56
60	5.49	160	5.49	260	5.53	360	5.58
62	5.45	162	5.5	262	5.54	362	5.58
64	5.48	164	5.55	264	5.47	364	5.6
66	5.44	166	5.47	266	5.52	366	5.56
68	5.5	168	5.5	268	5.51	368	5.55
70	5.49	170	5.5	270	5.57	370	5.58
72	5.45	172	5.51	272	5.55	372	5.59
74	5.43	174	5.48	274	5.52	374	5.59
76	5.45	176	5.51	276	5.49	376	5.61
78	5.48	178	5.53	278	5.49	378	5.57
80	5.45	180	5.5	280	5.53	380	5.59
82	5.51	182	5.48	282	5.5	382	5.59
84	5.43	184	5.48	284	5.49	384	5.55
86	5.41	186	5.5	286	5.55	386	5.59
88	5.43	188	5.53	288	5.49	388	5.65
90	5.52	190	5.51	290	5.5	390	5.56
92	5.45	192	5.53	292	5.49	392	5.63
94	5.27	194	5.53	294	5.21	394	5.61
96	5.38	196	5.53	296	5.56	396	5.6
98	5.49	198	5.54	298	5.5	398	5.61

Table XXIII: Raw data from microprobe scan of cerium-lanthanum specimen subjected to helium gas cooling to promote lanthanum microsegregation. Following helium cooling this sample was homogenized for four hours at 585°C. Scan indicated microsegregation of lanthanum suggesting incomplete homogenization.

Distance μm	La (wt. pct.)	Distance μm	La (wt. pct.)
0	5.69	100	5.57
2	5.68	102	5.62
4	5.67	104	5.63
6	5.62	106	5.71
8	5.61	108	5.63
10	5.62	110	5.63
12	5.59	112	5.61
14	5.67	114	5.63
16	5.64	116	5.64
18	5.58	118	5.62
20	5.62	120	5.57
22	5.56	122	5.64
24	5.57	124	5.54
26	5.57	126	5.61
28	5.59	128	5.67
30	5.6	130	5.56
32	5.61	132	5.57
34	5.58	134	5.6
36	5.62	136	5.59
38	5.59	138	5.55
40	5.59	140	5.6
42	5.59	142	5.57
44	5.57	144	5.51
46	5.56	146	5.51
48	5.56	148	5.49
50	5.61	150	5.58
52	5.6	152	5.59
54	5.55	154	5.52
56	5.6	156	5.55
58	5.56	158	5.55
60	5.53	160	5.55
62	5.55	162	5.56
64	5.61	164	5.56
66	5.59	166	5.59
68	5.63	168	5.56
70	5.61	170	5.51
72	5.67	172	5.51
74	5.64	174	5.53
76	5.58	176	5.58
78	5.61	178	5.56
80	5.59	180	5.55
82	5.58	182	5.56
84	5.61	184	5.53
86	5.59	186	5.52
88	5.63	188	5.62
90	5.61	190	5.58
92	5.63	192	5.52
94	5.62	194	5.52
96	5.58	196	5.51
98	5.6	198	5.52

Table XXIV: Raw data from microprobe scan of cerium-lanthanum specimen subjected to helium gas cooling to promote lanthanum microsegregation. Following helium cooling this sample was homogenized for eight hours at 585°C. Scan indicated some microsegregation of lanthanum suggesting significant homogenization.

Distance μm	La (wt. pct.)	Distance μm	La (wt. pct.)
0	5.47	100	5.61
2	5.46	102	5.6
4	5.42	104	5.51
6	5.41	106	5.47
8	5.47	108	5.47
10	5.44	110	5.48
12	5.47	112	5.48
14	5.48	114	5.45
16	5.53	116	5.39
18	5.48	118	5.4
20	5.54	120	5.41
22	5.54	122	5.42
24	5.5	124	5.44
26	5.54	126	5.45
28	5.54	128	5.48
30	5.43	130	5.45
32	5.5	132	5.45
34	5.5	134	5.13
36	5.44	136	4.63
38	5.52	138	4.47
40	5.49	140	5.1
42	5.51	142	5.48
44	5.51	144	5.46
46	5.45	146	5.5
48	5.44	148	5.44
50	5.44	150	5.53
52	5.42	152	5.52
54	5.43	154	5.49
56	5.44	156	5.5
58	5.44	158	5.45
60	5.41	160	5.42
62	5.43	162	5.45
64	5.42	164	5.44
66	5.43	166	5.5
68	5.43	168	5.45
70	5.43	170	5.44
72	5.37	172	5.47
74	5.45	174	5.48
76	5.49	176	5.5
78	5.46	178	5.56
80	5.44	180	5.56
82	5.45	182	5.59
84	5.49	184	5.58
86	5.48	186	5.59
88	5.52	188	5.54
90	5.49	190	5.58
92	5.54	192	5.6
94	5.63	194	5.54
96	5.55	196	5.53
98	5.56	198	5.53

Table XXV: Raw data from microprobe scan of cerium-lanthanum specimen subjected to helium gas cooling to promote lanthanum microsegregation. Following helium cooling this sample was homogenized for twenty hours at 585°C. Scan indicated complete homogenization of lanthanum.

Distance μm	La (wt. pct.)	Distance μm	La (wt. pct.)
0	5.39	100	5.31
2	5.37	102	5.32
4	5.37	104	5.3
6	5.38	106	5.29
8	5.35	108	5.3
10	5.36	110	5.28
12	5.33	112	5.29
14	5.33	114	5.36
16	5.38	116	5.23
18	5.3	118	5.29
20	5.28	120	5.26
22	5.33	122	5.27
24	5.3	124	5.25
26	5.33	126	5.26
28	5.34	128	5.26
30	5.28	130	5.28
32	5.33	132	5.25
34	5.31	134	5.35
36	5.34	136	5.27
38	5.3	138	5.27
40	5.29	140	5.31
42	5.31	142	5.26
44	5.34	144	5.27
46	5.3	146	5.33
48	5.32	148	5.3
50	5.26	150	5.23
52	5.32	152	5.25
54	5.36	154	5.3
56	5.32	156	5.24
58	5.36	158	5.25
60	5.31	160	5.24
62	5.33	162	5.31
64	5.3	164	5.29
66	5.29	166	5.33
68	5.32	168	5.33
70	5.32	170	5.27
72	5.32	172	5.28
74	5.28	174	5.28
76	5.3	176	5.3
78	5.3	178	5.32
80	5.3	180	5.27
82	5.29	182	5.26
84	5.29	184	5.29
86	5.31	186	5.27
88	5.3	188	5.28
90	5.31	190	5.31
92	5.3	192	5.3
94	5.33	194	5.3
96	5.27	196	5.3

Table XXVI: Raw data from microprobe scan of cerium-lanthanum specimen subjected to helium gas cooling to promote lanthanum microsegregation. Following helium cooling this sample was homogenized for four hours at 633°C. Scan indicated significant microsegregation of lanthanum.

Distance μm	La (wt. pct.)	Distance μm	La (wt. pct.)
0	5.75	102	5.6
2	5.67	104	5.61
4	5.78	106	5.65
6	5.73	108	5.62
8	5.7	110	5.58
10	5.69	112	5.61
12	5.72	114	5.64
14	5.7	116	5.6
16	5.7	118	5.6
18	5.66	120	5.6
20	5.7	122	5.62
22	5.65	124	5.63
24	5.67	126	5.64
26	5.64	128	5.57
28	5.59	130	5.64
30	5.58	132	5.63
32	5.6	134	5.67
34	5.53	136	5.64
36	5.47	138	5.61
38	5.47	140	5.57
40	5.43	142	5.53
42	5.46	144	5.54
44	5.42	146	5.53
46	5.42	148	5.52
48	5.39	150	5.49
50	5.46	152	5.63
52	5.48	154	5.62
54	5.5	156	5.72
56	5.5	158	5.71
58	5.55	160	5.78
60	5.59	162	5.76
62	5.62	164	5.75
64	5.63	166	5.79
66	5.66	168	5.82
68	5.68	170	5.75
70	5.73	172	5.79
72	5.67	174	5.76
74	5.71	176	5.75
76	5.66	178	5.77
78	5.7	180	5.7
80	5.7	182	5.78
82	5.67	184	5.72
84	5.71	186	5.71
86	5.68	188	5.73
88	5.67	190	5.73
90	5.64	192	5.72
92	5.66	194	5.7
94	5.54	196	5.7
96	5.59	198	5.64
98	5.64		
100	5.59		

Table XXVII: Raw data from microprobe scan of cerium-lanthanum specimen subjected to helium gas cooling to promote lanthanum microsegregation. Following helium cooling this sample was homogenized for eight hours at 633°C. Scan indicated essentially complete homogenization of lanthanum.

Distance μm	La (wt. pct.)	Distance μm	La (wt. pct.)
0	5.65	102	5.63
2	5.53	104	5.61
4	5.57	106	5.67
6	5.56	108	5.6
8	5.54	110	5.62
10	5.55	112	5.6
12	5.61	114	5.6
14	5.57	116	5.62
16	5.58	118	5.67
18	5.57	120	5.59
20	5.57	122	5.64
22	5.52	124	5.65
24	5.52	126	5.6
26	5.54	128	5.64
28	5.61	130	5.58
30	5.59	132	5.64
32	5.55	134	5.62
34	5.53	136	5.61
36	5.58	138	5.58
38	5.55	140	5.65
40	5.57	142	5.59
42	5.65	144	5.63
44	5.58	146	5.65
46	5.59	148	5.68
48	5.59	150	5.56
50	5.58	152	5.57
52	5.58	154	5.6
54	5.55	156	5.63
56	5.6	158	5.61
58	5.62	160	5.62
60	5.58	162	5.63
62	5.57	164	5.61
64	5.57	166	5.59
66	5.56	168	5.64
68	5.64	170	5.59
70	5.57	172	5.6
72	5.64	174	5.61
74	5.62	176	5.66
76	5.55	178	5.62
78	5.59	180	5.61
80	5.59	182	5.63
82	5.6	184	5.63
84	5.58	186	5.65
86	5.64	188	5.64
88	5.6	190	5.64
90	5.6	192	5.62
92	5.57	194	5.61
94	5.61	196	5.61
96	5.54	198	5.56
98	5.63		
100	5.69		

Table XXVIII: Raw data from microprobe scan of cerium-lanthanum specimen subjected to helium gas cooling to promote lanthanum microsegregation. Following helium cooling this sample was homogenized for twelve hours at 633°C. Scan indicated essentially complete homogenization of lanthanum.

Distance μm	La (wt. pct.)	Distance μm	La (wt. pct.)	Distance μm	La (wt. pct.)	Distance μm
0	10.72	100	10.81	200	10.9	300
2	10.63	102	10.72	202	10.89	302
4	10.64	104	10.8	204	10.84	304
6	10.64	106	10.82	206	10.8	306
8	10.51	108	10.64	208	10.9	308
10	10.6	110	10.8	210	10.83	310
12	10.66	112	10.79	212	10.75	312
14	10.66	114	10.81	214	10.96	314
16	10.65	116	10.82	216	10.86	316
18	10.62	118	10.79	218	10.76	318
20	10.67	120	10.82	220	10.9	320
22	10.59	122	10.77	222	11	322
24	10.53	124	10.7	224	11.02	324
26	10.41	126	10.89	226	10.98	326
28	10.6	128	10.71	228	11.04	328
30	10.6	130	10.8	230	10.96	330
32	10.59	132	10.67	232	11.02	332
34	10.44	134	10.72	234	11.11	334
36	10.46	136	10.75	236	10.98	336
38	10.48	138	10.7	238	11.01	338
40	10.36	140	10.71	240	10.97	340
42	10.38	142	10.68	242	10.84	342
44	10.36	144	10.6	244	10.83	344
46	10.28	146	10.63	246	10.81	346
48	10.3	148	10.59	248	10.72	348
50	10.18	150	10.61	250	10.72	350
52	10.17	152	10.53	252	10.66	352
54	10.25	154	10.63	254	10.77	354
56	10.09	156	10.52	256	10.66	356
58	10.23	158	10.56	258	10.63	358
60	10.16	160	10.51	260	10.51	360
62	10.15	162	10.67	262	10.49	362
64	10.14	164	10.57	264	10.46	364
66	10.2	166	10.57	266	10.44	366
68	10.33	168	10.68	268	10.51	368
70	10.34	170	10.67	270	10.56	370
72	10.44	172	10.69	272	10.55	372
74	10.39	174	10.75	274	10.69	374
76	10.55	176	10.83	276	10.69	376
78	10.64	178	10.88	278	10.7	378
80	10.6	180	10.74	280	10.74	380
82	10.69	182	10.83	282	10.71	382
84	10.67	184	10.79	284	10.78	384
86	10.62	186	10.88	286	10.67	386
88	10.74	188	10.81	288	10.63	388
90	10.77	190	10.86	290	10.63	390
92	10.76	192	10.96	292	10.54	392
94	10.73	194	11	294	10.56	394
96	10.81	196	11.02	296	10.52	396
98	10.77	198	11.05	298	10.46	398

Table XXIX: Raw data from microprobe scan of cerium-lanthanum specimen subjected to helium gas cooling to promote lanthanum microsegregation. Following helium cooling this sample was homogenized for twenty-four hours at 633°C. Scan indicated complete homogenization of lanthanum.

Distance μm	Lanthanum (wt. pct.)	Distance μm	Lanthanum (wt. pct.)
0	5.67	100	5.63
2	5.62	102	5.66
4	5.64	104	5.63
6	5.6	106	5.63
8	5.67	108	5.62
10	5.6	110	5.59
12	5.61	112	5.62
14	5.62	114	5.65
16	5.65	116	5.66
18	5.59	118	5.64
20	5.59	120	5.64
22	5.62	122	5.62
24	5.61	124	5.61
26	5.61	126	5.61
28	5.61	128	5.58
30	5.61	130	5.56
32	5.57	132	5.6
34	5.61	134	5.58
36	5.57	136	5.61
38	5.62	138	5.6
40	5.5	140	5.66
42	5.57	142	5.6
44	5.57	144	5.6
46	5.63	146	5.54
48	5.58	148	5.64
50	5.61	150	5.6
52	5.62	152	5.59
54	5.58	154	5.6
56	5.62	156	5.6
58	5.59	158	5.58
60	5.65	160	5.61
62	5.57	162	5.68
64	5.62	164	5.57
66	5.6	166	5.63
68	5.58	168	5.57
70	5.62	170	5.63
72	5.65	172	5.65
74	5.62	174	5.59
76	5.58	176	5.61
78	5.6	178	5.61
80	5.61	180	5.61
82	5.59	182	5.54
84	5.56	184	5.61
86	5.58	186	5.59
88	5.55	188	5.57
90	5.59	190	5.61
92	5.64	192	5.57
94	5.62	194	5.63
96	5.59	196	5.54
98	5.62	198	5.64

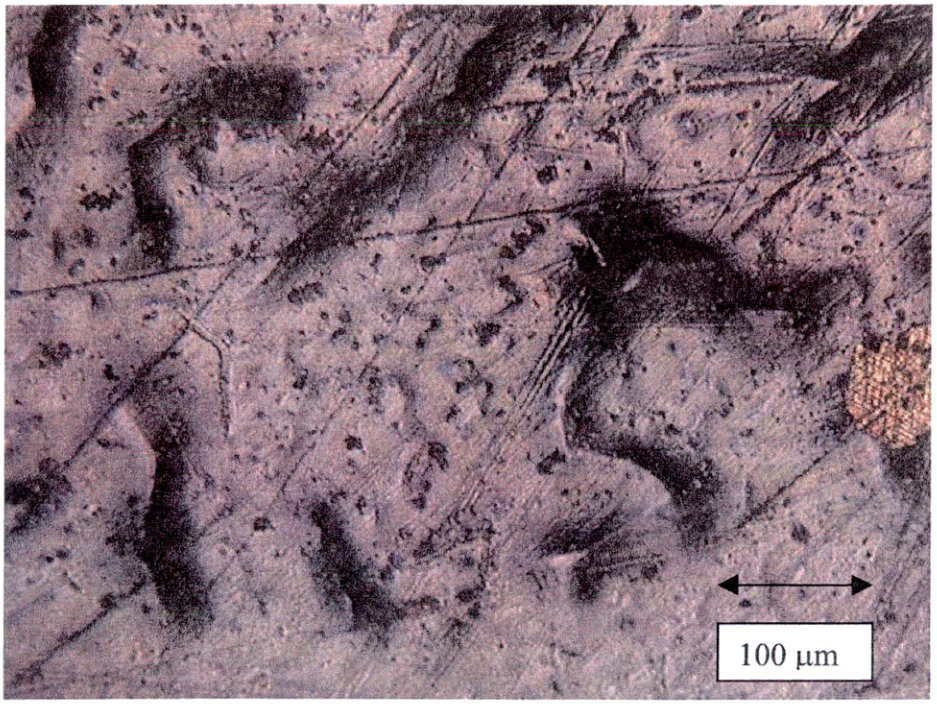

Figure 67: Photomicrograph of cerium-lanthanum alloy subjected to helium cooling through the two-phase $\gamma + \delta$ region at 60°C/min. Sample was homogenized at 546°C for four hours. Sample was over-etched to highlight the grain boundaries. Average grain size was approximately 90 μm.

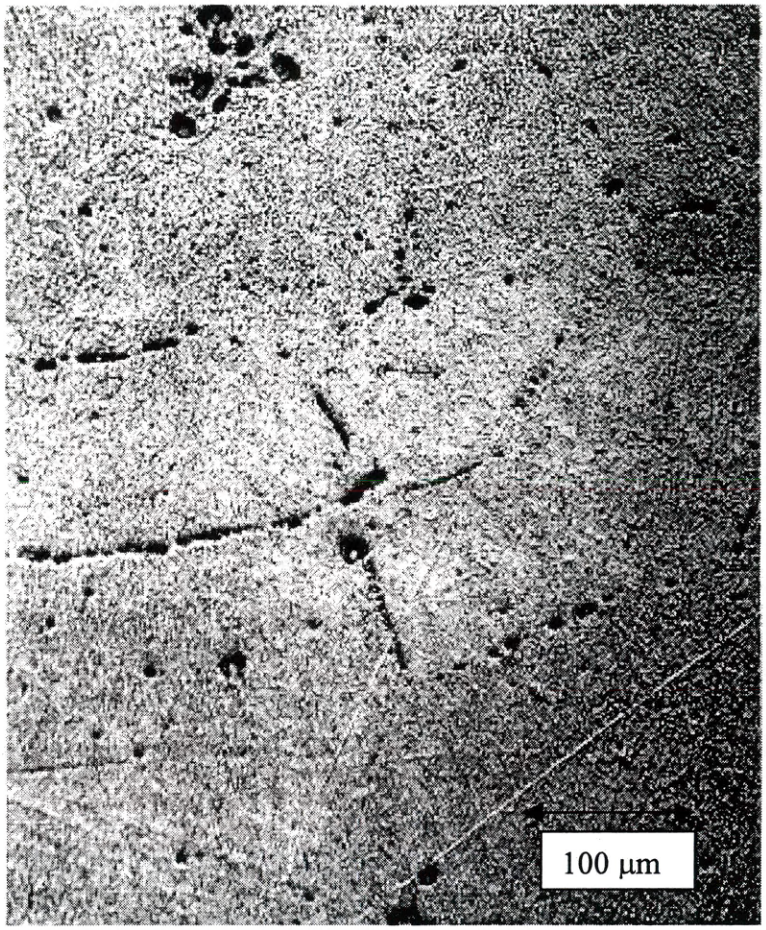

Figure 68: Photomicrograph of cerium-lanthanum alloy subjected to helium cooling through the two-phase $\gamma + \delta$ region at 60°C/min. Sample was homogenized at 546°C for twenty hours. Average grain size was 100 μm.

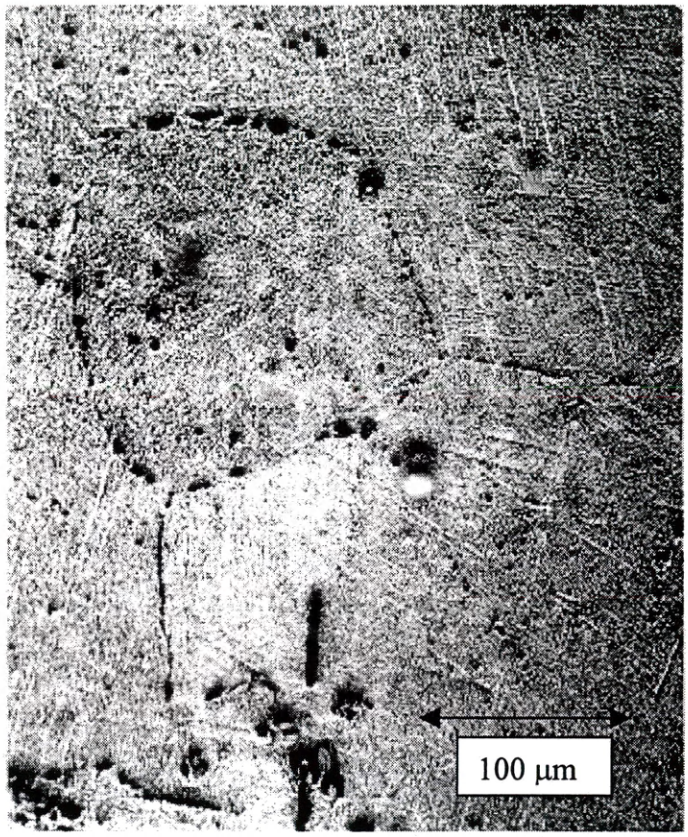

Figure 69: Photomicrograph of cerium-lanthanum alloy subjected to helium cooling through the two-phase $\gamma + \delta$ region at 60°C/min. Sample was homogenized at 546°C for thirty-six hours. Average grain size was 100 μm.



Figure 70: Photomicrograph of cerium-lanthanum alloy subjected to helium cooling through the two-phase $\gamma + \delta$ region at 60°C/min. Sample was homogenized at 585°C for four hours. Average grain size was 100 μm.

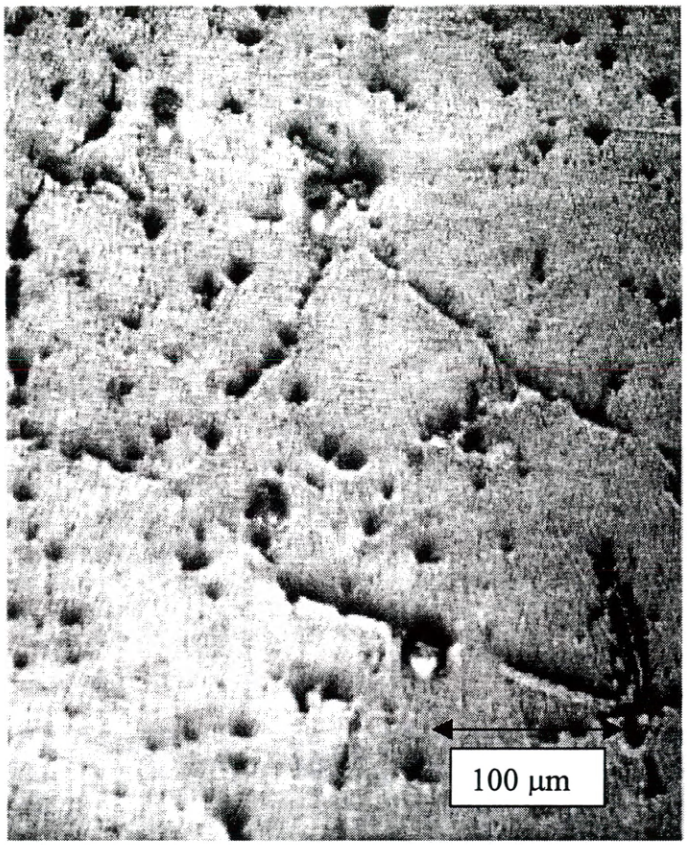

Figure 71: Photomicrograph of cerium-lanthanum alloy subjected to helium cooling through the two-phase $\gamma + \delta$ region at 60°C/min. Sample was homogenized at 585°C for eight hours. Average grain size was 100 μm.

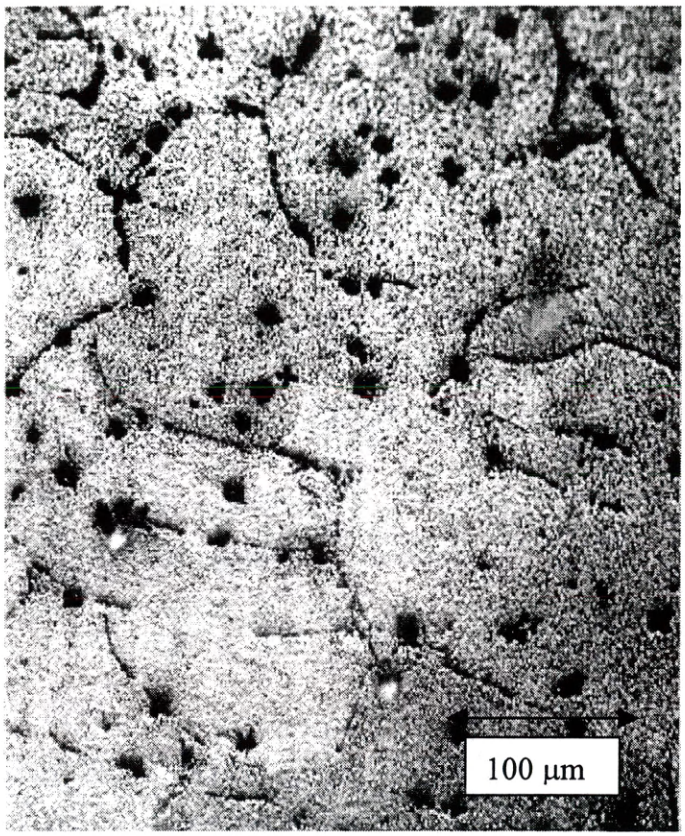

Figure 72: Photomicrograph of cerium-lanthanum alloy subjected to helium cooling through the two-phase $\gamma + \delta$ region at 60°C/min. Sample was homogenized at 585°C for twenty hours. Average grain size was 100 μm.

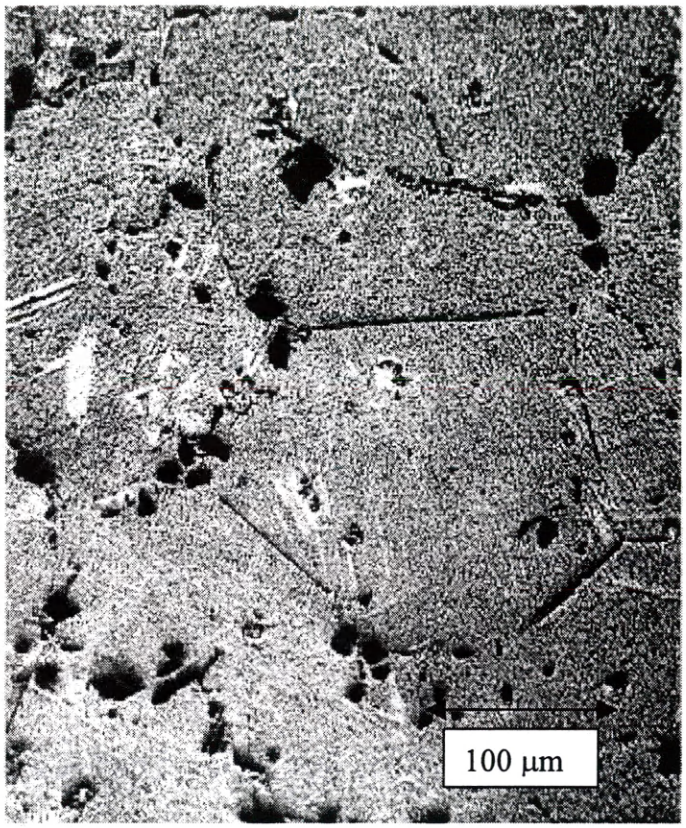

Figure 73: Photomicrograph of cerium-lanthanum alloy subjected to helium cooling through the two-phase $\gamma + \delta$ region at 60°C/min. Sample was homogenized at 633°C for four hours. Average grain size was 110 μm.

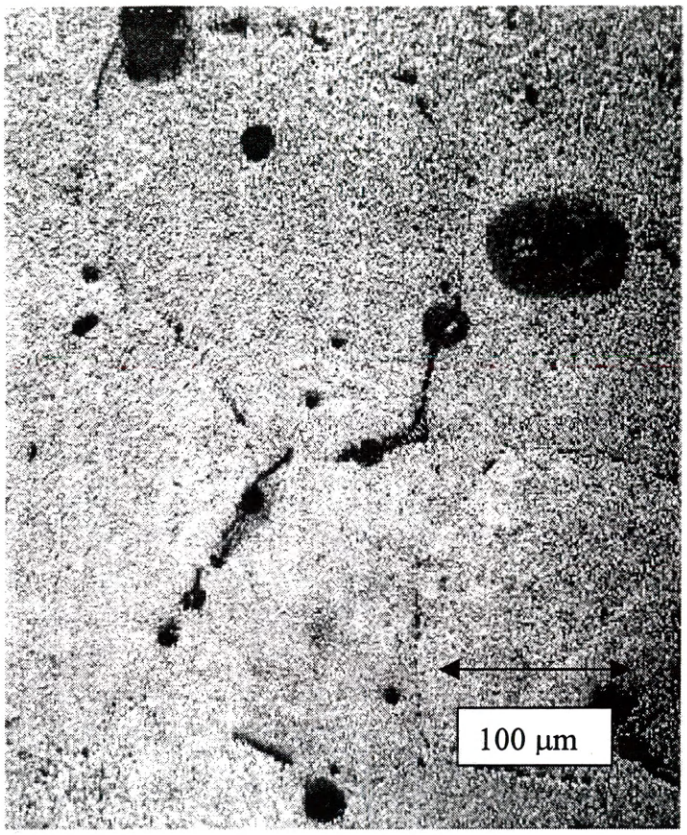

Figure 74: Photomicrograph of cerium-lanthanum alloy subjected to helium cooling through the two-phase $\gamma + \delta$ region at 60°C/min. Sample was homogenized at 633°C for eight hours. Average grain size was 115 μm.

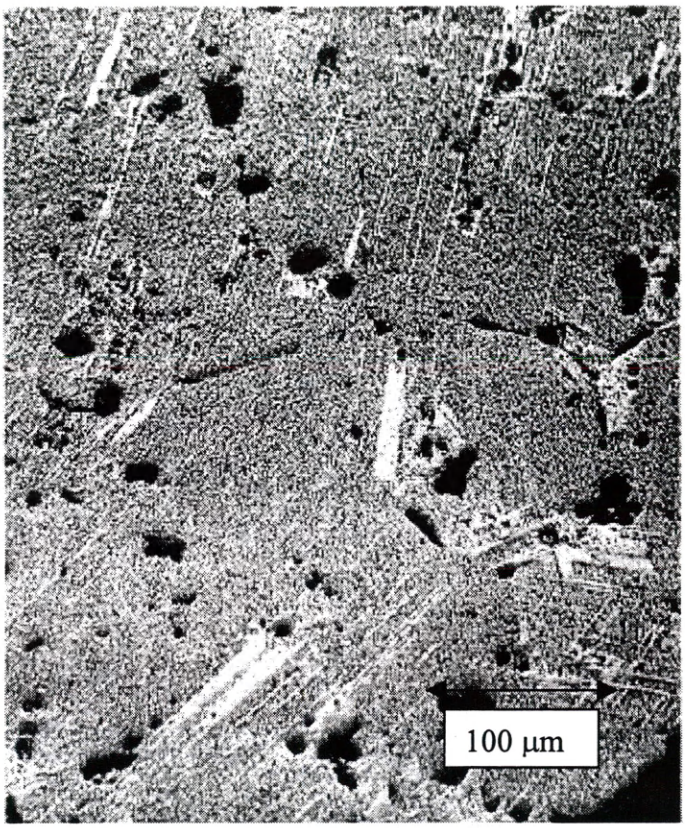

Figure 75: Photomicrograph of cerium-lanthanum alloy subjected to helium cooling through the two-phase $\gamma + \delta$ region at 60°C/min. Sample was homogenized at 633°C for twelve hours. Average grain size was 100 μm.

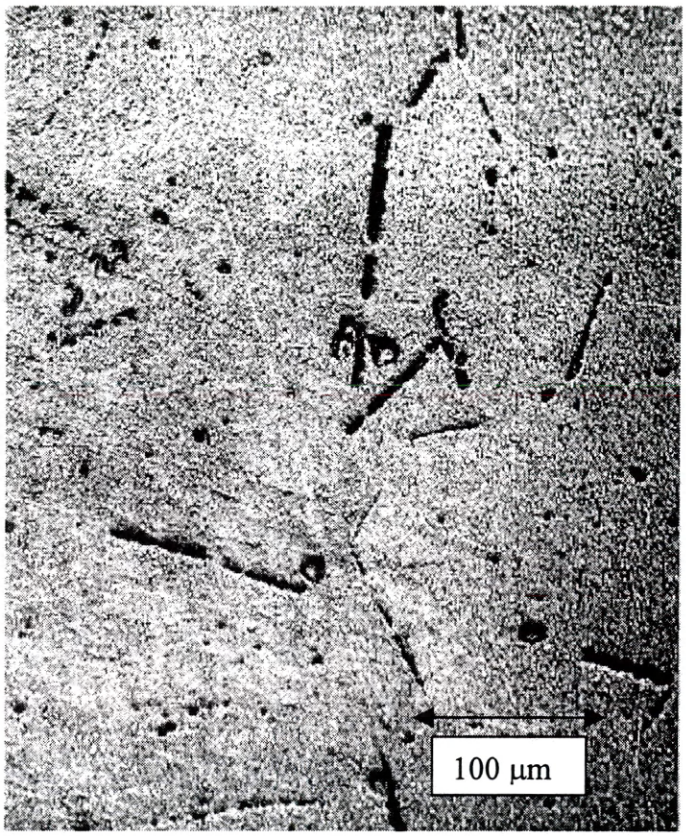

Figure 76: Photomicrograph of cerium-lanthanum alloy subjected to helium cooling through the two-phase $\gamma + \delta$ region at 60°C/min. Sample was homogenized at 633°C for twenty-four hours. Average grain size was 100 μm.

Similar to the results seen in the initial experimental work, microsegregation of lanthanum as a result of the δ to γ transformation was seen. The variation in the lanthanum concentration coincides with the approximate grain size indicated in the photomicrographs and was on average 0.5 wt. pct. prior to homogenization.

Homogenization Temperature - 546 °C

Variability in alloying during casting resulted in the four-hour specimen containing nominally 8.5 wt. pct. lanthanum. Additionally the twelve-hour specimen contained < 1 wt. pct. lanthanum and was not included in the data set as very little microsegregation was seen. The variation in the nominal lanthanum concentration of the four-hour specimen contributed to the variability in the determination of the activation energy for diffusion. The thirty-six-hour specimen showed the lanthanum to be fully homogenized.

Homogenization Temperature 585°C

Three samples were homogenized at 585°C for times of four hours, eight hours and twenty hours. Substantial homogenization appeared to occur in the four-hour specimen although microsegregation up to 0.3 wt. pct. occurred in the eight-hour specimen. The significant drop in lanthanum concentration in the eight-hour specimen at approximately 140 μm was attributed to a microstructural defect and not considered as

part of the microsegregation of lanthanum. The twenty-hour specimen showed the lanthanum to be fully homogenized.

Homogenization Temperature 633°C

Four specimens were homogenized at 633°C for times of four, eight, twelve, and twenty-four hours. Variability in the alloying resulted in a nominal concentration of lanthanum of 10.6 wt. pct. in the twelve- hour specimen. This variation predictably caused inaccuracy in the determination of the activation energy for diffusion. This alloy solidifies in the "broader" section of the $\gamma + \delta$ two-phase region resulting in a greater degree of microsegregation. The specimen heat treated for twenty-four hours resulted in complete lanthanum homogenization.

4.4 Determination of Activation Energy for Diffusion

As discussed earlier, Johnson [21] used the rate of homogenization as a way to determine the activation energy for diffusion in plutonium - 1 wt. pct. gallium and the same approach was used for cerium-lanthanum. The analytical development in Appendix A provides an atomistic basis for activation energy for diffusion and its relationship to the diffusion coefficient. The key equations are as follows:

$$D = D_o \exp [- Q / RT] \qquad (30)$$

$$Q = \Delta H_v + \Delta H_m \quad (31)$$

$$D_o = \gamma a_o{}^2 f \upsilon \exp [-\Delta S_m/R] \exp [-\Delta S_v/R] \quad (32)$$

The variable definitions are provided in the appendix.

Homogenization of lanthanum in the cerium - lanthanum alloys is controlled by diffusion of atoms via a vacancy mechanism. The lanthanum variation can be described by a sinusoid as shown in Figure 77 where the amplitude of the sine wave decreases as homogenization proceeds. The rate at which the amplitude of the sinusoidal variation decreases can be used to determine the activation energy for diffusion.

The general solution of Fick's Second Law of Diffusion that applies to the homogenization process is provided in Appendix D. A simplified form of this solution can be expressed:

$$C = C_{avg} + \beta_o \sin (\pi x/l) \exp (-\beta t) \quad (33)$$

where C is equal to the lanthanum concentration, C_{avg} is the nominal lanthanum concentration, β_o is the initial amplitude of the variation, x and l are defined in Figure 77, and β is related to the homogenization rate. This equation was manipulated by applying the natural logarithm to both sides resulting in the following equation:

$$\ln C = \ln C_{avg} + \ln (\beta_o \sin (\pi x/l)) - \beta t \quad (34)$$

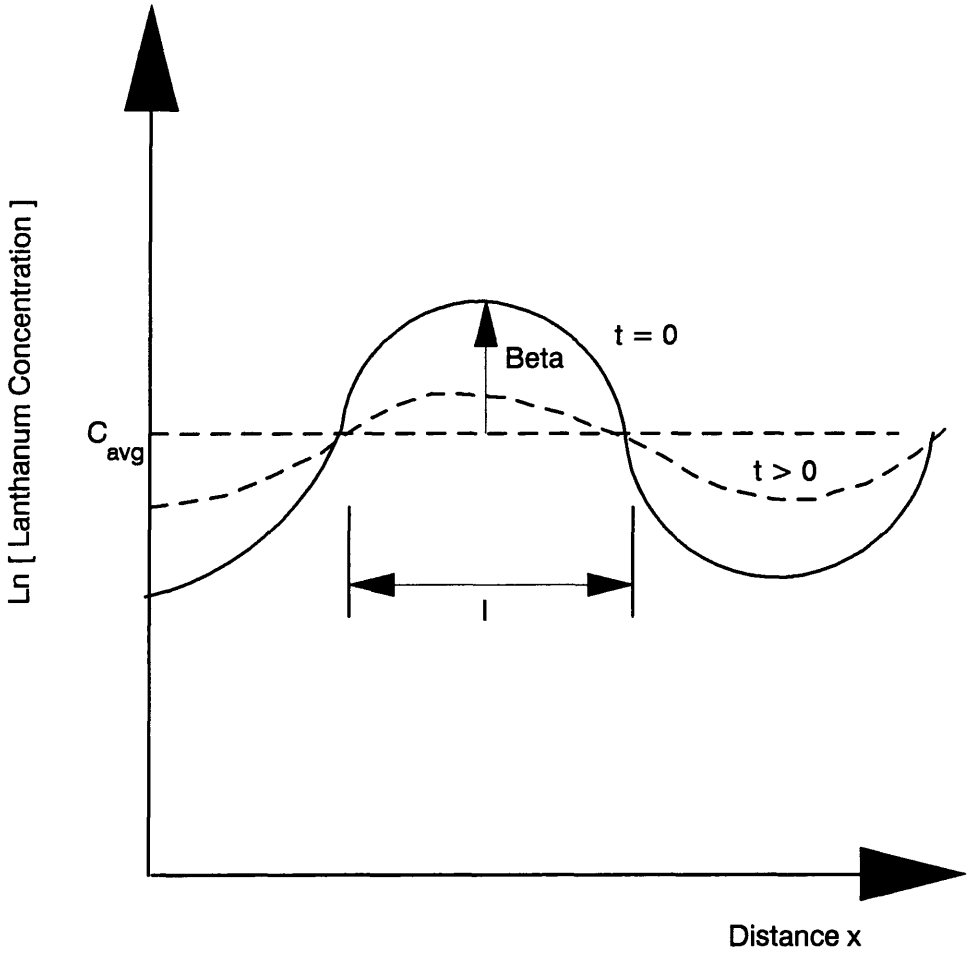

Figure 77: The effect of diffusion on a sinusoidal variation of the lanthanum composition [23].

Plotting the natural logarithm of the peak lanthanum concentration as a function of homogenization time results in the determination of β from the slope. Table XXX summarizes the lanthanum microsegregation data a function of time including an exponential regression analysis to determine the slope for each temperature. Figures 78, 79, and 80 contain plots of the data from Table XXX.

Given the rates of homogenization for each temperature as calculated from Figures 78, 79, and 80, an Arrhenius plot was developed relating the log of the homogenization rate to the reciprocal of the absolute temperature according to:

$$\text{Rate} = C \exp [-Q / RT] \qquad (35)$$

Table XXXI summarizes the rate data and Figure 81 contains the Arrhenius plot which resulted in the following equation describing the diffusion characteristics of this cerium-lanthanum alloy:

$$\text{Rate} = 5.6 \times 10^2 \exp [-30{,}200/RT] \qquad (36)$$

where R is the universal gas constant of 2 calories/mole and T is the absolute temperature in degress Kelvin.

Table XXX: Data showing the degree of microsegregation as a function of homogenization temperature and time. Initial variation in lanthanum prior to homogenization was shown to be 0.5 wt. pct. on average. Raw data is plotted in Figures 78, 79 and 80 with the exponential regression lines plotted according to the regression results shown.

Temperature (deg C)	**Homogenization Time (hours)**	**Lanthanum Microsegregation (wt. pct.)**	**Regression Results Exponential fit**
546 (819K)	0	0.5	Slope = -4.23 E-06 Intercept = -0.911
546 (819K)	4	0.3	
546 (819K)	20	0.27	
546 (819K)	36	0.25	
585 (858K)	0	0.5	Slope = -1.94 E-05 Intercept = -0.995
585 (858K)	4	0.2	
585 (858K)	8	0.2	
585 (858K)	20	0.1	
633 (906K)	0	0.5	Slope = -2.55 E-05 Intercept = -0.863
633 (906K)	4	0.36	
633 (906K)	8	0.1	
633 (906K)	12	0.18	
633 (906K)	24	0.05	

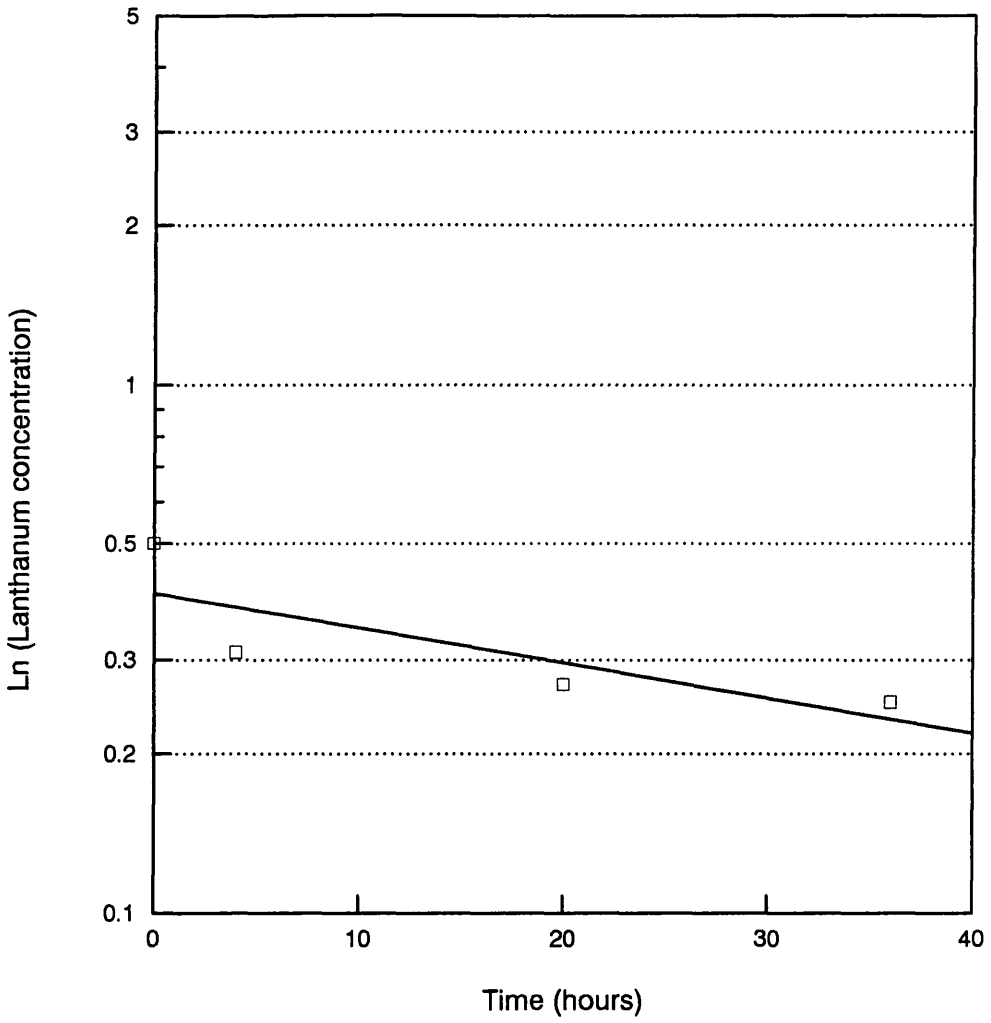

Figure 78: The natural log of the lanthanum concentration variation is plotted as a function of homogenization time. Homogenization temperature was 546 C. The exponential regression parameters are listed in Table XXX. The degree of microsegregation was determined by averaging the profile peaks taken from the electron microprobe peaks.

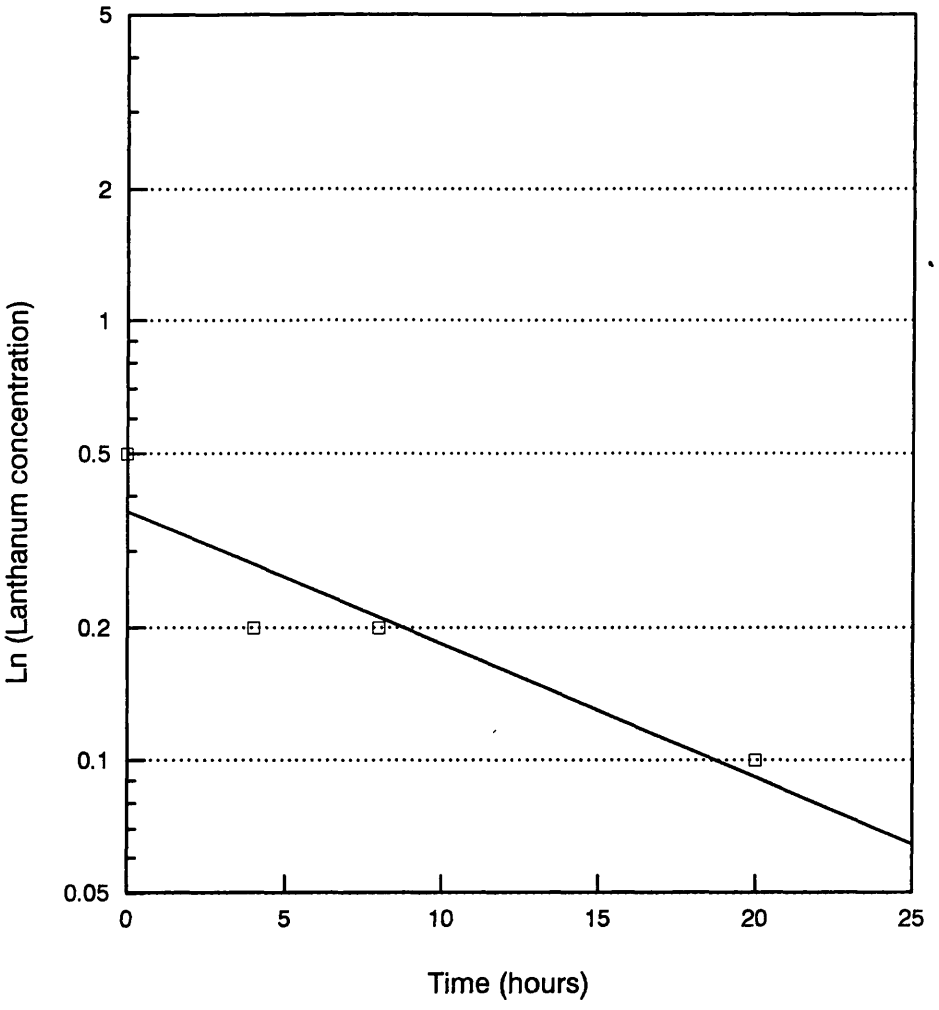

Figure 79: The natural log of the lanthanum concentration variation is plotted as a function of homogenization time. Homogenization temperature was 585 C. The exponential regression parameters are listed in Table XXX. The degree of microsegregation was determined by averaging the profile peaks taken from the electron microprobe peaks.

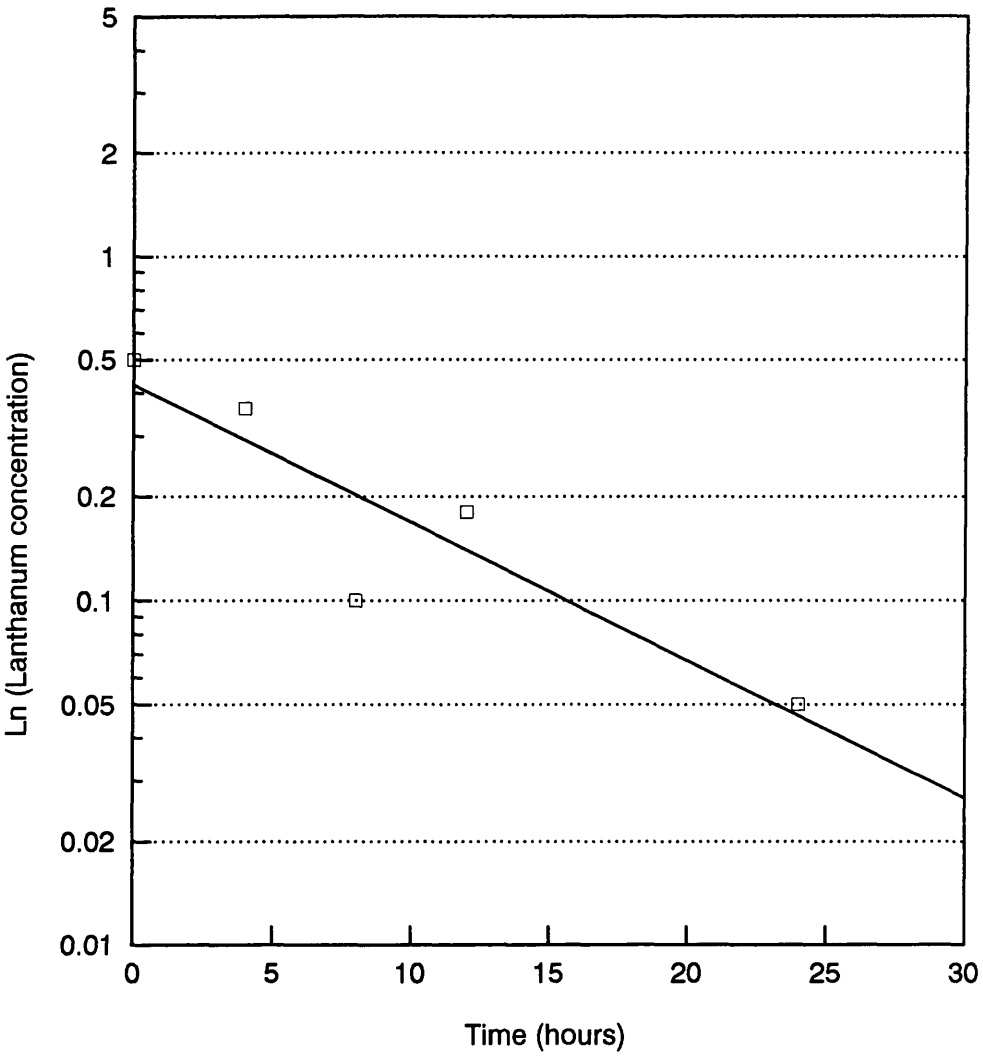

Figure 80: The natural log of the lanthanum concentration variation is plotted as a function of homogenization time. Homogenization temperature was 633 C. The exponential regression parameters are listed in Table XXX. The degree of microsegregation was determined by averaging the profile peaks taken from the electron microprobe peaks.

Table XXXI: Homogenization rate data used to determine the activation energy for diffusion as plotted in Figure 81. Regression data is also shown.

Homogenization Temperature (deg C)	**Reciprocal Temperature (deg K^{-1})**	**Homogenization Rate (wt. pct. La / sec)**	**Regression Analysis**
546 (819K)	1.22E-03	4.23E-06	Slope = -15100
585 (858K)	1.17E-03	1.94E-05	Q = 30200 cal/mole
633(906K)	1.1E-03	2.55E-05	Intercept = 6.3

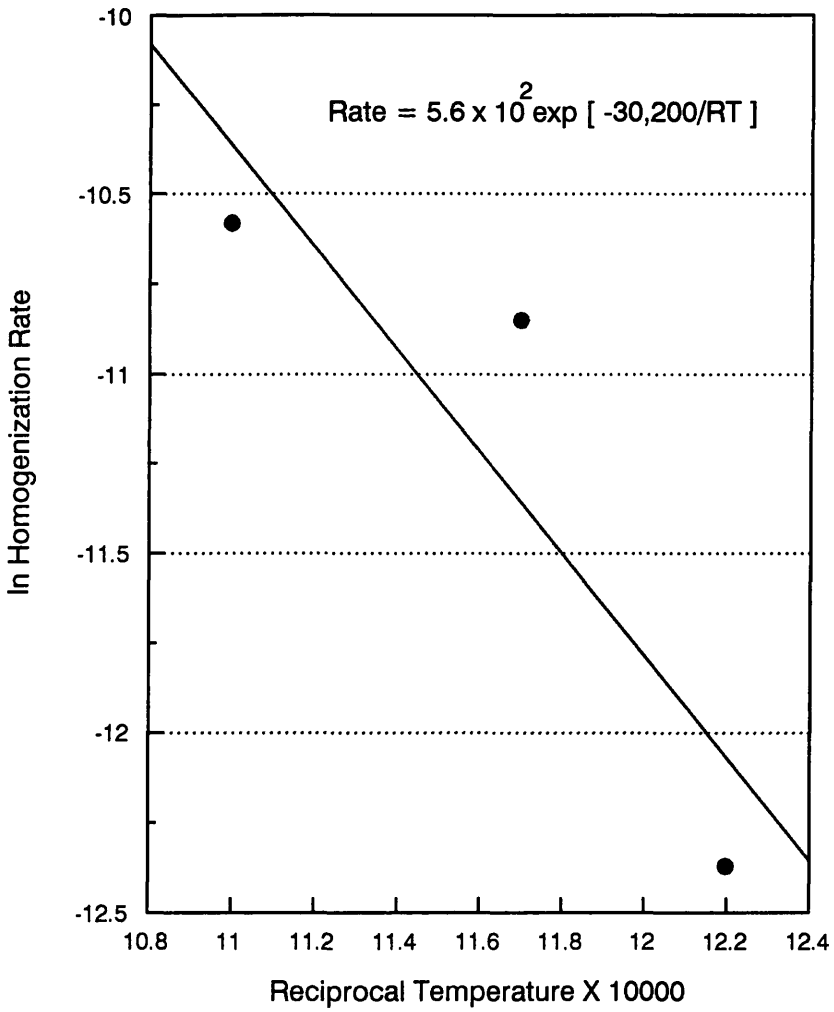

Figure 81: Plot used to determine the activation energy for diffusion utilitizing the rate of homogenization The rate equation is shown above based on a regression analysis. The correlation factor (R^2) was 0.8.

The activation energy is somewhat lower than expected for the diffusion of lanthanum and cerium. The variability in the microprobe data combined with the experimental approach using the rate of homogenization can result in variability in the activation energy determination. The determination of diffusion parameters is difficult in the best experimental conditions, but as discussed earlier both cerium and plutonium exhibit unusual behavior.

Some insight into the difficulty in sorting out the diffusion mechanisms particularly in cerium is provided by its negative activation volume (-0.17) [26]. The activation volume is related to the free energy of formation of a vacancy, ΔG_v, and the free energy associated with activated complexes, ΔG_m, via the fundamental thermodynamic relationship:

$$(dG / dP)_T = V \qquad (37)$$

Using the atomistic development for the diffusion coefficient and activation energy in Appendix A, the free energies, ΔG_v and ΔG_m , are related to the diffusion coefficient as follows:

$$D = a_o^2 \nu \exp(-\Delta G_v/RT) \exp(-\Delta G_m/RT) \qquad (38)$$

This leads to the following relationship:

$$[\, d\ln (D/a_o^2\, \nu) / dP \,]_T = -(1/RT)\,[\, (dG_v/dP)_T + (dG_m/dP)_T \,] \quad (39)$$

$$= -(1/RT)\,[\, V_v + V_m \,] \quad (40)$$

$$= -V_{SD} / RT \quad (41)$$

where, V_{SD} is the activation volume. V_v is the partial molar volume of the vacancies and its magnitude depends on the degree to which atoms surrounding a vacancy relax into it. V_m is the partial molar volume of activated complexes which is a measure of the volume of activated complex at a saddle point between atoms. Generally, the activation volume for metals is positive whereby an increase in pressure would lower the diffusion coefficient. This behavior is due to a decrease in the number of vacancies that is the key for vacancy-mechanism diffusion. The significance of the negative activation volume for cerium is that it suggests an alternative mechanism to vacancy diffusion (presumably leading to a lower activation energy). While the experimental method employed in this work is prone to some variability, the negative activation volume in cerium, perhaps related to the "ragged-edge" itineracy of its 4f electron, indicates that a lower activation energy may be expected. Fundamental conclusions regarding the mechanisms of diffusion in cerium-lanthanum will require further measurements. The rate equation

measured from this work does provide an initial step in relating the diffusion characteristics between plutonium and the surrogate which was the original objective of this work.

Variability in diffusion measurements is also seen with plutonium alloys that exhibit many of the same characteristics as cerium. One example includes the measurement of the interdiffusion coefficient for the plutonium - 6 at. pct. aluminum alloy by Tate and Edwards [45]. The plutonium - aluminum phase diagram is virtually identical to the plutonium-gallium phase diagram and solid state microsegregation of aluminum occurs in a similar fashion upon cooling. The activation energy for diffusion was expected to be similar (Q = 37,500 cal/mole) but was measured at 25,500 cal/mole using an identical technique as that reported earlier for plutonium-gallium. Several thermodynamic and electronic based theories were investigated to explain the difference, but no definitive reason was identified.

The overriding objective of this work was to identify a fundamental connection between plutonium - gallium and a surrogate material using the homogenization data as an initial link. Cerium - 5 wt. pct. lanthanum was proven as a homogenization surrogate with the opportunity to develop an analytical relationship between the two alloys tested. While the variability of the determination of the activation energy can be attributed partially to the experimental approach, the value of 30,200 calories/mole is reasonable given the unusual behavior seen in cerium and plutonium.

4.5 Surrogate Relationship

The determination of the activation energy for diffusion in the cerium-lanthanum alloy presents an opportunity to relate the two systems such that a diffusion rate in the plutonium alloy can be analytically related to the same rate in the cerium alloy. A homogenization temperature used in the surrogate can be directly related to a temperature in the plutonium system that represents the identical diffusion rate. The analytical development begins by identifying a proportionality constant to relate the two activation energies for diffusion:

$$Q_{Pu\text{-}Ga} = \beta Q_{Ce\text{-}La} \qquad (42)$$

Given the activation energies for plutonium - 1 wt. pct. gallium and cerium - 5 wt. pct. lanthanum of 38,000 cal/mole and 30,200 cal/mole, the proportionality constant is 1.3. Using this proportionality constant and a Larson-Miller [46], analytical development as described in Appendix E, the two alloys can be related. The first step is to equate the rate expressions from equation 35 for each alloy to determine the temperature in each system at which homogenization occurs at the same rate:

$$Rate_{Pu\text{-}Ga} = C_{Pu\text{-}Ga} * \exp\left[-Q_{Pu\text{-}Ga}/RT_{Pu} \right] = Rate_{Ce\text{-}La} = C_{Ce\text{-}La} \exp\left[Q_{Ce\text{-}La}/RT_{Ce} \right] \qquad (43)$$

Taking the natural log of both sides:

$$\ln [C_{Pu-Ga}] - Q_{Pu-Ga}/RT_{Pu} = \ln [C_{Ce-La}] - Q_{Ce-La}/RT_{Ce} \quad (44)$$

$$R [\ln C_{Pu-Ga} - \ln C_{Ce-La}] = [Q_{Pu-Ga}/T_{Pu} - Q_{Ce-La}/T_{Ce}] \quad (45)$$

Solving for T_{Ce}

$$Q_{Ce-La} / T_{Ce} = Q_{Pu-Ga} / T_{Pu} - R [\ln C_{Pu-Ga} - \ln C_{Ce-La}] \quad (46)$$

$$Q_{Ce-La} / T_{Ce} = [Q_{Pu-Ga} - T_{Pu} R [\ln C_{Pu-Ga} - \ln C_{Ce-La}]] / T_{Pu} \quad (47)$$

$$T_{Ce} = Q_{Ce-La} T_{Pu} / [Q_{Pu-Ga} + R T_{Pu} [\ln C_{Ce-La} - \ln C_{Pu-Ga}]] \quad (48)$$

This equation can be used then to determine the homogenization temperature in the cerium-lanthanum alloy at which the same homogenization rate would be expected in the plutonium-gallium alloy. Table XXXII contains the predicted cerium-lanthanum homogenization temperature for a given set of conditions in the plutonium gallium system. Figure 82 contains a plot of this data to graphically relate the homogenization rates between the two alloys.

Table XXXII: Predicted homogenization temperatures for a cerium - 5 wt. pct. lanthanum alloy to be used as a surrogate for a plutonium - 1 wt. pct. gallium alloy.

Homogenization Temperature Plutonium - 1 wt. pct. Gallium		Homogenization Temperature Cerium - 5 wt. pct. Lanthanum	
Degrees C	**Degrees K**	**Degrees C**	**Degrees K**
350	623	140	413
360	633	145	418
370	643	151	424
380	653	156	429
390	663	162	435
400	673	167	440
410	683	173	446
420	693	178	451
430	703	183	456
440	713	189	462
450	723	194	467
460	733	199	472
470	743	204	477
480	753	209	482
490	763	215	488
500	773	220	493
510	783	225	498
520	793	230	503
530	803	235	508

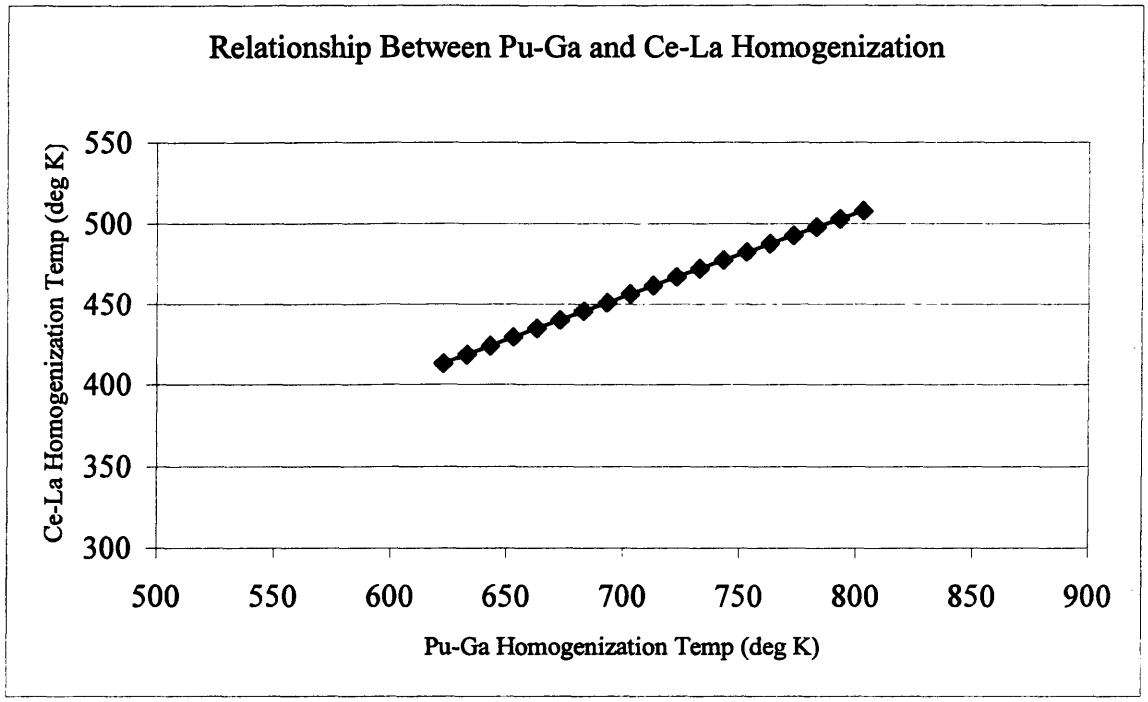

Figure 82: Relationship between the plutonium - 1 wt. pct. gallium alloy and cerium - 5 wt. pct. lanthanum alloy for an equivalent homogenization rate as detailed in the text.

Using the Larson-Miller development from Appendix E, Table XXXIII was constructed to illustrate how a homogenization time and temperature for the plutonium - 1 wt. pct. gallium alloy can be related to a homogenization time and temperature for a cerium - lanthanum alloy. The analytical relationship between the two systems is as follows:

$$\ln t_{Ce} = \ln t_o + T_{Pu} / \beta T_{Ce} [\ln t_{Pu} - \ln t_o] \qquad (49)$$

where the variables are defined in Appendix E.

4.6 Phase Transformations in Cerium

The fundamental ties between cerium and plutonium that have been developed suggest that the phase transformation behavior in cerium is similar to that seen in plutonium. A summary of the phase transformation in cerium is provided to establish a basis for comparison to plutonium [26].

The specific study of the phase transformations in cerium is difficult due to large hysteresis effects with a variation in temperature or pressure. The kinetics of the transformations are sluggish and generally do not go to completion which makes mechanisms difficult to sort out. Tables XXXIV and XXXV provide crystal structures and transformation temperatures for each of the cerium phases. Figure 83 [26] shows the equilibrium phase diagram for cerium showing the multiple phases and the relative

Table XXXIII: Determination of equivalent cerium - 5 wt. pct. lanthanum homogenization parameters for homogenization times and temperatures for the plutonium- 1 wt. pct. gallium alloy.

Plutonium Temperature (deg K)	Plutonium Homogenization Time (hours)	Cerium Temperature (deg K)	Cerium Homogenization Time (hours)
693	12	498	209.6
693	12	523	26.2
693	12	548	4.0
693	12	573	0.7
703	12	498	392.4
703	12	523	47.7
703	12	548	7.0
703	12	573	1.2
693	8	498	135.8
693	8	523	17.4
693	8	548	2.7
693	8	573	0.5
703	8	498	252.7
703	8	523	31.4
703	8	548	4.7
703	8	573	0.8

Table XXXIV: Crystal structures and lattice data for cerium phases.

Phase	Crystal Structure	Lattice Parameters (Å)			Conditions		Metallic Radius (Å)	Atomic Volume ($Å^3$)
		a	b	c	Temp (K)	Pressure GPa		
α'	c-centered orthorhombic	3.049	5.998	5.215	298	5.8	1.615	23.84
α	fcc	4.824 4.85			298 77	0.81 0	1.706 1.71	28.06 28.5
β	dhcp	3.6810	11.857		298	0	1.8321	34.784
γ	fcc	5.1610			298	0	1.8245	34.367
δ	bcc	4.11			1041	0	1.83	34.7

Table XXXV: Phase transformation temperatures for cerium.

Transformation	Temperature		Pressure	Comments
	deg K	deg C		
$\alpha \rightarrow \beta$	96	-177	Atmospheric	pseudo-equilibrium
$\beta \rightarrow \gamma$	326	53	Atmospheric	pseudo-equilibrium
$\gamma \rightarrow \delta$	999	726	Atmospheric	Equilibrium
$\delta \rightarrow L$	1071	798	Atmospheric	Equilibrium
$\alpha \rightarrow \gamma$	141	-132	Atmospheric	Metastable, pseudo-equilibrium

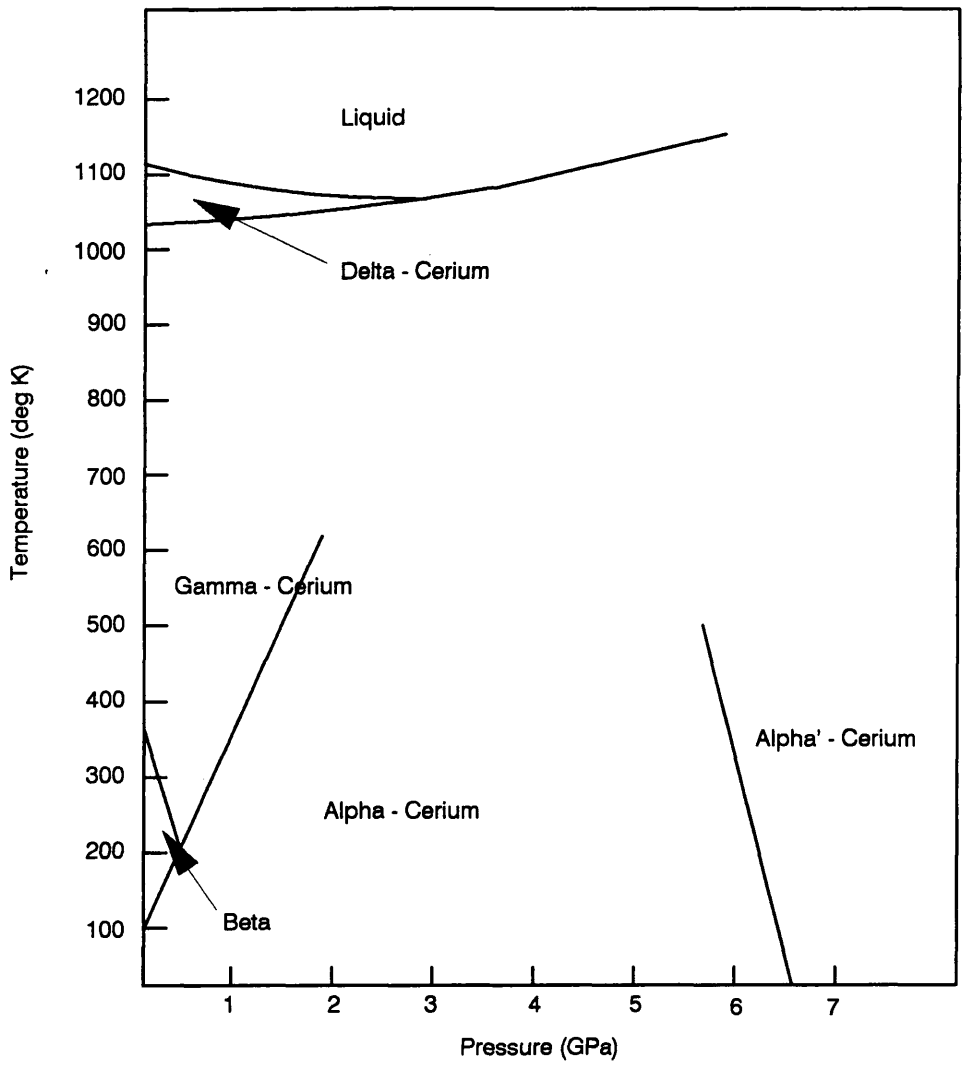

Figure 83: Pseudo - equilibrium pressure - temperature diagram for cerium. Cerium is the only material known to exhibit a solid-solid critical point (C.P.).

sensitivity to pressure of the transformations. Cerium is the only known material to exhibit a solid-solid critical point. As mentioned, the phase transformations in cerium exhibit large hysteresis effects and the non-equilibrium phase diagram in Figure 84 [26] is a better description of the behavior.

The phase transformation behavior of cerium upon cooling was described schematically by Spedding and Daane as shown in Figure 85 [47]. When γ - cerium is cooled, the β-phase begins to form at 263°K. β - cerium is hexagonal and continues to form until 103°K when α-cerium begins to form from the remaining γ - cerium. The $\gamma \Rightarrow \beta$ transformation does not occur isothermally, and forms optimally between 263 and 230°K. The amount of β - cerium formed depends on the cooling rate and impurities and on the previous history of the specimen (e.g., thermal history and cold work). It is possible to form α - cerium directly from γ - cerium and with proper thermal cycling and cold work, a specimen can be produced which contains only α - cerium. Experimenters have been unable to cool bulk cerium specimens quickly enough to avoid the formation of the β phase. Upon warming, the α phase transforms back to β and γ and at room temperature the sample will consist of two phases, β and γ. Conversion back to single phase γ - cerium requires heating the sample to above 500°K. A more detailed discussion of the specific transformations follows.

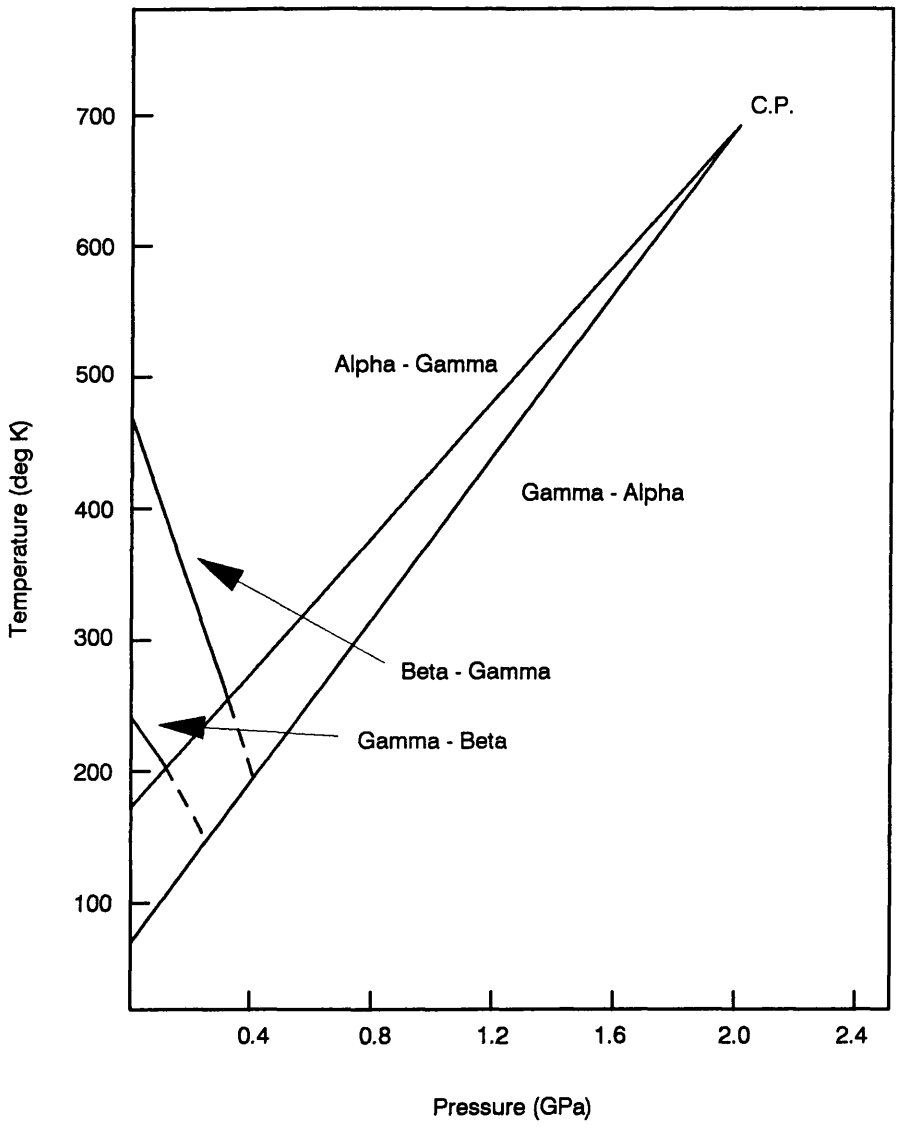

Figure 84: The non-equilibrium phase diagram for cerium. Results were averaged based on several studies. The significant hysteresis effects are shown on the diagram [47].

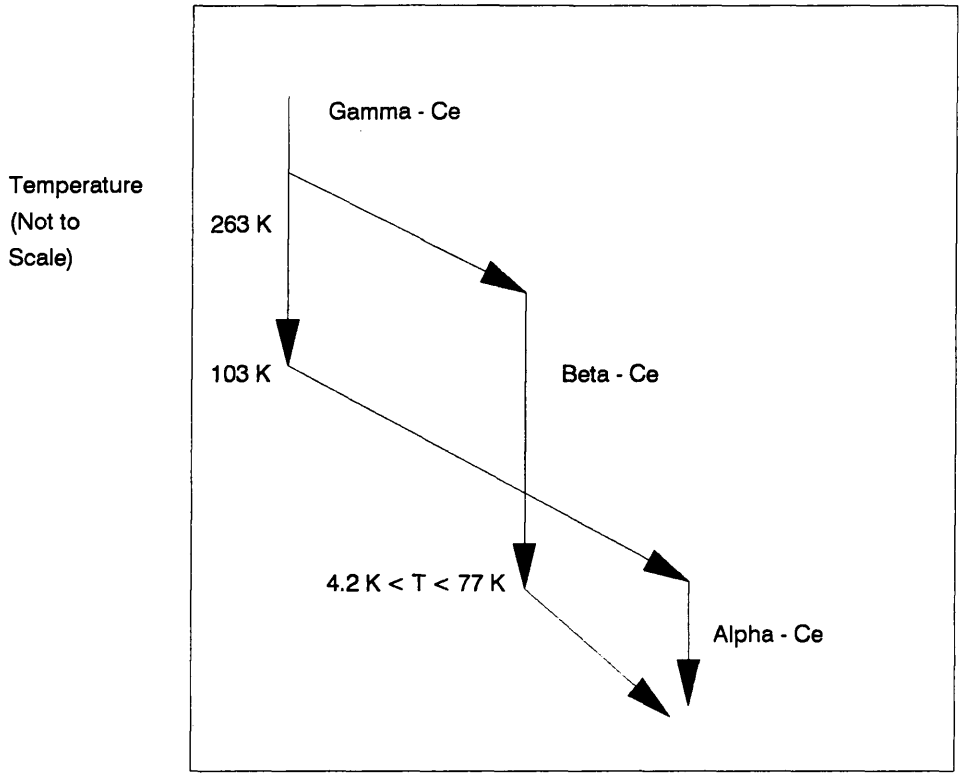

Figure 85: Schematic diagram showing the behaviour of cerium upon cooling [47].

β⇔γ Transformation

The transformations of γ-Ce to β-Ce is reported to be martensitic [26,47]. The M_s temperature is affected by overall purity and grain size with the amount of β-Ce formed dependent on the following:

- Cooling rate
- Temperature to which sample is cooled
- Number of thermal cycles between liquid nitrogen (77K) and room temperature.

A shear mechanism for this transformation has been theorized via dislocation glide along A/6<112> on close packed planes (111). Accordingly, plastic deformation can induce the transformation by promoting the crystallographic shear process. Limited studies have been performed on the β→γ transformation which apparently proceeds by dislocation glide on the 0001 planes in the <1010> directions. The transformation is pressure sensitive (i.e., as pressure increases the A_s decreases) and purity sensitive.

γ⇔α Transformation

The γ→α phase transformation does not involve a change in crystal structure, rather a significant volume reduction of approximately 17 pct. The mechanism of the transformation is not well characterized, but the volume collapse is seen to occur randomly with no apparent interaction between transformed and un-transformed areas.

Given the dramatic volume change it follows that the transformation is pressure dependent.

Two general theories are proposed to explain the large volume collapse associated with this transformation. The first theory suggests that the localized 4f electrons are promoted to the $(5d6s)^3$ conduction band in α-Ce. Zachariasen and Pauling [26] suggested that when the 4f electron was promoted, the valence electrons were no longer shielded from the nucleus and the result was a volume collapse. Two models, Coqblin-Blandin and Ramirez-Falicov were proposed to describe the 4f-electron promotion. The second theory states that the 4f electronic state itself becomes de-localized via a Mott transition or by a type of hybridization mechanism. The de-localization of the 4f state appears to be supported by positron annihilation results. Positron lifetimes in a metal can be directly correlated to the number of conduction electrons and results indicate that there is little or no change in positron lifetimes between α and γ cerium. This result would support the de-localization theory rather that an electron transfer mechanism.

<u>β→α Transformation</u>

The β→α transformation is believed to occur via a shear mechanism producing a fcc lattice from a dhcp lattice. To accommodate the large volume change, (~17 pct.) β is believed to first transform to γ and then to α.

Other phase transformations

Ellinger and Zachariasen [26] observed a high-pressure phase of cerium (α'') which possesses a body-centered-monoclinic crystal structure. This phase exists at pressures in excess of 6 GPa and is metastable.

4.7 Metallurgical Surrogate

Cerium-lanthanum has been shown to exhibit solid state microsegregation similar to that seen in the plutonium - 1 wt. pct. gallium alloy. Using the relatively extensive diffusion data for the plutonium - 1 wt. pct. gallium alloy, a direct analytical relationship was developed such that a homogenization surrogate was established. This link between the two systems immediately provides an alternative material to conduct further homogenization studies without the radiological risks posed by plutonium. Furthermore, this grounding point established between plutonium-gallium and cerium-lanthanum is a first step in justifying the use of cerium as a metallurgical surrogate for plutonium. The following discussion highlights the metallurgical similarities between the two systems beginning with general correlations in diffusion, phase transformations, and general properties ending with two detailed case studies where cerium-lanthanum could be used as a metallurgical surrogate.

Diffusion related comparisons between plutonium-gallium alloys and rare-earth materials have been made [2]. Erfurdt [2] summarized the work by Dariel in an

investigation of ultra-fast diffusion of iron in rare-earth solutes. Dariel measured the diffusivity of a radioactive tracer ^{59}Fe in the light rare-earth metals cerium, praseodymium, and neodymium. Rapid diffusion rates were documented with activation energies ranging between 7.7 and 13.6 kcal/mole. Dariel observed that self-diffusion in the rare-earth close packed structures take place by means of the regular vacancy mechanism. Whereas, in the bcc phases diffusion results are unusually fast. Further, he observed that the striking feature common to the diffusivities of iron in all three rare-earth metals is their extremely high values (characteristic of diffusion in liquids). Based on the results of his work, he concluded that the lowest activation energies and highest diffusivities of metallic solutes are found in those systems in which the solvent is a metal which has a bcc allotropic phase and the solute is either a noble metal or transition element of the first long period. In addition, he observed that contrary to self-diffusion behavior, the diffusivities of iron are only slightly or not affected by the phase transformation occurring in the solvent rare-earth matrices.

Erfurdt [2] showed enhanced diffusion of iron in plutonium - 1 wt. pct. gallium which contributed to the more rapid homogenization of a cored microstructure. He attributed this behavior to an interstitialcy mechanism promoted by the presence of iron atoms. A "solubility in solvent interstitial sites" has been suggested for ultra-fast diffusion of iron in rare-earth matrices. As discussed earlier, another mechanism was proposed by Lograsso and Helawell [30] involving a re-melting, or metatectic type transformation which leads to enhanced iron diffusion. Interestingly, the plutonium- iron

phase diagram and the cerium-iron phase diagram are similar in that iron is not appreciably soluble in either material and both form a eutectic that forms at a significantly lower temperature (410°C for plutonium and 640°C for cerium). While the mechanisms for enhanced iron diffusion can be debated the results are similar in both the plutonium and cerium matrices. This result offers additional justification for the use of cerium as a metallurgical surrogate for plutonium in the study of impurity diffusion and the impacts of the impurities on homogenization rates.

Comparisons between the crystal structures of plutonium and cerium have been drawn and there are definite similarities between the two materials. Generally, the low temperature phase transformations proceed via a shear type mechanism that is affected in a similar fashion by cooling rate, impurities, and thermal cycling. The impact of the de-localization of the 5f electron (plutonium) and 4f electron (cerium) states with the application of temperature and pressure is comparable. The change in the electronic structure manifests itself in large volume changes between phases (β-α in plutonium and γ-α in cerium) and in the formation of non-symmetrical structures (α-plutonium and α"-cerium are both monoclinic). The correlations in electronic structure, diffusion relationships, and phase transformation mechanisms, provide a basis to explore other important issues such as crystallographic relationships between phases or the impact of impurities on phase transformation behavior. These issues represent a subset of the potential for studies of the plutonium manufacturing processes including rolling, forming, machining or joining.

In addition to diffusion and phase transformation similarities, cerium has similar room temperature tensile properties to those values reported for homogenized plutonium - 1 wt. pct. gallium. The as-cast 0.2 pct.-offset yield strength of cerium is reported as 91 MPA The ultimate tensile strength is reported to be 103 MPA and percent elongation reported as 24 pct.[47]. The as-cast 0.2 pct.-offset yield strength for the plutonium -1 wt. pct. gallium alloy is reported as 79 MPA. The ultimate tensile strength is reported as 128 MPA with the percent elongation reported as 25 pct.[18]. Further, the oxidation of cerium is nearly equivalent to the oxidation of α-phase plutonium, which provides an opportunity to study important storage, handling and fire safety issues.

4.8 Case Studies

A direct link between cerium - 5 wt. pct. lanthanum and plutonium - 1 wt. pct. gallium has been established using the homogenization process to relate the activation energies for diffusion. Several correlations between the behavior of plutonium and cerium have been made justifying the use of cerium as a metallurgical surrogate for plutonium. Two issues of metallurgical importance have been identified to demonstrate how cerium would be used as a surrogate to investigate the behavior of plutonium. These issues are presented in the form of case studies.

Fixture Annealing

Homogenization is a key step in the processing of plutonium - 1 wt. pct. gallium alloys and the identification of cerium - 5 wt. pct. lanthanum as a homogenization surrogate provides a useful tool. An important process step that is presently being studied is the homogenization of a cast product in a optimally designed fixture which will utilize the phenomenon of creep to achieve near-net shape dimensions prior to machining. In this case, a cast product is homogenized as before, but creep is used to simultaneously produce the optimum casting dimensions for subsequent machining. As outlined in Appendix F, creep can be directly related to the activation energy of diffusion making this case an attractive application for the cerium surrogate.

$$\dot{\varepsilon} = (\rho)\,(b)\,(\text{constant})\,(\sigma/\mu)^n \exp[-Q/kT]\sinh(\sigma bA/kT) \qquad (50)$$

It should be noted that the homogenization of the cerium - 5 wt. pct. lanthanum alloy involves the interdiffusion coefficient as determined in this work, but the creep would involve the self-diffusion coefficient for cerium.

Implementation of the cerium surrogate in this process development, would involve replacement of plutonium in the casting process with the cerium - 5 wt. pct. lanthanum alloy using the same mold materials and adjusting for the higher melting temperature of cerium. The casting parameters would be modified to ensure a sufficient cooling rate (60°C/min minimum) to induce coring in the cerium-lanthanum alloy. The

cast shape would then be placed into a machined fixture (e.g., graphite) possessing the desired dimensions for the final product. The appropriate annealing temperature would then be identified using the interdiffusion coefficient measured in this work for homogenization and the published self-diffusion coefficient for cerium to ensure sufficient dimensional movement to "creep" the component into the desired dimensions. Given the similar mechanical properties, the cerium-lanthanum alloy could be machined in the same fixtures designed for plutonium and the associated behavior could be studied. This example provides a viable application for the development of a key process step utilizing the cerium-lanthanum homogenization surrogate and taking advantage of the similar properties of plutonium and cerium.

Effect of Pressure on the Stabilization of the α-Phase

The effects of temperature and pressure on the stability of α-phase plutonium is important in the processing of plutonium. As shown in Figures 86 and 87 [47,48], the α-phases of plutonium and cerium have similar relationships with pressure and temperature and as discussed earlier each have been attributed to the "ragged-edge" itineracy of the 5f and 4f electrons respectively. This correlation provides an opportunity for the use of the cerium metallurgical surrogate to study the behavior of plutonium. Specifically, the impact of impurities such as carbon, iron, and nickel on the pressure/temperature relationship is an area of interest that presently requires further study. The impact of these impurities can be studied by alloying with cerium and studying the change in the

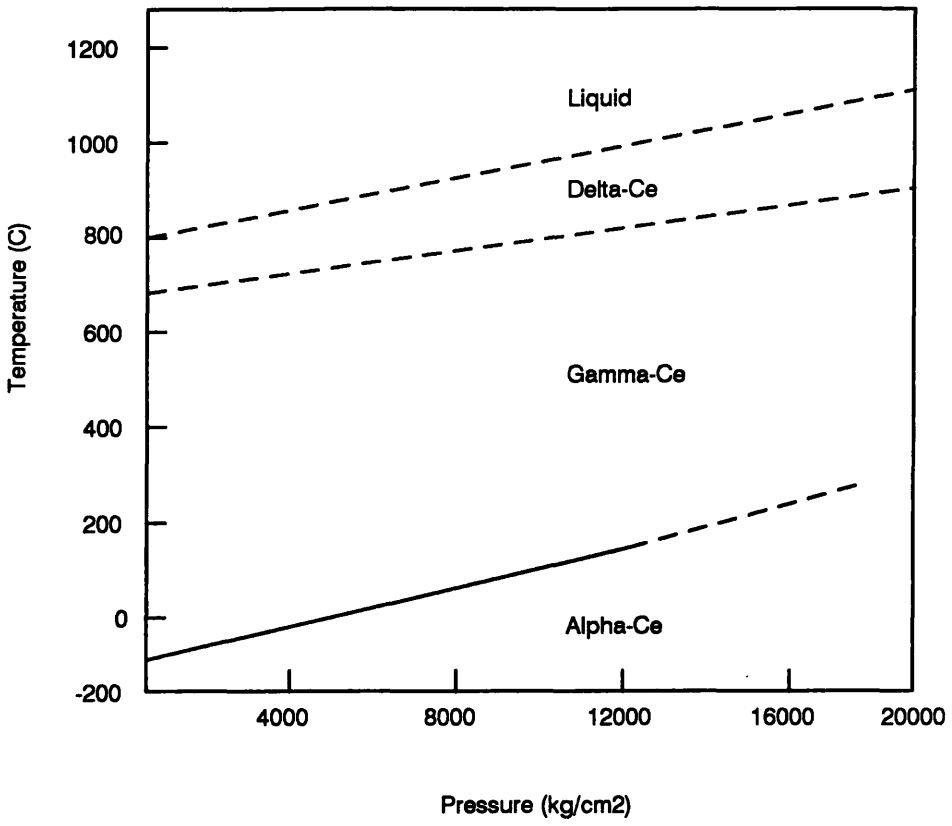

Figure 86: Proposed cerium temperature-pressure diagram [48]

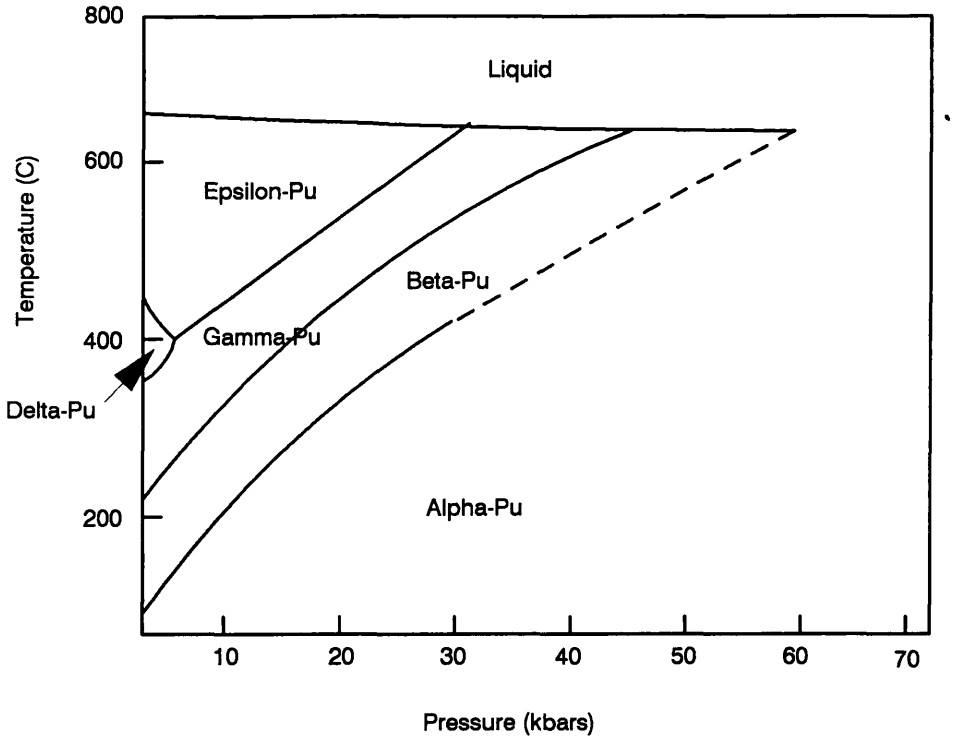

Figure 87: Temperature-pressure diagram for plutonium [48].

relationship of Figure 87 and relating it to the changes in plutonium. As discussed above, iron affects the rate of homogenization of plutonium - 1 wt. pct. gallium alloys and is expected to affect the stability of the alpha phase. This effect is important in the determination of plutonium material impurity specifications for the long-term stewardship of plutonium components in the weapons stockpile.

Cerium as a Analytical Model Verification Tool

Recently, extensive efforts have been initiated to analytically model the behavior of plutonium in manufacturing and related applications such as casting, rolling, or welding [49]. These models involve numerical techniques to solve differential equations such as finite element analysis each of which require accurate description of the material behavior of plutonium. The ability to verify modeling predictions through the use of a surrogate such as cerium provides a vital tool. Coupling the cerium surrogate with the use of analytical models further reduces the need to perform extensive studies with plutonium. The metallurgical similarities described above make cerium a critical tool in any plutonium modeling effort given the cost and hazards associated with obtaining actual plutonium verification data.

5.0 CONCLUSIONS

The viability of a cerium-based surrogate for the plutonium - 1 wt. pct. gallium alloy has been investigated. The following conclusions are presented as a result of this work:

1. A cerium - 5 wt. pct. (nominal) neodymium alloy was shown to exhibit microsegregation similar to that seen in the plutonium - 1 wt. pct. gallium alloy indicating a positive partitioning coefficient.
2. A cerium - 5 wt. pct. (nominal) lanthanum alloy was shown to exhibit microsegregation similar to that seen in the plutonium - 1 wt. pct. gallium alloy indicating a positive partitioning coefficient.
3. The activation energy for interdiffusion for the cerium - 5 wt. pct. (nominal) lanthanum alloy was determined to be 30,200 cal/mole with a rate equation of:

$$\text{Rate} = 5.6 \times 10^2 \exp [-30200/RT]$$

where R is the universal gas constant = 2 calories / mole * deg K and T is the absolute temperature in Kelvin.

4. An analytical homogenization surrogate relationship between cerium - 5 wt. pct. (nominal) lanthanum and plutonium - 1 wt. pct. gallium was developed with a relationship between activation energies for interdiffusion determined to be:

$$Q_{Pu\text{-}Ga} = 1.3\, Q_{Ce\text{-}La}$$

5. A fundamental link between cerium and plutonium was established using the itineracy of the 4f and 5f electron states (respectively) and the material behavior (crystal structure, phase transformation, diffusion behavior, phase equilibria) derived from this electronic behavior to justify the use of cerium as a physical metallurgy surrogate. Two case studies were presented where the cerium - lanthanum alloy could be used to investigate the behavior of the plutonium - 1 wt. pct. gallium alloy.

6. The width of the two-phase $\delta + \gamma$ region on the cerium - lanthanum phase diagram was better defined indicating the broadening of the region at approximately 2 wt. pct. lanthanum as suggested by the onset of lanthanum microsegregation.

REFERENCES

1 Raraz, Alcides G., Optimization of Plutonium Electrorefining Through modeling and Model Materials. PhD Thesis, T4306, Colorado School of Mines, Golden Colorado, June 24, 1994.

2 Erfurdt, R. J., "An Investigation of the Effect of Iron Content on the Homogenization Response of Plutonium-1Wt% Gallium Alloy. PhD Dissertation, T-2220, December 7, 1979.

3 Carnal, W. T., Choppin, G. R., Plutonium Chemistry, American Chemical Society, Washington, D.C., 1983.

4 Johansson, Borje, Eriksson, O. R., "Structural and Elastic Properties for Plutonium from First-Principles Theory", LA-UR-96-1405, March 6, 1996.

5 Miner, W. N., Plutonium 1970 and the Other Actinides, Part I., "Proceedings for the Fourth International Conference on Plutonium and Other Actinides, Santa Fe, New Mexico, October 5-9, 1970.

6 Rosen, M., Peterson, R. G., and Lloyd, L. T., "The Beta $\rightarrow$ Alpha Transformation in High Purity Plutonium", USAEC Report ANL-7135, Argonne National Laboratory, February, 1966.

7 Selle, J.E., PhD Thesis, "An Internal Friction Study of Allotropic Transformations.", University of Cincinatti, 1967.

8 Miner, W. N., Plutonium 1970 and Other Actinides, Part II., "Proceedings for the Fourth International Conference on Plutonium and Other Actinides, Sante Fe, New Mexico, October 5-9, 1970.

9 Loasby, R. G., Lowe, J. N., "Kinetics of the $\beta \rightarrow \alpha$ Transformation in Plutonium", in Plutonium 1960, , E. Grison, W. B. H. Lord, and R. D. Fowler, Eds. (Cleaver-Hume Press, Ltd., London, 1960), 97.

10 Nelson, R. D., Bowman, F. E., Trans. Met. Soc. AIME 245, 967 (1969).

11 Pascard, R., "Etude par Dilatometrie de la Transformation $\delta \rightarrow \gamma$ du Plutonium Pur," in Plutonium 1960, E. Grison, W. B. H. Lord, and R. D. Fowler, Eds. (Cleaver-Hume Press, Ltd., London, 1960), 16-25.

12 Selle, J. E. , Focke, A. E. , J. Nucl. Mater., 33, 149 (1969).

13 Orme, J. T., Faiers, M. E., Ward, B. J., "The Kinetics of the Delta to Alpha Transformations in Plutonium Rich Pu-Ga Alloys", in Plutonium 1975 and Other Actinides, Eds H. Blank and R. Lindner 1976, North-Holland Publishing Company Amsterdam, pp. 761-773.

14 Adler, P.H., Olson, G.B., Margolies, D. S., "Kinematics of $\delta \rightarrow \alpha$ and $\alpha \rightarrow \delta$ Martensitic Transformation in Plutonium Alloys", Acta Metall, vol 34., No. 10 2053-2064, 1986.

15 Waber, J. T., Some Principles of the Alloying Behavior of Plutonium, Los Alamos Scientific Laboratory, University of California, Los Alamos New Mexico.

16 Barret, C. S., Massalski, T.B., Structure of Metals, Crystallographic Methods, Principles and Data, 3rd Revised Edition, Pergamon Press, 1980.

17 Peterson, D. E., Kassner, M. E., "The Ga-Pu (Gallium-Plutonium) System, Bulletin of Alloy Phase Diagrams, Vol 9, No. 3, 1988, 261-267.

18 Gardner, H. R., "Physical and Mechanical Metallurgy Studies on Delta Stabilized Plutonium Gallium Alloys," BNWL-13, UC-25 Metals, Ceramics and Material (TID-4500, 38th edition), U. S. Atomic Energy Commission, April, 1965.

19 Harvey, M. R. et al, "Chemical Diffusivities of Plutonium-Gallium Alloys in the Epsilon (BCC) Phase" J. Less Common Metals 23:446.SO, 1971.

20 Rafalski, A. L., Harvey, M. R., Riefenberg, D. H., "Gallium Diffusion in Delta Stabilized Pu-Ga Alloys," American Society for Metals Transactions Quarterly, 60:721, 1967.

21 Johnson, K. A., "Homogenization of Gallium-Stabilized Delta-Phase Plutonium,", LA-2989, UC-25, Metals, Ceramics, and Materials, TID-4500 (26th edition), Los Alamos National Laboratory of the University of California, February 28, 1964.

22 Ferrera, D. W., Doyle, J. H., Harvey M. R., "Gallium Coring Profiles for Plutonium-1 Weight Percent Gallium Alloys," RFP-1800, Rocky Flats Plant, Golden, Colorado, May 11, 1972.

23 Porter, D. A., Easterling, K. E., Phase Transformations in Metals and Alloys, page 208, Chapman and Hall, New York, 1992.

24 Edwards, G.R., Tate R. E., Hakkila, E A., J. Nuclear Materials 25 (1968), 304.

25 Shewman, P.G., Diffusion in Solids, The Minerals, Metals and Materials Society, Warrendale, McGraw Hill, New York, New York, Pennsylvania, 1989.

26 Gschneidner, K. A., Eyring, Le Roy, "Handbook on the Physics and Chemistry of Rare Earths, Volume 1 - Metals, North Holland Publishing Company, New York, 1978.

27 Tittman, B. R. correspondence to Westphal, D. A., "Selection of an Analogous Binary Alloy System," Rockwell International, July 2, 1986.

28 Beitscher, S., "Hot Shortness in Plutonium 1 Weight Percent Gallium", Plutonium 1970 and the Other Actinides, Part I., "Proceedings for the Fourth International Conference on Plutonium and Other Actinides, Sante Fe, New Mexico, October 5-9, 1970, 449-456.

29 Erfurdt, R. J., "A Study of Homogenization Rates in Plutonium - 1 Weight Percent Gallium Alloy as a Function of Percent Cold Rolling, RFP-2235, Rocky Flats Plant October 18, 1974.

30 Lograsso M. , Hellawell, A., "The Cata- or Metatectic Reaction - Occurrence and Microstructural Development", Metallurgical Transactions, Vol 19A, (12) 1988, 3097-3100.

31 Johansson, B. and Rosengren, A. "Generalized phase diagram for the rare-earth elements: Calculations and correlations of bulk properties.", Physical Review B, Vol 11, No. 8, April 15, 1974.

32 Haire, R. G. , "Comparison of the Chemical and Physical Properties of f-element Metals and Oxides: Their Dependence on Electronic Properties.", J. Alloys and Compounds 223 (1995) 185-196.

33 N. M. Edelstein, "Comparison of the Electronic Structure of the Lanthanides and Actinides." J. Alloys and Compounds 223 (1995) 197-203.

34 Johansson, B. "Crystal and Electronic Structure Connections Between the 4f and the 5f Transition Metals.", J. Alloys and Compounds, 223 (1995) 211-215.

35 M.S.S. Brooks, O. Eriksson, B. Johansson, "From the Transition Metals to the Rare Earths - Via the Actinides.", J. Alloys and Compounds 223 (1995) 204-210.

36 Gschneidner, K. A., Rare Earth Alloys, A Critical Review of the Alloy Systems of the Rare Earth, Scandium and Yttrium Metals., D. Van Nostrand Company Inc., Princeton, New Jersey, 1961.

37 Katz, J. J., Seaborg, G. T., Morss, L.R., The Chemistry of the Actinide Elements, 2nd ed., Volume 1, 1986.

38 Katz, J. J., Seaborg, G. T., Morss, L.R., The Chemistry of the Actinide Elements, 2nd ed., Volume 2, 1986.

39 Coqblin, B., "The Electronic Structure of Rare-Earth Metals and Alloys: The Magnetic Heavy Rare-Earths, 1977.

40 Kaindl, G., "Bulk and Surface Electronic Structure of Lanthanide Metals", J. Alloys and Compounds 223 (1995) 265-273.

41 Dariel, M. P., "Diffusion of ^{140}La in b.c.c. γ-Lanthanum and δ-Cerium", Philosophical Magazine, 1973, Vol. 28, page 915-922.

42 Cornet, J. A., 1971, J. Phys. Chem. Solids, 32, 1489.

43 Gschneidner, K.A., Jr., Calderwood, F. W. "The Ce-Nd (Cerium-Neodymium) System." Bulletin Alloy Phase Diagrams; 3 (1), 1982; p. 90.

44 Gschneidner, K. A. Jr., personal communication.

45 Tate, R. E., Edwards, G. H., and Hakkila E. A., "Diffusion in Stabilized Delta Plutonium - 2% Aluminum", Journal of Nuclear Materials, 29 (1969), 154-160.

46 Reed-Hill, R. E., Physical Metallurgy Principles, Second Edition, D. Van Nostrand Company, New York, 1973.

47 Spedding, F. H., Daane, A. H., The Rare Earths, Ames Laboratory, Iowa State University, John Wiley and Sons, New York, 1961.

48 Liptai, R. G., Lloyd, L. T., Friddle, R. J., "The Effects of High Pressure and Temperature on the Microstructure of Plutonium", Journal of Nuclear Materials, 17, Argonne National Laboratory, May 31, 1965.

49 Kothe, D., personal communication, Los Alamos National Laboratory, December, 1998.

APPENDIX A

Diffusion Equation Development

An expression for the diffusion coefficient can be developed starting with an atomistic development. The following variable definitions are given:

Variable Definitions	
	a_o = lattice parameter
t = time	ΔS_v = entropy for the creation of vacancies
Γ = jump frequency	ΔS_m = entropy associated with atom motion
υ = Debye frequency	ΔH_v = enthalpy associated with the creation of vacancies
N_v = equilibrium concentration of vacancies	ΔH_m = enthalpy associate with atom motion
ΔG_v = Gibbs free energy for vac. formation	Q = activation energy
ΔG_m = Gibbs free energy for atom motion	J = flux of atoms
n = # atoms / area	f = jump correlation factor
β = jump distance	γ = geometric factor

The flux of atoms between two equidistant planes can be analytically described as follows:

$$J = \left\{ n_1 \frac{\text{atoms}}{\text{area}} \right\} * \left\{ \Gamma \frac{\text{jumps}}{\text{sec}} \right\} * \Delta t$$

$$- \left\{ n_2 \frac{\text{atoms}}{\text{area}} \right\} * \left\{ \Gamma \frac{\text{jumps}}{\text{sec}} \right\} * \Delta t$$

$$J = \Gamma (n_1 - n_2) \Delta t$$

For a cubic system: Only one sixth of the atoms jump in a given direction because there are five other choices of places to jump. Therefore the flux relationship becomes:

$$J = \tfrac{1}{6}\Gamma (n_1 - n_2) \Delta t$$

Relate the number of atoms to concentration:

$$C_1 = \frac{\#\text{ atoms}}{\text{volume}} = \frac{\#\text{ atoms}}{\text{area}} * \left\{ \frac{1}{\text{distance}} \right\} = \frac{n_1}{\beta}$$

$$C_2 = \frac{n_2}{\beta}$$

Plug into flux equation

$$J = \tfrac{1}{6}\Gamma\beta (C_1 - C_2)$$

Note: $C_1 - C_2 = -\beta\, dC/dx$ **Assumption**: Jumps from one plane to another are the same so that if there are more atoms on plane 1 than on plane 2 then the net flux is from 1 to 2.

Equating the above equations:

$$J = \tfrac{1}{6}\Gamma\beta^2\, dC/dx$$

The above equation can be related to Fick's First Law $J = - D\, dc/dx$

Therefore:

$$D = \tfrac{1}{6}\Gamma\beta^2$$

If the relationship for D is generalized such that β is not simply considered as a jump between two planes, but as a general jump distance identified as α, then:

$$D = \tfrac{1}{6} \Gamma \alpha^2$$

Conceptually, the average number of jumps can be written:

Avg. # of jumps = (# of attempted jumps) * (# of nearest neighbor sites) * (probability of successful jumps) * (probability that the site is vacant)

Analytically this equation is written

$$(\Gamma)(\Delta t) = (\upsilon)(Z) \exp [- \Delta G_m/RT] (N_v) (\Delta t)$$

Solving for the Jump Frequency

$$\Gamma = (\upsilon)(Z) \exp [- \Delta G_m/RT] (N_v)$$

The equilibrium concentration of vacancies can be shown to be:

$$N_v = \exp [- \Delta G_v/RT]$$

Using the above equations, develop an expression for the diffusion coefficient

$$D = \tfrac{1}{6} \Gamma \alpha^2$$

$$D = \tfrac{1}{6} \upsilon Z \alpha^2 \exp [- \Delta G_m/RT] \exp [- \Delta G_m/RT]$$

$$D = \tfrac{1}{6} \upsilon Z \alpha^2 \exp [-\Delta S_m/R] \exp [-\Delta S_v/R] \exp[- (\Delta H_v + \Delta H_m) /RT]$$

The diffusion coefficient can be generalized and put in terms of a crystal lattice parameter using a geometric factor γ:

$$D = \gamma a_o^{\,2} f \upsilon \exp[-\Delta S_m/R] \exp[-\Delta S_v/R] \exp[-(\Delta H_v + \Delta H_m)/RT]$$

The generalized equation for the diffusion coefficient is written:

$$\mathbf{D = D_o \exp[-Q/RT]}$$

The activation energy associated with diffusion then is the sum of the enthalpy terms and the pre-exponential factor D_o is also defined:

$$\mathbf{Q = \Delta H_v + \Delta H_m}$$

$$\mathbf{D_o = \gamma a_o^{\,2} f \upsilon \exp[-\Delta S_m/R] \exp[-\Delta S_v/R]}$$

APPENDIX B

The following appendix includes the binary phase diagrams which were reviewed as potential surrogate systems. The initial review involved identification of a potential two-phase region that may lead to microsegregation similar to that in plutonium - 1 wt. pct. gallium.

Al-Ti

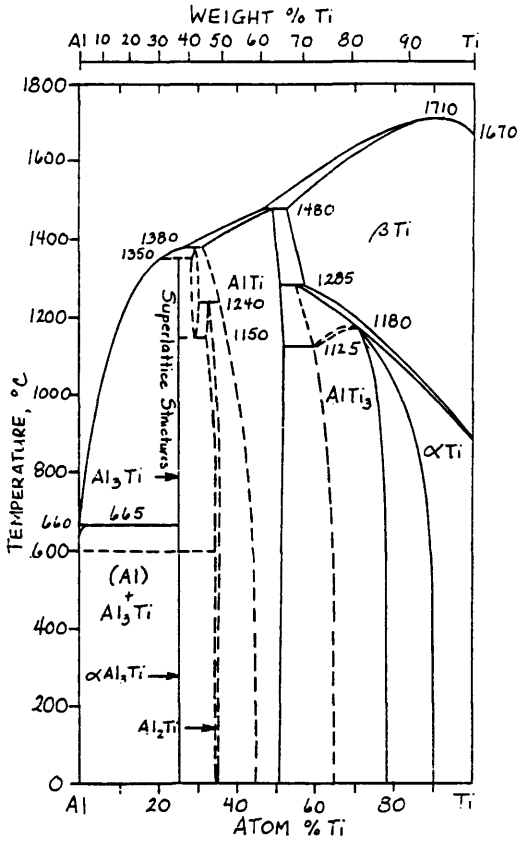

The diagram shown which differs in only detail from the 11/85 Handbook assessment is based on an exhaustive analysis of the literature through 1984, ref (1). Despite the large number of studies of this system uncertainties remain, for example the structures Al_5Ti_3 and $Al_{11}Ti_7$ are believed not to be equilibrium bulk phases and some phase boundaries, shown dotted are not known with precision. Phase boundaries in ref. (1) are shown down to 500°C but have been extended here to room temperature assuming no low temperature transformations. $TiAl_3$ ($TiAl_3$ type), ∝ $TiAl_2$* (Ga_2Zr type), $TiAl_2$ (Ga_2Hf type), TiAl (AuCu type) and Ti_3Al (Ni_3Sm type).

*Not shown on the diagram.

(1) Murray, J.L.
"The Al-Ti (Aluminum-Titanium) System."
"Phase Diagrams of Binary Titanium Alloys"
ASM INTERNATIONAL, 1987; pp 12-24.

REC 3/90

Zr-Al Phase Diagram

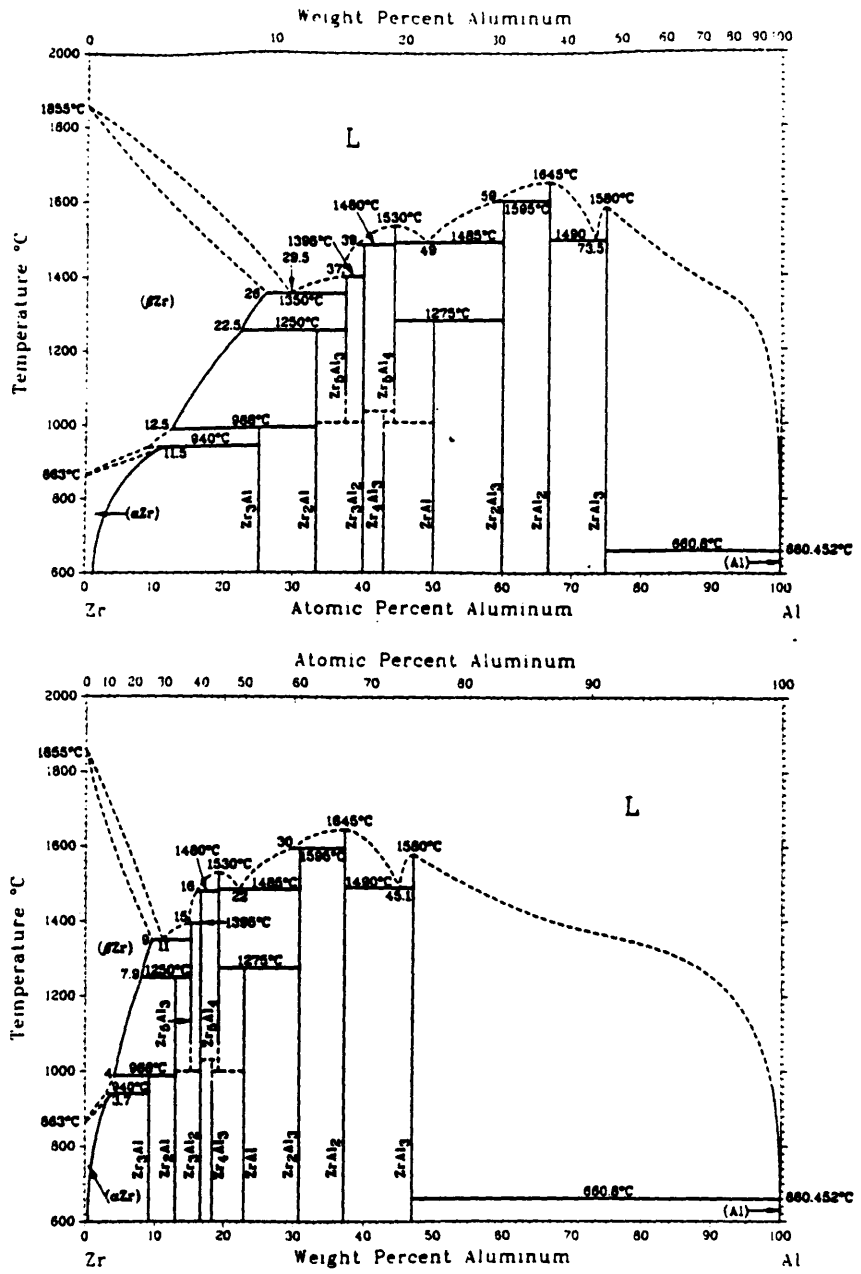

A. Peruzzi and J.P. Abriata, submitted to the APD Program.

Bi-Zr Phase Diagram

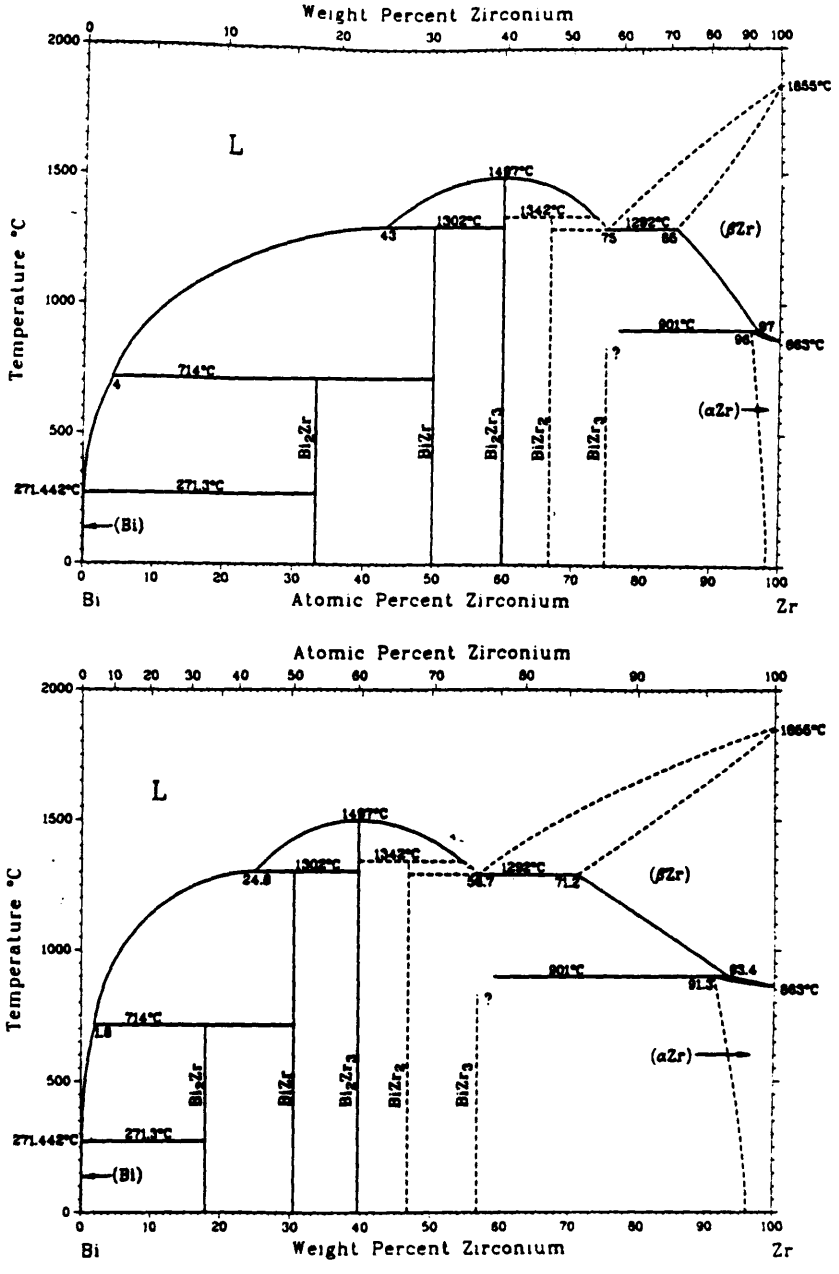

H. Okamoto, 1990.

Ca-Sr

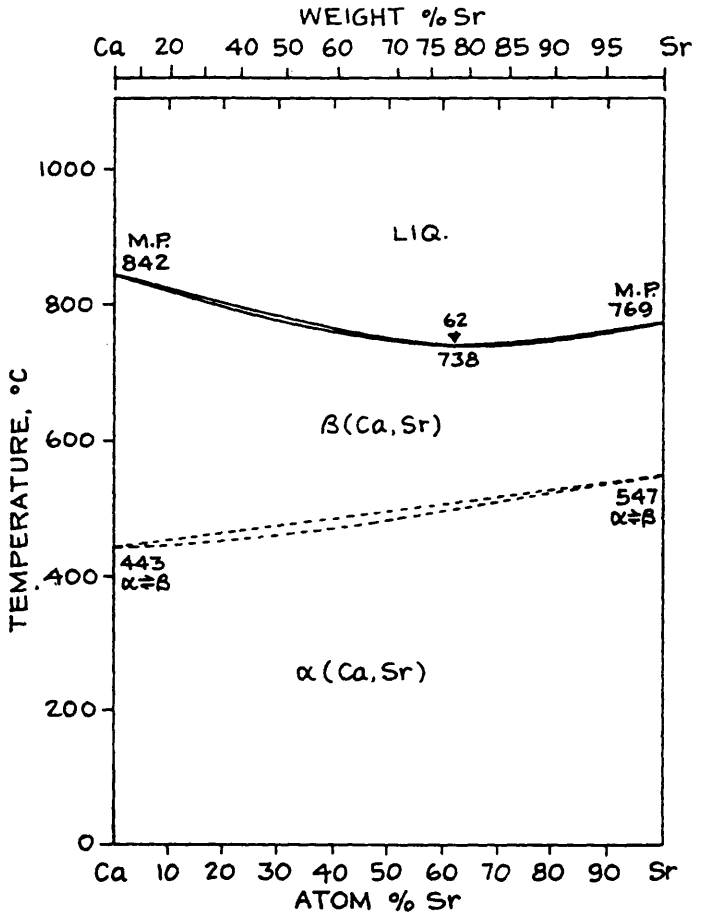

Diagram redrawn from ref. 1 which reviewed the literature through 1984. The diagram includes two continuous solid solutions and not three, as shown in Elliott Fig. 126; it is now known that the third, CPH, continuous solid solution is associated with the presence of more than 0.002 wt.% hydrogen in the alloy.

(1) Alcock, C.B. and Itkin, V.P.
"The Ca-Sr (Calcium-Strontium) System."
BULL. ALLOY PHASE DIAGRAMS; 7(5), 1986; pp 455-457.

11/88

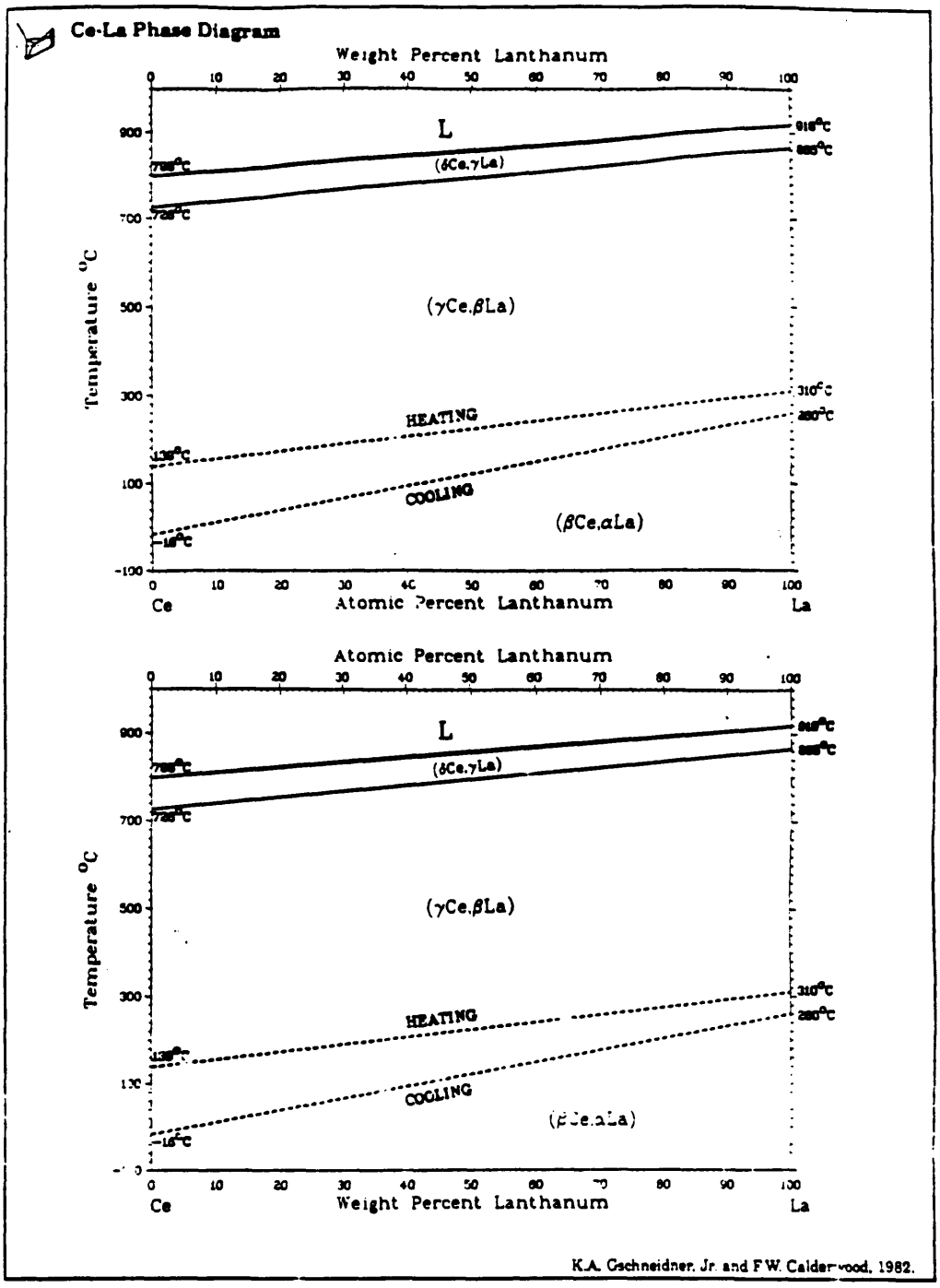
Ce-La Phase Diagram
Weight Percent Lanthanum
0 10 20 30 40 50 60 70 80 90 100
900
700
500
300
100
-100
Temperature °C
L
(δCe,γLa)
(γCe,βLa)
HEATING
COOLING
(βCe,αLa)
Ce
Atomic Percent Lanthanum
La
Atomic Percent Lanthanum
Weight Percent Lanthanum
K.A. Gschneidner, Jr. and F.W. Calderwood, 1982.

Ce-Nd

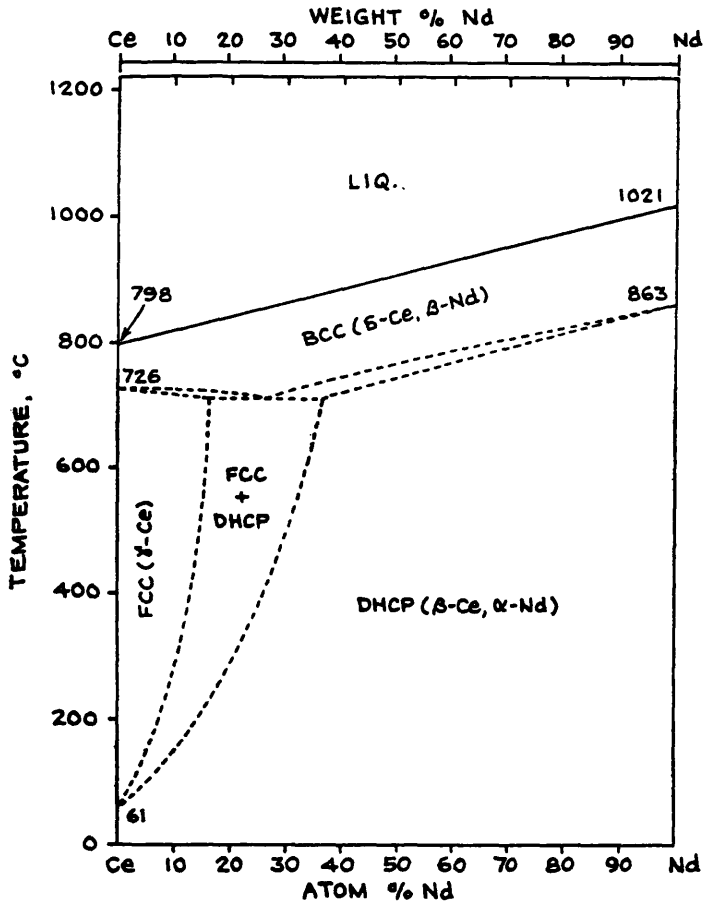

No diagram found in literature; above sketch provided by Handbook compiler as likely form of diagram. Alloys quenched from 600°C are FCC at 10 at.% Nd, two-phase at 20 and 30 at.% Nd and DHCP at 40 to 100 at.% Nd. The 61°C Ce $\beta \rightleftharpoons \gamma$ is a mean value for heating (139°C) and cooling (-16°C). See, also, ref. 2.

(1) Speight, J.D.; Harris, I.R.; and Raynor, G.V.
"Alloys of Cerium with Neodymium, Samarium and Terbium, and of Praseodymium with Terbium."
JLCM; 15 (1968); pp 317-330

(2) Gschneidner, K.A., Jr. and Calderwood, F.W.
"The Ce-Nd (Cerium-Neodymium) System."
BULL. ALLOY PHASE DIAGRAMS; 3(1), 1982; p. 90

Ce-Sm

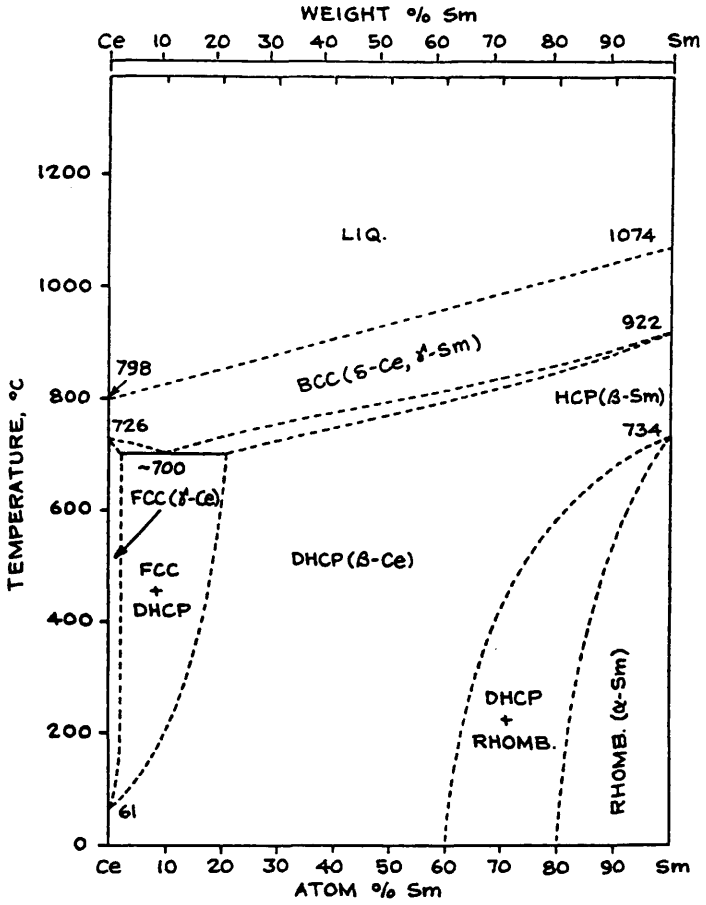

Diagram redrawn from ref. 1. A continuous series of solid solutions exists between DHCP and HCP at elevated temperature. The 61°C Ce $\beta \rightleftharpoons \delta'$ is a mean value for heating (139°C) and cooling (-16°C).

(1) Gschneidner, K.A., Jr. and Calderwood, F.W.
"The Ce-Sm (Cerium-Samarium) System."
BULL. ALLOY PHASE DIAGRAMS; 3(2), 1982; pp 190-192

Ce-Zr

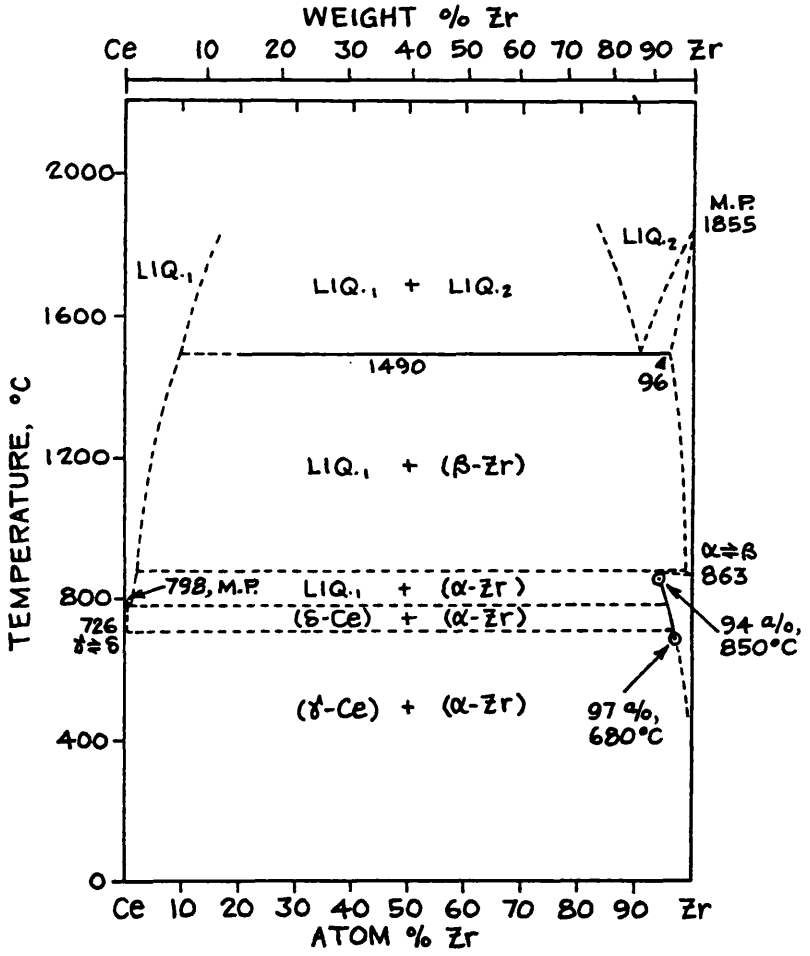

Schematic diagram constructed by Handbook compiler from limited data cited and presented in ref. 1, and assumption that Ce-Zr is similar to Ce-Ti. Liquid immiscibility and absence of intermediate phases is characteristic of this system.

(1) Harris, I.R. and Raynor, G.V.
"The Electronic State of Cerium in Zirconium-Cerium Alloys."
JLCM; 6, 1964; pp 70-80.

7/87

Co-Os Phase Diagram

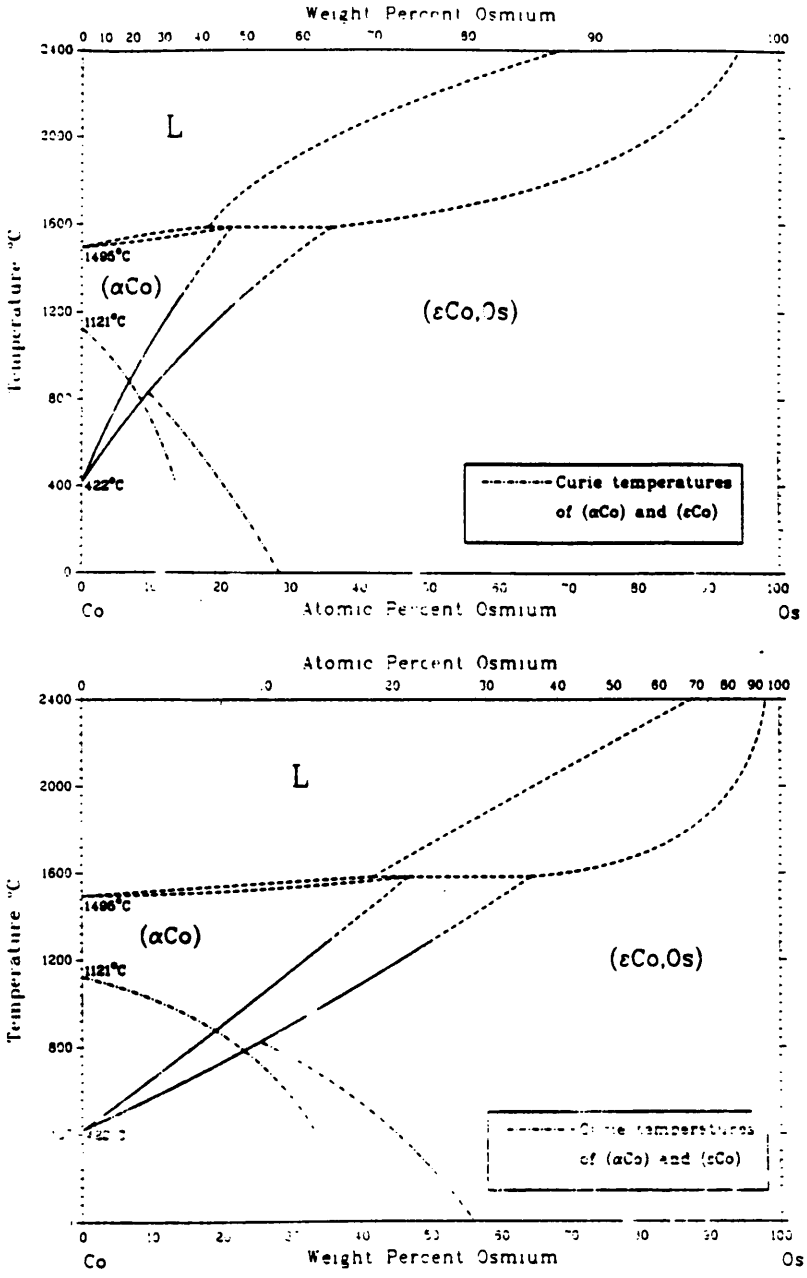

From [52Kos].

Eu-Yb

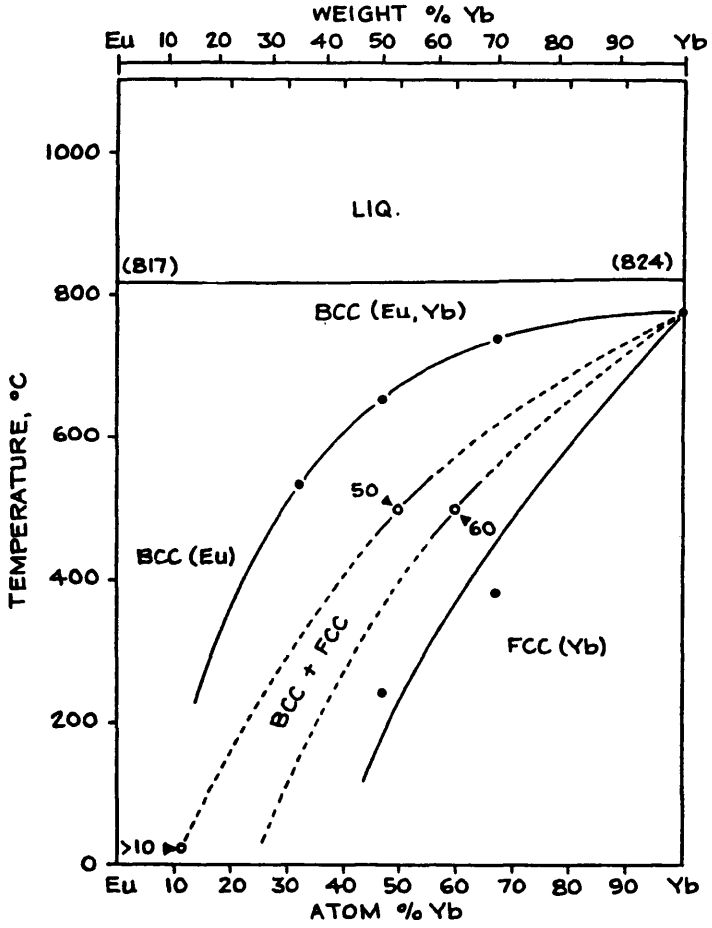

BCC+FCC boundaries, solid lines and data points, redrawn from ref. 1. Dashed lines and open circles, data from ref. 2 which indicates a much narrower width of the two-phase field (50 to 60 at. pct Yb at 500°C). M.P. of Eu and Yb, selected values from Hultgren, et al.

(1) Koziov, V.G.; Stanolevich, G.F.; and Kulifeev, V.K. "Interactions in the Europium-Ytterbium System." (in Russian) NAUCHN. TR. MOSKOV INST. STALI SPLAVOV; 117 (1979); pp 99-101

(2) King, E. and Harris, I.R. "The Pressure-Resistance Behavior of some Ytterbium-Europium Alloys." JLCM; 20 (1970); pp 237-244

11/82

Ga-Ti

220

Ti-Ga Phase Diagram

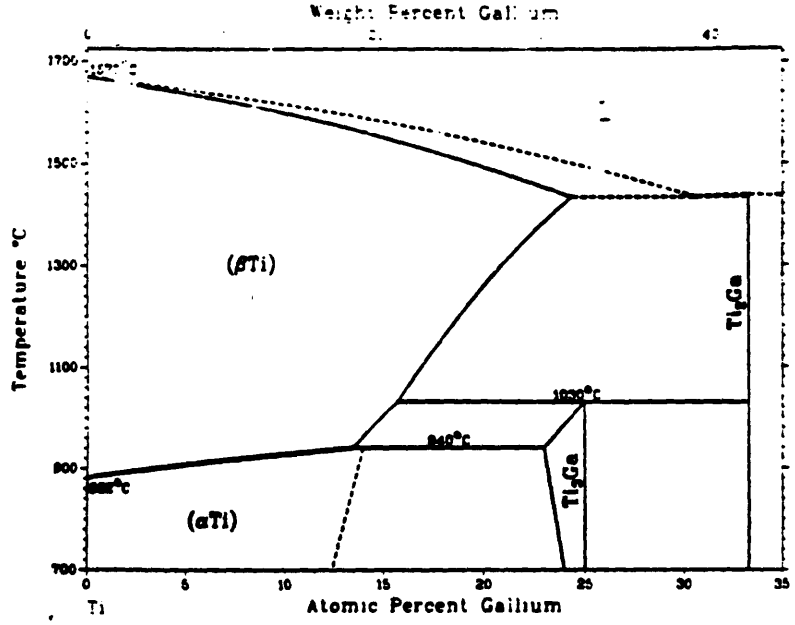

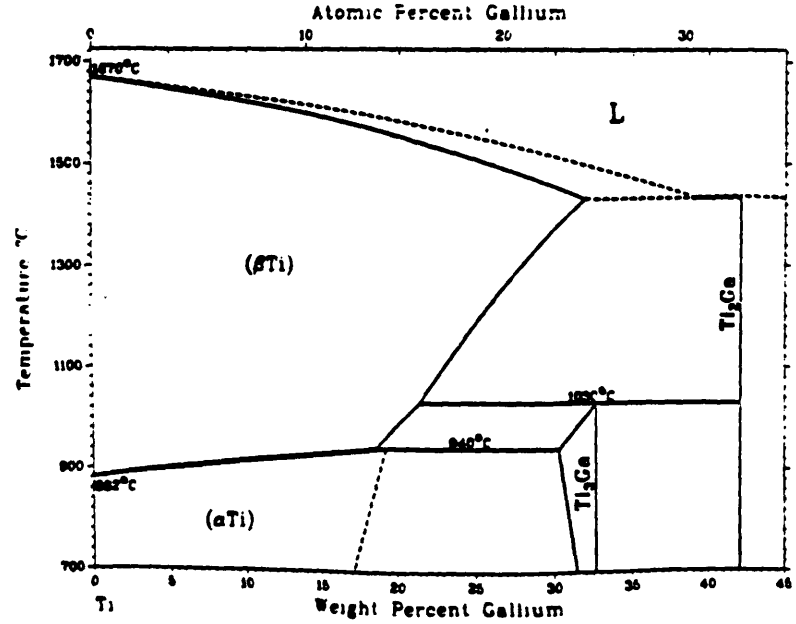

J.L. Murray, 1987.

Hf-Zr

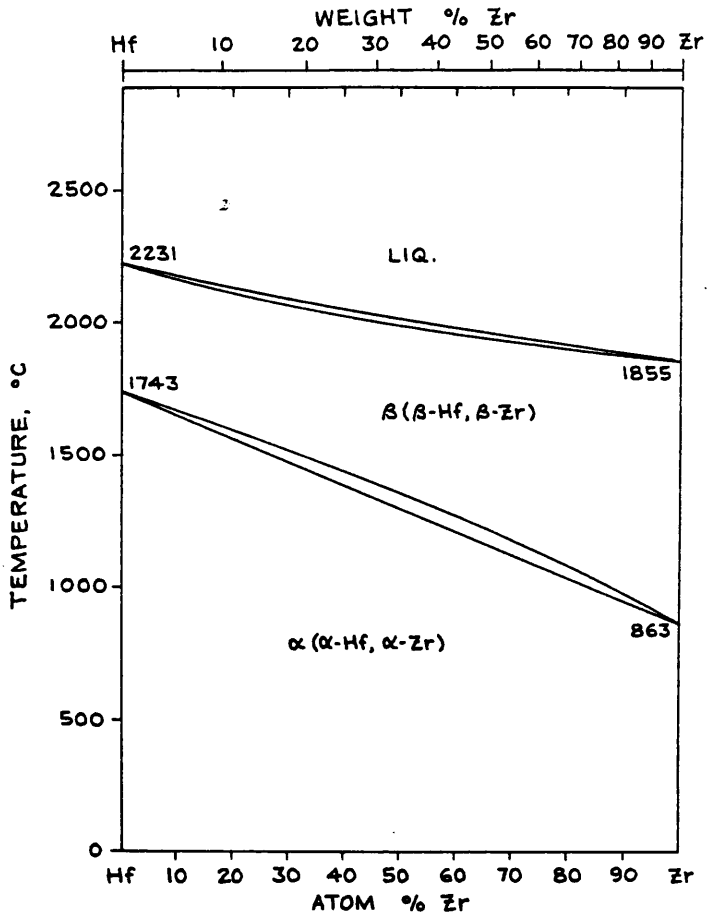

Diagram redrawn from ref. 1 which reviews the literature through 1981. Complete miscibility exists between the constituent metals in the liquid state and in both high and low temperature crystal modifications, in the solid state. No ordering reactions in the solid state have been reported. See ref. 1 for information on high pressure equilibria.

(1) Abriata, J.P., Bolcich, J.C.; and Peretti, H.A.
"The Hf-Zr (Hafnium-Zirconium) System."
BULL. ALLOY PHASE DIAGRAMS; 3(1), 1982; pp 29-34.

11/84

La - Th

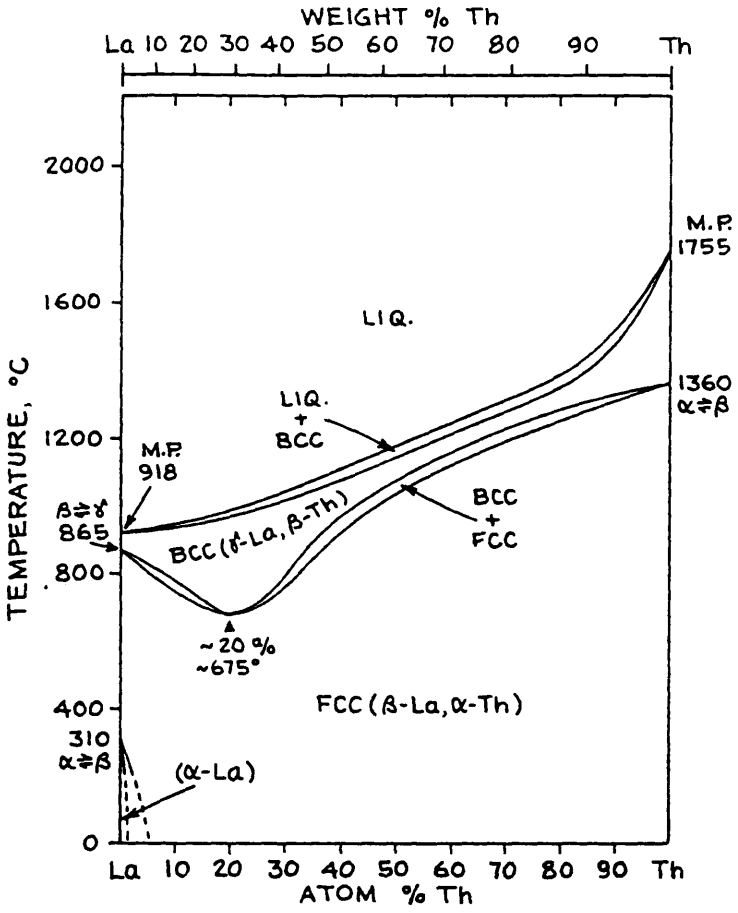

Diagram redrawn from ref. 1 which cites a source paper not readily available. The diagram in ref. 1 does not contain temperature notations; however, scaling the diagram yields melting points and transition temperatures close to currently accepted values and those values are indicated on the above diagram.

(1) Badayeva, T.A. and Kuznetsova, R.I.
"Nature of the Interactions between Thorium and R.E. Metals."
RUSSIAN METALLURGY (Metally); 1969, No. 5; pp 101-106.

11/88

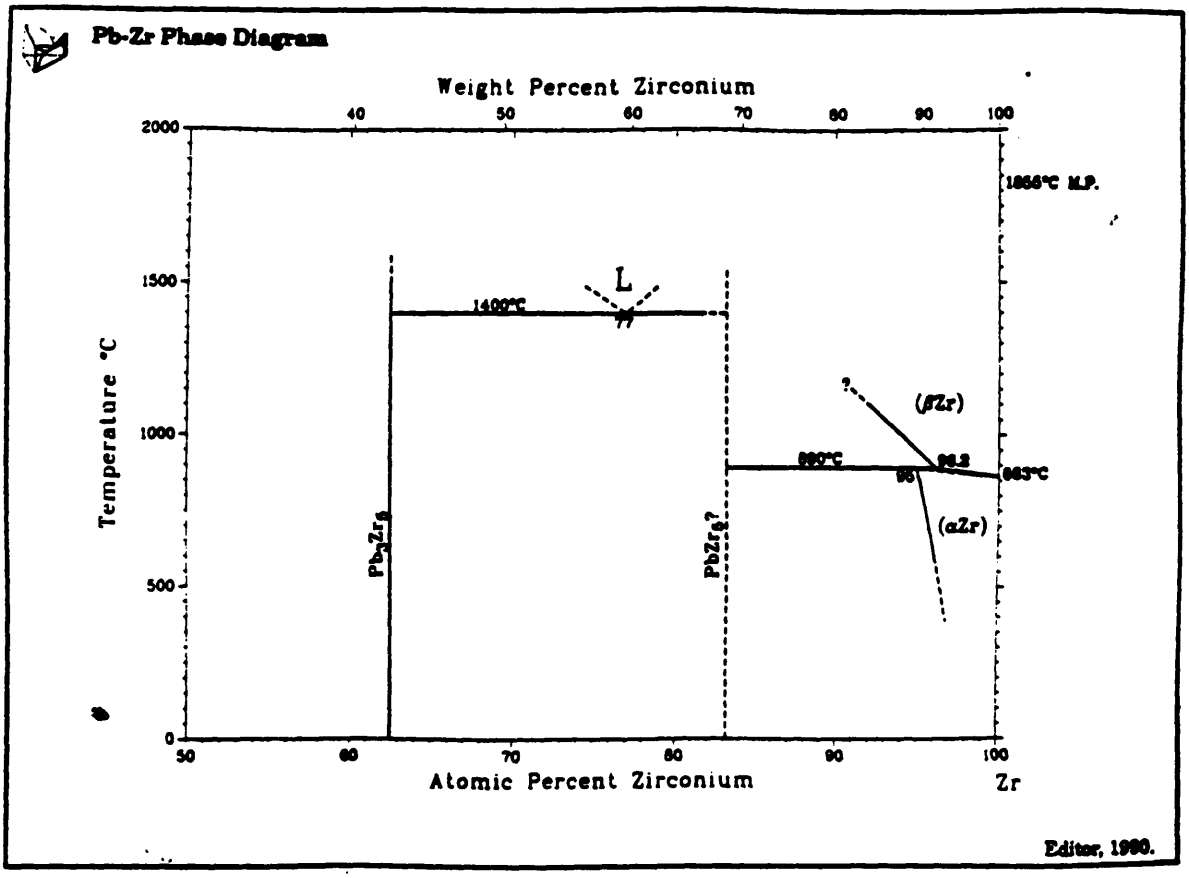
Pb-Zr Phase Diagram
Weight Percent Zirconium
40
50
60
70
80
90
100
2000
1500
1000
500
0
Temperature °C
1855°C M.P.
L
1400°C
?
(βZr)
990°C
98.2
863°C
98
(αZr)
Pb3Zr5
PbZr5?
50
60
70
80
90
100
Atomic Percent Zirconium
Zr
Editor, 1980.

Sb-Zr Phase Diagram

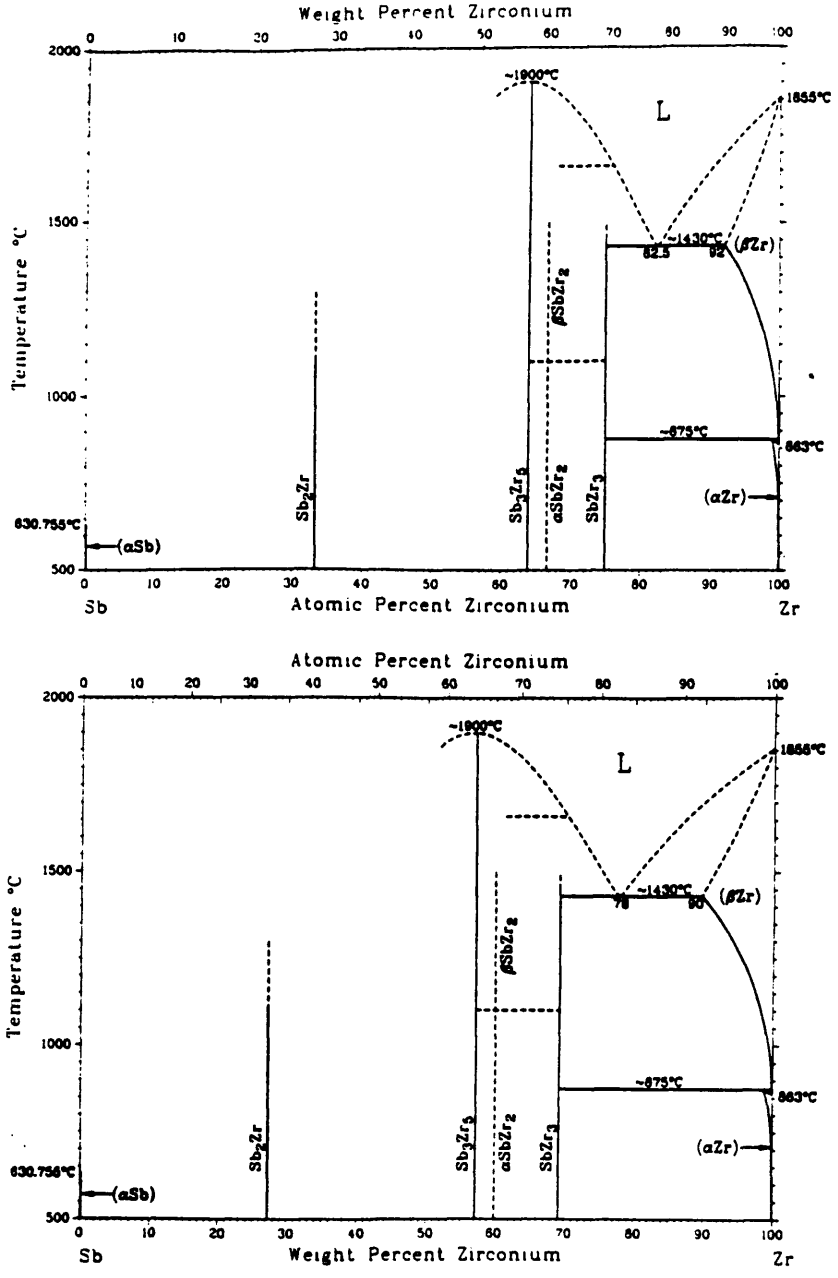

H. Okamoto, submitted to the APD Program.

Sn-Zr

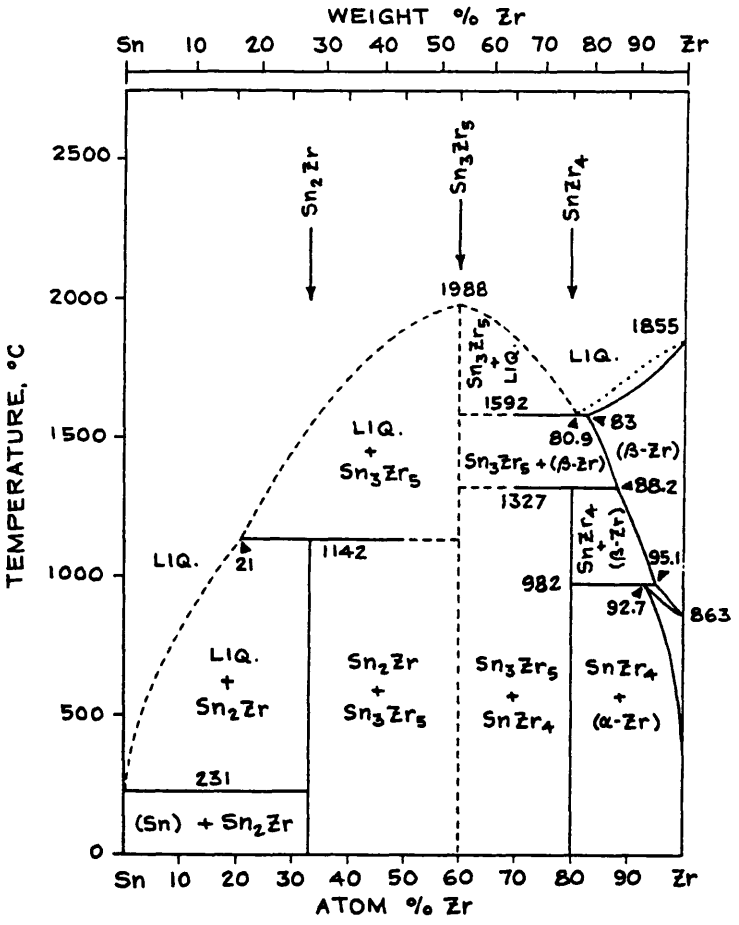

Diagram redrawn from ref. 1 which searched the literature through 1981. The diagram is not different in kind from that of Hansen Fig. 660; however the congruently melting intermediate phase (1988°C) is designated Sn_3Zr_5, although it occurs at about 60 at.% Zr, because it has the Mn_5Si_3 type crystal structure. See ref. 1 for more detailed information on phase boundaries, thermodynamics, and a brief discussion of metastable states (which evidently are associated only with Zr-rich, oxygen-contaminated alloys).

(1) Abriata, J.P.; Bolcich, J.C.; and Arias, D.
"The Sn-Zr (Tin-Zirconium) System."
BULL. ALLOY PHASE DIAGRAMS; 4(2), 1983; pp 147-154.

11/84

APPENDIX C

Metallographic Preparation Procedure for Cerium Alloys

Mounting: Cerium specimens were mounted using a LECO "cold-mount" liquid epoxy material. A "cold mount" was required due to the pyrophoric nature of cerium. Traditional methods cause the cerium to ignite due to the elevated temperature.

Grinding: Specimens were ground on a belt sander using water as a lubricant until the specimen was flush with the mount. Hand grinding was then used starting with a 240 grit paper and ending with a 600 grit paper. Water or kerosene can be used us a lubricant although kerosene limits oxide and hydride formation. Following grinding with 600 grit paper, the specimen was ultrasonically cleaned with ethyl alcohol for approximately 1 minute.

Polishing: Polishing was accomplished with oil suspension diamond polish starting with a 6 μm and ending with a 1μm suspension. Polishing time on each wheel was conducted for approximately 45 seconds and specimens were ultrasonically cleaned in ethyl alcohol for 1 minute after each polish.

Etching: Etching was accomplished with a 5% Nital solution for approximately 30 seconds. After etching, the specimen was covered with an optically clear immersion to inhibit oxidation and preserve the specimen for subsequent photography.

APPENDIX D

Solution of Fick's Second Law - Method of Separation of Variables

Fick's Second Law:

$$\frac{dc}{dt} = D\frac{d^2c}{dx^2}$$

Separation of variables assumes that the solution to the differential equation can be written in terms of a "distance" function and a "time" function. Then assume the solution can be written as a product of these two functions:

$$C = X(x) * T(t)$$

Substituting into Fick's Second Law equation:

$$X\frac{dT}{dt} = DT\frac{d^2X}{dx^2}$$

Separating the variables:

$$\frac{1}{T}\frac{dT}{dt} = \frac{D}{X}\frac{d^2X}{dx^2}$$

Note: The left hand side is dependent on "t" only while the right hand side is dependent on "x" only. This can only be true if both sides are equal to the same constant. Let this constant be:

$$\text{Constant} = -\lambda^2 * D$$

Therefore:

$$\frac{1}{T}\frac{dT}{dt} = -\lambda^2 * D$$

$$\frac{1}{X}\frac{d^2X}{dx^2} = -\lambda^2$$

Solutions to the separated equations:

$$T = \exp(-\lambda^2 Dt)$$

$$X = A \sin \lambda x + B \cos \lambda x$$

Overall solution:

$$C = (A \sin \lambda x + B \cos \lambda x) * \exp(-\lambda^2 Dt)$$

A, B are constants of integration

Since this is a linear equation, the most general solution is found by summing solutions of this type:

$$C = \Sigma (A_m \sin \lambda_m x + B_m \cos \lambda_m x) * \exp(-\lambda_m^2 Dt)$$

The constants A_m, B_m, λ_m are determined by the particular boundary conditions of a particular problem.

For the following problem:

Diffusion out of a plane sheet of thickness l, through which the diffusing substance is initially uniformly distributed and the surfaces of which are kept at zero concentration. The initial and boundary conditions are as follows:

$$C = C_o \qquad 0 < x < l \quad t = 0$$

$$C = 0 \qquad x = 0, \; x = l, \; t > 0$$

This results in the following:

$$C_o = \Sigma A_m \sin(m\pi x/l), \qquad 0 < x < l$$

Multiply both sides by sin ($p\pi x/l$) and integrate from 0 to l, the solution is:

$$A_m = \frac{4\,C_o}{m\pi} \qquad m = 1, 3, 5, \ldots.$$

Final Solution:

$$C = \frac{4\,C_o}{\pi} \sum 1/(2n+1) * \exp[\, -D(2n+1)^2\, \pi^2\, t / l^2\,] \sin((2n+1)\, \pi x)/l$$

APPENDIX E

The following development provides a methodology to relate the time for homogenization in the surrogate alloy to the plutonium - 1 wt. pct. gallium alloy. Using the Larson - Miller [46] development, the rates at which homogenization takes place in each system are equated. This development assumes that the mechanism for diffusion in both alloys is consistent and the atomic jumps are directly related to the Debye frequency.

$$\text{Rate} = 1/t_{Pu} = 1/t_o \exp [-Q_{Pu} / kT_{Pu}] = 1/t_{Ce} = 1/t_o \exp [-Q_{Ce} / kT_{Ce}]$$

Where t_{Pu} and t_{Ce} are homogenization times for plutonium and cerium respectively, Q_{Pu} and Q_{Ce} are the activation energies, k is the Boltzman constant, T is the absolute temperature in degrees Kelvin and t_o is the Debye frequency. Taking the natural log of both sides of these equations results in the following:

$$-\ln t_{Pu} = -\ln t_o - Q_{Pu} / kT_{Pu}$$

$$-\ln t_{Ce} = -\ln t_o - Q_{Ce} / kT_{Ce}$$

Utilizing the proportionality constant determined in this work from the determination of the activation energy for diffusion:

$$Q_{Pu} = \beta Q_{Ce}$$

where $\beta = 1.3$

Solving for activation energy:

$$Q_{Pu} = kT_{Pu} [- \ln t_o + \ln t_{Pu}]$$

$$Q_{Ce} = kT_{Ce} [- \ln t_o + \ln t_{Ce}]$$

Equating the activation energies and using the proportionality constant the homogenization time for the cerium alloy can be determined:

$$\ln t_{Ce} = \ln t_o + T_{Pu} / \beta T_{Ce} [\ln t_{Pu} - \ln t_o]$$

APPENDIX F

Relationship Between Creep and Activation Energy for Diffusion

Creep can be directly related to the activation energy for diffusion by relating the energy associated with atoms "jumping" over an energy barrier and the mechanisms associated with thermally assisted dislocation motion. Using the concept of a Maxwell-Boltzmann distribution of atoms, the rate of atomic jumps over the energy barrier an be written as the product of a frequency of jumps and a probability term as shown in Figure E-1. The net jump rate is the difference between the forward and backward jumps and can be written:

$$\nu_{net} = \nu_{forward} - \nu_{backward}$$

$$\nu_{net} = \nu_e \exp [- G_A / kT] - \nu_e \exp [-(G_A + G_T) / kT]$$

$$\nu_{net} = \nu_e \exp [- G_A / kT] [1 - \exp [G_T / kT]$$

where the variables are as defined in Figure E-1.

The atomic jump described above is analogous to the thermally activated motion of a dislocation. The energy barrier associated with a section of dislocation moving is related to the activation energy for diffusion and the energy needed to initiate dislocation motion.

Using the energy associated with dislocation motion described in Figure E-2, a net jump rate can be expressed:

$$\nu_{net} = \nu_e \exp [-Q^* / kT] - \nu_e \exp [-(Q^* + \sigma bA) / kT]$$

The jumping rate can be related to the dislocation velocity as follows:

velocity = [# segments that move by a thermally activated mechanism] [Distance moved] [Breakaway frequency]

Analytically this expression is written:

$$\text{velocity} = (n/N)\ (\delta)\ (\nu_{net})$$

where n is equal to the number of segments which can move an average distance δ and N is equal to the number of dislocation segments.

Substituting for ν_{net}:

$$\text{velocity} = \nu_o \exp [Q^* / kT] [1 - \exp [\sigma bA / kT]$$

where ν_o is a constant which is a function of applied stress, dislocation density and distribution and temperature.

Using the relationship $Q = Q^* + \sigma bA$

$$\text{velocity} = 2 \nu_o \exp [-Q/ kT] \sinh (\sigma bA / kT)$$

In order to relate dislocation velocity to creep rate, the Bailey - Orowan equation is used:

$$\dot{\varepsilon} = (\rho) (b) (\text{velocity})$$

where ρ is the dislocation density, b is the Burger's vector and $\dot{\varepsilon}$ is the creep rate.

The relationship between creep rate and the activation energy for diffusion is generalized as follows:

$$\dot{\varepsilon} = (\rho) (b) (\text{constant}) (\sigma/\mu)^n \exp [-Q / kT] \sinh (\sigma bA / kT)$$

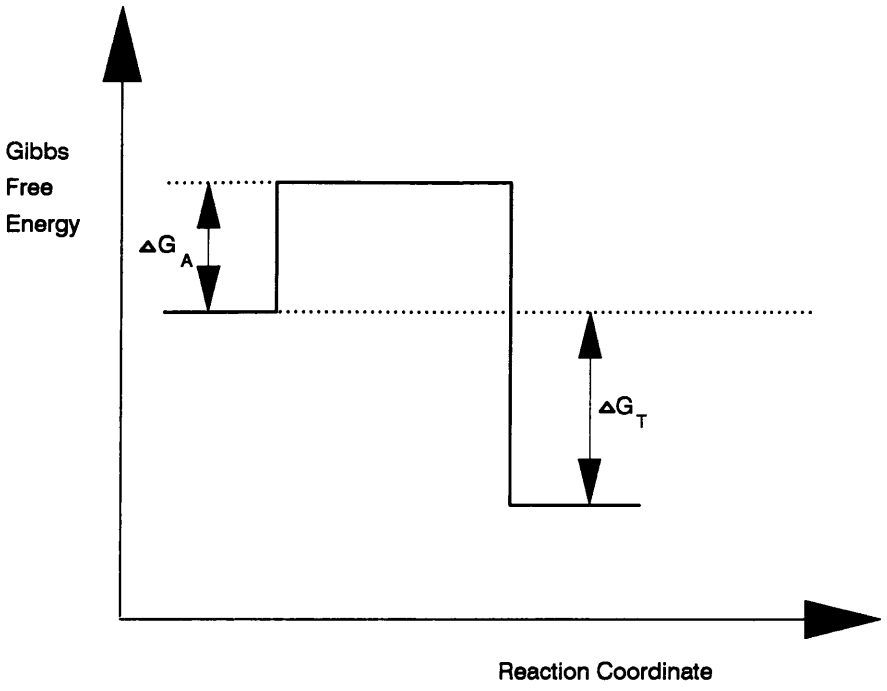

$$V_{\text{forward jump}} = V_e \left[\exp \left[-\Delta G_A / kT \right] \right]$$

V_e = Einstein frequency

ΔG_A = barrier energy

ΔG_T = driving force to jump

$\exp \left[-\Delta G_A / kT \right]$ = probability that jump is successful

Figure F-1: Conceptual development of the rate of atomic jumps using Maxwell-Boltzman distribution

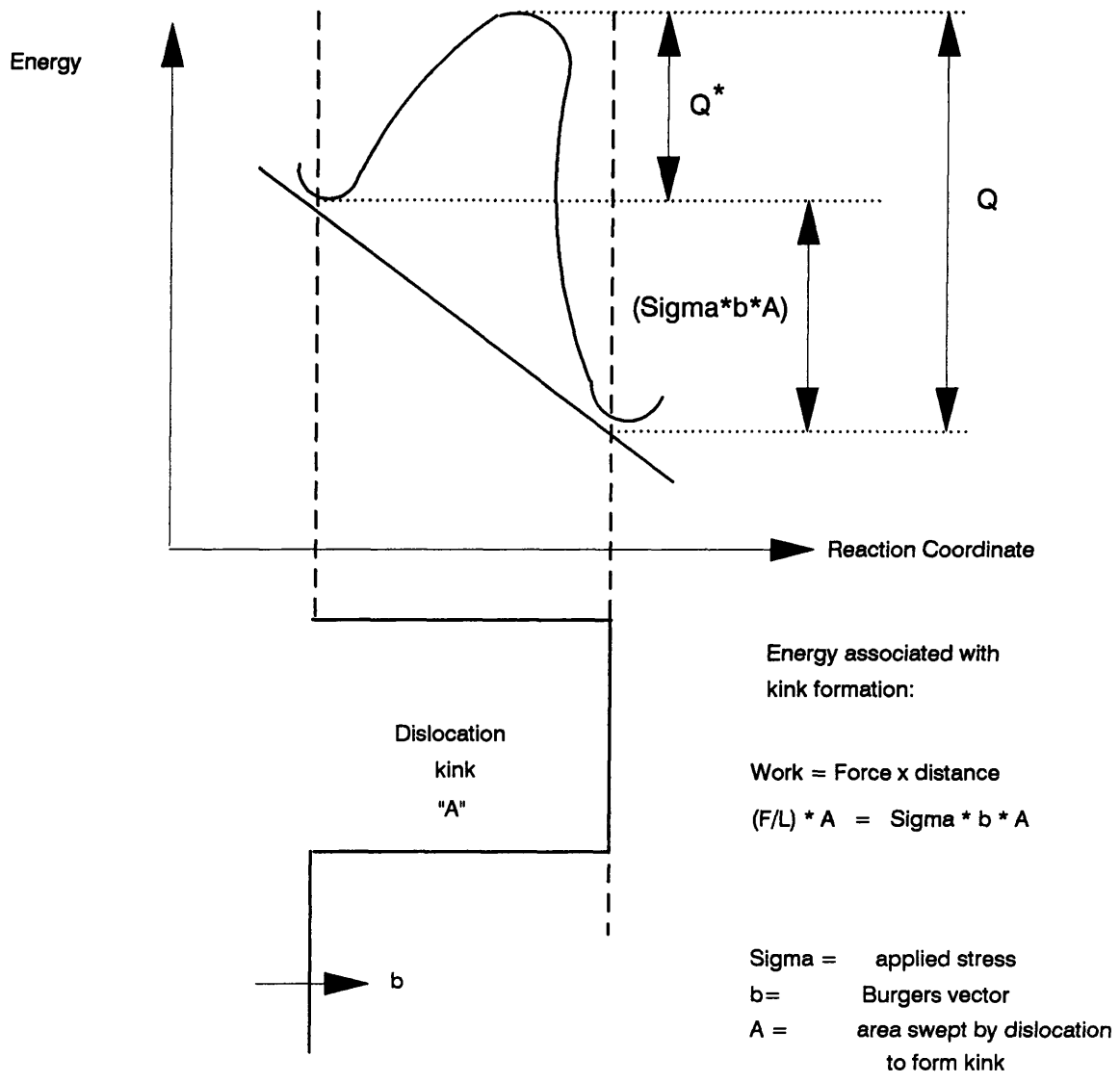

Figure F-2: Impact of applied stress, the formation of a dislocation kink and the relationship to Maxwell-Boltzman barrier energies.